

The Impact of ENSO on Tropical and Extratropical  
Atmospheric Variability on Intraseasonal and Synoptic  
Time Scales as Inferred from Observations and GCM  
Simulations

Chi-Yung Tam

A dissertation  
presented to the Faculty  
of Princeton University  
in candidacy for the degree  
of Doctor of Philosophy

Recommended for acceptance  
by the Program in  
Atmospheric and Oceanic Sciences

January 2004

© Copyright by Chi-Yung Tam, 2003. All rights reserved.

# Contents

<b>Abstract</b>	<b>ix</b>
<b>Acknowledgments</b>	<b>x</b>
<b>1 Introduction</b>	<b>1</b>
<b>2 Description of GCM Experiment and Datasets</b>	<b>5</b>
2.1 Numerical model and GCM Experiment . . . . .	5
2.2 Reanalysis Data . . . . .	7
<b>3 Climatological Behavior of the Madden-Julian Oscillation</b>	<b>10</b>
3.1 Introduction . . . . .	11
3.1.1 Observations of the MJO . . . . .	11
3.1.2 Theoretical and modeling studies . . . . .	12
3.2 Temporal Characteristics and Spatial Modulation of Intraseasonal Oscillation in the Tropics . . . . .	14
3.2.1 Spectral analysis . . . . .	14
3.2.2 Intraseasonal variance . . . . .	20
3.3 MJO Propagation as inferred from Lag Correlation . . . . .	25
3.3.1 Computation method . . . . .	25

3.3.2	Growth rates and phase speeds . . . . .	27
3.4	CEOF Analysis . . . . .	32
3.4.1	Computation procedures . . . . .	32
3.4.2	MJO composite anomalies . . . . .	34
3.5	Evolution of Moist Static Energy . . . . .	39
3.5.1	A measure of instability . . . . .	39
3.5.2	Frictional convergence of moisture . . . . .	43
3.6	Summary . . . . .	47
<b>4</b>	<b>Impact of ENSO on the Madden-Julian Oscillation</b>	<b>49</b>
4.1	Introduction . . . . .	50
4.1.1	Previous studies on the relationship between ENSO and MJO	50
4.1.2	Selection of ENSO events . . . . .	51
4.2	Effects of ENSO on MJO Amplitude and Propagation Characteristics	52
4.2.1	Intraseasonal Variance . . . . .	52
4.2.2	Results based on lag correlation . . . . .	58
4.3	Circulation and Convection . . . . .	64
4.3.1	Convective and low-level activity . . . . .	64
4.3.2	Upper-level activity . . . . .	66
4.4	Moist Static Energy Consideration . . . . .	70
4.4.1	Evolution of moist static energy . . . . .	70
4.4.2	Transport of moisture . . . . .	75
4.5	Discussion and Summary . . . . .	78
<b>5</b>	<b>North Pacific Low-Frequency Circulation Anomalies- Climatological Characteristics</b>	<b>80</b>

5.1	Introduction . . . . .	80
5.1.1	Low-frequency perturbations, teleconnection patterns and instabilities of the time mean flow . . . . .	81
5.1.2	Blocking circulation and its development . . . . .	82
5.1.3	The role of intraseasonal oscillation . . . . .	83
5.1.4	Westward traveling patterns . . . . .	84
5.1.5	Interaction with synoptic-scale eddies . . . . .	86
5.2	Spacetime Characteristics and Dynamics of Low-Frequency Anomalies . . . . .	87
5.2.1	Spatial variability and its interannual fluctuations . . . . .	87
5.2.2	Life cycle of anomalies . . . . .	93
5.2.3	The role of synoptic-scale eddies . . . . .	103
5.2.4	Wave sources from intraseasonal convection . . . . .	106
5.2.5	A brief summary . . . . .	112
5.3	Relationship with other modes of low-frequency variability: MJO and WTP . . . . .	113
5.3.1	Circulation anomalies related to the MJO and WTP . . . . .	113
5.3.2	Circulation related to MJO-WTP interaction . . . . .	120
5.3.3	Linearity of MJO-WTP interaction . . . . .	127
5.3.4	Discussion and Conclusion . . . . .	132
<b>6</b>	<b>Low-Frequency Circulation Anomalies- the Impact of ENSO</b>	<b>135</b>
6.1	Introduction . . . . .	135
6.1.1	Observational and modeling studies . . . . .	135
6.1.2	Possible mechanisms considered in previous studies . . . . .	137
6.1.3	Questions to be asked . . . . .	138

6.2	How ENSO Affects Low-Frequency Activity in the North Pacific	
Sector	.....	139
6.2.1	Intraseasonal variability and occurrence of persistent events	139
6.2.2	Anomalous circulation features .....	144
6.3	Relationship with Basic State Variations and Tropical Convection	153
6.3.1	The role of changes of mean circulation during ENSO .....	153
6.3.2	Intraseasonal convection .....	159
6.3.3	A brief summary .....	163
6.4	Effects of ENSO on Circulation Anomalies due to changes in the MJO and WTP	164
6.4.1	MJO and WTP activity .....	164
6.4.2	MJO-WTP interaction .....	173
6.5	Discussion .....	176
6.6	Conclusion .....	178
<b>7</b>	<b>Variability of Synoptic-scale Activity in the Tropics</b>	<b>180</b>
7.1	Introduction .....	180
7.1.1	Synoptic-scale disturbances .....	180
7.1.2	Relationship with equatorial waves .....	182
7.1.3	Wave accumulation theory .....	184
7.1.4	Previous studies on the impact of ENSO .....	185
7.2	Climatological Behavior .....	186
7.2.1	Amplitudes, propagation and growth rates of wave-like disturbances .....	186
7.2.2	Wave dispersion of synoptic-scale activity .....	193
7.2.3	Western Pacific activity .....	200

7.2.4	Wavelength of disturbances . . . . .	206
7.2.5	A brief summary . . . . .	210
7.3	Behavior during ENSO . . . . .	212
7.3.1	Impact of ENSO on western Pacific activity . . . . .	212
7.3.2	Modulation of dispersion characteristics . . . . .	218
7.3.3	Effects on equatorial disturbances . . . . .	225
7.3.4	Discussion . . . . .	230
7.3.5	Conclusion . . . . .	232
<b>8</b>	<b>Discussion and Summary</b>	<b>235</b>
<b>A</b>	<b>Analysis of Variance (ANOVA)</b>	<b>241</b>
<b>References</b>		<b>243</b>

# Abstract

The impact of El Niño and Southern Oscillation (ENSO) on different types of atmospheric transient activity is studied, based on data from an ensemble general circulation model (GCM) experiment and the National Centers for Environmental Prediction (NCEP)- National Center for Atmospheric Research (NCAR) Reanalysis Project. In particular, the Madden-Julian Oscillation (MJO), North Pacific low-frequency (subseasonal/intraseasonal) circulation anomalies and summertime tropical synoptic-scale disturbances are considered. Extensive comparisons between reanalyses results and those based on ensemble GCM integrations are carried out.

The MJO activity from the GCM and reanalyses agree in several aspects, such as their spectral characteristics, regions with large amplitudes and their phase speed. MJO convection within the central Pacific is enhanced during warm ENSO events, suppressed during cold events. Positive values of the instability index, based on the vertical gradient of the moist static energy, are found to precede MJO convection at the equator. During warm events, there are stronger signals of this index over the central Pacific, which could be important for the further eastward penetration of convective anomalies in the region.

The life cycle of low-frequency circulation anomalies over the North Pacific is studied. During cold ENSO events, eddies in general are stronger, with more prominent dispersion downstream over the west coast of U.S.. GCM results show that stronger incoming wave activity from the subtropics is accompanied by stronger intraseasonal convection in the tropical western Pacific, suggesting that

the MJO plays a role on how ENSO affects extratropical low-frequency activity.

The GCM is able to reproduce qualitatively the propagation and growth/decay behavior of tropical summertime synoptic-scale disturbances. During warm ENSO events, storm tracks over the western Pacific are displaced eastward. Stronger barotropic conversion from the mean to eddy kinetic energy is related to increased low-level cyclonic wind shear in the region. Finally, equatorward energy dispersion from eddies is also located more to the east in the warm phase of ENSO. The relationship between the structure of the eddies and their related dispersion pattern is examined.

# Acknowledgments

I would like to express my deep gratitude to my thesis adviser Gabriel Lau. He has given me many degrees of freedom from the beginning, which could be frightful had he not also provided his guidance and shared his knowledge about climate dynamics and various techniques of analysis. I have learned a lot from his methods of tackling scientific problems. I especially appreciate his bearing with my wandering and being distracted from time to time. This work would not be possible without his patient guidance and constant encouragement. His many suggestions are crucial in transforming some raw material and barely readable text into a thesis.

I am also grateful to Isaac Held and Paul Kushner, who also serve on my thesis committee. Like other faculty members, they are willing to have long scientific discussion, and it is always a pleasure talking to them. In various stages of the project, they have provided ideas which help to improve the quality of my research work. They have also given useful comments on my presentation skill. I particularly appreciate their careful reading of my thesis, and for pointing out a number of scientific issues which I tend to overlook.

I thank Mary Jo Nath and John Lanzante, who have provided some of their computational codes for data analysis and for accessing the data from the GCM

experiments. They have helped me a lot, especially when I first started this project and had no experience in handling data. The help from Jeff Ploshay and Brian Soden in accessing the ECMWF and NCEP-NCAR reanalyses products is also appreciated.

I appreciate Isidoro Orlanski and Geoff Vallis for reading my thesis, and the faculty and staff members of the Program in Atmospheric and Oceanic Sciences for maintaining a favorable environment for scientific research. I also thank the administrative staff for solving some of the non-scientific (but not unimportant) problems during my graduate study in Princeton.

Discussion with Adam Sobel of Columbia University in the early stage of the project benefits this work. I also received help from Jones Wan for electronically archiving this thesis.

This thesis is dedicated to my parents in Hong Kong.

# Chapter 1

## Introduction

The El Niño and Southern Oscillation (ENSO) phenomenon is the major source of climate variability in the interannual time scale. Its impact on the mean circulation of the atmosphere in both tropical and extratropical regions continues to be a subject of intense study. Huge observational and modeling effort have been devoted to studying the phenomenon, bringing much advance in understanding the dynamics of the atmosphere-ocean system (see, e.g., Trenberth et al. 1998; Wallace et al. 1998; Alexander et al. 2002).

The impact of ENSO on the behavior of transient weather systems is also of great interest. It is an important part of the influence of ENSO on the general circulation, and better understanding of the problem also has implications on weather predictions. However, researchers are only beginning to touch upon the subject. Part of the reason is that relatively large amount of data is required for this type of research, since eddy statistics tend to be noisier than those of the time mean circulation. This is a serious constraint for observational studies on

the variability of eddy activity. For those interested in tropical disturbances, they are further hampered by the sparse observations over much of the tropics before the 1970s. Reanalysis projects using time-frozen data assimilation and processing schemes certainly help in providing more complete datasets, but still one has to be vigilant in handling statistics of data in the pre-satellite era, as noted by Kistler et al. (2001).

Recently, there are a number of studies in which the ability of general circulation models (GCMs) in simulating the interannual variation of atmospheric transient activity is explored (Straus and Shukla 1997; Renshaw et al. 1998; Slingo et al. 1998; Thorncroft and Rowell 1998). At first glance, the use of GCM outputs seems to circumvent many of the above issues using observational data. Sampling is not a problem because large datasets are available from GCM integrations. Furthermore, GCM data have a global coverage and are guaranteed to be self-consistent, as they are numerical solutions to dynamical equations. Yet the realism of GCM simulations is always an issue; simulated eddy characteristics can sometimes deviate substantially from their observational counterparts, especially for those related to transient activity in the tropics.

There is also another notable advantage of using numerical models for climate studies: ensemble integrations with prescribed boundary forcing can provide valuable information on the variability of the general circulation associated with that of the imposed forcing. For instance, based on repeated integrations with the same SST conditions (which, say, vary interannually), ensemble means of statistics could reveal some robust climate signals related to the SST variability. Such

robust signals of climate variability are often hard to obtain from observations.

The primary objective of this study is to make use of both reanalyses and GCM data to access the impact of ENSO on the following transient phenomena: tropical intraseasonal oscillations, tropical synoptic-scale disturbances and North Pacific low-frequency activity. The use of datasets from simulations would enhance statistical significance of results, while observations are also used to ensure that modeling data are realistic. To this end, extensive comparisons between GCM and reanalyses results will be carried out. For each of these topics concerning different types of transients activity, climatological behavior of eddies will be considered first, followed by examination of the effect of ENSO. Various diagnostic tools will be introduced during the course of investigation. Many of these tools are found to be useful in considering transient activity in previous studies.

Finally, it should be pointed out that the GCM experiment to be studied was not designed primarily to test hypotheses of the mechanisms through which ENSO affects different transient phenomena. Nevertheless, the GCM experimental outputs often provide useful hints of the underlying important processes. Possible follow-up works based on these hints will be suggested for some of the topics considered.

The outline of the rest of the study is as follows. A description of datasets and the GCM experiment can be found in Ch. 2. Climatological behavior of tropical intraseasonal oscillations, and the effect of ENSO, is the subject of Ch. 3 and Ch. 4, respectively. Ch. 5 is concerned with behavior of low-frequency activity

within the North Pacific sector in the climatological sense. Ch. 6 is about the impact of ENSO on these perturbations. Ch. 7 deals with summertime tropical synoptic-scale disturbances, focusing on both their climatological behavior and the impact of ENSO. More detailed introduction can be found in each of these chapters. A summary is given in Ch. 8.

# Chapter 2

## Description of GCM Experiment and Datasets

### 2.1 Numerical model and GCM Experiment

In this study, the GCM used is the Geophysical Fluid Dynamics Laboratory (GFDL) spectral model with rhomboidal truncation at 30 wavenumbers, which corresponds to a resolution of  $3.75^\circ$  in longitude and about  $2.24^\circ$  in latitude at the equator, and with 14 unevenly spaced sigma levels. The model has a smoothed realistic topography, and includes processes such as radiative transfer, ground hydrology and gravity-wave drag. Seasonally varying climatological sea ice and insolation are prescribed, but with fixed values for each calendar day. Model clouds are predicted, and parametrization of convection makes use of the moist convective adjustment scheme of Manabe et al. (1965). Soil moisture is predicted using the bucket method, and bulk aerodynamic formula are used for surface wind stress, sensible heat flux and evaporation. Vertical diffusion of

momentum, temperature and water vapor are also incorporated. The same GCM is used in a recent study of Lau and Nath (2003) on how ENSO affects air-sea interaction over the Indian-western Pacific Oceans. Gordon and Stern (1982) and Broccoli and Manabe (1992) gave more detailed descriptions of the model. Various climatological statistics of the GCM were documented by Alexander and Scott (1995).

Regarding the ability of this GCM to simulate different types of transient activity, Hendon (2000) showed that the spectral characteristics of intraseasonal oscillations from this GCM are in good agreement with those based on observations. However, the intraseasonal activity from the simulations is too strong. It is also noticed that the placement of the MJO circulation relative to convection is not reproduced correctly. For summertime synoptic-scale activity, Lau (1991) studied eddies from a GCM very similar to the one considered in this study. He noticed that the locations of enhanced activity could be sensitive to the simulated ambient flow field. On the other hand, the study of Lau and Nath (1999) demonstrates that this model can reproduce low-frequency variability in the extratropics with a reasonable degree of realism.

All model results are based on outputs from an atmospheric GCM experiment, prepared by the Climate Diagnostic group of GFDL. The experiment was conducted with monthly-varying sea surface temperature (SST) prescribed within the deep tropical eastern Pacific (DTEP) from 1950 to 1999, where DTEP is defined as the region of  $15^{\circ}\text{N}$ - $15^{\circ}\text{S}$ ,  $172^{\circ}\text{E}$  to the South American coast. Outside of DTEP, climatological SST was imposed<sup>1</sup>. In other words, interannual variation

---

<sup>1</sup>The climatological SST came from results of a parallel set of experiment with a mixed-layer ocean coupled to the atmospheric GCM. Values are close to those based on observations. See Alexander et al. (2002) for further details.

in these parts of the world oceans was excluded. Output from the experiment comprises eight integrations with 50 years of duration, each carried out with the same boundary forcing but different initial conditions. Daily archived values are used in all analyses. Final results presented are based on ensemble averages over the eight individual integrations.

As discussed in the Introduction, climate studies using GCM outputs generally benefit from having a large amount of data. The ensemble GCM experiment considered here provides a dataset eight times as large as its observational counterpart. This enhances the ratio of signal to noise substantially. By the design of the experiment, interannual variability can be attributed to the changing boundary condition, i.e. the varying SST in the DTEP region, except for the part of variability which exists internally (so-called natural variability). One expects in the experimental outputs the presence of robust signals associated with ENSO or SST variability in the DTEP.

## 2.2 Reanalysis Data

Products from the National Centers for Environmental Prediction (NCEP)- National Center for Atmospheric Research (NCAR) Reanalysis Project (Kalnay et al. 1996), during the period of 1950 to 1999, are used as the main observational dataset. In providing a record of global analyses of atmospheric fields, the project makes use of various types of observational data such as those from land surface, rawinsondes, aircrafts and satellites. Complex quality control and monitoring procedures are used in preprocessing the input data. Data assimilation is based on a three-dimensional variational scheme, using the NCEP global spectral model

to provide first guess fields (Parrish and Derber 1992). The NCEP model uses a simplified Arakawa-Schubert convective parametrization (see Kalnay et al. 1996). The assimilation scheme is kept constant during the process of reanalyses. For upper-air variables, final products are archived on a  $2.5^\circ \times 2.5^\circ$  lat-lon grid, on 17 pressure levels.

It is important to note that reanalysis products are model dependent to some extent. This is especially so for outputs over data sparse regions, and for variables which depend heavily on model characteristics. According to Kistler et al. (2001), geopotential, rotational winds and upper-air temperature are strongly influenced by observations. This type of variables are the most reliable. On the other hand, some variables are influenced by both observations and the numerical model. Examples of these include moisture, divergent winds and surface temperature. Thus, analyses based on the latter type of variables have to be interpreted with due caution, as they might be affected by model behavior.

It is worth mentioning that intraseasonal variance of the OLR and precipitation were found to be about half of that from in situ and satellite observations by Shinoda et al. (1999). In other words, the strength of the intraseasonal convection could be underestimated in the NCEP-NCAR products.

Although the data assimilation scheme is 'frozen' in time, changes of observational systems during the period of reanalyses still have an impact on the final product. Based on the discussion of Kistler et al. (2001), the climatology is computed using post-1979 data (i.e. the satellite era). This would enhance the reliability of results, especially within data sparse oceanic regions in the tropics. For studying ENSO-related variability, data from the full period of 1950-99 will be used, keeping in mind that there can be spurious trends or jumps.

Besides the NCEP-NCAR dataset, data from the European Center for Medium Range Weather Forecast (ECMWF) reanalyses, for the period of 1979 to 1993, are also used in section 3.2.1 of the study. For ease of comparison with GCM results, all reanalyses data was interpolated on the same grid as that of the GCM.

# **Chapter 3**

## **Climatological Behavior of the Madden-Julian Oscillation**

In this chapter, the space-time structure of the Madden-Julian Oscillation (MJO) as manifested in various meteorological fields is studied. Before embarking on a study of the ENSO impact on intraseasonal activity, it is important to have some knowledge of their climatological behavior. Moreover, the realism of the simulated MJO should be assessed by comparison with observations. To serve these purposes, different analysis methods are employed. Power spectra, variance plots, lag-correlation methods and complex empirical orthogonal functions (CEO) analysis are used to delineate the relevant time scales, regional dependence of amplitudes, propagation characteristics and associated circulation features of the MJO. In most cases, GCM results are compared with those based on NCEP-NCAR reanalyses during 1979-99, while the ECMWF dataset is also used in section 3.2.1 for spectral analyses. Some of the aforementioned analysis tools will be used again in the next chapter.

## 3.1 Introduction

### 3.1.1 Observations of the MJO

Named after the investigators who discovered it (Madden and Julian 1971, 1972, 1994), the MJO is a phenomenon with intraseasonal time scales, prominent in tropical regions. Originally called the 40-50-day oscillation, it was soon realized to have a broadband spectral character, with periods from 25 to more than 60 days. The MJO is manifested in a number of meteorological variables, such as the upper and low-level zonal wind and the sea-level pressure. It has a baroclinic structure in the vertical, as indicated by the out-of-phase relationship between upper and low-level zonal winds in the tropics. Anomalies propagate eastward at about  $10\text{ms}^{-1}$ .

Later observational works after the 1970s document various aspects of the MJO in further detail. By studying the outgoing longwave radiation (OLR), a proxy indication of deep convection, Lau and Chan (1985) showed that the MJO affects convective activity strongly over the Indian Ocean and the western Pacific. Intraseasonal convective signals are also known to be strongest in the eastern hemisphere (Salby and Hendon 1994). The impact of the MJO on the Indian and Australia summer monsoon (Lau and Chan 1986; Hendon and Liebmann 1990), and its influence on phenomena with shorter time scales such as tropical cyclones (Maloney and Hartmann 2000), highlight its importance in the tropical climate. The extratropical circulation also feels its impact (Weickmann et al. 1985; Knutson and Weickmann 1987), but effects are less significant than those in the tropics.

### **3.1.2 Theoretical and modeling studies**

Chang (1977) showed that equatorial Kelvin wave solutions in an viscous environment are similar to the MJO in terms of phase speeds and vertical scale. Yamagata and Hayashi (1984), on the other hand, considered the atmospheric response to an imposed localized heating that oscillates with a period of 40 days. Eastward moving Kelvin waves are found, but there are also Rossby waves propagating westward from the heating- a feature inconsistent with observations. In these studies, convective heating is either ignored or prescribed, and its interaction with the circulation is unclear.

Conditional instability of the second kind (CISK) provides a way to relate circulation with convective heating. It assumes heating to be given by the surface (or low-level) convergence of moisture, multiplied by a prescribed vertical structure function. Using CISK but with positive-only heating, Lau and Peng (1987) found that large-scale 20-30-day Kelvin waves could be obtained. Their results, however, could depend on model characteristics such as resolution and parameters chosen (see discussion by Hayashi and Golder 1993).

Evaporation-wind feedback (Neelin et al. 1987) or wind-induced surface heat exchange (WISHE) (Emanuel 1987; Yano and Emanuel 1991), provide an explanation of the MJO completely different from CISK. It is argued that convective heating is totally offset by adiabatic cooling. Instead, the main driving mechanism of the MJO is the fluctuation of surface evaporative flux. Low-level anomalous easterlies, east of strong upward motion, would increase evaporation ahead of convection. The enhanced surface flux provides energy and serves as a mechanism of eastward propagation. Notice that the assumption of a basic state with low-level easterlies is crucial here; no instabilities are found under mean tropical wester-

lies. In fact, one major criticism on WISHE is the fact that within regions where the MJO is strongest, namely over the Indian Ocean and the western Pacific, the mean equatorial surface wind is mostly directed *westward* (Wang 1988).

Numerical models of various degree of complexity continue to shed light on our understanding of the MJO. Lau and Lau (1986) demonstrated that the MJO simulations from a full GCM are realistic in several aspects. Results of Hayashi and Sumi (1986) suggest that the MJO can exist in a zonally symmetric basic state. Neelin et al. (1987) demonstrated that the MJO could be severely suppressed when evaporation-wind feedback is turned off in their GCM experiment. Bladé and Hartmann (1990), based on a simple model with CISK, suggested that in-situ development of instability might be responsible for the onset of the MJO. Waliser et al. (1999) suggested that an interactive ocean might help in organizing intraseasonal convective activity, as their MJO simulations are greatly improved by coupling a mixed-layer ocean to their atmospheric GCM.

After more than 30 years since its discovery, the MJO is still one of the most active research topics in tropical meteorology. There are a number of theories accounting for its existence not included above (e.g., air-sea coupling proposed by Wang and Xie 1998, or cloud-radiation interaction by Raymond 2001). Finally, the MJO is also related to some important climate problems, due to its impact on the monsoon circulation and possibly on the evolution of the ENSO.

## 3.2 Temporal Characteristics and Spatial Modulation of Intraseasonal Oscillation in the Tropics

### 3.2.1 Spectral analysis

Fig. 3.1 shows normalized power spectra of the velocity potential ( $\chi$ ) at 200 mb and 850 mb, averaged over 10°N-10°S, at various longitudes. Data is taken from the GCM experiment, NCEP-NCAR and ECMWF reanalyses. The  $\chi$  field is defined as the inverse Laplacian of the divergence  $D$ , i.e.  $\chi = \nabla^{-2}D$ , and is characterized by large spatial scales. For a sinusoidal divergence  $D \sim e^{ikx}$ ,  $\chi \sim -k^{-2}e^{ikx}$ , which gives a large value for small  $k$  or large spatial scales. In this case  $\chi$  and  $D$  also have the opposite sign. The  $\chi$  field therefore represents the large-scale component of divergence (hence vertical motion), and is intimately related to deep convection. The variable has been used in many MJO studies (e.g. Lorenc 1984; Knutson and Weickmann 1987; Lau et al. 1988). Prior to computation of spectra, the annual mean and first four harmonics (i.e. variation with period of 12, 6, 4, and 3 months) of the seasonal cycle, defined as the climatological mean for each calendar day, were removed from the data. A lag window estimation of spectra is used, with an effective resolution of  $\sim 0.002 \text{ day}^{-1}$  (see, e.g., Chatfield 1989). Frequency spectra are normalized by the 10-100-day variance at each longitude, and results are multiplied by  $\delta\omega = 2\pi \cdot 0.0045 \text{ day}^{-1}$  to obtain non-dimensional values<sup>1</sup>. Normalized spectra are shown in order to better compare spectral characteristics of the velocity potential from different datasets, since the GCM and reanalyses data have very different magnitudes of spectral

---

<sup>1</sup> $\delta\omega$  is chosen as the value resulted from dividing the 10-100-day interval into 20 equally-spaced frequency segments.

power (see section 3.2.2).

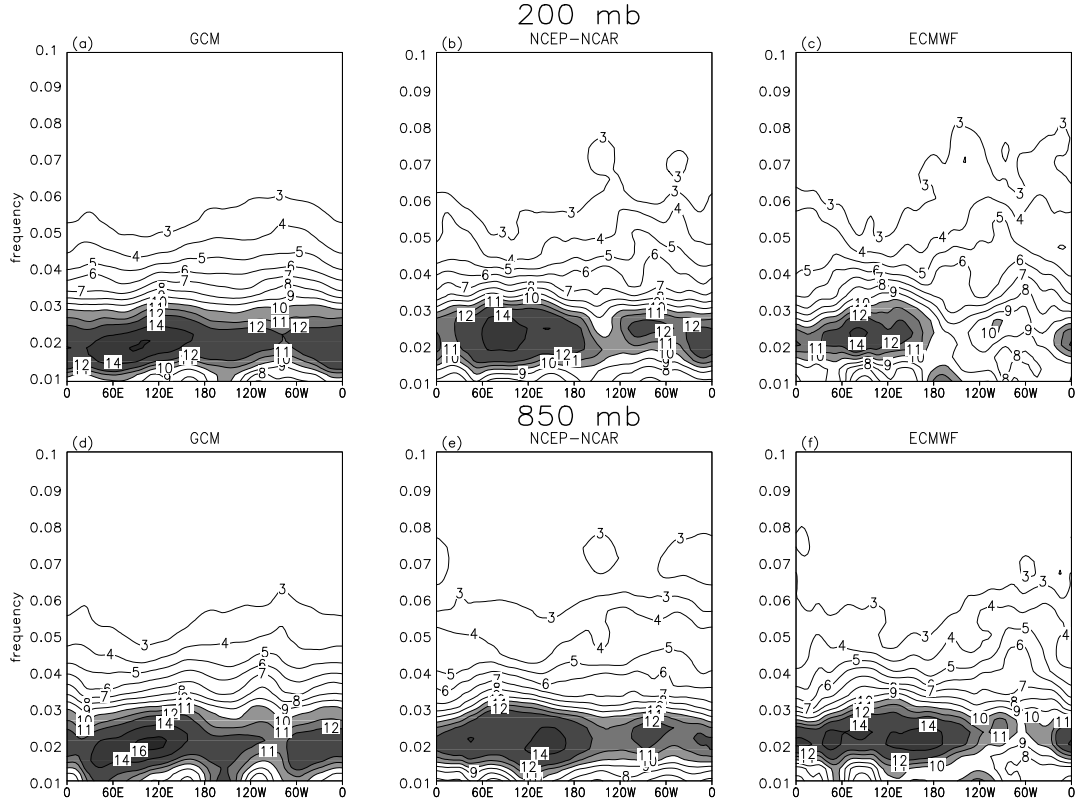


Figure 3.1: Normalized spectra (in percent), averaged over  $10^{\circ}\text{N}$ - $10^{\circ}\text{S}$ , of the velocity potential. Spectra based on datasets from GCM [(a) and (d)], NCEP-NCAR reanalyses, [(b) and (e)] and ECMWF reanalyses [(c) and (f)]. The upper (lower) panel shows spectra at 200 mb (850 mb). Values  $> 10\%$  are shaded. Unit of frequency:  $\text{day}^{-1}$ .

For all panels in Fig 3.1, large spectral power is found in the 30-100-day period band, with a prominent peak at about 50 days in the eastern hemisphere. Ratio of 40-65-day variance to its total power is about 28% within the equatorial region of  $60^{\circ}$ - $180^{\circ}\text{E}$ . Upper and low-level  $\chi$  basically exhibit the same temporal behavior. For the GCM, the spectral peak at about  $120^{\circ}\text{E}$  is slightly sharper than that in the other two datasets. Overall, reasonable agreement is found among results

based on different data.

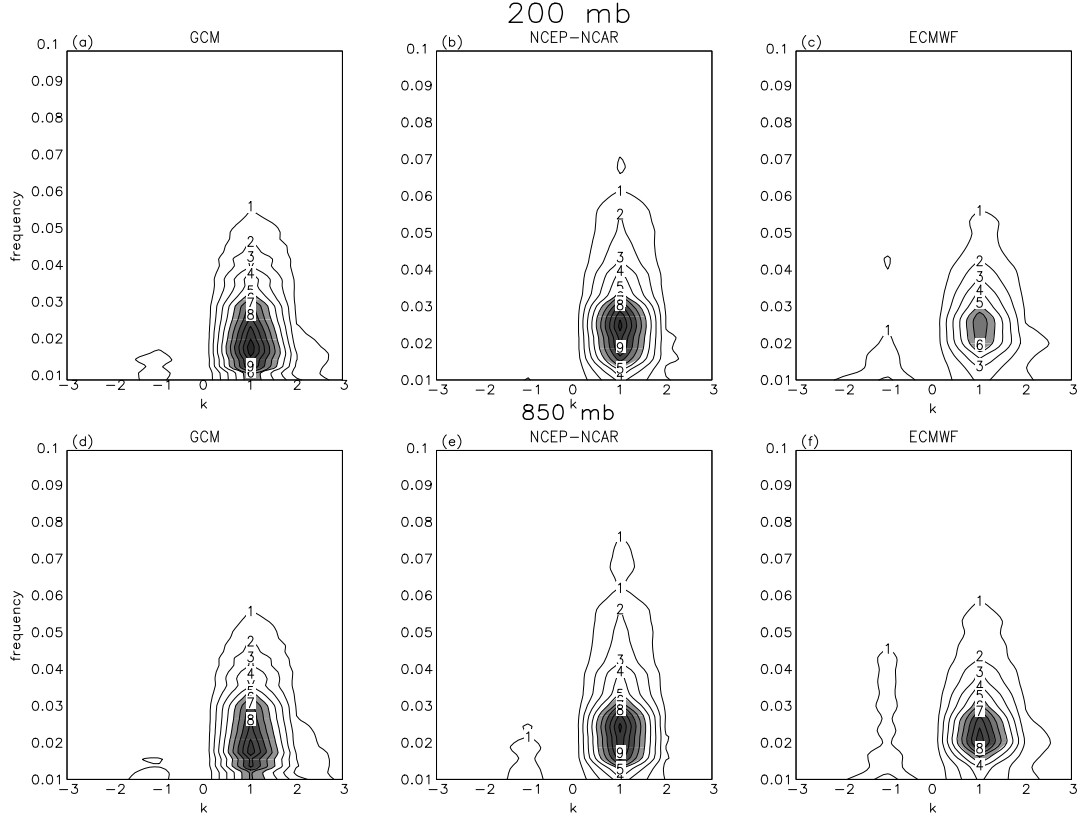


Figure 3.2:  $10^{\circ}\text{N}$ - $10^{\circ}\text{S}$ -averaged normalized wavenumber-frequency spectra (in percent) of the velocity potential. Upper panel shows results based on 200-mb data from (a) GCM, (b) NCEP-NCAR and (c) ECMWF. Lower panels [(d), (e) and (f)] are same as the upper panels, except for 850-mb level data. Values  $> 5\%$  are shaded. Unit of frequency:  $\text{day}^{-1}$ .

Fig. 3.2 shows normalized wavenumber-frequency spectra of 200-mb and 850-mb  $\chi$ , with positive (negative) wavenumber  $k$  representing eastward (westward) propagating variances. Computational methods of Hayashi (1971) is used. Normalization is done by dividing all power spectra for different  $k$  by the variance summed over all wavenumbers and frequencies, and the result is multiplied by the same  $\delta\omega$  as before. A strong peak is found with a roughly 50-day period at

$k = 1$ , indicating that a large fraction of variance is due to an eastward moving wavenumber-one component. Spectral power drops rapidly for higher wavenumbers, due to the fact that the  $\chi$  field emphasizes large-scale features. Overall, anomalies move predominately eastward; westward propagation is almost absent.

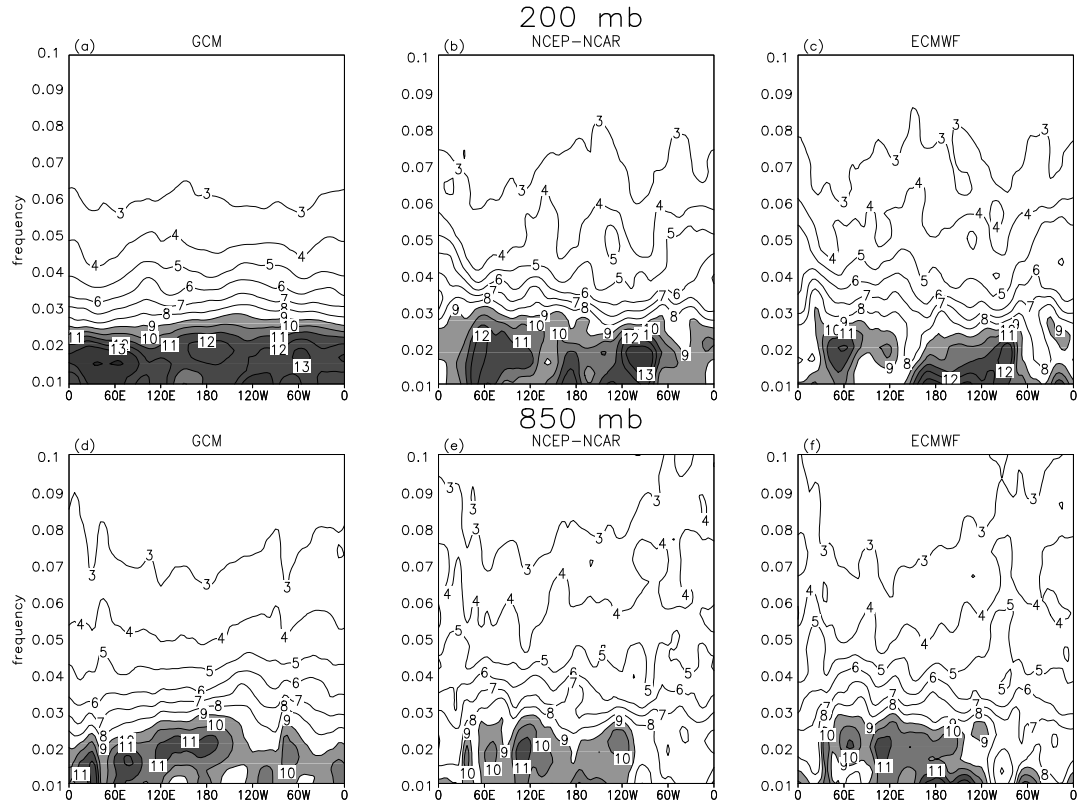


Figure 3.3: As in Fig. 3.1 but for 200 and 850-mb zonal wind. Values  $> 9\%$  are shaded.

Normalized power spectra of the zonal wind ( $u$ ) at 200 mb and 850 mb are shown in Fig. 3.3. Again, large spectral power resides in the range of 30-100 days, similar to the case of velocity potential. However, the  $u$  winds are redder; large power can be found at very low frequencies. In some geographical locations, large spectral signals do not really stand out as peaks from the background, which

exhibits increasing power toward lower frequencies. Zonal winds at the two levels have very similar spectral characteristics; there is a hint that 200-mb  $u$  variance tends to be less confined to the eastern hemisphere.

Wavenumber-frequency spectra of 200-mb and 850-mb  $u$  are given by Fig. 3.4. Spectral maxima are located at  $k = 1$  with 50-60-day periods, with the exception of ECMWF 200-mb  $u$  which has the strongest power at even lower frequencies. Compared with the velocity potential, zonal winds have stronger westward moving variance, and spectral power is less confined to wavenumber one. A substantial standing-wave component in the intraseasonal time scales is found for the upper-level wind. Although not a focus of this study, the intraseasonal zonal mean component might be physically meaningful. Madden and Julian (1994) noted that a zonal manifestation of the MJO might be related to intraseasonal perturbations of the atmospheric angular momentum.

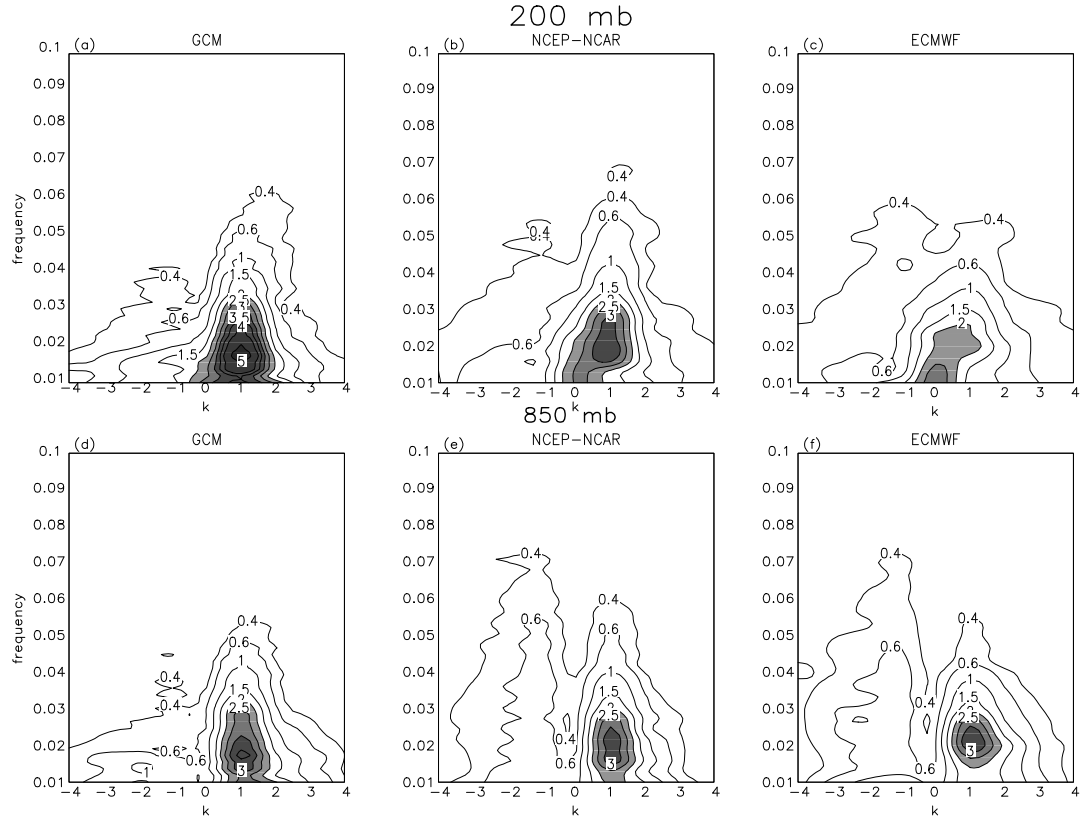


Figure 3.4: As in Fig. 3.2 but for 200 and 850-mb zonal wind. Values  $> 2\%$  are shaded.

The existence of prominent oscillatory signals with intraseasonal periods of 30-60 days for both tropical zonal winds and velocity potential is clearly shown, by considering power spectra at selected vertical levels. Associated anomalies exhibit a strong eastward-moving wavenumber-one signature. Results shown here are in broad agreement with many previous studies on the MJO, which consider spectral behavior of different variables such as zonal winds, sea-level pressure and the OLR (see Madden and Julian 1994). More importantly, it is shown that the GCM is able to reproduce the phenomenon, and simulations agree reasonably

with reanalyses results in terms of their spectral characteristics.

### 3.2.2 Intraseasonal variance

Many studies show that the MJO has different amplitudes at various geographical locations (see, e.g., Salby and Hendon 1994). The variance of velocity potential are plotted in Fig. 3.5, in order to examine the spatial dependence of amplitudes. It shows the 25-100-day variance at 200-mb and 850-mb levels, for the period of November to March, for GCM and NCEP-NCAR reanalyses data. The choice of this frequency band is based on results of spectral analyses in section 3.2.1. Here, and in the rest of the study, filtering is achieved by applying a 141-weight Lanczos filter. Large variance is found within the eastern hemisphere; as one moves eastward to the central-eastern Pacific, amplitudes decrease rapidly. They are in general much smaller in the western hemisphere. For both the upper and low-level  $\chi$  field from the GCM dataset, there are three regions of strong activity: Africa, South America, and the maritime continent where the largest amplitude is located. Reanalyses data give roughly the same spatial patterns, especially for the 850-mb level. Interestingly, the NCEP-NCAR upper-level  $\chi$  has its largest variance over the Indian Ocean- a region where its low-level counterpart has much weaker amplitudes. Overall, reanalyses results are much weaker, with values half to one-third of those from GCM. The simulated MJO seems to be too strong. The variance calculated based on the ECMWF reanalyses shows patterns very similar to those from the NCEP-NCAR dataset, with comparable magnitudes (not shown).

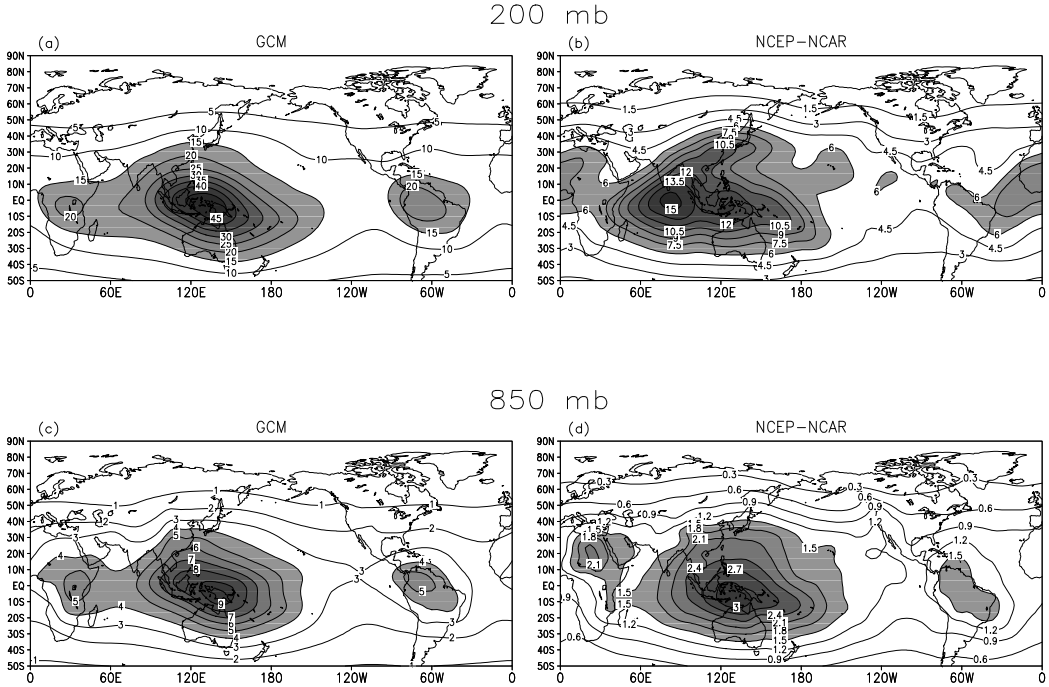


Figure 3.5: 25-100-day variance of velocity potential for GCM [(a) and (c)] and NCEP-NCAR reanalysis [(b) and (d)], for the period of November to March. Top (bottom) panel shows variances at 200 mb (850 mb). Contour intervals (in unit of  $10^{12} \text{m}^4 \text{s}^{-1}$ ): 5, 1, 1.5 and 0.3 for (a), (b), (c) and (d), respectively.

Variance of the 200-mb and 850-mb zonal winds are shown in Fig. 3.6. Large values appear in both the tropics and extratropics, in contrast to the distribution of velocity potential variance. For both the GCM and reanalyses, large upper-level perturbations in the extratropics are found within the proximity of the strong jet streams: along the North African-Asian jet, and the North Pacific and the North Atlantic in regions where the mean jets decelerate. These features, however, are not primarily due to the MJO, although intraseasonal oscillation can excite circulation responses in the extratropics (see section 3.4.2). Within the tropics, the GCM data shows a broad region with strong intraseasonal activity along the equatorial central-eastern Pacific, with maximum amplitude at about

$10^{\circ}\text{S}$ , east of the dateline. Strong peaks are also found over the Indian and the Atlantic Oceans. However, NCEP-NCAR results in the tropics show a weaker and different pattern: one active region is found spanning the Arabian Peninsula and Indian subcontinent, while another is located in the eastern Pacific off the coast of Ecuador and Peru.

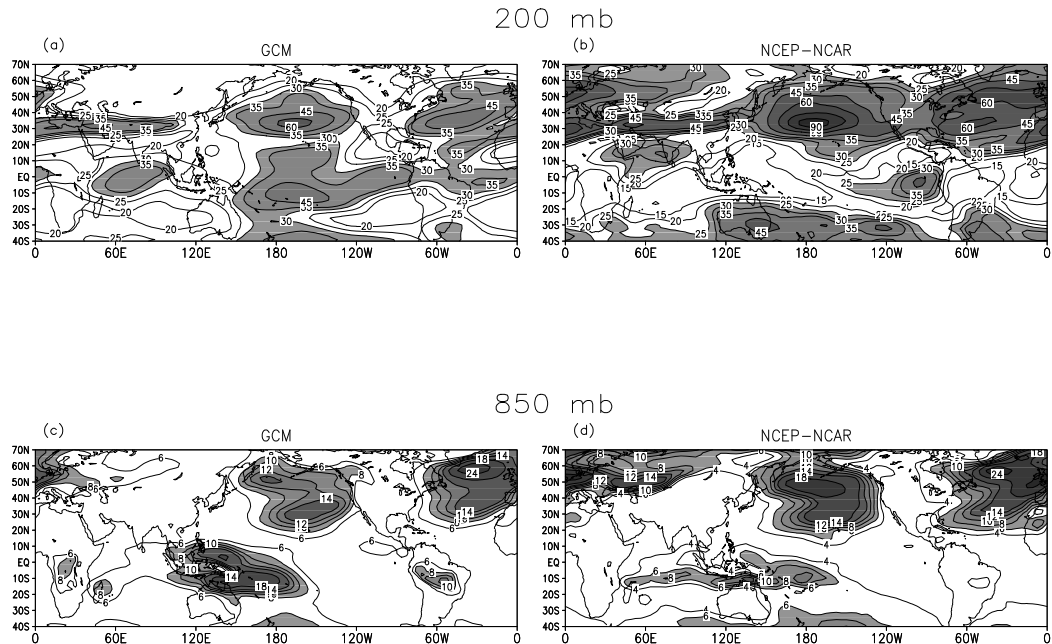


Figure 3.6: As in Fig. 3.5 but for 200 and 850-mb zonal wind. Contour levels, in unit of  $\text{m}^2\text{s}^{-2}$  for (a): 20, 25, 30, 35, 45 and 60; (b) has the same contour levels as (a) but with additional contours of 15, 75 and 90  $\text{m}^2\text{s}^{-2}$ . Contour levels for (c): 6, 8, 10, 12, 14, 18 and 24  $\text{m}^2\text{s}^{-2}$ ; (d) has the same contour levels as (c) expect with an additional contour of 4  $\text{m}^2\text{s}^{-2}$ .

Variance of 850-mb zonal wind from GCM and NCEP-NCAR dataset display more similarity of their spatial patterns. Within equatorial regions strong activity is found over the maritime continent and the western Pacific. GCM results also show moderate amplitudes in Africa and South America, reminiscent of the pattern of velocity potential variance. NCEP-NCAR reanalyses give similar regions

of large amplitudes, except that over the Indian Ocean a band-like region with strong anomalies is also found; this feature is not obvious in the GCM. Again, magnitudes of tropical perturbations in the reanalyses are weaker than those in the GCM, although the discrepancies are smaller than those based on the velocity potential variable.

The variance of  $\chi$  for the period of May-September is also examined. It has much smaller values (not shown) compared with those for the northern cold season. Variances of the zonal winds (not shown) have smaller magnitudes in the extratropical northern hemisphere, while active regions are found in Indian subcontinent, Indochina and the western Pacific for 850-mb  $u$ , with maximum amplitudes at about 10°-20°N. It seems that the MJO is most active during the northern winter season, while during summertime its strongest impact is over the Asian Monsoon region. In the remaining sections, only the season of November to March will be considered.

In summary, while the MJO has a eastward-propagating wavenumber-one structure, a substantial spatial modulation of its amplitude exists. This is clearly shown by the bandpass variance of zonal winds and velocity potential, the latter being related to the divergent part of the MJO circulation. This divergent motion is found to be mostly confined to the eastern hemisphere, probably due to the warm SST there. Such confinement is also true for perturbations of low-level zonal wind, but not so for those in the upper level. In fact, magnitude of the 200-mb  $u$  anomalies remains large over the tropical eastern Pacific, whereas their 850-mb counterparts are weak in the same region. This result suggests that the *amplitudes* of the zonal wind perturbations at the upper and low levels do not evolve coherently in space during the MJO. A more detailed study of the MJO

circulation, given in section 3.4.1, shows that this is indeed the case.

It is noticed that the MJO as simulated by the GCM is much stronger than that found in NCEP-NCAR reanalyses. On the other hand, NCEP-NCAR data show that intraseasonal activity over the Indian Ocean is at least as strong as those in the western Pacific, apparent in variance maps of both low-level  $u$  and velocity potential, whereas emphasis over the western Pacific is much stronger in the GCM. Patterns for the upper-level  $u$  variance in the tropics, based on the two datasets, are also quite different: a region of strong activity over the central Pacific found in the GCM simulations is absent in reanalyses data. These discrepancies should be kept in mind; nevertheless, temporal and spatial behavior of the GCM-simulated MJO still share a number of common features with those found in reanalyses. This gives one some support that the GCM is useful for studying the MJO, given that simulations seem realistic in several aspects.

## 3.3 MJO Propagation as inferred from Lag Correlation

### 3.3.1 Computation method

In order to study the propagation of the MJO, a lag-correlation analysis is employed. This method has been used for studying mid-latitude baroclinic waves (Blackmon et al. 1984; Wallace et al. 1988), and tropical synoptic scale disturbances by Lau and Lau (1990). An outline of computation procedures is as follows. First, using the 25-100-day filtered velocity potential as variable<sup>2</sup>, 8-day-forward and 8-day-backward lag correlation maps for a chosen reference point is computed within the domain of 40°N-40°S. Fig. 3.7 shows lag correlation values for the reference point of 120°E at the equator. It is obvious that anomalies from the Indian Ocean move eastward, passing the maritime continent, and propagate to the central Pacific.

Based on these correlation maps, one can estimate the phase speed of the MJO. This is done by first searching for points with maximum forward and backward lag correlation; the phase velocity is then the corresponding displacement vector divided by the total time lag (i.e. 16 days)<sup>3</sup>. Local growth of anomalies can also be found: the rate of change of amplitude is defined as the difference between the forward and backward regression, evaluated at the aforementioned

---

<sup>2</sup>The use of the velocity potential is meant to capture the propagation of divergent motions with the largest spatial scales. For examining the evolution of variables with a more localized nature, the composite method used in section 3.4.1 might be more suitable.

<sup>3</sup>A note on details of computation procedure: the choice of lag= ± 8 days is found to give a more satisfactory result, compared with say 5 or 10 days. Correlation maps, phase vectors and growth rates are computed and determined on a year-to-year basis. The 'climatology' is defined as the time mean of these quantities. Resulting statistics is found to be less noisy, while investigation of any interannual variability can be performed readily.

grid points that give maximum correlations, divided by the total time lag.

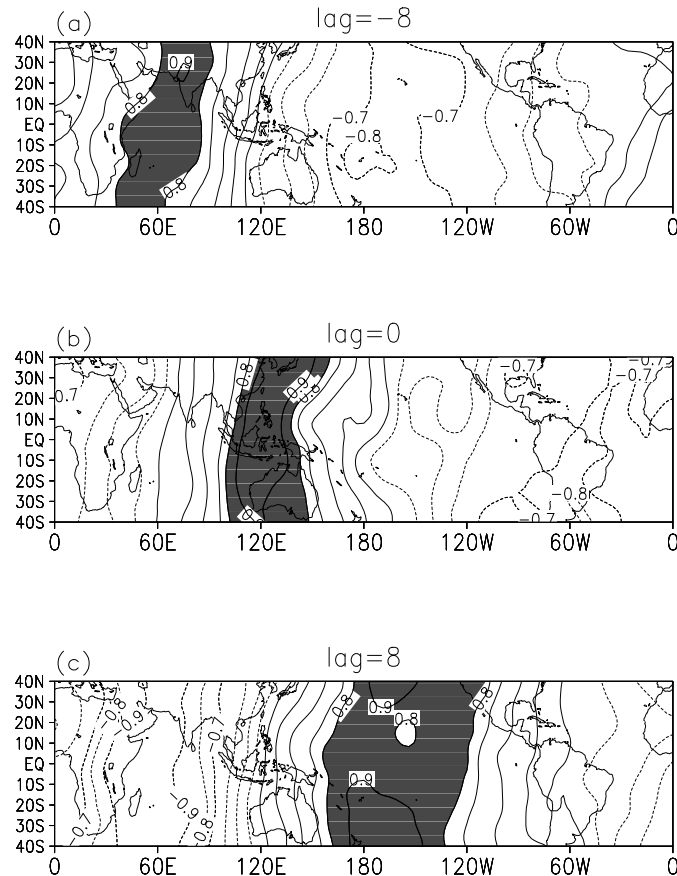


Figure 3.7: One-point lag correlation of 200-mb velocity potential, with  $120^{\circ}\text{E}$  at the equator as the base point. (a) 8-day backward lag correlation ( $\text{lag}=-8$ ), (b) contemporaneous correlation ( $\text{lag}=0$ ) and (c) 8-day forward correlation ( $\text{lag}=8$ ). 25-100-day-filtered data is used; computation based on one season of data during November-March. Contour levels: -0.9 -0.8 -0.7 -0.5 -0.3 -0.1 0.1 0.3 0.5 0.7 0.8 0.9. Values  $> 0.8$  are shaded.

### 3.3.2 Growth rates and phase speeds

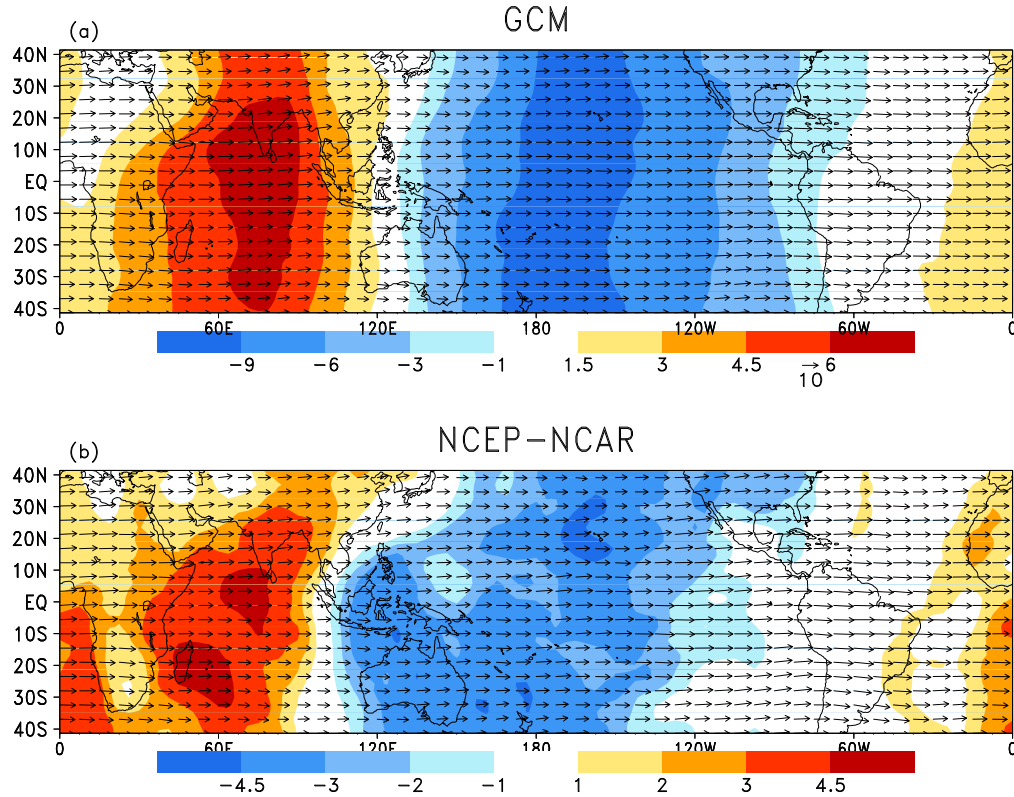


Figure 3.8: Phase velocities (magnitude in  $\text{ms}^{-1}$ ) and growth rates of 200-mb velocity potential for (a) GCM and (b) NCEP-NCAR data, for the November-March period.

Applying the above procedure for every grid point, one arrives at a holistic picture describing the propagation and growth of the MJO. Results from the GCM and NCEP-NCAR data are shown in Fig. 3.8 and Fig. 3.9 respectively, for the 200 and 850-mb velocity potential. Arrows depict the phase velocity at each point, and shading depict the growth and decay of disturbances. It is found that anomalies propagate eastward predominately; meridional movement is much smaller. Strong growth of anomalies exists over the Indian Ocean from  $60^{\circ}\text{E}$  to about  $90^{\circ}\text{E}$ . Decay of the MJO occurs over the maritime continent and is strongest over the central

Pacific, while amplification over South America and the Atlantic is small. NCEP-NCAR data show weaker growth rates than the GCM, particularly for the 200-mb  $\chi$  field, and also with a region of zero growth located at about 100°E, slightly displaced to the west compared with the same feature from GCM results. These discrepancies are possibly related to the difference of magnitudes and patterns of the variance of  $\chi$  (see Fig. 3.5). Due to the smaller size of the dataset, reanalyses results are noisier, and the detail meridional structure of the growth pattern is probably not significant. Better agreement between the two datasets is found for the results using the 850-mb velocity potential. Overall, the upper and low-level anomalies have very similar propagation and patterns of growth rates.

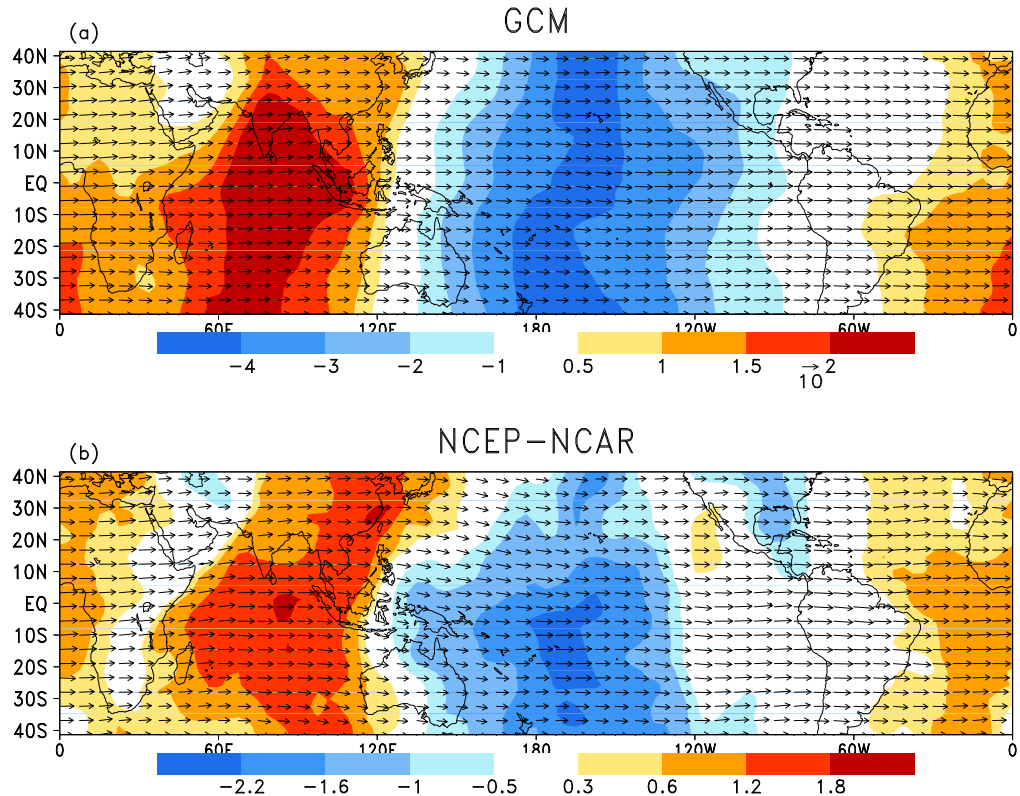


Figure 3.9: As in Fig. 3.8 but for 850-mb level.

Fig. 3.10 and 3.11 show the zonal phase speed of the MJO as inferred from lag correlation (i.e. zonal components of the phase velocity in Fig. 3.8 and 3.9), for GCM and NCEP-NCAR data, respectively. Propagation is found to be slowest around the maritime continent, and fastest over the eastern Pacific, South America and the Atlantic, with values ranging from  $8.5$  to  $12 \text{ ms}^{-1}$ . The averaged value of about  $10 \text{ ms}^{-1}$  agrees with that given by Madden and Julian (1994). Variation of speeds from the eastern to western hemisphere has been reported in a number of observational works (Knutson and Weickmann 1987; Salby and Hendon 1994); they are consistent with the values shown here. GCM and NCEP-NCAR results are in agreement, despite the latter being nosier. Phase speeds based on 200 and 850-mb  $\chi$  fields are found to be almost identical.

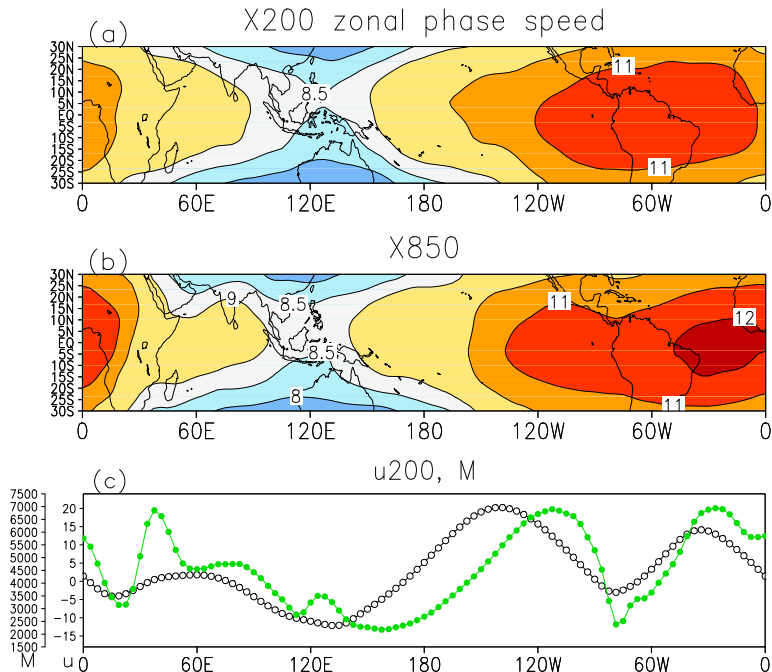


Figure 3.10: GCM result of zonal phase speed of velocity potential at (a) 200 mb and (b) 850 mb. (c) Mean 200-mb zonal wind (open circle) and moist stability  $M$  (filled circle, in unit of  $\text{J kg}^{-1}$ ),  $10^\circ\text{N}$ - $10^\circ\text{S}$ -averaged, during November to March. Unit of phase speed and 200-mb zonal wind:  $\text{ms}^{-1}$ .

It is instructive to compare the phase speed results to some theoretical predictions. Based on a quasi-equilibrium assumption of tropical convection, Neelin and Yu (1994), and Yu and Neelin (1994) showed that the speed ( $c$ ) of MJO is given by:  $c^2 \propto M$ , where  $M$  is the moist stability. Following Neelin and Held (1987),  $M$  is defined as  $M_1 - M_2$ , where  $M_1$  is the moist static energy ( $h$ ) averaged over the upper levels, namely between  $\sigma = 0.177$  and  $\sigma = 0.676$ , and  $M_2$  is averaged over the low levels, between  $\sigma = 0.676$  and  $\sigma = 0.935$ . This definition aims at emphasizing the continuous variation of  $h$ , while retaining a form analogous to its counterpart for a two-level model used by Neelin and Held (1987). Values of  $M$  is also shown in Fig. 3.10. A marked minimum is present over the western Pacific, and  $M$  rises rapidly toward the eastern Pacific. The zonal variation of  $M$  roughly corresponds to that of the MJO phase speed within the Pacific, but in other regions their relationship is less clear.

Values of the phase speed from NCEP-NCAR data, shown in Fig. 3.11 (a) and (b), agree qualitatively with those based on GCM, with the exception over Africa where a sharp decrease is found. Fig. 3.11 (c) shows the values of  $M$  based on reanalyses data. It is defined in a similar fashion as its GCM counterpart, where  $M_1$  is  $h$  averaged over the pressure levels from 150 to 600 mb, and  $M_2$  is  $h$  averaged over 600 to 925 mb. The change of  $M$  from the western to eastern Pacific is roughly consistent with that of the propagation speed of the MJO.

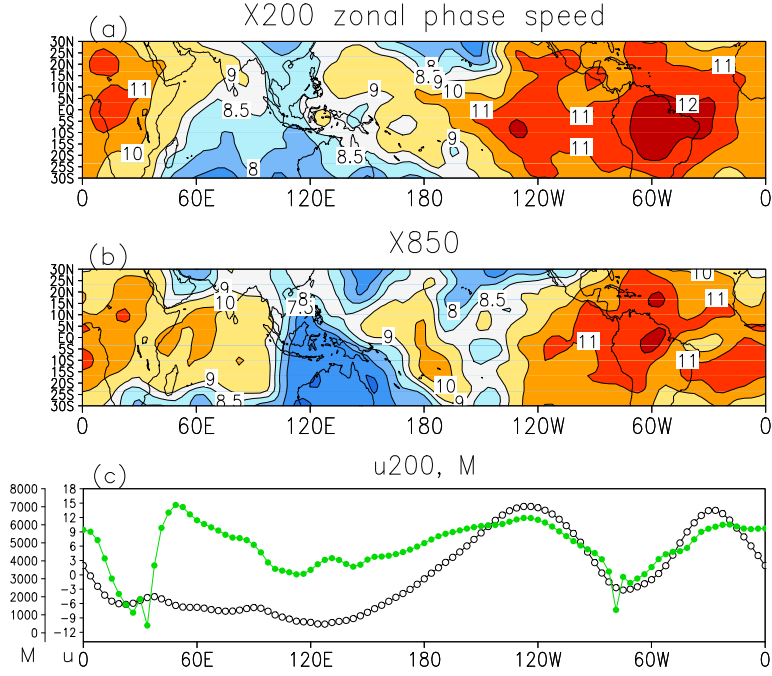


Figure 3.11: Same as Fig. 3.10 but for NCEP-NCAR data.

It is also noticed that the variation of  $c$  matches partially with that of the equatorial upper-level zonal wind, which also has a minimum about  $120^{\circ}\text{E}$  and maximum over the eastern Pacific. The mean 200-mb zonal wind is shown in Fig. 3.10 and Fig. 3.11 as well. It seems plausible that the ambient flow might also have an effect on the MJO zonal phase speed. The possible role of these factors in affecting the speed of the MJO in terms of its interannual variability will be revisited again in section 4.2.2 of the next chapter.

## 3.4 CEOF Analysis

### 3.4.1 Computation procedures

One way to study the spatial structure and temporal evolution of the MJO is to make use of eigenanalysis techniques. CEOF's of the GCM 200-mb velocity potential are computed, following Horel (1984), for the domain of 20°N-20°S. This domain is chosen in order to minimize any extratropical signature; prior to computation, data was sub-sampled such that 1 out of every 3 grid points was selected in the longitudinal direction. There are 20 points in the latitudinal and 32 points in the longitudinal direction. The total number of grid points selected is  $32 \times 20 = 640$ . The annual cycle, defined on each calendar day as the 31-day running mean of the long-term averaged value of the field for each day, was removed from the data. Filtered to retain variations from 10 to 100 days, data within the period of November to March are used and the corresponding correlation matrix is computed. The first complex eigenvector or CEOF accounts for more than 70% of variance. Its real and imaginary part, together with its associated principal component (PC) time series, are shown in Fig. 3.12. The CEOF patterns, originally defined within the band 20°N-20°S and on a number of selected grid points, are extended to cover the whole globe by regressing the filtered data onto the real and imaginary part of the PC. Notice that patterns found this way match exactly the eigenvector on those grid points selected for computing the EOF's.

The resulting real and imaginary EOF pattern, both having a wavenumber-one structure, are in quadrature in space. The real part of the EOF has a strong negative center over the western Pacific and a positive center over South America.

This can be interpreted as large scale 200-mb divergence in the former region and convergence in the latter (see section 3.2.1). Similarly, the imaginary part of the EOF indicates intense rising over the Indian Ocean, sinking over the eastern Pacific. The real and imaginary PC's, on the other hand, are in quadrature in time, with the imaginary part leading the real part. Together the PC's and their associated EOF's represent a wavenumber-one eastward propagating wave, consistent with the wavenumber-frequency spectra of the velocity potential.

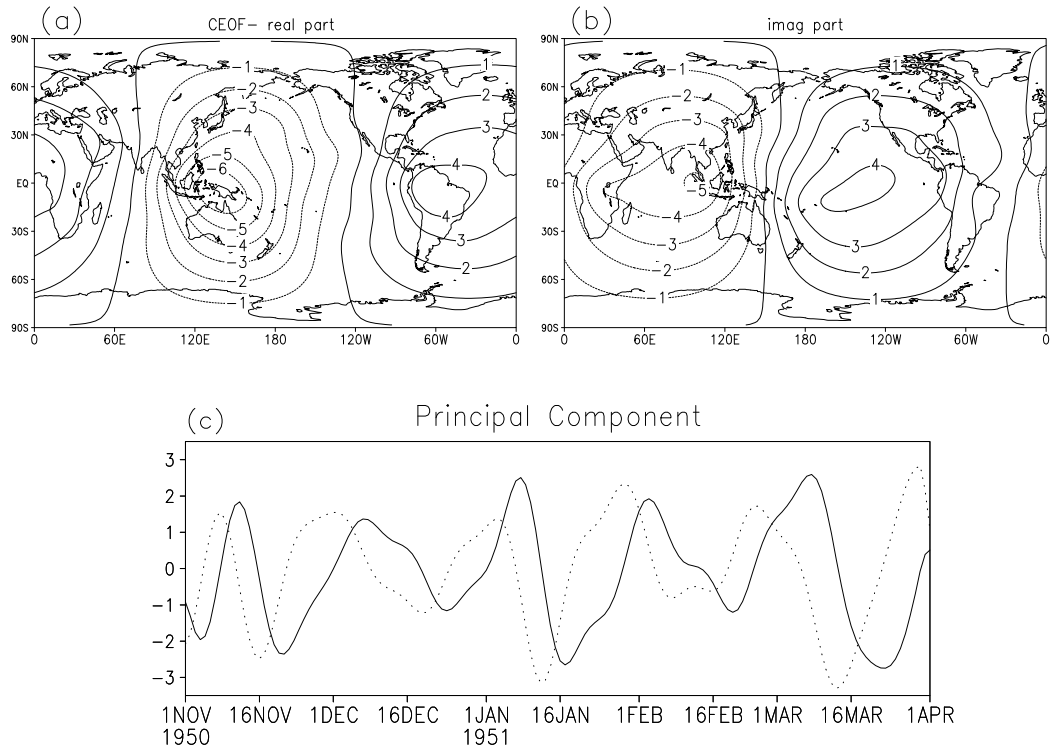


Figure 3.12: (a) Real and (b) imaginary part of the first complex EOF of 10-100-day 200-mb velocity potential, November to March, from GCM data; (c) a selected part of the real (solid line) and imaginary (dotted line) part of the principal component time series.

In order to examine the evolution of meteorological variables during the MJO cycle, composite maps are constructed, as outlined in the following. First, time

series of the phase and amplitude of the complex PC, defined respectively as the argument and absolute modulus of a complex number in the standard way, are found. A ‘strong MJO event’ is defined when the amplitude of the PC stays greater than 0.75 standard deviation for at least 20 days, and when the phase elapsed is at least one complete cycle or  $2\pi$  for the whole event<sup>4</sup>. Values of lowpass filtered ( $>10$  days) variables during all selected ‘events’ are noted and averaged over, according to the phase of the MJO: here eight phase bins are chosen for compositing:  $0$  to  $\pi/4$ ,  $\pi/4$  to  $\pi/2$ , ...,  $7\pi/4$  to  $2\pi$ . A complete cycle is therefore divided into eight intervals. These phase intervals will be simply referred to as ' $\theta = \pi/4$ ', ' $\theta = \pi/2$ ', ..., ' $\theta = 2\pi$ '.

### 3.4.2 MJO composite anomalies

Fig. 3.13 shows MJO composite anomalies of the 850-mb streamfunction and precipitation; all fields are 99% significant (see, e.g., Krishnan et al. 2000, for establishing significance levels of composites). Only four phases, representing half of a cycle, are shown; composite maps in the other half of the cycle are almost identical, but with the opposite sign. An eastward-moving, wavenumber-one structure is apparent in the streamfuction anomalies. It is noteworthy that, although large-scale tropical circulation is emphasized by using the streamfunction, extratropical features are still obvious in the North Pacific. Precipitation moves eastward, but its evolution is characterized by strong spatial modulation. In particular, it attains local maximum at equatorial Africa, the Indian Ocean, the western Pacific with an extension to the northeast of Australia, and South

---

<sup>4</sup>The mean MJO period, based on statistics of strong MJO events, is found to be much longer than 20 days.

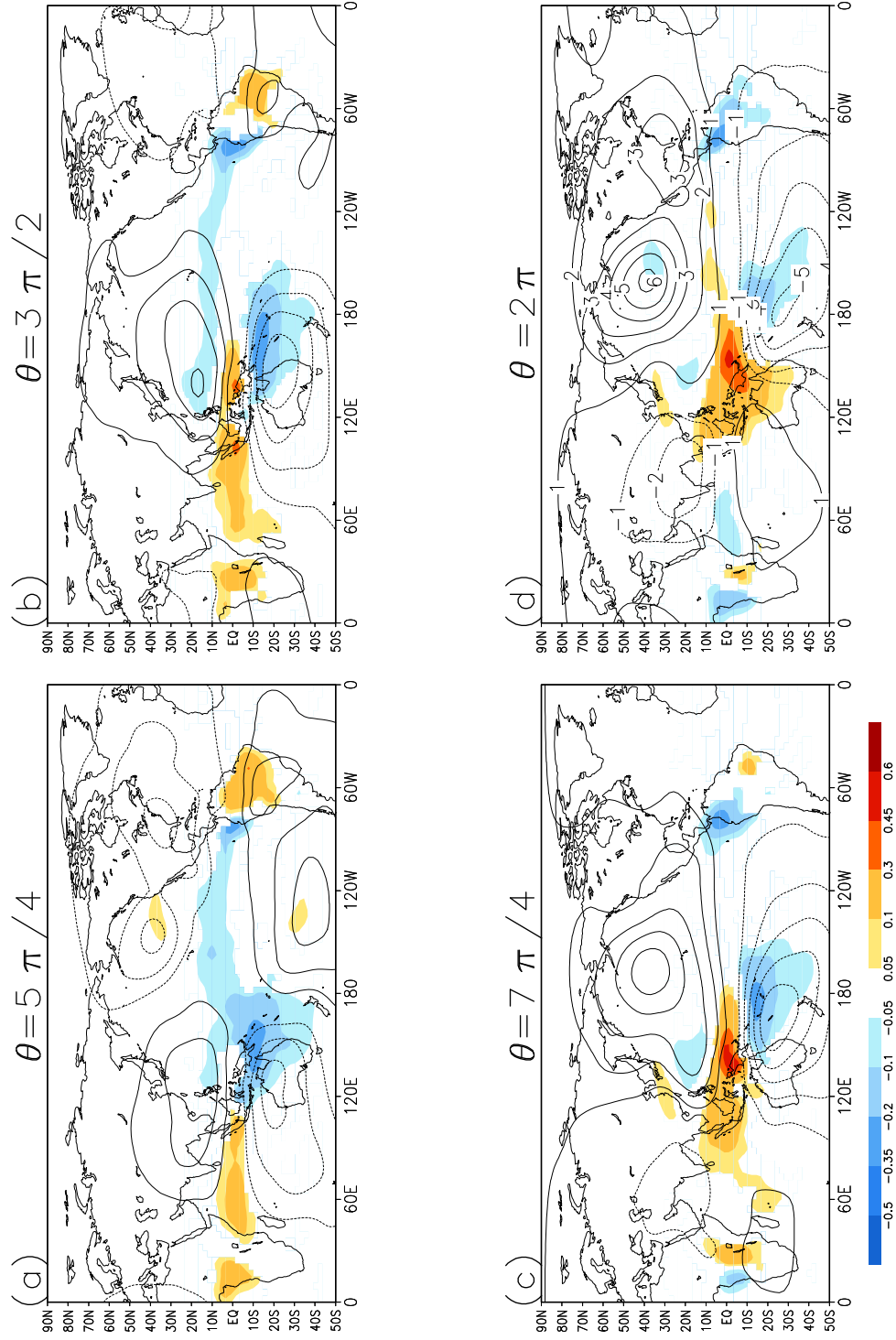


Figure 3.13: MJO composite maps of precipitation (shading, in unit of  $\text{cm day}^{-1}$ ) and 850-mb streamfunction anomalies (contour interval:  $10^6 \text{m}^2 \text{s}^{-1}$ ). Temporal phase of (a)  $\theta = 5\pi/4$ , (b)  $\theta = 3\pi/2$ , (c)  $\theta = 7\pi/4$  and (d)  $\theta = 2\pi$  are shown. All fields exceed 99% significance level.

America. Local growth and decay is very prominent in these locations. Anomalies sometimes remain almost stationary; the eastward propagation of precipitation signals seems slower than that of the circulation patterns. Weickmann and Khalsa (1990), in their observational study, also noticed the apparently slower propagation of convective signals compared with large-scale anomalies, such as the velocity potential. Precipitation anomalies with opposite signs often coexist within the eastern hemisphere, giving the field a wavenumber-two signature.

During the phase of  $\theta = 5\pi/4$ , precipitation within the western Pacific is strongly suppressed; to the west, there is a pair of anticyclones straddling the equator. This circulation pattern is reminiscent of the Gill-type response of the atmosphere to anomalous heating in the tropics (Gill 1980). In the next phase of  $\theta = 3\pi/2$ , positive precipitation anomalies extend eastward from the Indian Ocean toward the western Pacific. Negative anomalies now move southeastward along the South Pacific Convergence Zone (SPCZ) and northward east of the Philippines. The aforementioned anticyclones extend poleward with increased magnitude. At  $\theta = 7\pi/4$ , precipitation becomes very strong over the western Pacific, where anomalous easterly wind is found. The anticyclone to the north becomes prominent in the extratropics, while its southern counterpart has a large magnitude over subtropical South Pacific. At  $\theta = 2\pi$ , positive rainfall anomalies attain their largest values over the western Pacific, but otherwise move very little and remain almost quasi-stationary. The extratropical anticyclone over the North Pacific has gained further strength. The cyclones in the eastern hemisphere, located to the west of the strong positive rainfall, have increased their magnitude and moved eastward. Part of the configuration of positive/negative anomalies east of Australia is reminiscent of the OLR dipole observed by Lau and Chan

(1985). In the western hemisphere, strong perturbations of precipitation are found in South America throughout the MJO cycle; activity over the Atlantic, however, is weak.

Composites of streamfunction and wind fields at 200 mb are shown in Fig. 3.14. Tropical circulation in the opposite sense to that in the low level is found; in other words the vertical structure is baroclinic. Equivalent barotropic circulation is apparent in the extratropics in the phase of  $\theta = 2\pi$ , when anticyclonic flow appears over the North Pacific. One striking difference between the low and upper-level flow is that, for the latter, the pattern continues to propagate eastward into the western hemisphere. Wind anomalies actually increase their amplitudes while moving from the western to central Pacific. Over the eastern Pacific and the Atlantic magnitudes of anomalies are maintained. Such difference in spatial modulation of the wind anomalies amplitudes at the two levels is consistent with the different patterns of variance of the zonal wind (see Fig. 3.6). One plausible explanation of the difference was given by Salby and Hendon (1994). They noticed a more global extension of coherent upper-level  $u$  wind compared with convective signals, which are much confined within the Indian Ocean and the western Pacific. It is suggested that there is a Kelvin-wave response emanating from region with strong anomalous convective heating. The Kelvin wave, having a zonal wind signature, continues to propagate eastward in the western hemisphere even when convection is absent. On the other hand it seems that low-level wind perturbations are more confined to regions where the MJO convection is active. This confirms the impression by examining intraseasonal variance of the low-level  $u$  and the  $\chi$  field in section 3.2.2.

At  $\theta = 5\pi/4$ , westerly perturbations over the maritime continent are found

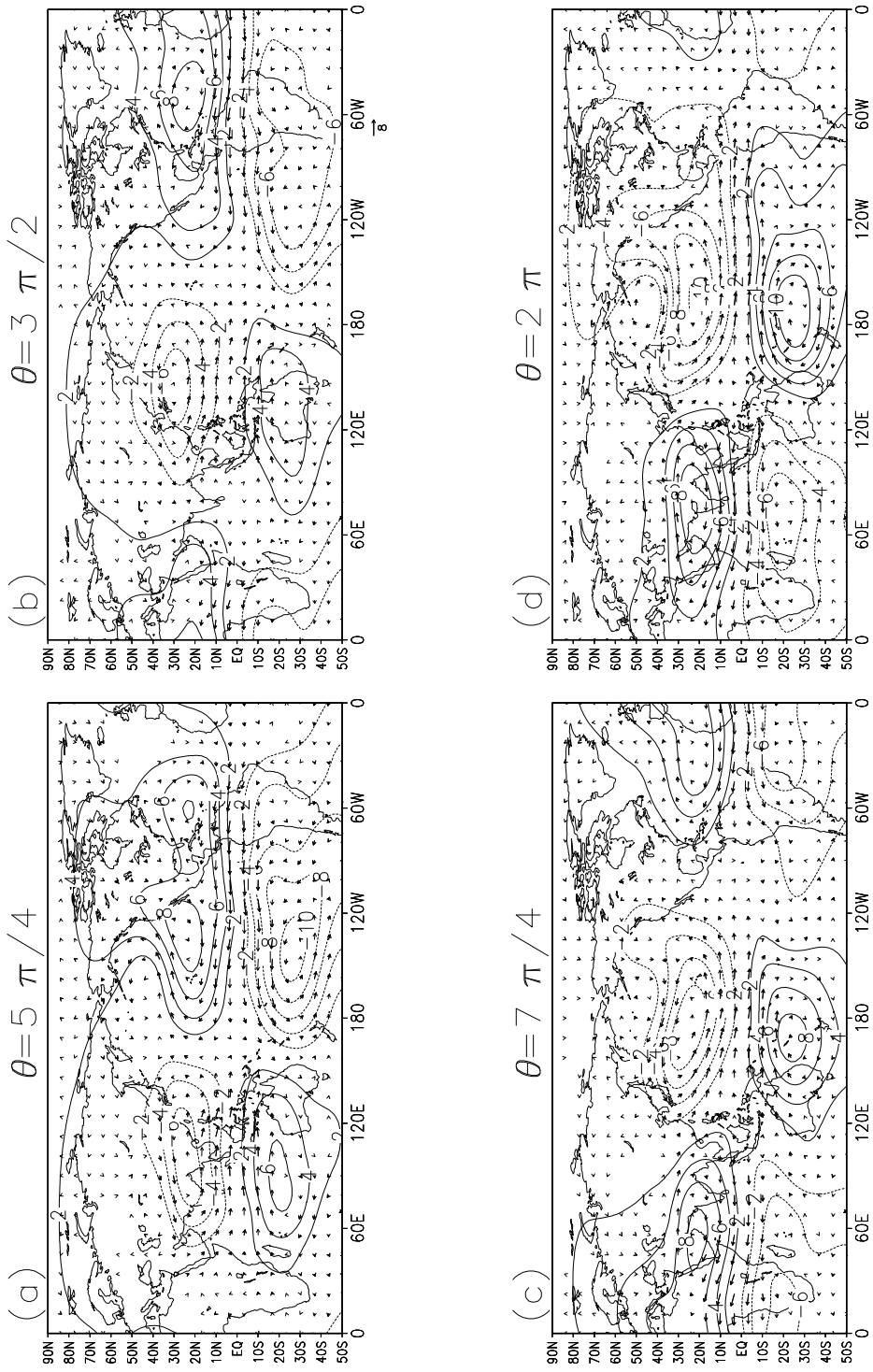


Figure 3.14: As in Fig. 3.13 but for 200-mb streamfunction (in  $10^6 \text{ m}^2 \text{s}^{-1}$ ) and wind anomalies (magnitude in  $\text{ms}^{-1}$ .)

above the easterlies at 850 mb in the same region. Associated with the westerlies is a pair of cyclones, straddling the equator and extending from 30°N to 30°S; again this seems to be the Gill-type response to suppressed convection over western Pacific (see Fig. 3.13 (a)). During  $\theta = 3\pi/2$ , the cyclonic gyres move to the east with the northern one slightly displaced poleward. At the time of  $\theta = 7\pi/4$  the cyclones become quasi-stationary; westerlies begin to appear over the central Pacific. Extratropical circulation begins to take shape, with anomalous zonal wind going against the climatological mean jet in the North Pacific. In the next phase of  $\theta = 2\pi$ , strong westerly wind perturbations are found over most part of the eastern Pacific. Anticyclonic circulation appears in the North Pacific just south of the Aleutians, and there are strong perturbations of the  $u$  wind in the vicinity of the mean Pacific jet exit. The latter feature is consistent with the variance plot of 200-mb  $u$ , which shows strong intraseasonal activity there (see Fig 3.5). Many of these circulation features in the tropics and subtropics, as well as the anomalous response of the jet stream, are similar to the observational results of Knutson and Weickmann (1987), with the exception that anomalous circulation over Eurasia (see their Fig. 12) seems missing in the GCM results.

## 3.5 Evolution of Moist Static Energy

### 3.5.1 A measure of instability

Concerned with the triggering of the MJO, Bladé and Hartmann (1993) suggested that a pre-conditioning of the atmosphere is essential to the occurrence of strong convection. Such pre-conditioning process can take the form of an accumulation

of low-level moist static energy ( $h$ ). (Here  $h \equiv C_p T + \phi + Lq$ , with  $C_p$  being the heat capacity of air at constant pressure,  $T$  the temperature,  $\phi$  the geopotential.  $L$  is the latent heat of vaporization, and  $q$  is the specific humidity.) Kemball-Cook and Weare (2001; hereinafter referred to as KW01) examined the onset of the MJO in off-equatorial sites. Based on radiosonde data, they showed that a slow increase of the low-level  $h$ , mainly due to moistening, precedes MJO convection. This is followed by a rapid drying of the atmosphere. In this section, evolution of  $h$  and responsible mechanisms are examined, in order to further understand the relationship between the MJO circulation and its convection.

Fig. 3.15 (a) shows Hovmoller diagrams of  $5^{\circ}\text{N}$ - $5^{\circ}\text{S}$ -averaged anomalous precipitation and  $\Delta h$ , where  $\Delta h = h(\sigma = 0.935) - h(\sigma = 0.46)$ , and values of  $h$  at the two vertical levels, associated with the MJO based on GCM data.  $\Delta h$  can be interpreted as an ‘instability index’, defined in a way analogous to KW01, in which it is defined as the difference of values of  $h$  at 1000 and 500 mb<sup>5</sup>. Anomalies are found by taking lag regression of variables with the real part of the PC. It is found that strong positive  $\Delta h$  always precedes positive precipitation anomalies. Furthermore,  $\Delta h$  changes sign when convection takes place and becomes negative when convection subsides and precipitation is suppressed, suggesting that it is reasonable to take  $\Delta h$  as an instability measure. The result supports the idea that some pre-conditioning is needed for the convection to occur. Fig. 3.15 (b) shows values of  $h$  at the two different levels. It can be seen that there is a time lag, from 2 to 5 days, with the low-level  $h$  always leading the middle-upper level  $h$ , which tends to be more in phase with convection. Similar relationship

---

<sup>5</sup>It is interesting that  $\Delta h$  is defined similarly to the moist static stability  $M$ , except with a reversed sign and that  $\Delta h$  is more concerned with difference of moist static energy values near the surface and at the middle troposphere.

between  $h$  at different levels and the MJO convection was reported by KW01 in off-equatorial locations. (However, they did not show results at the equator.)

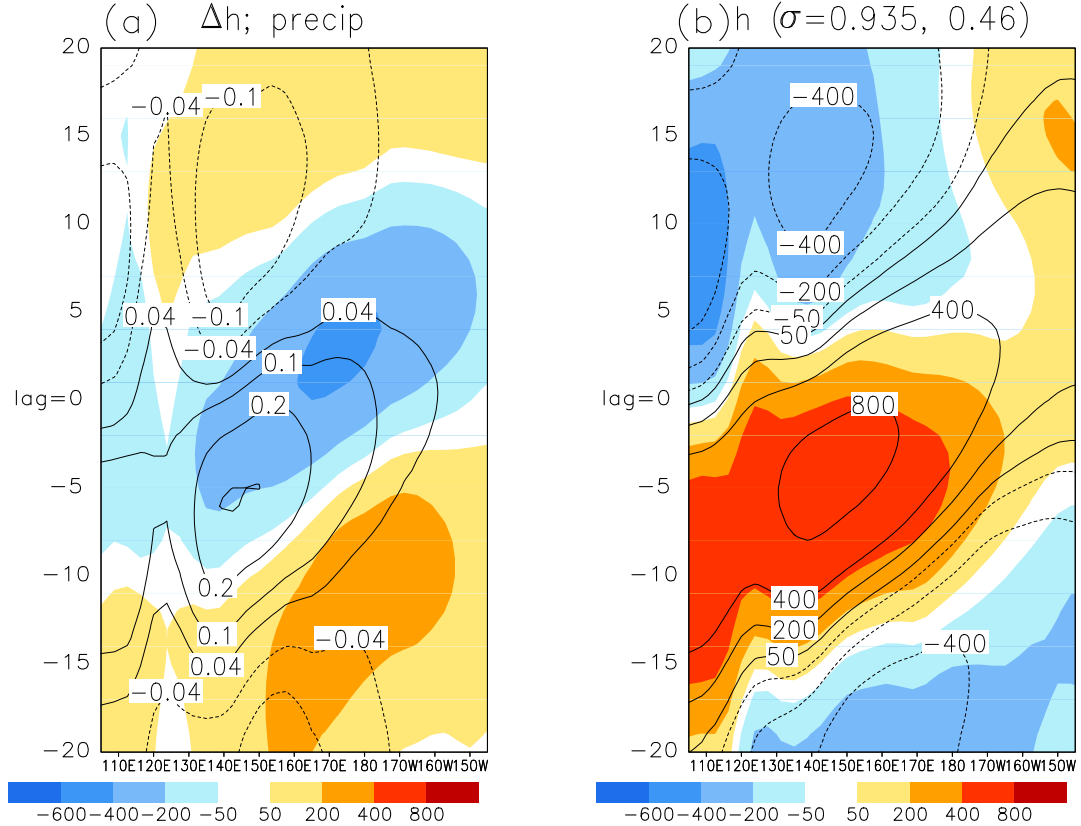


Figure 3.15: (a) Hovmoller diagram showing lag regression, onto the real part of principal component, of moist static energy difference ( $\Delta h$ , in shading) between the levels  $\sigma = 0.935$  and  $\sigma = 0.46$ , and precipitation (contour). (b)  $h$  at the  $\sigma = 0.935$  (shading) and  $\sigma = 0.46$  level (contour). All fields are averaged over  $5^\circ\text{N}$ - $5^\circ\text{S}$ . Unit of  $h$  and  $\Delta h$ :  $\text{J kg}^{-1}$ . Contour levels for precipitation (in  $\text{cmday}^{-1}$ ): -0.1 -0.04 0.04 0.1 0.2 0.3.

The vertical cross section of  $h$  is shown at various time lags in Fig. 3.16. Here regression maps for the period of -12 to -9, -7 to -4 and -2 to 1 lag days are shown. Anomalies of  $Lq$  and  $C_pT$  are also shown as well for comparison. These three time frames are referred to as the onset, mature and decay stage of the convection, which attains its maximum magnitude in the region of 140°-160°E. During the onset stage, the low to middle troposphere has already been moistened up, around and to the west of 140°E; a westward vertical tilt in  $Lq$  is seen to the east. Such a tilt is related to the frictional convergence of moisture within the region with strong surface easterlies, and appears clearly in the moisture perturbations (see also section 3.5.2). Large  $\Delta h$ , which occurs before the convection in Fig. 3.15, mainly results from such a tilt in  $q$ . It is noticed that the temperature variable also has a westward tilt in middle-upper levels, and there is a hint of a reverse tilt in low levels. Previous studies using essentially the same GCM (Lau et al. 1988; Hayashi and Golder 1993) also report similar tilting of variables. Temperature anomalies are weaker and perturbations of  $q$  control those of  $h$  at this time. During the mature stage when convection is strongest,  $h$  is distributed almost uniformly within the tropospheric column at 150°E. There is a maximum of  $q$  in the low to middle levels, as well as  $T$  at the middle to upper levels. The latter, which now makes an important contribution to  $h$ , is likely due to convective heating (supported by inspecting the MJO diabatic heating; not shown). Both the extension of anomalous  $q$  to the middle levels and increase of  $T$  in the middle-upper levels make the value of  $\Delta h$  small. Finally, when convection decays, moisture is much eroded, especially in the lower troposphere. Temperature anomalies also become weaker in low levels, but otherwise maintain roughly the same magnitudes in the upper troposphere. The combined effect is to strongly

reduce the low-level  $h$  but not the upper-level value.  $\Delta h$  turns negative and the troposphere is stabilized.

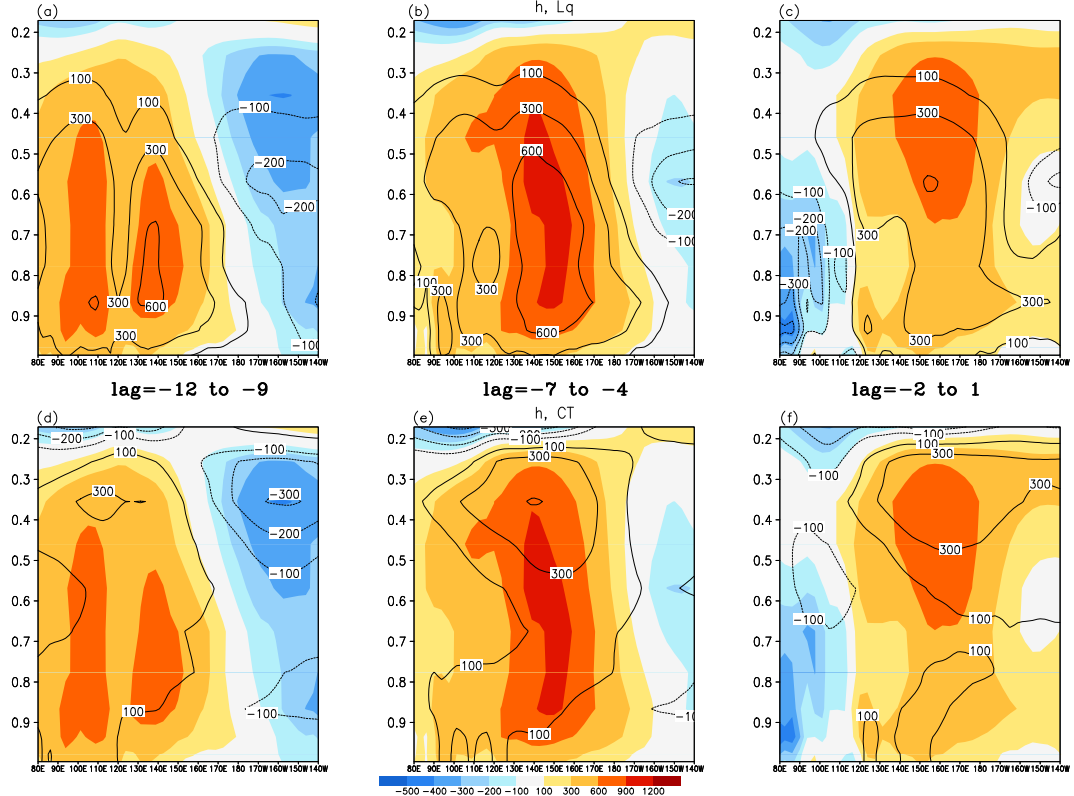


Figure 3.16: Vertical cross section of lag regression of moist static energy  $h$  (shading) onto the real part of principal component,  $5^{\circ}\text{N}$ - $5^{\circ}\text{S}$ -averaged. Regression maps of neighboring lags are averaged over for three periods: lag = -12 to -9 [(a) and (d)], lag = -7 to -4 [(b) and (e)] and lag = -2 to 1 [(c) and (f)]. Regression of specific humidity (multiplied by  $L$ ) are depicted by contours in upper panels, and temperature (multiplied by  $C_p$ ) by contours in lower panels. Shading in both upper and lower panels depicts the same values of  $h$ . Unit of both shading and contours:  $\text{Jkg}^{-1}$ .

### 3.5.2 Frictional convergence of moisture

The prominent westward tilt of moisture in low levels suggests that near-surface frictional convergence is operative. In particular, easterlies along the equator

to the east of strong MJO convective updraft would lead to convergence due to surface friction. This could be a mechanism for the accumulation of low-level moisture. To verify this, composite maps of the 925-mb moisture tendency  $dq/dt$ , surface wind and surface pressure are constructed, as shown in Fig. 3.17. The phase is chosen to be  $\theta = 3\pi/2$ , which approximately corresponds to the previously defined onset stage of convection. The surface wind field partially reflects the circulation at 850 mb as depicted in Fig. 3.13 during this phase, in which easterlies are found within the western Pacific. On the other hand, convergence of the surface wind field is also noticed. Strongest convergence is found along within the western Pacific within  $140^{\circ}$ - $160^{\circ}$ E,  $7^{\circ}$ S to  $7^{\circ}$ N (not shown). The cross-isobaric nature of the wind supports the idea that frictional force plays a role in the convergence along the equator. Hendon and Salby (1994) found very similar surface convergence preceding anomalously enhanced convection in observations. Compared with their results, however, the GCM surface convergence is located much closer to the strong convection to its west (see again Fig. 3.13). Large  $dq/dt$  above the surface is collocated with this region, confirming that surface convergence is responsible of moistening the low levels along the equator, *before* strong convection takes place. Very similar process is found in a number of observational studies (Jones and Weare 1996; Maloney and Hartmann 1998).

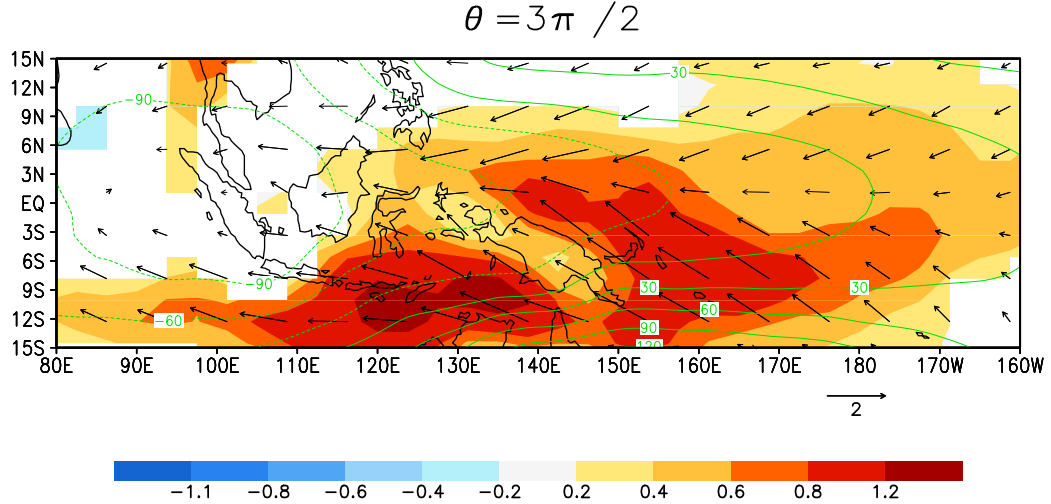


Figure 3.17: MJO composite of 925-mb moisture tendency  $dq/dt$  (in unit of  $10^{-9}\text{s}^{-1}$ , shading), surface wind (arrows, magnitudes  $\text{ms}^{-1}$ ) and surface pressure (contours, in Pa), at the phase of  $\theta = 3\pi/2$ . Moisture tendency and wind field exceed 99% significance level.

Although frictional convergence seems to account for moisture accumulation along the equator, it should be emphasized that this may not be the case in other regions. It is noticed that large moisture tendencies also exist outside regions of strong surface convergence, say at about  $10^\circ\text{S}$  north of Australia. Examination of the moisture budget (not shown) shows that moisture advection by the anomalous 925-mb wind from regions with a higher time mean  $q$  is responsible for the strong tendency there. Since frictional convergence is operative only along the equator, other mechanisms must be responsible for moistening the low levels in off-equatorial regions, as suggested by KW01.

It is also instructive to examine the effect of the anomalous surface evaporation on the MJO moisture budget. Evaporation anomalies at the phase of  $\theta = 3\pi/2$ , together with surface wind perturbations, are plotted in Fig. 3.18 (a). During this onset stage of strong convection, positive evaporation is found at about  $5^\circ\text{-}10^\circ$  over

the western Pacific, instead of along the equator. Near New Guinea, evaporation anomalies actually acquire a negative sign. Mean surface wind is easterly east of the Philippines, westerly north of Australia (not shown). This explains the signs of evaporation anomalies, as easterly wind perturbations, prevalent over the whole domain of interest at this phase of the MJO, would enhance (reduce) the wind speed in the former (latter) region.

It can be seen that the anomalous evaporation does not contribute to the accumulation of moisture along the equator. In fact it even serves to slightly reduce moisture anomalies over the warm pool region at this phase of the MJO. To further compare the effect of evaporation to the transport of moisture, Fig. 3.18 (b) shows composite anomalies of the quantity  $-\nabla \cdot (\mathbf{u}q)$ , vertically integrated for the whole atmospheric column, in the same phase of the MJO. It can be readily shown that the column-integrated moisture storage term is given by  $\langle \partial q / \partial t \rangle = \langle -\nabla \cdot (\mathbf{u}q) \rangle + E - P$ , where  $E$  is the evaporation and  $P$  is the precipitation. Vertical integration is denoted by  $\langle \cdot \rangle^6$ . Notice that the anomalous moisture flux  $\langle -\nabla \cdot (\mathbf{u}q) \rangle'$  comprises convergence as well as advection of moisture. This term is found to be strongest at the equator spanning Indonesia and New Guinea, consistent with the low-level convergence in this MJO phase. More importantly, its overall magnitudes are about 5 times stronger than those of the anomalous evaporation. Evaporation probably plays a less significant role in moisture accumulation for the GCM, at least over the warm pool region<sup>7</sup>.

---

<sup>6</sup>It is equal to  $\frac{P_s}{g} \int d\sigma(\cdot)$ , where  $P_s$  is the surface pressure.

<sup>7</sup>However, this does not rule out the possibility that evaporation can be important in other regions, or that it can even be crucial for the existence of the MJO.

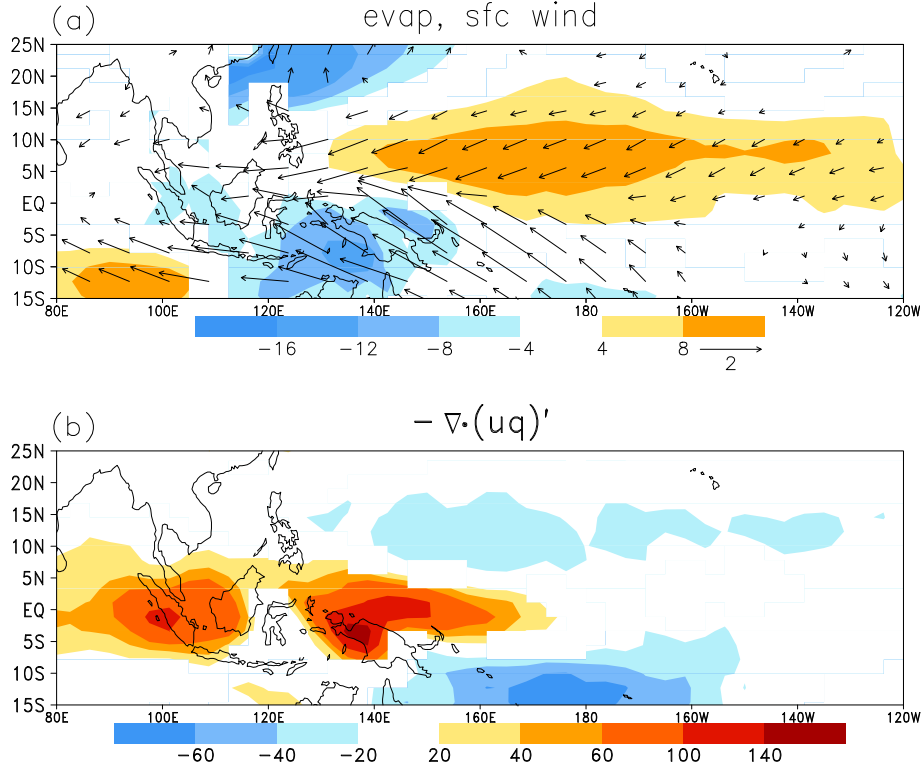


Figure 3.18: As in Fig. 3.17 but for (a) anomalous evaporation multiplied by latent heat of vaporization  $L$  (in  $\text{Wm}^{-2}$ , shading) and surface wind (arrows; magnitudes  $\text{ms}^{-1}$ ), and (b) vertically integrated moisture flux convergence  $< -\nabla \cdot (\mathbf{u}q) >'$  multiplied by  $L$  (in  $\text{Wm}^{-2}$ ). Note that shading information in (a) and (b) are different. All fields exceed 95% significance level.

## 3.6 Summary

The space-time structure of the MJO is examined by studying frequency spectra and variance of both the velocity potential and the zonal winds. Anomalies of these variables show a strong wavenumber one signature, with periods of 30 to 60 days. Large amplitudes are generally found in the eastern hemisphere for convection and low-level zonal wind; perturbations of upper-level zonal wind have a much more global extension.

The propagation characteristics of MJO are studied using lag-correlation analysis based on the velocity potential. There is strong growth of amplitudes over the Indian Ocean, and rapid dissipation over the western-central Pacific. The MJO is also found to be slowest over the western Pacific, fastest over the eastern Pacific and to its east. An estimate of the moist stability is given, and its zonal variation is roughly consistent with that of the MJO phase speed over the Pacific region. It is noticed that the ambient upper-level zonal flow also shows a similar variation. It is possible that this ambient flow may also influence the phase speed of the MJO.

It is shown that the GCM-simulated MJO is realistic in a number of different aspects, such as its space-time characteristics, growth rate and phase speed. However, its amplitudes are much larger than those appeared in reanalyses data. Complex EOF analysis of the 200-mb velocity potential, which enables a closer look at circulation features during the MJO cycle, is performed. These features are consistent with results based on spectra and variance maps, and also with many previous observational works.

Finally, positive signals of the instability index, defined as the negative vertical gradient of the moist static energy, is found to always precede strong convection during the MJO cycle, based on GCM simulations. This is mainly due to a buildup of moisture in low levels. When convection subsides, moisture anomalies are reduced while upper-level temperature anomalies remain positive, resulting in an increase of the moist static energy with height. Along the equator, frictional convergence of moisture is the main mechanism for the accumulation of low-level moist static energy. These processes seem to correspond to those observed during the cycle of the MJO.

# **Chapter 4**

## **Impact of ENSO on the Madden-Julian Oscillation**

Modulation of the MJO during ENSO, and possible dynamical processes involved, is the subject of this chapter. As discussed in Ch. 3, MJO-related convective activity is much confined to the eastern hemisphere. Convective signals, being strongest over the Indian Ocean and the western Pacific, decay rapidly about the dateline as they propagate eastward. This suggests that the underlying SST has a strong control on the MJO convection, as colder SST is usually found in the eastern Pacific. During El Niño years, it is plausible that the anomalously warm SST would enhance the level of intraseasonal convective activity in the central-eastern Pacific, and the reverse could happen during La Niña events. This will be shown to be the case, for both the observations and the GCM simulations. By using some of the analysis tools introduced in Ch. 3, characteristics of the MJO during warm and cold ENSO events will be compared in detail.

## 4.1 Introduction

### 4.1.1 Previous studies on the relationship between ENSO and MJO

There are not many studies on the impact of ENSO on the MJO based on observations. Gutzler (1991) examined intraseasonal variance of 200 and 850-mb zonal wind using station data. In the season of December to February during El Niño events, enhanced (suppressed) activity of the 850-mb  $u$  was found east (west) of the dateline. Anyamba and Weare (1991), based on OLR data, reported that during two out of the three warm ENSO events considered, there is more eastward penetration of intraseasonal activity around the central Pacific, and the propagation speed is slower. Later studies using the OLR with a longer base period (Fink and Speth 1997; Vincent et al. 1998; Hendon et al. 1999) come to a similar conclusion: during warm ENSO events, convective activity is intensified over the central or central-eastern Pacific, while those over the western Pacific are suppressed. This east-west dipole-like perturbation of activity is reversed during cold ENSO events. Interestingly, there are indications that upper-level activity is affected by ENSO rather differently, compared with those appearing in low levels as well as those related to convection. Wang and Murakami (1988) found a decrease of the kinetic energy of the 200-mb intraseasonal flow, during the strong El Niño of 1982-83 over the eastern Pacific. It is well known that the mean upper-level westerlies are also reduced in this region during warm events. Suppressed variability there might be related to the modulation of the westerly duct through which extratropical activity can propagate equatorward, as proposed by Webster and Holton (1982).

A positive correlation between the magnitude of the MJO and the value of underlying SST has been hinted at in a few numerical studies. Wang and Li (1994) studied the MJO using a simple model which governs the dynamics of a baroclinic mode and a boundary layer. Stronger growth of their unstable mode was found when the model SST was increased. The GCM simulations of Hayashi and Golder (1993) indicate that SST distribution has a great influence on regions where strong MJO convection is found.

Despite various suggestions that warmer SST should lead to stronger MJO, the *overall* amount of MJO activity may not be strongly affected by SST anomalies during ENSO. Slingo et al. (1999), based on NCEP-NCAR reanalyses data, found that the zonal mean of the intraseasonal 200-mb zonal wind, a measure of the overall MJO magnitude, is only weakly related to ENSO. Furthermore, they carried out GCM integrations forced by monthly varying global SST, and reported that observed year-to-year variability of the amount of MJO activity was not reproduced. They concluded that internal variability of the MJO is much stronger than the variation caused by the change of the SST. Results of Hendon et al. (1999) also support this conclusion.

#### **4.1.2 Selection of ENSO events**

Before considering how ENSO affects the MJO, the selection of ENSO episodes is outlined here. Within the period of 1950-99, nine El Niño (warm) events are chosen. They are the episodes in 1957-58, 1965-66, 1969-70, 1972-73, 1976-77, 1982-83, 1987-88, 1991-92 and 1997-98. The nine La Niña (cold) events selected are: 1950-51, 1954-55, 1955-56, 1964-65, 1970-71, 1973-74, 1975-76, 1988-

89 and 1998-99. All chosen events satisfy the criteria put forward by Trenberth (1997), namely that the magnitude of anomalous SST, averaged over the Niño-3.4 region ( $120^{\circ}\text{W}$ - $170^{\circ}\text{W}$ ,  $5^{\circ}\text{N}$ - $5^{\circ}\text{S}$ ), is greater than  $0.4^{\circ}\text{C}$  for at least six consecutive months. Exactly the same nine warm and cold episodes are chosen in Alexander et al. (2002). Also, the Niño-3 index, defined as the SST averaged over the domain of  $5^{\circ}\text{N}$ - $5^{\circ}\text{S}$ ,  $90^{\circ}$ - $150^{\circ}\text{W}$ , will be used on some occasion as an index for ENSO. (The same warm and cold events are selected for studying the ENSO-related variability of the low-frequency circulation and synoptic-scale activity in Ch. 6 and 7, respectively.)

## 4.2 Effects of ENSO on MJO Amplitude and Propagation Characteristics

### 4.2.1 Intraseasonal Variance

Variance maps are useful in locating regions with strong activity, and have been used in section 3.2.2 to study the climatological behavior of the MJO. Here the difference of 25-100-day variance of 200 and 850-mb velocity potential between warm and cold events, during the period of November to March, are shown in Fig. 4.1. Results are based on GCM and NCEP-NCAR reanalyses data. In order to retain anomalies pertaining to the MJO, time series of velocity potential are reconstructed using the leading CEOF as follows. First, CEOF's are obtained from the 25-100-day filtered  $\chi$  field based on data from warm events only. The velocity potential is then reconstructed following a standard EOF expansion, by keeping the first eigenvector and principal component only. The same procedure is re-

peated based on data from cold events. The EOF reconstruction serves to reduce the noise level and extract prominent eastward propagating signals. Notice that the CEOF's computed for warm and cold events *separately* are not necessarily the same. In particular, if intraseasonal anomalies have different magnitudes in different geographical locations during warm and cold events, different eigenvectors would result from CEOF analyses.

Results from both datasets indicate a robust eastward extension of strong anomalies during warm events, compared with cold events. Enhancement of MJO activity is generally found within the western-central Pacific during El Niño years. Inspection of the variance plots for warm and cold events (not shown) reveals a shift of 20°-40° eastward of locations of strongest anomalies from cold to warm events. This is consistent with the results from a number of studies (Fink and Speth 1997; Vincent et al. 1988; Hendon et al. 1999).

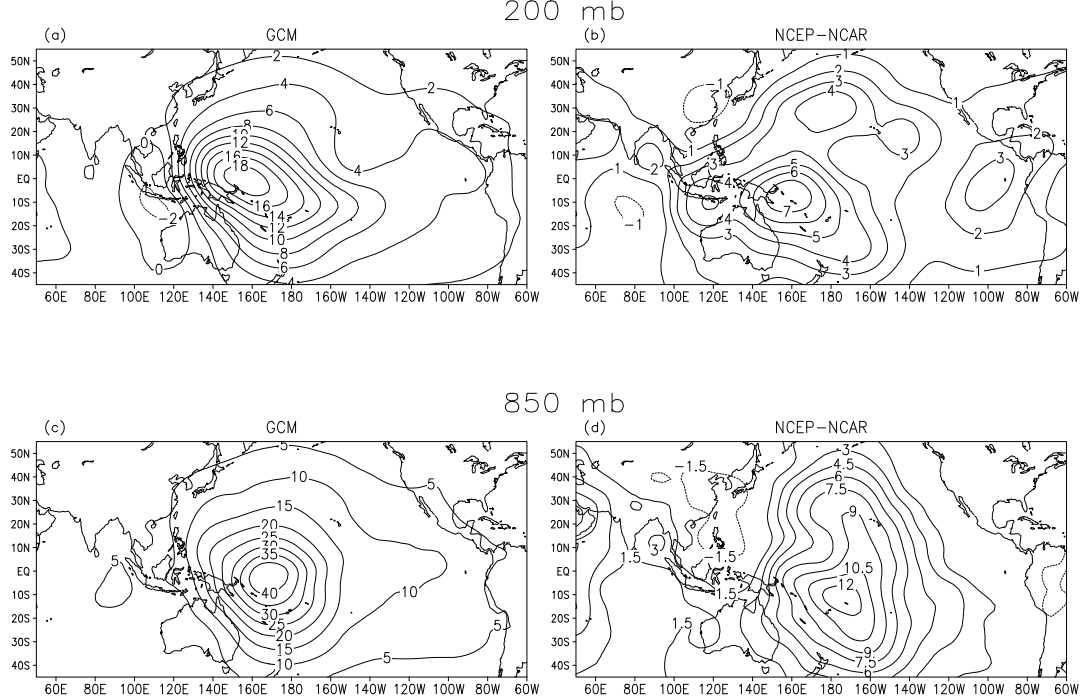


Figure 4.1: Warm minus cold 25-100-day variance of the velocity potential, for GCM [(a) and (c)] and NCEP-NCAR reanalyses [(b) and (d)]. Anomalous velocity potential is reconstructed from the leading CEOF for the period of November to March, with EOF analysis carried out separately for warm and cold ENSO events. Top and bottom panels show results for 200 and 850-mb velocity potential, respectively. Contour intervals (in unit of  $m^4 s^{-2}$ ):  $2 \times 10^{12}$ ,  $1 \times 10^{12}$ ,  $5 \times 10^{11}$  and  $1.5 \times 10^{11}$  for (a), (b), (c) and (d), respectively. (Zero contours are removed from NCEP-NCAR results.)

There is also a modest increase of the overall amount of activity during El Niño events, which can be inferred from large areas with positive polarity in Fig 4.1. However, the change is small, and is about 5-10% of the total variance. Such an amount of change could be sensitive to the base period and the choice of the 'MJO index'. Hendon et al. (1999) reported that overall MJO activity is reduced during strong El Niño years, based on a shorter base period and different MJO indices. In any case the most robust impact of ENSO seems to be an east-west

shift of MJO activity, and this will be the main focus here.

Results from GCM and NCEP-NCAR reanalyses agree well in showing enhanced MJO amplitudes eastward of its climatologically active regions, during warm events. Interestingly, the reanalyses results reveals a shift of activity in subtropical/mid-latitude regions as well: during cold events, strong activity in east Asian and northern western Pacific is found, much like the climatological situation (see Fig. 3.5), whereas during warm events anomalies are suppressed. Such modulation is not found in the GCM data.

Fig. 4.2 shows the 25-100-day variance of 200 and 850-mb zonal wind for November to March, regressed onto the Niño-3 index, which is averaged over the same season. Data from 1950 to 1999 is used. For the NCEP-NCAR data, an 11-year running mean, smoothed by a 1-2-1 filter, is subtracted from the time series of variance to remove decadal signals. At the 850-mb level, regression maps show perturbation of strong activity in the form of a dipole in the tropics. More eastward extension of anomalous zonal wind around the dateline and to its east is found during El Niño events; during La Niña, there is an increase of amount of activity over the maritime continent and the western Pacific. The latter regions are also where intraseasonal anomalies of 850-mb  $u$  are strong in the climatological sense. The east-west displacement of activity associated with the low-level zonal wind during ENSO agrees with results of Gutzler (1991) and Hendon et al. (1999, see their Fig. 9). Extratropical impact related to ENSO is also present: a large part of the North Pacific shows suppressed level of activity during warm events. GCM and reanalyses results agree reasonably well. For the latter, modulation in the tropics has a smaller magnitude and less well-defined patterns, but the dipole structure is still apparent.

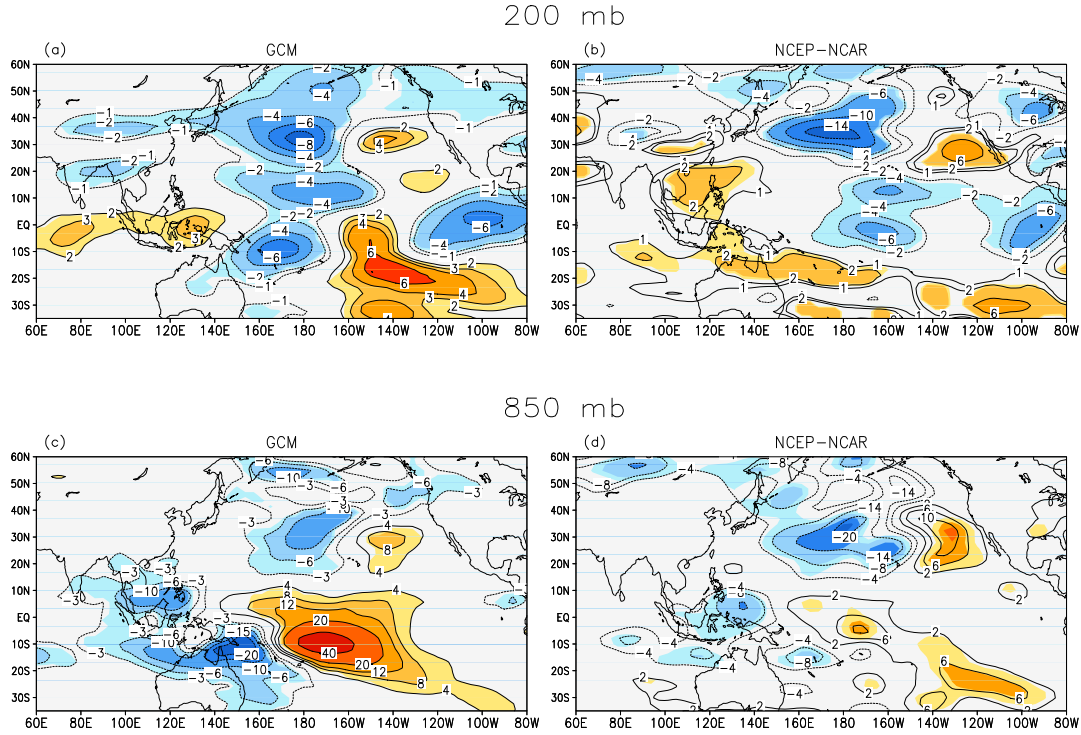


Figure 4.2: Regression of 25-100-day variance of 200 and 850-mb zonal wind onto the Niño-3 index, averaged over the season of November to March. Upper panels show results for 200-mb level based on (a) GCM and (b) NCEP-NCAR data. Lower panels [(c) and (d)] are the same as upper ones except for 850 mb. Regressions exceeding 95% (90%) significance level are shaded for GCM (NCEP-NCAR) values. Unit for 200 mb zonal wind variance:  $\text{m}^2\text{s}^{-2}$ ; for 850 mb:  $0.1\text{m}^2\text{s}^{-2}$ .

At the 200-mb level, zonal wind anomalies are suppressed in the North Pacific during warm events. The change of extratropical activity can be readily linked to that of the 850-mb level, and they tend to have the same polarity. Within the tropics, however, the change of upper-level activity is quite different from its low-level counterpart. In the central and part of the eastern equatorial Pacific, amplitudes of anomalies actually *decrease* during warm events. The change of amplitudes in the central Pacific has off-equator maxima at about  $10^\circ\text{N}$  and

$10^{\circ}\text{S}$ , while another region with suppressed activity is found over the extreme eastern Pacific. This is in broad agreement with results of Wang and Murakami (1988). Comparison with Fig. 3.6 reveals that the aforementioned locations are also where strong activity is found in the climatological sense. In other words, during cold events 200-mb  $u$  anomalies are enhanced within these climatologically active regions. Results from GCM and NCEP-NCAR data agree concerning the above features, though there are also some discrepancies. In particular, the GCM dataset shows enhanced magnitudes of  $u$  in part of the southeastern Pacific during warm events, whereas reanalyses results give an analogous but southward-shifted pattern. Patterns from the two datasets are also different over north to northeastern Australia and in part of southeast Asia.

The above analyses give evidence that MJO activity, using the amplitude of velocity potential as a measure of their magnitudes, penetrates more eastward during warm ENSO events. For the low-level zonal wind, an extension of intraseasonal activity into the central Pacific is also found during the warm ENSO phase, whereas there is an enhancement of anomalies in their climatologically active regions during the cold phase. For the upper-level zonal wind, on the other hand, amplitudes of anomalies increase during cold events in the central-eastern equatorial Pacific. Gutzler (1989) noticed that interannual variation of the *magnitudes* of intraseasonal upper and low-level  $u$  are not coherent. Such a discrepancy suggests that the low and upper-level intraseasonal flow are governed by different dynamical processes. Inspection of the ENSO modulation on GCM precipitation variance (not shown) reveals a dipole pattern much similar to that associated with the low-level zonal wind. Enhanced magnitudes at the dateline and eastward, suppressed magnitudes over northeastern Australia and

New Guinea are found during warm events, while reversed changes of amplitudes are found during cold events. These ENSO effects on the MJO circulation and convection will be discussed in section 4.3 in detail, by examining MJO composite maps during warm and cold events.

#### 4.2.2 Results based on lag correlation

To investigate the effects of ENSO on the propagation of the MJO, lag correlation analysis, introduced in section 3.3.1, is applied based on velocity potential data from warm and cold events. Fig. 4.3 shows results based on the GCM 200-mb  $\chi$  field. The most striking difference between the warm and cold case is that for the former, there is an eastward shift of about 20-30° of the growth-decay pattern over a broad region from the Indian Ocean to the Pacific. During warm events MJO anomalies amplify strongly until reaching 140°E, where they begin to decay. During cold events, growth of anomalies is also found over the Indian Ocean, but they begin to decay east of about 100°E. The region of strong growth is larger during warm events as well. Results from NCEP-NCAR reanalyses, as shown in Fig. 4.4, agree well with the GCM in several aspects: an eastward shift of growth-decay pattern and enhanced growth rate over the Indian Ocean are present during warm events.

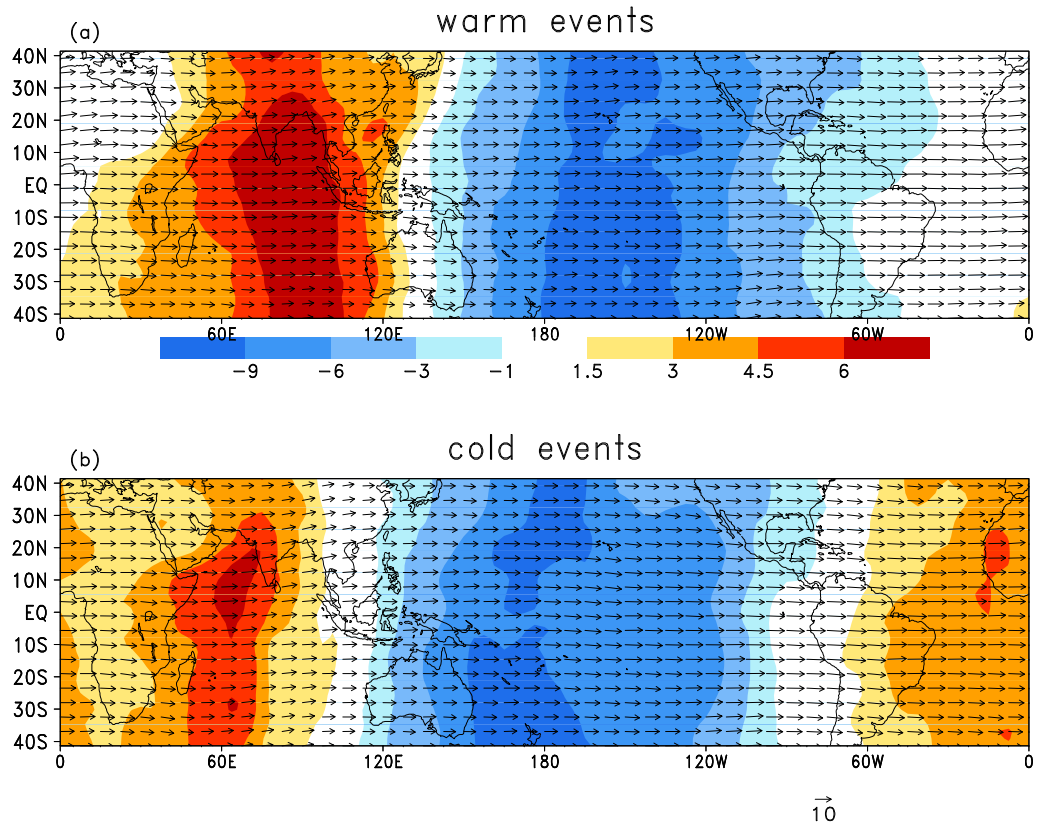


Figure 4.3: Phase velocities and growth rates of 200-mb velocity potential for (a) warm and (b) cold events during the November-March period. Computation based on GCM data. Unit of phase vector magnitude:  $\text{ms}^{-1}$ . Unit of growth rate:  $10^4 \text{m}^2 \text{s}^{-1} \text{day}^{-1}$ .

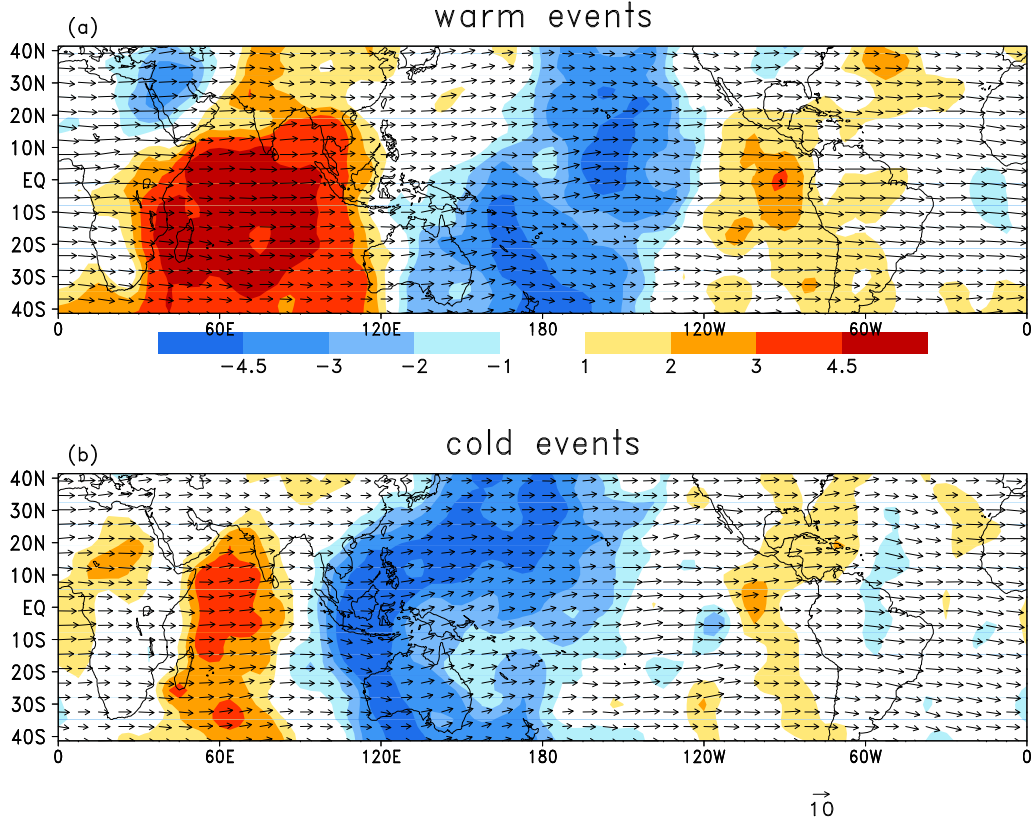


Figure 4.4: As in Fig. 4.3 but for NCEP-NCER reanalyses.

These ENSO effects are consistent with previous results of an eastward shift of the region of strong convective anomalies during El Niño years. The same plots but for the 850-mb  $\chi$  field from GCM and reanalyses datasets are shown in Fig. 4.5 and Fig. 4.6, respectively. Together with the previous results at the 200-mb level, they indicate that the more eastward penetration of the MJO during warm events is a robust feature. It is plausible that the warmer SST within the central Pacific supports more continuous eastward propagation of the MJO during the warm ENSO phase, compared with the situation in the cold phase.

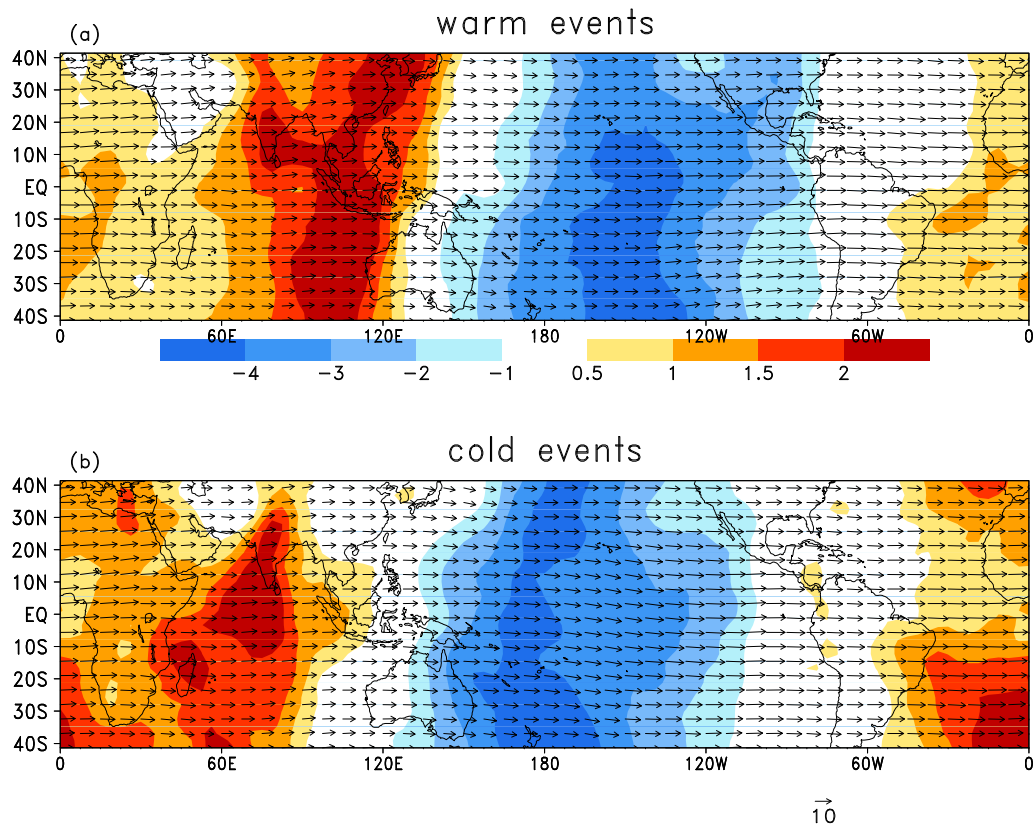


Figure 4.5: As in Fig. 4.3 except at the 850-mb level, with computation based on GCM data.

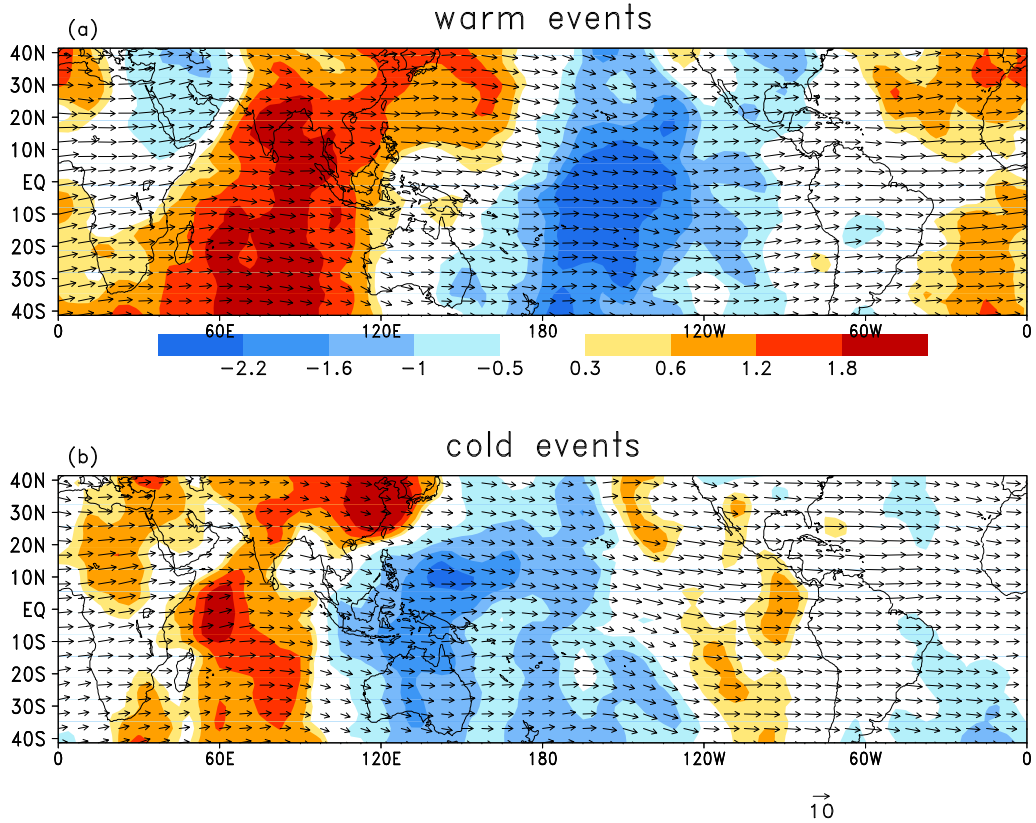


Figure 4.6: As in Fig. 4.5 but for NCEP-NCAR reanalyses.

Besides a shift of MJO activity, ENSO also affects their zonal phase speed. Fig. 4.7 shows warm-minus-cold composites of the MJO phase speed based on the 200 and 850-mb velocity potential from GCM data. A modest change of speed is found within the equatorial central Pacific for signals at 200 mb, with slower propagation of the MJO during the warm ENSO phase, and faster during the cold phase. There are also indications of similar changes of propagation for 850-mb signals. A slower propagation of the MJO during El Niño events is consistent with results of Anyamba and Weare (1995).

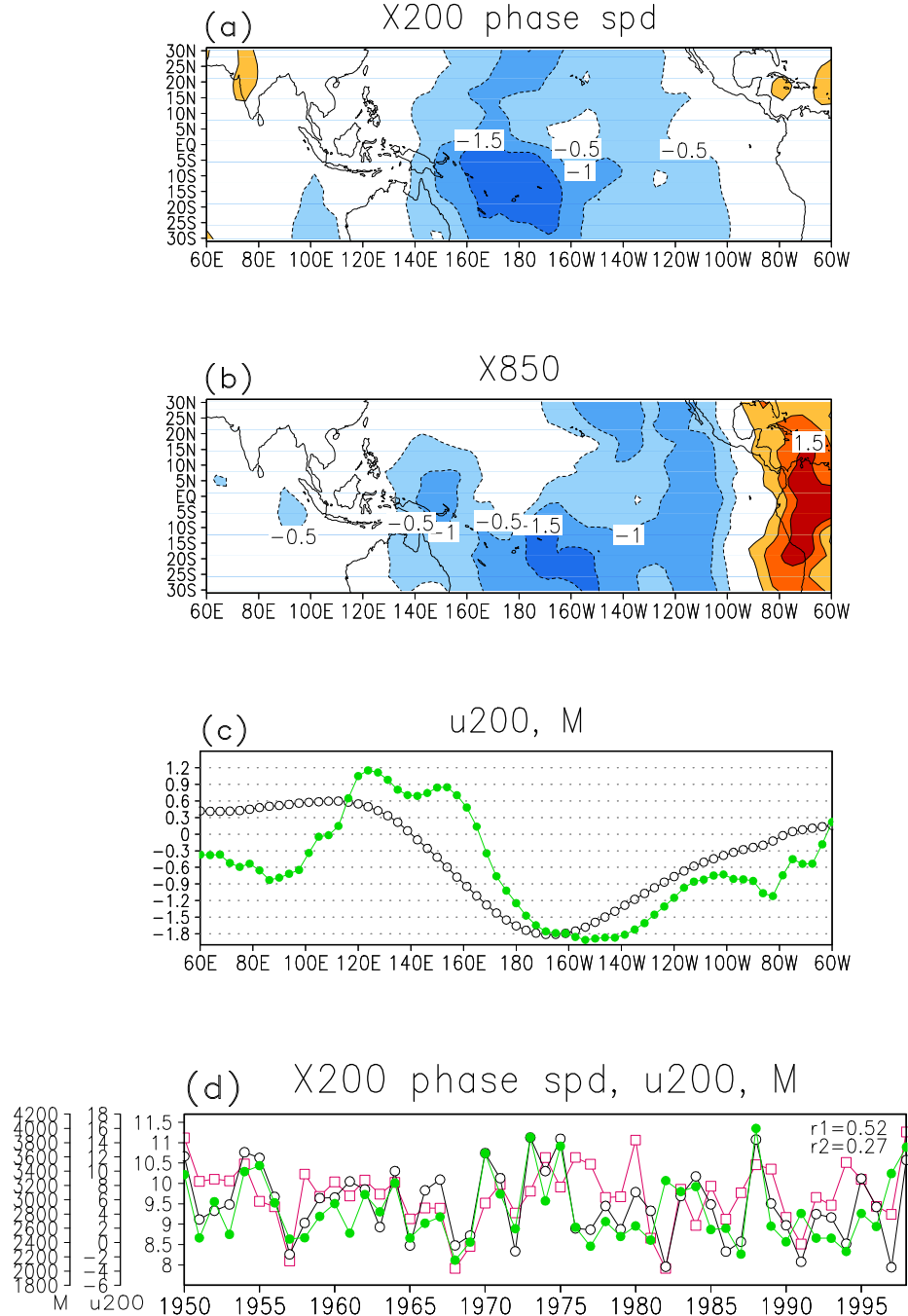


Figure 4.7: (a) Warm minus cold zonal phase speed of 200-mb velocity potential ( $\chi$ ), in unit of  $\text{ms}^{-1}$ . (b) Same as (a) but for 850-mb  $\chi$ . (c) Warm minus cold mean 200-mb zonal wind ( $u$  in  $10\text{ms}^{-1}$ , open circles) and moist stability ( $M$  in  $\text{kJkg}^{-1}$ , filled circles),  $10^\circ\text{N}-10^\circ\text{S}$ -averaged. (d) Time series of phase velocity (based on 200-mb  $\chi$ , open squares), mean 200-mb  $u$  (open circles) and  $M$  (filled circles), for the period 1950-99. Values are averaged over  $165^\circ\text{E}-165^\circ\text{W}$ ,  $10^\circ\text{N}-10^\circ\text{S}$ .

As discussed in Ch. 3, the phase speed could be influenced by both the ambient zonal flow (represented here by the seasonal mean 200-mb  $u$ ) and the moist stability  $M$ . Warm minus cold composite of these two variables, 10°N-10°S-averaged, are also shown in Fig. 4.7.  $M$  is defined in the same way as in Ch. 3 (see section 3.3.2). Both of them have negative anomalous values within the central-eastern Pacific, consistent with what one would expect. Interannually varying seasonal mean 200-mb  $u$ ,  $M$  and MJO phase speed, averaged over the domain 10°N-10°S, 165°E-165°W, are also compared to gain further insight of their possible relationship. Both  $u$  and  $M$  are positively correlated to the phase speed, with correlation coefficient of 0.53 and 0.27<sup>1</sup>, respectively. Thus  $M$  is only marginally correlated with the MJO phase speed, and the ambient flow seems a more important factor in determining its interannual variation.

## 4.3 Circulation and Convection

### 4.3.1 Convective and low-level activity

To examine and understand further the effects of ENSO on the intraseasonal circulation and convection, MJO composite maps are computed. Fig. 4.8 shows composite maps of 850-mb streamfunction and precipitation, during warm and cold events, based on the method outlined in section 3.4.1. For brevity, only three out of eight temporal phases of a complete cycle are shown, namely  $\theta = 3\pi/2$ ,  $\theta = 7\pi/4$  and  $\theta = 2\pi$ . The most obvious difference between warm and cold events is that, for the former, there is a continuous propagation of precipitation

---

<sup>1</sup>The same computation was repeated, using the formulation of  $M$  by Yu et al. (1998), with essentially the same result.

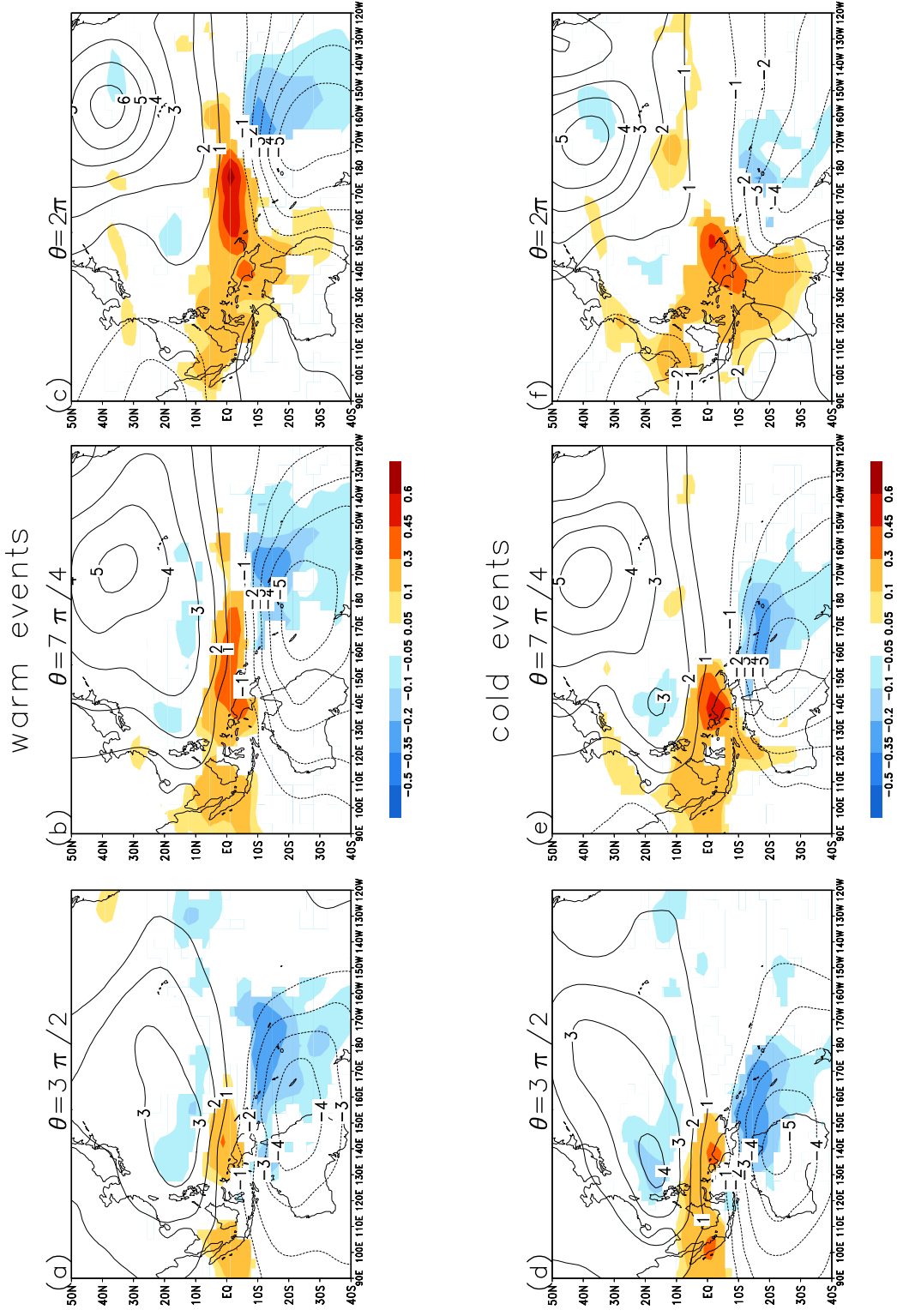


Figure 4.8: MJO composite maps of precipitation (shading, in unit of  $\text{cm day}^{-1}$ ) and 850-mb streamfunction anomalies (contours, in unit of  $10^6 \text{ m}^2 \text{s}^{-1}$ ), at the temporal phase of  $\theta = 3\pi/2$  [(a) and (d)],  $\theta = 7\pi/4$  [(b) and (e)] and  $\theta = 2\pi$  [(c) and (f)]. Uppers and lowers panels show results for warm and cold events, respectively. All fields exceed 95% significance level.

and low-level circulation anomalies from the western into central Pacific. Strong activity exists in the vicinity of the dateline and even to its east. During cold events, disturbances tend to become quasi-stationary over the western Pacific, as seen in composite maps at  $\theta = 7\pi/4$  and  $\theta = 2\pi$ . Strong anomalous rainfall is found over the Indonesian Archipelago, its amplitude decreases sharply to the east, and convective signals collapse east of 160°E.

It is also noticed that within 120°-150°E, cold events MJO convection is *stronger* (see  $\theta = 3\pi/2$  and  $\theta = 7\pi/4$  composite maps). Stronger anomalies of 850-mb  $u$  are also found in the same equatorial region, supported by the inspection of zonal wind composites (not shown). The subtropical anticyclone in the North Pacific, as well as its accompanying negative precipitation, also has a moderately larger amplitude east of the Philippines. Over north to northeastern Australia, perturbations are also stronger during cold events. The above ENSO modulation of activity reflects earlier results concerning the change of 850-mb  $u$  variance, in which its perturbation exhibits a dipole-like pattern. It shows enhanced (suppressed) activity over the central to eastern Pacific and suppressed (enhanced) activity over a large region in the western Pacific during the warm (cold) phase (see section 4.2.1).

### 4.3.2 Upper-level activity

Composite anomalies of the 200-mb wind and streamfunction are shown in Fig. 4.9, during warm and cold events. The pair of cyclones in the upper level is found to propagate more eastward for about 20°E during El Niño years, apparent in the phase of  $\theta = 2\pi$ . Considering the cyclone pair as a Gill-type response

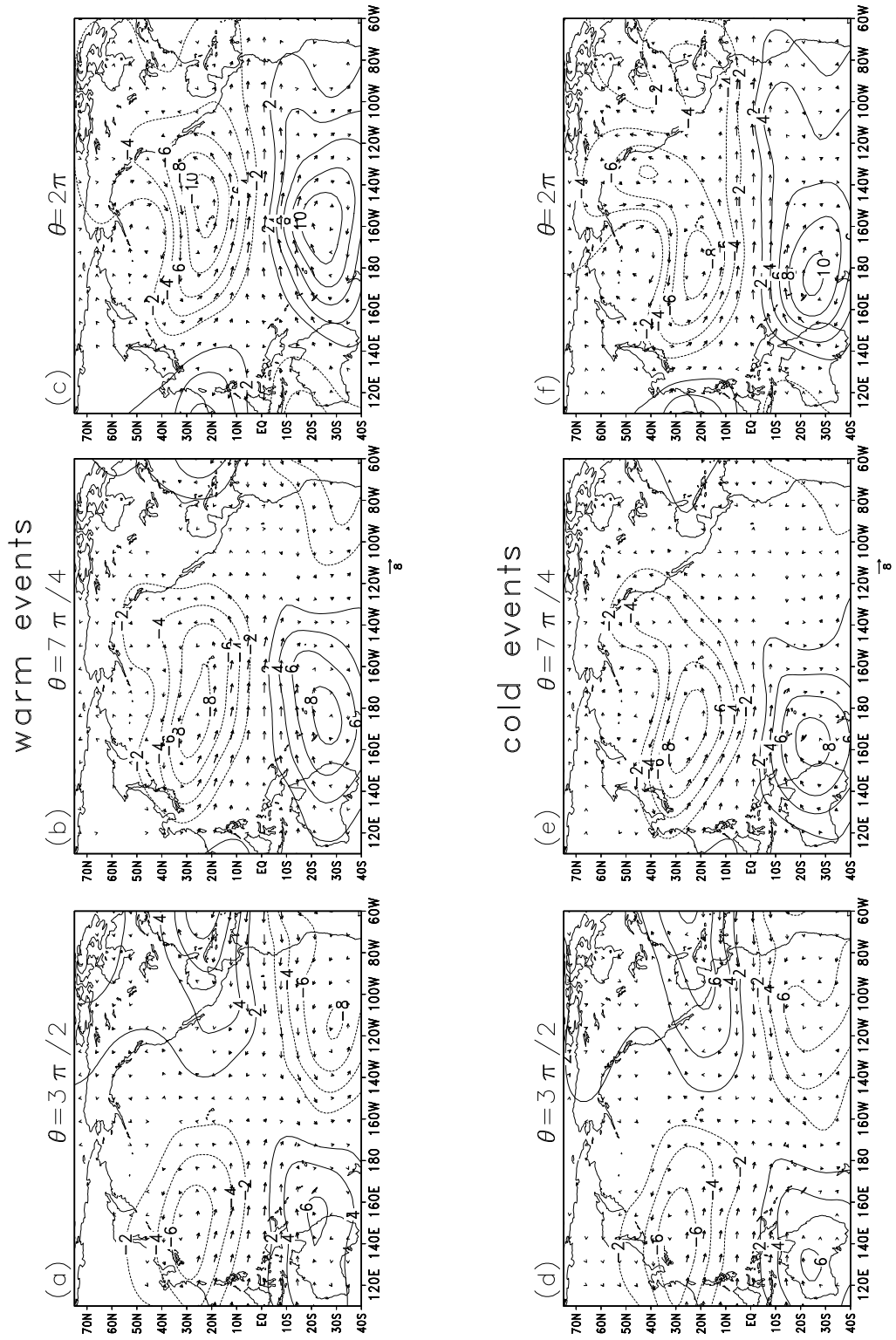


Figure 4.9: As in Fig. 4.8 but for 200-mb streamfunction (in  $10^6 \text{m}^2 \text{s}^{-1}$ ) and wind anomalies (magnitude in  $\text{ms}^{-1}$ ).

to heating, this is consistent with the more eastward extension of anomalous convection. Although not the main focus of this chapter, it is noteworthy that there are indications of different MJO-related extratropical circulation in different phases of ENSO, especially over the North Pacific/North America region. (A more thorough consideration of the intraseasonal circulation in the extratropics can be found in Ch. 5 and 6.)

However, it is also noticed that zonal wind anomalies with substantial amplitudes are present in the far eastern equatorial Pacific during cold events, despite the fact that the pair of upper-level cyclone is more confined to the eastern hemisphere. To take a closer look at their evolution, MJO composite maps of 200-mb zonal wind anomalies are shown in Fig. 4.10, in the phases of  $\theta = 7\pi/4$  and  $\theta = 2\pi$ . During warm events,  $u$ -wind perturbations are found to propagate eastward and acquire strongest amplitudes at about  $160^{\circ}\text{W}$  along the equator. During cold events, perturbations seem to stall just west of the dateline, but at the same time strong anomalies also appear over the extreme eastern Pacific around  $100^{\circ}\text{W}$  in the phase of  $\theta = 2\pi$ .

The mean 200-mb zonal wind during warm and cold events is also shown in the same figure. East of about  $140^{\circ}\text{W}$ , strong deceleration of the mean zonal flow is found. According to Webster and Chang (1988), this deceleration would lead to wave energy accumulation. During warm ENSO events, the deceleration is smaller over the eastern Pacific, and accompanied with this are weaker zonal wind perturbations in the region. It has been proposed that upper-level circulation anomalies in the western hemisphere can be regarded as the Kelvin wave response of the MJO heating located further west (see Salby and Hendon 1994). Accumulation of the wave energy could lead to the variability related to ENSO

over the extreme eastern Pacific.

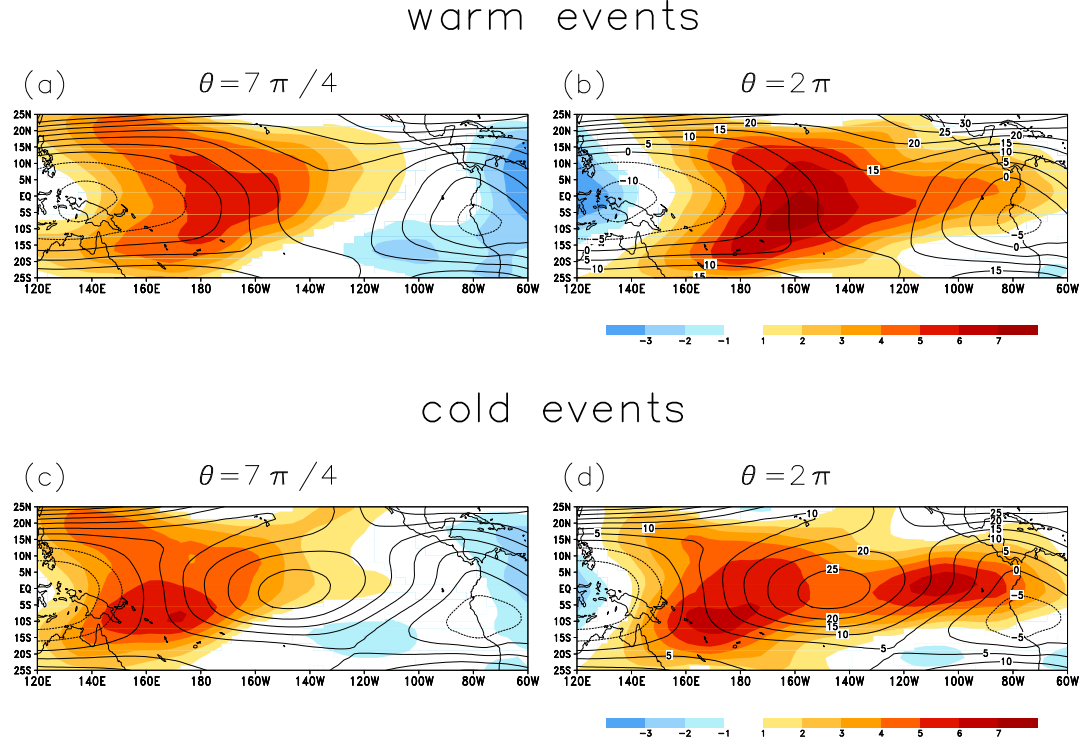


Figure 4.10: As in Fig. 4.8 but for 200-mb  $u$  anomalies (shading) at the temporal phase of  $\theta = 7\pi/4$  [(a) and (c)] and  $\theta = 2\pi$  [(b) and (d)]. Contours in the upper (lower) panels depict the mean 200-mb  $u$  during November to March for warm (cold) events. Units for both shading and contour:  $\text{ms}^{-1}$ .

It is instructive to compare which feature of the difference of the  $u$  variance shown in Fig. 4.2 is related to the difference of the MJO-related  $u$  at 200 mb. For the stronger MJO perturbations of the  $u$ -wind located in the extreme eastern Pacific during cold events, they can be readily associated with variance signals negatively correlated to the Niño3 index in Fig. 4.2. However, over the central Pacific in the northern hemisphere, there is no discernible change of  $u$ -wind anomalies during ENSO based on the MJO composite maps just shown. En-

hanced variability in the region during cold events (see Fig. 4.2) therefore might not be directly related to the MJO. Influences from extratropical low-frequency perturbations could be more important in determining the variability there.

These results based on the MJO composites during warm and cold events further substantiate those concerning intraseasonal variances. It is seen that upper-level anomalous flow is influenced by characteristics of wave propagation over the central-eastern Pacific. On the other hand, low-level wind anomalies are more tightly coupled with convection. These factors make the impact of ENSO on the upper and low-level anomalies markedly different (see also Gutzler 1991).

## 4.4 Moist Static Energy Consideration

It has been shown that during the warm ENSO phase, MJO-related convection penetrates more eastward into the central Pacific. The continuous eastward propagation suggests that the primary role of the warmer SST is to support anomalous convection there during El Niño events. On the other hand, accumulation of low-level moist static energy  $h$  is arguably an important mechanism for the onset and maintenance of MJO convection, as shown in Ch. 3. Further insight on the impact of ENSO on the MJO convection could be gained by studying the evolution of  $h$  during warm and cold events.

### 4.4.1 Evolution of moist static energy

As in section 3.5.1, the instability index  $\Delta h$  is defined as the difference between the low and upper-level moist static energy. Fig. 4.11 shows Hovmoller dia-

grams of  $\Delta h$  and precipitation related to MJO, during warm and cold events. The anomalies are obtained from the lag regression of the variables onto the real part of the PC (same as the regression method used in section 3.5.1). Consistent with results in the last section, precipitation anomalies penetrate further eastward during warm events, with large amplitude found in the vicinity of the dateline. Notice that anomalies propagate eastward continuously in the warm ENSO phase, while in the cold phase they attain their maximum at lag  $\approx -5$  day and do not propagate further. (It is also noticed that the peak over the western Pacific is stronger in the cold ENSO phase, consistent with Fig. 4.8.) As in the climatological situation, strong positive  $\Delta h$  always precedes enhanced rainfall, with a lag of about 5 days. It can be seen that ENSO also affects the evolution of  $\Delta h$ : much stronger signals within the central Pacific are found during the warm compared with cold events. This is consistent with the interpretation that some pre-conditioning is necessary for MJO convection to occur. Failure to develop such a favorable environment results in the collapse of the continuous propagation of convective anomalies, suggested by comparison between the warm with cold ENSO situation.

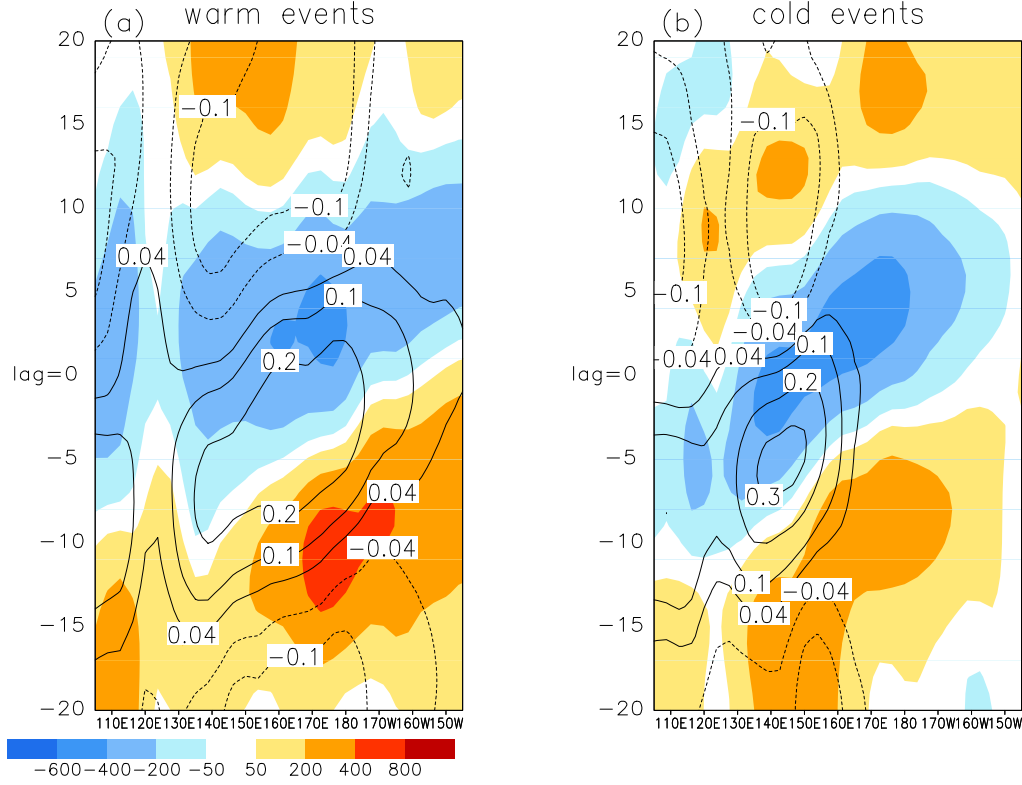


Figure 4.11: (a) Hovmöller diagram showing lag regression, onto the real part of principal component, of moist static energy difference  $\Delta h$  (shading, in  $\text{J kg}^{-1}$ ) between the level  $\sigma = 0.935$  and  $\sigma = 0.46$  and precipitation (contour, in  $\text{cm day}^{-1}$ ), during warm events. (b) As in (a) but for cold events. Values are averaged over  $5^\circ\text{N}$ - $5^\circ\text{S}$ .

The vertical cross section of  $h$  during warm and cold events is shown in Fig. 4.12 during the MJO cycle, averaged over  $5^\circ\text{N}$ - $5^\circ\text{S}$ . As in Fig. 3.16, lag regression maps of  $h$ , as well as the contribution from the moisture field (i.e.  $Lq$ ), are plotted for the three time frames referred to as the onset, mature and decay stage of convection in section 3.5.1.

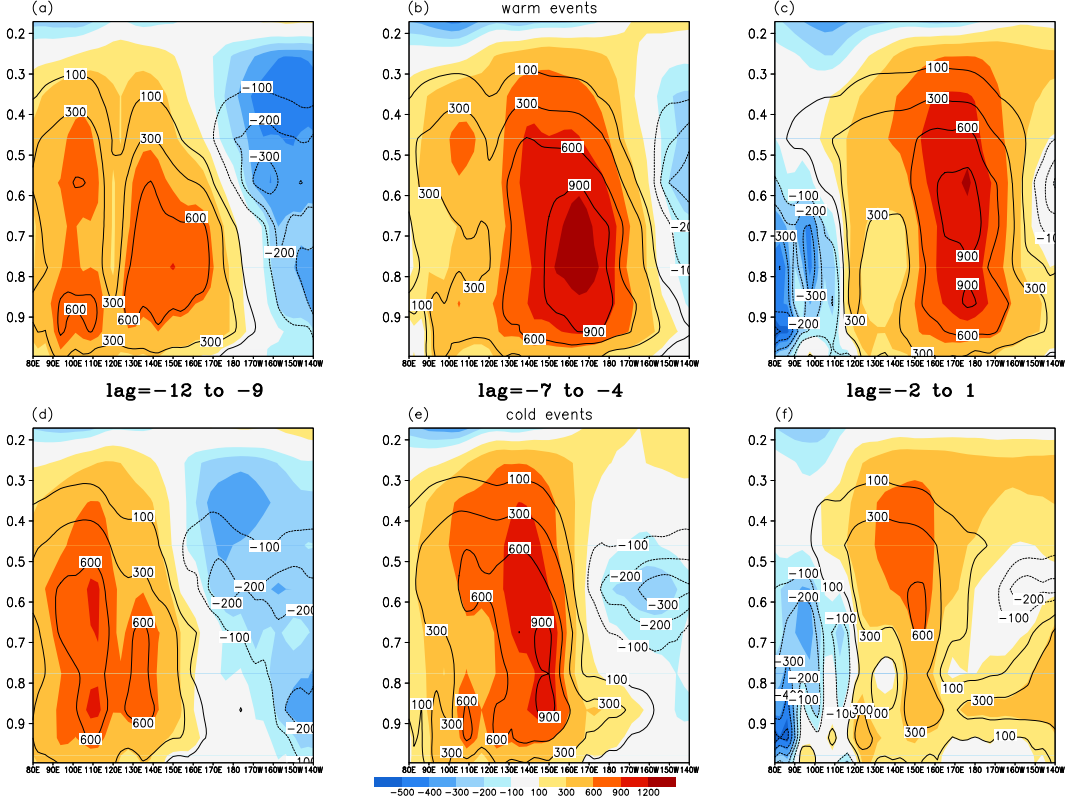


Figure 4.12: Vertical cross section of lag regression of moist static energy  $h$  (shading) onto the real part of principal component,  $5^{\circ}\text{N}$ - $5^{\circ}\text{S}$ -averaged. Regression maps of neighboring lags are averaged over for three periods:  $\text{lag}=-12$  to  $-9$  [(a) and (d)],  $\text{lag}=-7$  to  $-4$  [(b) and (e)] and  $\text{lag}=-2$  to  $1$  [(c) and (f)]. Regression of specific humidity (multiplied by  $L$ ) are depicted by contours. Upper and lower panels show results for warm and cold events, respectively. Unit for both shading and contours:  $\text{J kg}^{-1}$ .

As in Fig. 3.16, during the onset stage,  $h$  is largely determined by the moisture anomalies, in both ENSO phases. It is noteworthy that more low-level moisture is found in the vicinity of the data line for during warm compared with cold events. The extra accumulation of the low-level  $q$  is mainly responsible for the large  $\Delta h$  at about  $\text{lag}=-12$  days during warm events in the central Pacific (see Fig. 4.11), setting the stage for stronger convection there. During the mature stage, the vertical gradient of  $h$  is much reduced. However, during warm ENSO

episodes, there is still a substantial amount of  $h$  in the middle to low levels around  $170^{\circ}\text{E}$  and to its east. This suggests that convective anomalies would continue to develop there, which is consistent with the evolution of convection shown in Fig. 4.11. During the decay stage, precipitation signals have passed their maxima and begin to subside, accompanied by negative values of  $\Delta h$ .

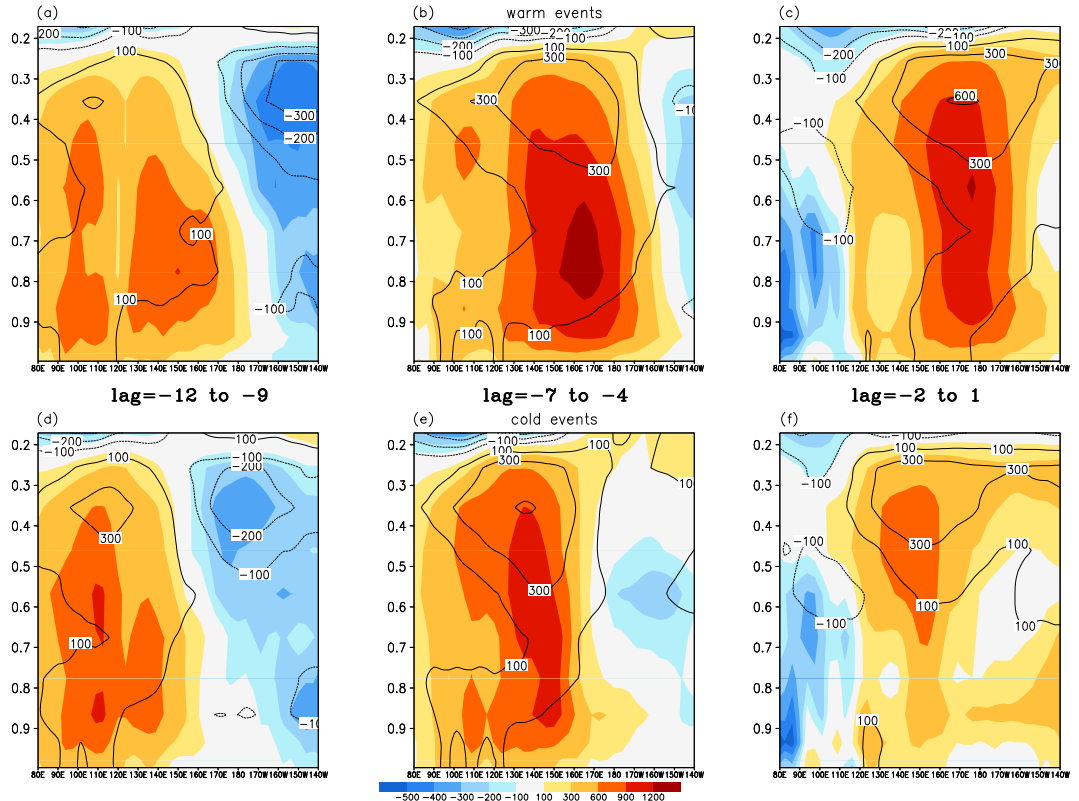


Figure 4.13: As in Fig. 4.12 but with contours depicting anomalous temperature (multiplied by  $C_p$ ).

Fig. 4.13 shows the same evolution of  $h$  and contribution from temperature anomalies (i.e.  $C_p T$ ) during the MJO cycle. Similar to the climatological situation, convective heating, with maximum magnitude in middle-upper levels and being prominent during mature and decay stage, offsets the large positive value

of  $\Delta h$  and turns it negative. For warm events, the temperature perturbations extend further eastward, as expected, accompanying the convection.

#### 4.4.2 Transport of moisture

The previous analysis suggests that warmer SST in the central Pacific is crucial in setting an unstable environment, thus maintaining the eastward propagation of MJO convection. In view of the important role played by the moisture field in the evolution of the moist static energy, it seems fit to consider processes for moisture accumulation and depletion. Fig. 4.14 shows, during warm and cold events, cross section of moisture tendency ( $dq/dt$ ) as well as advection of seasonal mean moisture ( $\bar{q}$ ) by the anomalous vertical motion ( $\dot{\sigma}$ ), i.e.  $-\dot{\sigma}\partial_{\sigma}\bar{q}$ . Here  $\dot{\sigma} \equiv D\sigma/Dt$  is the vertical velocity based on the sigma coordinate of the GCM. Examination of the MJO moisture budget (not shown) shows that, of various budget terms, this is the main term which almost balances the moisture source (or sink).  $dq/dt$  is usually much smaller and can be crudely approximated by the residue from the sum of the vertical advection and source term. Cross section of anomalous circulation, as well as values of  $\bar{q}$  are also shown to facilitate interpretation. As before, anomalies are computed as lag regressions onto the real part of the PC, and three stages of convection are shown. For comparison, column-integrated values of the vertical advection and the precipitation field are also included (below each panel depicting vertical cross sections).

Vertical transport of moisture is generally found within regions of strong precipitation. This is not surprising given the main balance is between the two processes, which is shown by the close match between precipitation and the

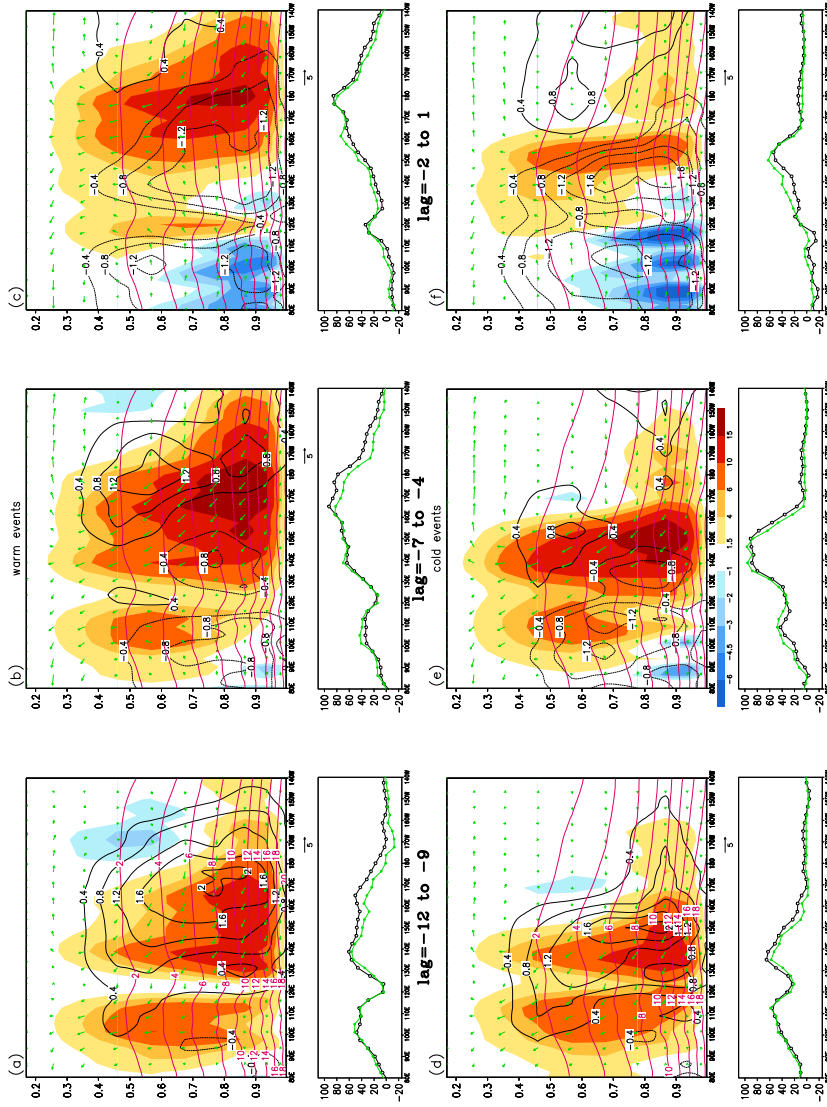


**Figure 4.14:** Cross section of vertical advection of moisture by anomalous circulation (arrows) is computed as lag regression of the zonal wind and vertical velocity onto the real part of the PC. Regression maps shown are averaged over three periods: lag=-12 to -9 [(a) and (d)], lag=-7 to -4 [(b) and (e)] and lag= -2 to 1 [(c) and (f)]. Seasonal mean moisture (magenta contours, in  $\text{gkg}^{-1}$ ) and regression of moisture tendencies (black contours) are also shown. Values of column-integrated vertical advection (black curves) and precipitation (green curves) are shown in the box below each panel. Upper and lower panels are results for warm and cold events, respectively. All budget terms are multiplied by the latent heat of vaporization. Horizontal arrow below each panel represents zonal velocity of  $5\text{ms}^{-1}$ ; a vertical arrow of same length represents vertical velocity of  $0.05\text{Pa s}^{-1}$ . Unit of moisture advection and tendency:  $10^{-3}\text{Jkg}^{-1}\text{s}^{-1}$ . Unit of column-integrated advection and precipitation:  $\text{Wm}^{-2}$ .

vertically-integrated advection. The moisture tendency term is much smaller. The difference between vertically integrated advection and moisture sink has a sign which matches that of  $dq/dt$  shown as cross section. During the onset stage, large values of  $dq/dt$  are found to be partially overlapping but also to the east of the maximum in  $-\dot{\sigma}\partial_\sigma\bar{q}$ . East of where strongest convection is located (about 140°E), moisture advection is more confined to middle-low levels, consistent with the weaker vertical motion there. During the mature stage, when precipitation reaches its maximum, strong advection exists but is now mostly canceled by the moisture sink.  $dq/dt$  is now small and even negative west of 150°E. During the decay stage,  $dq/dt$  is negative, with the magnitude of the advection term now smaller than the moisture sink. Convection and vertical transport of moisture begin to subside, while as a whole the precipitation is now drying up the atmosphere.

Comparing the basic state of warm and cold events, it is apparent that for the latter  $\bar{q}$  decreases rapidly east of 170°E. Accompanying this difference of  $\bar{q}$  is the dramatically suppressed vertical advection of moisture. Part of the difference of vertical advection can be attributed to the different values of  $\bar{q}$  during warm and cold events (based on further analysis of the advection term; not shown). This suggests that the near-surface moisture field could be important in determining regions of strong MJO convection. It is noteworthy that, during the mature stage for the cold ENSO case,  $dq/dt$  becomes very small, whereas for the warm ENSO case strong positive  $dq/dt$  and moisture advection is still present around the dateline, again east of strongest convection. Overall, these results suggest that the continuous supply of moisture during warm events, to which the stronger  $\bar{q}$  contribute, supports the more eastward movement of MJO convective signals.

## 4.5 Discussion and Summary

It is shown that ENSO has a strong impact on the convective anomalies of the MJO. During warm ENSO events, convection is much enhanced eastward of their climatologically active regions. Amplification of the MJO signals extends more eastward, presumably due to the warmer underlying SST. The MJO eastward phase speed is also decreased around the central Pacific during El Niño years, which can be at least partially attributed to the slower upper-level mean zonal flow there.

During warm ENSO events, the anomalous instability index as measured by the negative vertical gradient of the moist static energy has stronger fluctuations over the central Pacific. MJO convection is able to propagate to the region. During cold events, weaker instability signals are found and convective anomalies stall in the western Pacific without propagating further. Examination of the moisture budget reveals that vertical transport of moisture ahead of strong convection extends much further to the dateline, during the warm compared with cold events. It is suggested that the distribution of low-level mean moisture is important in determining the eastward extension of convective signals during ENSO.

Low and upper-level intraseasonal flow is also affected by ENSO. The low-level  $u$  wind exhibits enhanced (suppressed) activity over the central-eastern Pacific, suppressed (enhanced) activity over the western Pacific, during warm (cold) events. Such a perturbation pattern of activity is similar to that associated with convective anomalies. The change of upper-level  $u$  anomalies, however, is very different. Activity is generally enhanced over large equatorial regions in the central Pacific and the extreme eastern Pacific in the cold ENSO phase. The stronger upper-level zonal wind near the central Pacific and stronger deceleration of the

flow further east might account for the enhanced variability in these regions.

Finally, in view of the markedly different impact on intraseasonal activity in the low and upper levels due to ENSO, one should be cautious about choosing an 'index' for studying interannual variability of the MJO. Results here suggest that totally different conclusion could be arrived at by choosing different variables. Given the manifestation of the MJO in so many aspects of the tropical circulation and its complexity, this point is not too surprising, but nevertheless can still be overlooked.

# **Chapter 5**

## **North Pacific Low-Frequency**

### **Circulation Anomalies-**

### **Climatological Characteristics**

#### **5.1 Introduction**

Besides synoptic-scale storm activity, episodes of persistent circulation are also dominant features of the extratropical wintertime circulation. With typical time scales from about a week to a month, low-frequency perturbations have an impact on day-to-day weather through their ability to alter the preferred regions of occurrence of extratropical storms. Understanding low-frequency fluctuations is therefore important, in view of their importance in the atmospheric general circulation and their implications on improving extended range forecasts.

### **5.1.1 Low-frequency perturbations, teleconnection patterns and instabilities of the time mean flow**

The existence of ‘teleconnection patterns’ has been known to synopticians and researchers in meteorology for a long time. These patterns are characterized by having centers of action located rather remotely from each other, but connected by wave-like structures with planetary scales. It seems that low-frequency variability of the general circulation tends to be organized about some preferred spatial patterns (see, e.g., Kutzbach 1970; Dickson and Namias 1976; Namias 1978; van Loon and Rogers 1978; also the review section of Wallace and Gutzler 1981). Corroborating earlier results, Wallace and Gutzler (1981) systematically studied anomalies of the monthly mean surface pressure and 500-mb height field, and were able to identify a set of teleconnection patterns using techniques of objective data analysis. Of all those examined in Wallace and Gutzler (1981), the Pacific/North America (PNA) pattern is most relevant to this study. It has a north-south seesaw in the North Pacific, and also connects centers of action located in Canada and southeastern U.S.. It bears some resemblance with features of Rossby wave dispersion on a sphere, studied by Hoskins and Karoly (1981). Vertically, it is equivalent barotropic. The PNA pattern has a strong presence in various low-frequency phenomena, such as blocking episodes over the North Pacific.

In order to understand the existence of these preferred circulation patterns, Simmons et al. (1983) studied numerical solutions to initial-value problems and also normal modes of a barotropic model on a sphere. The basic state being used is the 300-mb climatological circulation in January. It is found that fastest growing perturbations in initial-value problems often resemble the PNA pattern.

Moreover, these perturbations, and also the most unstable mode of the linearized equations, oscillate with a period of about 50 days, consistent with the range of time scales one would expect. These results strongly suggest that recurrence of the PNA pattern can be understood as the manifestation of barotropic instabilities of the time mean flow. Furthermore, the most unstable mode is shown to be able to grow due to barotropic conversion of energy from the mean flow, and this occurs in the vicinity of the Pacific jet exit.

### **5.1.2 Blocking circulation and its development**

While teleconnection patterns in Wallace and Gutzler (1981) are found based on monthly height anomalies, some of them also appear in events of persistent circulation or blocking flow. These events have life times ranging from a few days to weeks. Dole (1986a) showed that, during North Pacific blocking events, perturbations acquire a PNA-like pattern. Interestingly, examination of geopotential anomalies at various levels also reveals a westward tilt in the vertical. The importance of baroclinic processes is evaluated by the more recent work of Black (1997). Using observational data, he calculated wave-activity fluxes during the life cycle of blocking flow, based on Plumb (1986). The only proximate wave source that leads to growth of perturbations is one which is baroclinic. This suggests that baroclinic dynamics is also important in low-frequency activity, despite their being broadly equivalent barotropic.

The existence of remote perturbations as catalysts responsible for blocking development is also suggested by both observational and numerical studies. Dole (1986b) demonstrated that during the early stage of the development of persistent

circulation, there are perturbations of the Pacific jet at about  $130^{\circ}\text{E}$ . Associated with these are height anomalies originating from east Asia with a vertical westward tilt, which subsequently propagate eastward into the central North Pacific. Frederiksen (1982; 1983) studied unstable normal modes of a two-level baroclinic model. Apart from those resembling the PNA pattern, there are other unstable modes which are distinctly baroclinic and which he labeled as ‘onset-of-blocking modes’. They have large amplitudes over east Asia, upstream of where the blocking frequency is highest over the North Pacific. The evolution of these onset-of-blocking modes is studied in the more recent work of Frederiksen (1998) using a tangent linear model. Large-scale initial baroclinic perturbations over east Asia are seen to propagate into and grow over the North Pacific, meanwhile becoming more equivalent barotropic, similar to the evolution of anomalies during blocking development described by Dole (1986b) and Black and Dole (1993).

### 5.1.3 The role of intraseasonal oscillation

The MJO, or intraseasonal oscillations in general, is one of the dominant types of variability of the tropical climate. Intraseasonal oscillation is also relevant to extratropical low-frequency circulation because of its ability to affect convective activity over a broad region from the Indian Ocean to the western Pacific. Convective heating located in these places is able to excite PNA-like patterns or Rossby wavetrains in the extratropical Pacific. Considering also its intraseasonal nature, the MJO could be closely related to low-frequency anomalies in higher latitudes over the Pacific.

The fact that intraseasonal convection can excite extratropical perturbations

was demonstrated by Knutson and Weickmann (1987), and was considered by Kiladis and Weickmann (1992) in a more detailed manner. Intraseasonal oscillation is shown to be able to excite large-scale wavetrains, from the subtropical western Pacific into higher latitudes and with anomalies reaching the northwestern seaboard of North America. There are also strong perturbations of the Pacific jet, associated with clear signs of baroclinic development. Overall, Kiladis and Weickmann (1992) conveyed a picture in which subtropical rotational circulation, induced by convective heating in the tropics, can subsequently affect the extratropical flow, leading to wavetrains extending into the North Pacific and further downstream.

Higgins and Mo (1997) further examined the idea of extratropical low-frequency flow being connected with intraseasonal convection. Events of persistent circulation anomalies in the North Pacific are studied. They found that these persistent anomalies are preceded one to two weeks by convection and large-scale divergent circulation over the western Pacific. Furthermore, these latter perturbations are reminiscent of the circulation associated with the MJO, and their development is similar to that shown by Kiladis and Weickmann (1992).

#### **5.1.4 Westward traveling patterns**

Disturbances associated with the PNA or other teleconnection patterns are quasi-stationary, i.e. centers of action are fixed geographically and anomalies show little propagation. Branstator (1987) and Kushnir (1987), however, independently reported retrograding patterns in northern high latitudes. These perturbations are found to be the dominant type of low-frequency variability in these latitudes

during northern winter, with planetary scales and typical periods of about three weeks. They are equivalent barotropic, but do not resemble any teleconnection patterns of Wallace and Gutzler (1981). In fact they behave more like propagating external Rossby waves. This impression is confirmed by the vorticity budget analysis of these westward traveling patterns (WTP), computed by Lau and Nath (1999). Their study also provides detailed comparisons between WTP as observed and those simulated by an atmospheric GCM, showing that WTP can be realistically simulated in numerical models.

Interestingly, by analyzing solutions of the linearized non-divergent barotropic vorticity equation, Branstator and Held (1995) found that the most unstable normal mode indeed resembles the WTP (in terms of both its spatial pattern and temporal characteristics). The main difference from Simmons et al. (1983) is that the climatological mean 300-mb flow during the period of November to March, instead of the flow during January, is used as the basic state. It seems that normal modes and their spectra are rather sensitive to the basic state being used. On the other hand, these results also suggest that barotropic conversion from the mean into eddy kinetic energy could be important to the growth of both WTP and PNA-like disturbances. Perturbations of the Pacific jet by WTP (see Kushnir 1987 and discussion therein) are in nature similar to those related to the PNA, i.e. there are strong zonal wind anomalies in the vicinity of the mean jet exit. This is known to be a key signature of low-frequency anomalies which leads to barotropic energy conversion from the time mean flow (see Wallace and Lau 1985).

Finally, while the WTP phenomenon has aroused much theoretical interest, its relationship with blocking episodes also makes it an important subject on

practical grounds. Lejenäs and Madden (1992) were able to show that 20-40% of blocking events are related to the presence of retrograding wavenumber-one waves. Alternatively, amplitudes of these waves also increase whenever blocking flow occurs, implying that these two phenomena are closely related to each other.

### **5.1.5 Interaction with synoptic-scale eddies**

North Pacific low-frequency variability could be affected by a variety of processes, some in the vicinity of the region of interest and some in more remote sites. To first approximation, it can be understood as resulting from the fact that the time mean flow is barotropically unstable, although baroclinic conversion also contributes to the growth of anomalies. One intriguing aspect of the dynamics of low-frequency circulation, however, is its interaction with the high-frequency component of the flow.

As mentioned before, low-frequency perturbations can affect synoptic-scale activity by changing the ambient flow ‘felt’ by the latter. Interestingly, changes of high-frequency eddies also have an impact on the low-frequency flow. This ‘scale-interaction’ is examined in the study of Lau (1988), in which variability of storm tracks and its associated monthly flow anomalies are studied. Major modes of storm tracks variation are found to be associated with circulation anomalies closely related to teleconnection patterns found by Wallace and Gutzler (1981). Moreover, these flow perturbations seem to be maintained by forcing resulted from changes of storm tracks themselves. The implication is that there exists a positive feedback between changes of the ambient flow and their associated modulation of synoptic-scale activity. Changes of the latter are often found to

reinforce low-frequency perturbations.

These ideas are extended in the study of Nakamura and Wallace (1990), in which the possibility of baroclinic activity in initiating strong blocking episodes is examined. Occurrence of intense baroclinic waves *prior* to the onset of blocking events is found. Further diagnostics and modeling studies by Nakamura et al. (1997) confirm that synoptic-scale activity is essential to both the onset and evolution of strong blocking events over the North Pacific.

Many of these observations and theoretical/modeling results concerning low-frequency variability will be referred to later in the study. The above serves as a brief review of the subject, though not intended to be a complete one- there are important ideas not covered at all, e.g. the theory of multiple equilibria by Charney and DeVore (1979). The rest of the chapter will begin with some basic consideration of spacetime behavior of low-frequency flow anomalies, followed by more detailed analyses on recurrent circulation anomalies over the North Pacific, and also variability related to the MJO and the WTP. Some useful diagnostic tools will be introduced at the same time.

## 5.2 Spacetime Characteristics and Dynamics of Low-Frequency Anomalies

### 5.2.1 Spatial variability and its interannual fluctuations

In this and the next chapter, the focus will be on perturbations with subseasonal to intraseasonal time scales (referred to as 'low-frequency perturbations'). To examine amplitudes of low-frequency anomalies at various geographical lo-

cations, root-mean-squares (rms) of the 10-60-day filtered 300-mb height field ( $Z_{300}$ ) during the period of November to March are computed. Fig. 5.1 (a) and (b) show results for both GCM and NCEP-NCAR (1979-99) data, respectively. The 10-day cutoff for filtering is chosen in order to exclude fluctuations related to synoptic-scale activity. Many studies on extratropical low-frequency variability adopt similar period ranges for time filtering (see, e.g., Nakamura et al. 1997; Lau and Nath 1999). Results being shown have no strong dependence on the exact frequency cutoffs. Both figures indicate that strongest activity is found over the North Pacific and the North Atlantic, and anomalies in these two oceanic regions have comparable magnitudes. Perturbations are strongest over the central to eastern part of the oceans, at about the same longitudes of the exits of the Pacific and Atlantic jets. Regions of strong activity also tend to extend to the landmass east of the oceans, i.e. into northwest North America and also Northern Eurasia.

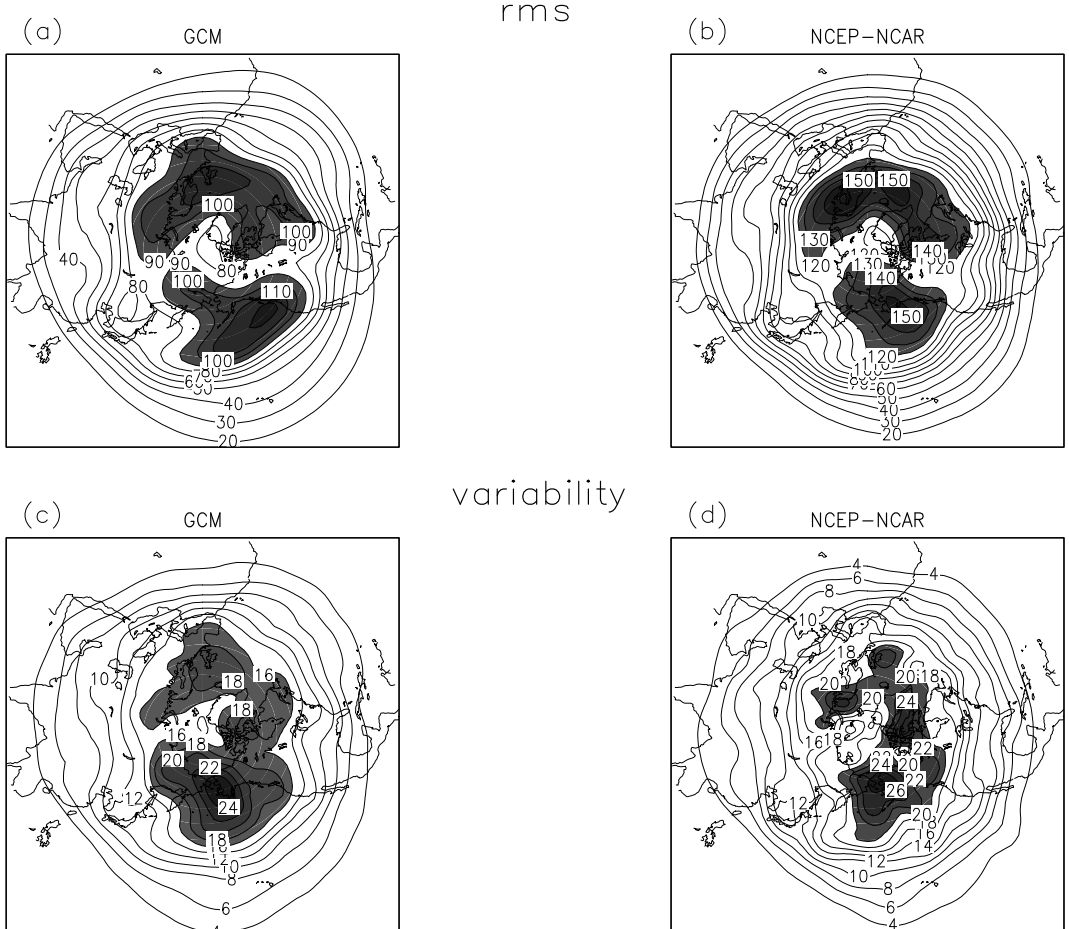


Figure 5.1: Top and bottom panels show, respectively, the rms of 10-60-day filtered 300-mb geopotential height during November to March, and standard deviation of the rms statistics  $\sigma$  (see text for details). Calculations are based on GCM [(a) and (c)] and NCEP-NCAR reanalyses [(b) and (d)]. Rms values are shaded if greater than 90m for (a), and 120m for (b). Values of standard deviation are shaded if they are greater than 16m for (c), and 20m for (d). All quantities are in unit of m.

Results from the two datasets agree broadly, though there are some quantitative differences. NCEP-NCAR reanalyses have eddy amplitudes about 25% stronger than those from the GCM. In terms of spatial distribution, one noticeable difference is the location of maxima of activity: for NCEP-NCAR results,

most vigorous activity is found over Alaska and also in a broad region from the western Atlantic to Northern Europe. Its GCM counterpart is distributed differently, however, especially over the North Pacific where maximum activity is close to the northwestern American seaboard. Reanalyses also tend to have largest perturbations located in higher latitudes.

It is well known that the amount of low-frequency activity varies from year to year. One measure of this interannual variation is the standard deviation of  $\sigma$ , where  $\sigma$  is the rms value of 10-60-day filtered  $Z_{300}$  during November to March, computed *each year*. The standard deviation is plotted in Fig. 5.1 (c) and (d), for GCM and reanalyses data respectively. Notice that for GCM data, values of  $\sigma$  vary from year to year and also from one ensemble realization to another. For both GCM and NCEP-NCAR data, computation is based on the period 1950-99<sup>1</sup>.

Strong interannual variability is found in regions where eddy amplitudes are large in the long-term mean. Comparison between the lower and upper panels of Fig. 5.1 reveals that typical amplitudes of year-to-year fluctuations are approximately one-fifth of the mean amplitudes of the eddies. Agreement between GCM and NCEP-NCAR results is good over the North Pacific, but less so over the Atlantic. In particular, GCM data show less variability in the Atlantic compared with the Pacific, while reanalyses suggest that the amount of activity over both regions are equally variable. It is not clear whether this is due to a deficient variability of the Atlantic low-frequency eddies as simulated, or that it is related to the design of the GCM experiment (e.g. lack of mid-latitude SST variability in the Atlantic). Since the main focus is on low-frequency circulation over the

---

<sup>1</sup>As suggested by Kistler et al. (2001), long term mean of  $\sigma$  or  $\bar{\sigma}$ , based on which the standard deviation is computed, is found separately for the period 1950-78 and 1979-99 for reanalyses data.

North Pacific, this point will be not be pursued further.

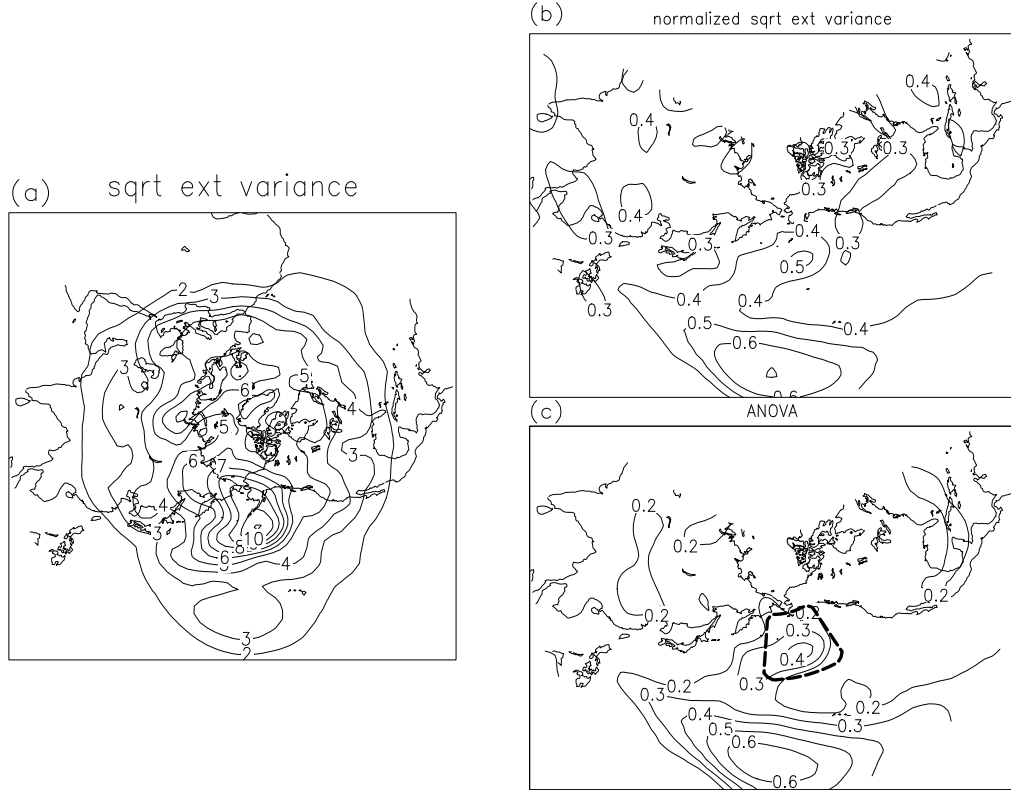


Figure 5.2: (a) Square root of external variance of the rms statistics  $\sigma$  of 300-mb height, based on GCM data, in unit of m. (b) As in (a) but normalized by the standard deviation of  $\sigma$ . (c) ANOVA estimate of the ratio in (b).

For GCM data, the external variance of  $\sigma$  can also be found. Ensemble-mean values of  $\sigma$  are first calculated each year, and the variance of the resulting time series is defined as the external variance. By the design of the GCM experiment, external variance can be attributed to the changing SST within the tropical eastern Pacific. For ease of interpretation, the square root of the external variance is plotted in Fig. 5.2 (a). It is found to be strongest over the North Pacific, with a maximum south of the Aleutians, and moderate amplitudes extending to the north and southwest directions. It is noticed that its distribution is different from

that of the interannual variability shown in Fig. 5.1 (c), which has a stronger emphasis in higher latitudes with a maximum over Alaska. In other extratropical regions outside the North Pacific, there is hardly any well-defined pattern.

The square root of the external variance divided by standard deviation of  $\sigma$  is shown in Fig. 5.2 (b). It is large over a broad region in the North Pacific, and is actually strongest near the tropical central Pacific. The latter feature is likely to be related to the impact of ENSO on tropical intraseasonal activity (see Ch. 4). Overall the signal from the data does not stand out sharply from its ‘background’. One method of achieving a better signal-to-noise ratio is to use the Analysis of Variance (ANOVA; see, e.g., von Storch and Zwiers 1999). The square root of the ratio of the SST-related variance to the total variance, as estimated by ANOVA, is shown in Fig. 5.2 (c)<sup>2</sup>. The result is largely similar to Fig. 5.2 (b) but with a sharper pattern. Within the region  $180-150^{\circ}\text{W}$ ,  $40-60^{\circ}\text{N}$  (its boundary outlined by dashed contours in Fig. 5.2 (c)), large values of the ratio (reaching about 30-40%) are found.

This region in the North Pacific, with  $30^{\circ} \times 20^{\circ}$  in longitudinal and latitudinal extents, will henceforth be referred to as the ‘key region’. In the following sections, low-frequency anomalies associated with fluctuations of  $Z_{300}$  over this key region will be examined. For the case of GCM simulations, these circulation anomalies would exhibit changes of behavior in the interannual sense, due to the imposed SST variability. This is the main motivation for studying low-frequency perturbations proximate to this key region. It is noteworthy that many studies of North Pacific persistent flow anomalies are involved in examining time series of the geopotential height (say at 500 mb) at some key points; key points chosen are

---

<sup>2</sup>See Appendix A for the ANOVA formulation.

often in the vicinity of this region (see, e.g., Dole 1986a; Nakamura et al. 1997).

### 5.2.2 Life cycle of anomalies

The evolution of low-frequency geopotential height anomalies at 300 mb over the North Pacific is studied using lag regression. The reference time series used is the 10-60-day filtered  $Z_{300}$ , with values averaged over the key region. Fig. 5.3 shows low-frequency perturbations found by this method, for both GCM and NCEP-NCAR data. Anomalies found this way are similar to those presented in many studies on North Pacific persistent circulation, despite the fact that composite procedures different from here are adopted (see. e.g, Black 1997; Feldstein 1998). From now on the 10-60-day filtered  $Z_{300}$ , area-averaged over the key region, will be referred to as the 'reference time series'. Based on this time series, various components of the low-frequency circulation can be studied using the same regression method.

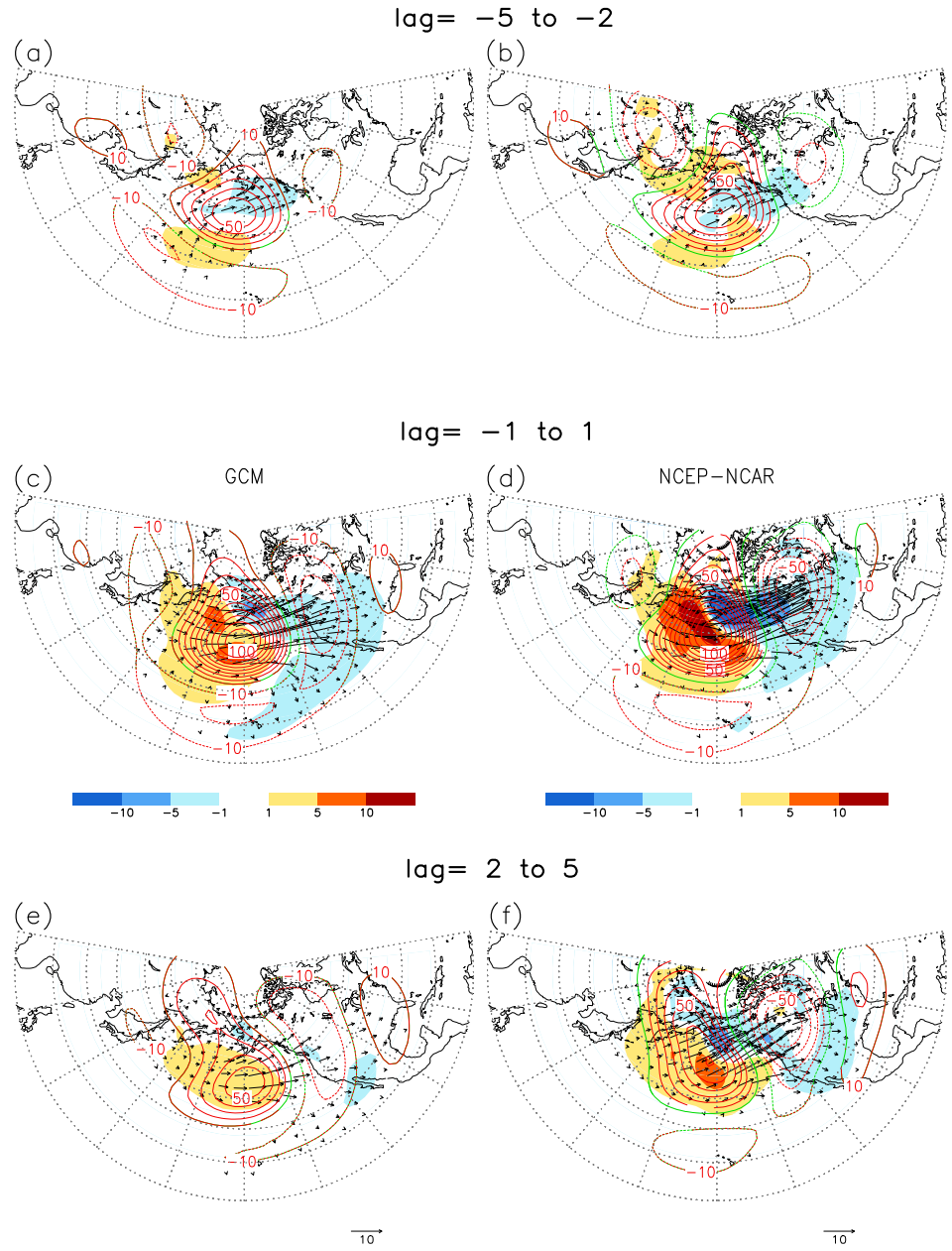


Figure 5.3: 300-mb height perturbations in contours, from lag regression based on the reference time series of 10-60-day filtered, area-averaged 300-mb height. Regression maps are averaged over periods of -5 to -2, -1 to 1, and 2 to 5 lag days, and are shown in the upper, middle and lower panels, respectively. Wave-activity vectors (magnitude in  $\text{m}^2\text{s}^{-2}$ ) and their divergence (shading, in  $10^{-6}\text{ms}^{-2}$ ) are found based on these maps. Only vectors collocating divergence with magnitude no less than  $0.5 \times 10^{-6}\text{ms}^{-2}$  are shown. For GCM results [(a), (c) and (e)], height anomalies exceeding 99% significance level are depicted by red contours, otherwise green. Zero contours are omitted. Likewise for NCEP-NCAR reanalyses [(b), (d) and (f)], except that perturbations 95% significant are denoted by red contours.

Three stages, labeled as the developing, mature and decay stage, are identified during the life cycle of low-frequency circulation, which correspond to three ranges of lag days: day -5 to -2, day -1 to 1 and day 2 to 5, respectively. During the developing stage, a ridge over the North Pacific is amplifying rapidly. To its south, negative height perturbations over a large subtropical region are found. Together with those over North America east of the ridge, these anomalies form a wavetrain, with centers of action reminiscent of those of the PNA pattern. It is noticed that there is another anomalous low located over Asia near sea of Okhotsk, so that an east-west oriented train of perturbations passing the key region can also be inferred.

The ridge attains its maximum amplitude during the mature stage. The north-south dipole of height perturbations over the central Pacific also implies strong zonal wind anomalies in mid latitudes. These anomalies are also located near the exit of the Pacific jet, suggesting barotropic conversion of kinetic energy from the mean flow to eddies. East of the ridge, the trough over northwestern U.S. having a strong growth and positive perturbations near Gulf of Mexico now appear. This suggests a southeastward development associated with Rossby waves dispersion. Meanwhile the subtropical low shifts eastward with centers located in the western hemisphere, and the one over east Asian coast moves to the south. Finally, during the decay stage, anomalies are much weakened, but the wavetrain extending into continental America is still present. Throughout its life cycle the anomalous ridge over the North Pacific remains quasi-stationary. In higher latitudes, however, there is an obvious westward propagation of anomalies; this retrograding behavior of perturbations resembles that typical of WTP. Results based on the NCEP-NCAR dataset agree well with the GCM, except that anomalies are stronger,

especially in high latitudes and over North America, consistent with maps of rms of  $Z_{300}$  considered earlier.

Shown together in the same figure are wave-activity vectors of Takaya and Nakamura (2001) at 300 mb, and their horizontal divergence. The activity vector at pressure coordinates, based on the perturbation streamfunction  $\psi$ , is given by:

$$\mathbf{W} = \frac{1}{2|\mathbf{U}|} \begin{pmatrix} U(\psi_x^2 - \psi\psi_{xx}) + V(\psi_x\psi_y - \psi\psi_{xy}) \\ U(\psi_x\psi_y - \psi\psi_{xy}) + V(\psi_y^2 - \psi\psi_{yy}) \\ \frac{f_0^2}{S_p}[U(\psi_x\psi_p - \psi\psi_{xp}) + V(\psi_y\psi_p - \psi\psi_{yp})] \end{pmatrix} + \mathbf{C}_U M,$$

in which subscripts on  $\psi$  represent partial derivatives;  $\mathbf{U} = (U, V)$  is the two-dimensional time mean flow,  $f_0$  the Coriolis parameter at the fixed latitude of 45°N and  $S_p = -\rho^{-1}\partial_p \log \theta$  is the static stability.  $\mathbf{C}_U$  is the projection of phase velocity of perturbations in the direction of the mean flow, i.e.  $\mathbf{C}_U = \mathbf{C}_p \cdot \mathbf{U}/|\mathbf{U}|$ . Finally, the wave action  $M$  is related to potential enstrophy  $q^2$  and energy  $e$  of perturbations by

$$M = \frac{1}{2} \left( \frac{1}{2} \frac{q^2}{|\nabla Q|} + \frac{e}{|\mathbf{U}| - C_p} \right),$$

where  $Q$  is the mean potential vorticity. Throughout this study, the phase speed of low-frequency perturbations is assumed to be zero, such that the part proportional to  $C_p$  (i.e.  $\mathbf{C}_U M$ ) does not contribute to the activity vector.

Interpretation of the wave-activity flux is as follows. Activity vectors can be shown to be parallel to the local group velocity of disturbances. Under the assumption of quasi-geostrophy and a slow spatial variation of the mean flow, it can be shown that  $\partial_t M + \nabla \cdot \mathbf{W} = S$  (see Takaya and Nakamura 2001), thus relating the wave action  $M$ , activity flux  $\mathbf{W}$ , and a forcing term  $S$  due to non-

conservative processes. Regarding  $M$  as a measure of perturbation magnitudes, both the forcing term and convergence of activity flux can lead to amplification of activity. The formalism can be regarded as a modified version of activity flux given by Plumb (1986), but in the case of Takaya and Nakamura (2001) the mean meridional wind can be non-zero. Also, this version provides a measure of activity that is phase independent, i.e. by construction, combinations of quadratic quantities have no spatial variation due to the presence of nodes or anti-nodes of  $\psi$  (nor due to those of its derivatives). Therefore, no phase averaging is required. Wave-activity vectors, computed based on regression maps of  $Z_{300}$ , are shown in Fig. 5.3. They are useful in providing snapshots of wave dispersion during each stage of the life cycle.

During the developing stage, incoming activity is found from two regions, one located over the subtropical Pacific and another one from northeast Asia. They accumulate over Gulf of Alaska, and there is an export of activity eastward. During the mature stage, strong divergence of activity flux is found near the center of the ridge. Convergence is found accompanying downstream development over the American continent. In high latitudes, activity coming from the coastal region of Asia exhibits zonal group propagation, reaching the northwestern American seaboard.

It is also noticed that wave activity seems to be split east of the North Pacific ridge, with a branch taking a sharp southward turn into the subtropical eastern Pacific. During the decay stage, some export of activity from the ridge is still present. There is a prevalent eastward dispersion over the North Pacific.

GCM results agree well with those based on reanalyses data. One noticeable difference is that, for reanalyses results, wave activity is stronger in high latitudes:

stronger incoming activity is found from northeast Asia during the development of the ridge, and there is also a stronger export into continental America.

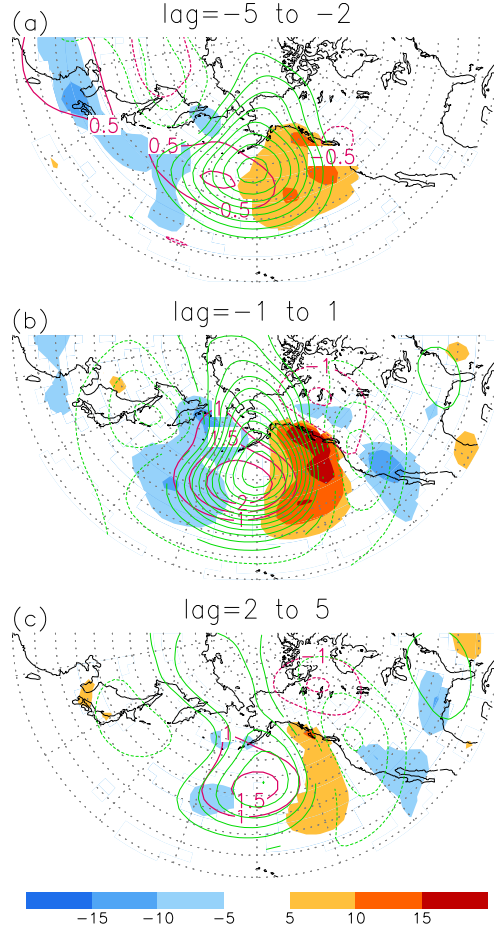


Figure 5.4: As in Fig. 5.3 but for 700-mb temperature (magenta contours, in unit of  $^{\circ}\text{C}$ ), pressure velocity (shading, in  $\text{mbday}^{-1}$ ) and height perturbations (green contours, in intervals of 5m), based on GCM data. All fields exceed 95% significance level. Notice that contours of temperature perturbation start from  $\pm 0.5^{\circ}\text{C}$  for (a), but from  $\pm 1^{\circ}\text{C}$  for (b) and (c).

Besides perturbations in the upper levels, low-level circulation anomalies are also examined. Fig. 5.4 shows anomalous temperature, geopotential height and pressure velocity at 700 mb, during different stages of the life cycle. Anomalies are computed as lag regression based on the reference time series, and results

shown here are based on the GCM dataset. A 700-mb ridge is found covering a broad region in the North Pacific during the developing stage, and is collocated with the one aloft at 300 mb (see Fig. 5.3). On closer examination, however, the upper level one is slightly displaced to the southwest of the ridge below. In other words the height field is westward-tilted vertically. This is consistent with the fact that warm anomalies are found southwest of the maximum of the 700-mb ridge. Sinking motion overlaps substantially the eastern part of the low-level ridge as well. Negative temperature perturbations over northeast Asia is found, similar in nature to those pointed out by Black and Dole (1993) during the onset of North Pacific persistent flow anomalies. Overall, the configuration of geopotential, temperature and vertical motion suggests the presence of a baroclinic growth of anomalies.

During the mature stage, there is substantial growth of temperature and vertical velocity perturbations, and the low-level ridge has attained its maximum magnitude. Sinking motion located in the eastern part of the ridge also amplifies. Cold anomalies are present in northern Canada and collocated with equatorward flow anomalies. Back to the western part of the North Pacific ridge, southerly geostrophic wind also overlaps warm perturbations. Strong rising is found ahead of the low formed over Japan. Finally, during the decay stage, temperature perturbations over the ridge become more collocated with the geopotential height maximum, i.e. the vertical tilt is reduced. Disturbances over the North Pacific hence become more equivalent barotropic.

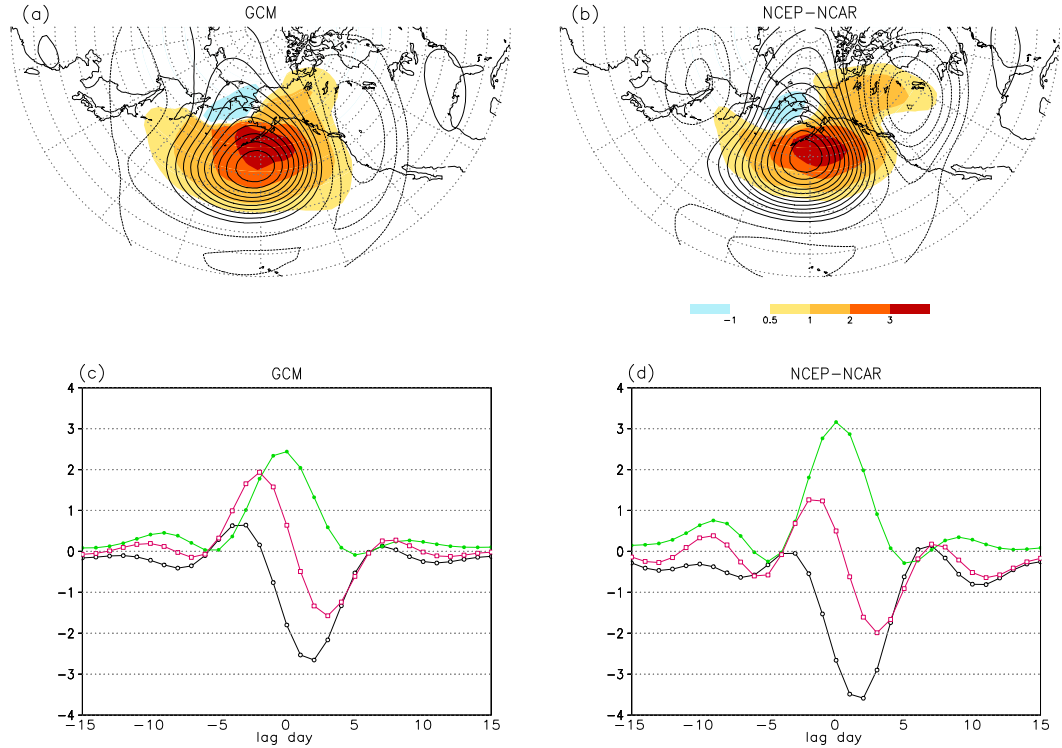


Figure 5.5: Upper panels show the vertical component of wave-activity vector at 700 mb (shading, in unit of  $0.1\text{Pa ms}^{-2}$ ) and 300-mb height perturbations (contours with 10m intervals, with zero contours omitted), during the lag days -1 to 1. Anomalies and wave activity components are computed as in Fig. 5.3. Lower panels show the horizontal (black contour) and vertical (green) convergence of wave activity at the 300-mb surface, with results averaged over  $170^\circ\text{E}-150^\circ\text{W}$ ,  $40^\circ\text{-}65^\circ\text{N}$ . Also shown is the three-dimensional convergence (i.e. sum of horizontal and vertical, in magenta). Unit of flux convergence:  $10^{-6}\text{ms}^{-2}$ . Left and right panels give results for GCM [(a) and (c)] and NCEP-NCAR data [(b) and (d)], respectively.

The above evolution sequence indicates that baroclinic growth is present during the life cycle of low-frequency anomalies, with key signatures similar to those of extratropical synoptic-scale storms. Low-frequency perturbations considered here, however, have a much larger spatial scale: the low-level trough-ridge-trough configuration, for instance, spans almost the entire North Pacific longitudinally. Associated with this baroclinic growth is the vertical propagation of wave ac-

tivity. It can be diagnosed by examining the vertical component of the activity vector, and its value at 700 mb is computed for both GCM and NCEP-NCAR data, during the mature stage. They are shown in Fig. 5.5, together with contemporaneous  $Z_{300}$  perturbations. Strong upward activity from 700 mb is found, covering a large region over the North Pacific, extending into the northwestern part of North America. A large part of the vertical flux is directly located under the 300-mb ridge. Results here confirm earlier impression that strong baroclinic development is taking place. Comparison with Fig. 5.4 reveals that the strongest vertical activity flux is proximate to where sinking motion overlaps the low-level ridge, and also where poleward advection of warm temperature by geostrophic wind perturbations is found. This configuration of variables essentially indicates a westward tilt of geopotential anomalies in the vertical. The vertical activity flux is seen to be doing a reasonable job in showing regions where baroclinic processes occur. NCEP-NCAR results agree well with the GCM pattern, but with even stronger activity over Canada. During the developing stage as well as the decaying stage, vertical activity flux is found to be much weaker (not shown). In other words, the low-level 'baroclinic source' is strongest around the time when the ridge aloft is fully developed.

Vertical wave activity at other levels is also examined. Activity flux (not shown) is largest at about 500 to 700 mb, and decreases rapidly further upward. Strong vertical flux in low levels therefore implies convergence aloft. To better understand the evolution of wave activity and its effect on the growth of anomalies, flux convergence at 300-mb level is computed from lag day -15 to 15. The horizontal and vertical convergence are shown in Fig. 5.5 (c) and (d), respectively for GCM and reanalyses data. Values of flux convergence are area-averaged over

the region of  $170^{\circ}\text{E}-150^{\circ}\text{W}$ ,  $40^{\circ}\text{-}65^{\circ}\text{N}$ , which is slightly larger than the key region and it covers most of the 300-mb ridge.

The vertical flux convergence is found to peak at zero lag, but it is rather small beforehand and drops rapidly afterwards. This is consistent with earlier consideration of baroclinic signatures in low levels during various stages of the life cycle. There is also a very modest amount of horizontal flux convergence at the lag of about day -3 in the GCM results. This is associated with the propagation of activity into the key region during the developing stage at 300 mb, as shown in Fig. 5.3. There is horizontal export of activity which begins before lag day zero, and strongest divergence occurs at day 2, at the time when the North Pacific ridge starts to decay.

Three-dimensional flux convergence (i.e. the sum of horizontal and vertical convergence), is also shown in Fig. 5.5 (c) and (d). Strong three-dimensional convergence (divergence) is found before (after) the ridge attains its maximum amplitude. As mentioned before, convergence of activity can lead to growth of perturbations. The tendency of wave action is also estimated at each time lag (not shown). It is found to have magnitudes comparable to the flux convergence, and with variation closely following the latter's at each time lag. This suggests that convergence of activity is an important mechanism governing the growth and decay of anomalies<sup>3</sup>. Since the vertical convergence is the dominant term, baroclinic processes therefore play an important role in amplifying the upper-level ridge. Export of wave activity in upper levels dominates later stages of the life cycle of anomalies, consistent with the decay of the mature ridge during these

---

<sup>3</sup>The equation of the wave action tendency, as discussed in Honda et al. (2001), is probably not suitable for an exact budget calculation. The forcing term is thus not estimated here. An estimate of forcing on the low-frequency circulation by high-frequency eddies, however, will be given in the next section.

times.

The above results agree well in several aspects, including the importance of a local baroclinic source and subsequent horizontal propagation of activity in the upper levels, with those of Black (1997). Results here should also be compared with those concerning blocking anomalies by Nakamura et al. (1997). They found no obvious incoming activity during the formation of blocking circulation over the North Pacific, and stressed the importance of feedback from synoptic-scale activity. Yet their plot of height anomalies and the associated Plumb's flux (see their Fig. 2) suggests wave activity similar to that depicted in Fig. 5.3, including some incoming activity from the subtropics and northeast Asia. In view of the importance of local baroclinic development, these incoming activity might not play a substantial role in the growth of anomalies. Still, they might indicate the presence of some remote catalysts. In the next section, changes of synoptic-scale activity during the life cycle of low-frequency circulation, and their feedback on the latter, will be investigated.

### 5.2.3 The role of synoptic-scale eddies

The important role of synoptic-scale activity in maintaining low-frequency anomalies has been pointed out by many studies (see Introduction). Modulation of the storm track is known to feedback upon low-frequency circulation anomalies through changes of vorticity flux convergence related to high-frequency eddies. Such feedback mechanism has been shown to be important in the evolution of blocking flow over the North Pacific (Nakamura et al. 1997).

Following Nakamura and Wallace (1990), the ‘envelop function’ is used to

study how storm tracks are modified during the life cycle of low-frequency anomalous flow. It is computed by first squaring the 2.5-6-day filtered  $Z_{300}$ . The result is then lowpass filtered to retain fluctuations with periods longer than 6 days, and finally multiplied by two. This envelop function is designed to capture low-frequency modulation of amplitudes of synoptic-scale eddies. Feedback on the low-frequency circulation, brought about by changes of characteristics of high-frequency eddies, can also be estimated. This is done by computing the induced geopotential height tendency, given by  $\partial z / \partial t \equiv \frac{g}{f} \nabla^{-2} [-\nabla \cdot (\widetilde{\mathbf{u}'\zeta'})]$ . Here  $(\widetilde{\cdot})$  represents 6-day lowpass filtering, primed values  $\mathbf{u}'$  and  $\zeta'$  being the 2.5-to-6-day filtered wind and vorticity field respectively, and  $\nabla^{-2}$  is the inverse Laplacian operator.

Fig. 5.6 shows the anomalous envelop function and induced height tendency related to synoptic-scale activity, and also the low-frequency  $Z_{300}$  perturbations. Anomalous fields are again computed as lag regression based on the reference time series. Enhanced synoptic-scale activity is found in the northwestern flank of the developing ridge, when the latter begins to appear on about day -5 over the North Pacific. Nakamura and Wallace (1990) showed similar modulation of storm tracks during the early stage of blocking development. The associated eddy-induced geopotential tendency is positive (negative) east (west) of where the storm track is enhanced, and is partly in quadrature with the ridge. This interesting configuration is similar to the findings of Feldstein (1998; see his Fig. 6). Later in the life cycle, storm tracks are modulated in such a way that enhanced (reduced) activity is found over regions where upper-level westerlies increase (decrease). This is observed starting from lag day -3 to about day 3, and is most obvious during the mature stage when the envelop function is large and positive

in the northern part of the anomalous ridge, negative over its southern part. Between this north-south dipole, positive eddy-induced tendency is found which also overlaps the low-frequency ridge. Synoptic-scale activity thus provides a positive feedback on the ridge when it becomes mature, and also opposes the decay of the ridge a few days later.

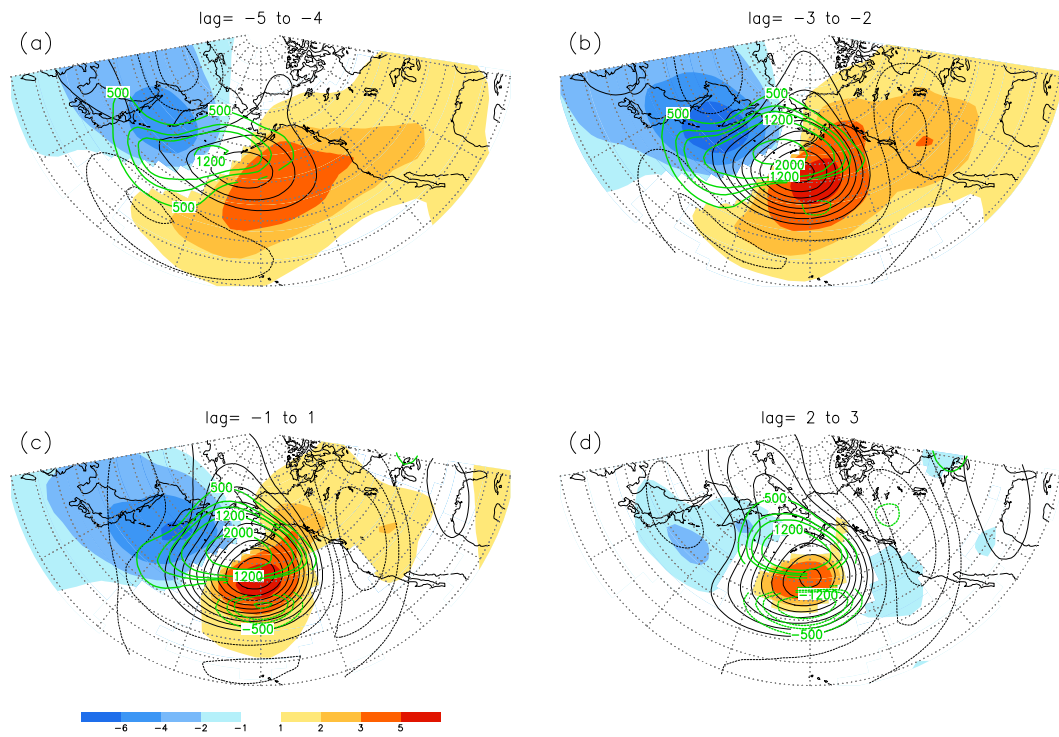


Figure 5.6: Anomalous envelop function (green contours, with contours levels  $\pm 500, \pm 750, \pm 900, \pm 1200$  and  $\pm 2000 \text{ m}^2$ ) and induced height tendency (shading, in  $\text{mday}^{-1}$ ) based on 2.5-6-day-filtered 300-mb geopotential height and wind, using GCM data (see text for computation procedure). Lag days of -5 to -4, -3 to -2, -1 to 1 and 2 to 3, are shown in (a), (b), (c) and (d), respectively. Also shown are the 300-mb height anomalies (black contours with 10m intervals). Anomalous fields are found as in Fig. 5.3. Values for the envelop function and height tendency exceed the 95% significance level.

On the other hand, the initially rapid intensification of the ridge (about 15-25  $\text{mday}^{-1}$ ) during its development is two to three times stronger than the induced

height tendency due to synoptic-scale activity. It seems unlikely that the latter alone could account for such amplification. In fact, feedback from high-frequency eddies found here is quite modest. Lau (1988) gave a forcing time scale of about 7-10 days. This is estimated from the ratio of amplitudes of monthly height anomalies to the synoptic-eddy induced geopotential tendency, and can be interpreted as an *e*-folding time scale. From the above results, this time scale is found to be roughly 20 days; the magnitude of feedback is thus half of that given by Lau (1988). Finally, results here do not necessarily contradict those of Nakamura et al. (1997). Their work focuses on the strongest blocking events in their data record, while this study employs a regression analysis to which *all* low-frequency anomalies contribute. While results here suggest synoptic-scale activity alone cannot account for the initial amplification of low-frequency anomalies, it certainly provides a positive feedback, especially during later stages of the life cycle.

### 5.2.4 Wave sources from intraseasonal convection

Examination of the life cycle of low-frequency anomalies reveals wave activity sources located near a Pacific subtropical cyclone, which in turn might be associated with disturbances in the tropics. Also, many previous works have demonstrated the ability of intraseasonal convection to excite Rossby wavetrains in the extratropical Pacific. In this section, this connection between extratropical anomalies and tropical intraseasonal activity will be considered.

Fig. 5.7 shows anomalous precipitation and 300-mb streamfunction, from lag day -19 up to day zero. Anomalies are again computed as lag regression based on the reference time series. Notice that regression maps earlier than the developing

stage of anomalies in the North Pacific are shown. It is noteworthy that well defined patterns of precipitation appear over southeast Asia, even at very early times.

Along the equator, negative precipitation within  $100^{\circ}$ - $150^{\circ}$ E appeared in Fig. 5.7 (a) is replaced by anomalies with the opposite sign as time progresses. The eastward propagation of convection is similar to that typically seen during intraseasonal oscillations. Also shown are hovmoller plots of precipitation and 200-mb velocity potential anomalies ( $\chi$ ) in Fig. 5.7 (e). There is a global eastward propagation of large-scale divergence anomalies, as depicted by the  $\chi$  field. Strong convective anomalies are confined to a few geographical locations, and they tend to have a more stationary nature. These features are also consistent with those known for the MJO (see Ch. 2). Overall, the above suggests that some robust MJO-like signatures are associated with the life cycle of low-frequency anomalies over the North Pacific, especially in the development stage or even earlier.

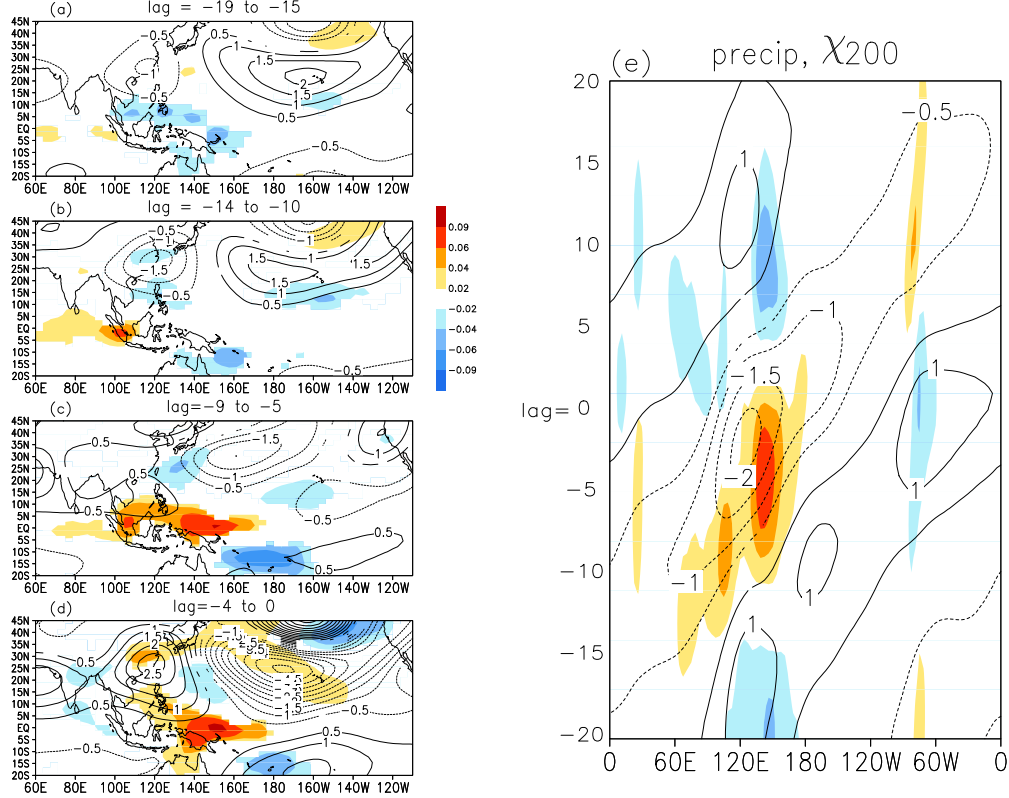


Figure 5.7: (a) to (d) show precipitation (shading, in  $\text{cm day}^{-1}$ ) and 300-mb streamfunction anomalies (contours, in  $10^6 \text{m}^2 \text{s}^{-1}$ ), computed as in Fig. 5.3, for lag days -19 to -15, -14 to -10, -9 to -5 and -4 to 0, based on GCM data. Hovmöller diagrams of anomalous precipitation and 200-mb velocity potential (contour, in  $10^6 \text{m}^2 \text{s}^{-1}$ ), averaged over  $10^\circ\text{N}$ - $10^\circ\text{S}$ , are shown in (e). All fields from (a) to (d), and the velocity potential in (e), are significant to the 95% level.

There is also meridional propagation of convective anomalies. Negative rainfall perturbations are found to migrate poleward in east Asia. Part of them reaches the subtropics (over the Philippines) on about day -10, then migrates to the east of Taiwan at about  $25^\circ\text{N}$  on day -5. Throughout these times, an upper-level cyclone is found to be in the vicinity of the suppressed convection. From day -19 to -10, it resembles a Gill-type response to tropical heating with cyclonic flow located north to northwest of reduced precipitation. After a rather

abrupt eastward shift with its center now located in the subtropical western Pacific, anomalous convection becomes located to its immediate west while it begins to amplify. The subtropical cyclone becomes mature on about lag day -4 to day zero. Interestingly, during lag day -9 to day zero, there is a north-south dipole of convection over the equatorial-subtropical western Pacific. Results of Simmons et al. (1983) suggest that a similar forcing pattern could lead to an effective extratropical response to tropical heating (see their Fig. 5).

The existence of intraseasonal convective signals 10-20 days prior to the development of North Pacific low-frequency flow, presented here based on GCM data, is in broad agreement with observational findings of Higgins and Mo (1997). While the evolution of convective anomalies is very much akin of the MJO, the possibility of extratropical influences could not be ruled out. Meehl et al. (1996) show that convection with intermediate time scales (14 to 30 days) over east Asia could in fact be triggered by disturbances originating from the extratropics. Nevertheless, the strong presence of MJO signatures implies that intraseasonal oscillations contribute significantly to the formation of low-frequency extratropical anomalies.

It is worthwhile to consider how the subtropical cyclonic flow can arise from the divergent part of the circulation, the latter being much determined by convection in the tropics. This can be achieved by examining the 'Rossy wave source' (RWS), following Sardeshmukh and Hoskins (1988). Linearized about the time mean flow, it is given by

$$\text{RWS} \equiv -\nabla \cdot [\mathbf{u}'_\chi(f + \bar{\zeta})] - \nabla \cdot (\bar{\mathbf{u}}_\chi \zeta'),$$

where  $\mathbf{u}_x$  is the divergent component of the wind, while primed values and those with an overbar denote anomalies and long term averages, respectively. Other symbols follow standard meteorological convention. The RWS and the rotational flow are related through the linearized vorticity equation:

$$\partial_t \zeta = -\overline{\mathbf{u}_\psi} \cdot \nabla \zeta' - \mathbf{u}'_\psi \cdot \nabla (f + \bar{\zeta}) + \text{RWS} + \text{Residual term},$$

in which  $\mathbf{u}_\psi$  is the rotational wind, and the residual term represents vorticity tendency due to tilting effect, non-linearities and dissipation (which are ignored in the general discussion here). The first two terms on the right represent advection of vorticity perturbations by the mean rotational flow, as well as mean absolute vorticity advection by wind anomalies. Notice that these two terms and also the left hand side depend only on the rotational component of flow anomalies. In a quasi-stationary situation with small time tendency, one would expect a balance between terms of vorticity advection by rotational winds and the RWS.

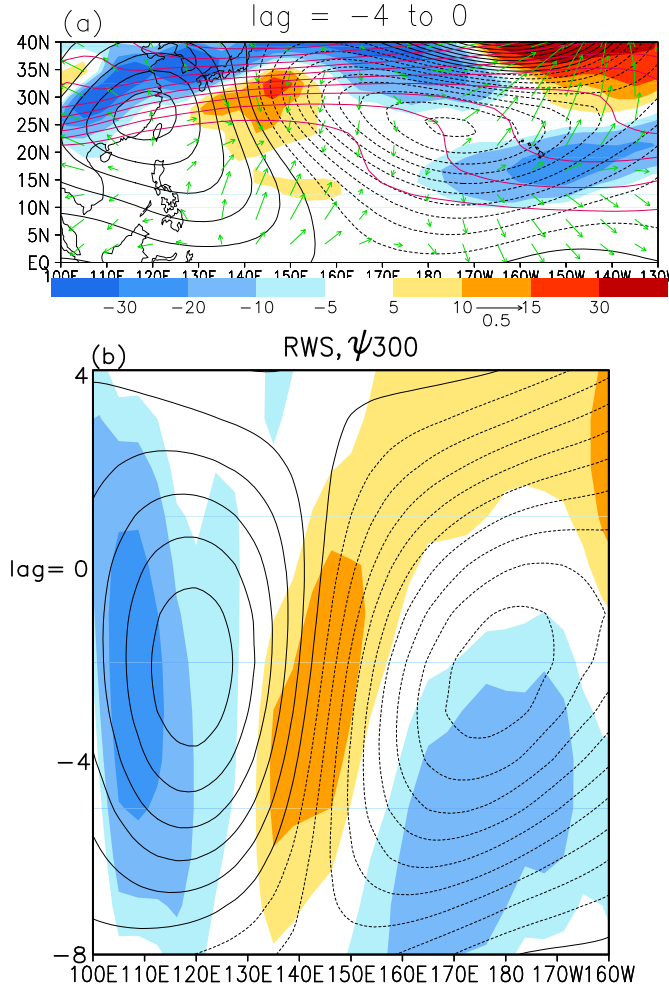


Figure 5.8: (a) Linearized anomalous Rossby wave source (shading, in  $10^{-12} \text{ s}^{-2}$ ), streamfunction (black contours with  $10^6 \text{ m}^2 \text{s}^{-1}$  intervals) and divergent wind (magnitude in  $\text{ms}^{-1}$ ) at 300-mb level, during the lag days of -4 to 0. Rossby wave source south of  $10^\circ\text{N}$  is not shown. Also shown is the mean absolute vorticity gradient (magenta contours, starting from  $3 \times 10^{-5} \text{ s}^{-1}$ , with  $10^{-5} \text{ s}^{-1}$  intervals). (b) Hovmöller diagram showing Rossby wave source and streamfunction from lag day -8 to 4, averaged over  $23^\circ\text{-}33^\circ\text{N}$ . Shading information and contour intervals are the same as (a).

RWS corresponding to Fig. 5.7 (d) during lag day -4 to 0 is shown in Fig. 5.8 (a), together with the anomalous divergent wind and streamfunction. Also shown is the absolute vorticity contours at the same 300-mb level. Large positive RWS is found in the subtropics southeast of Japan, where the absolute vorticity gradient

is strong. There is obvious vorticity advection by divergent flow anomalies in the same region, indicating a substantial contribution to the RWS from the term  $-\mathbf{u}'_\chi \cdot \nabla(f + \bar{\zeta})$ . The positive RWS is also located west (east) of a subtropical cyclone (anticyclone). The implied rotational wind means that RWS and the  $-\mathbf{u}'_\psi \cdot \nabla(f + \bar{\zeta})$  term have the same positive sign, and together they are balanced by the vorticity advection due to mean rotational wind, i.e.  $-\bar{\mathbf{u}}_\psi \cdot \nabla\zeta'$ . The latter is negative, which can be inferred from the east-west configuration of anticyclone and cyclone. This balance is demonstrated in the hovmoller diagram of the streamfunction and RWS, as shown in Fig. 5.7 (b). Throughout the evolution of the subtropical cyclone, positive RWS is found on its west. Notice that both the subtropical low and the RWS to its west reach their maximum amplitude on about lag day -2, i.e. before the North Pacific ridge is fully developed. For the anticyclone to the west, negative RWS is found near its western flank, suggesting that a similar balance holds there as well.

From a vorticity budget consideration, it is shown how rotational circulation anomalies are related to divergence perturbations. Strong RWS associated with suppressed convection is found in the western Pacific, suggesting that intraseasonal convection play an important role in setting up circulation anomalies in the subtropics.

### 5.2.5 A brief summary

North Pacific low-frequency circulation anomalies are considered using a lag regression method. Although being equivalent barotropic, they also exhibit some distinctly baroclinic behavior. The latter is shown to be instrumental in the am-

plification of anomalies in a broad extratropical region. Synoptic-scale activity is affected during the life cycle of anomalies. Changes of storm tracks, however, do not seem to be responsible for the intensification of low-frequency perturbations during their developing stage. During this early stage, wave activity is found to originate from two remote regions, namely northeast Asia and subtropical Pacific. From the former region to North America, the pattern of anomalies is an east-west oriented wavetrain, which also exhibit retrogression in high latitudes, reminiscent of the WTP. Wave sources located in the subtropics could be related to intraseasonal convection in the tropics. Motivated by these findings, the MJO and WTP, and also their interaction, will be studied in the second half of the chapter.

## **5.3 Relationship with other modes of low-frequency variability: MJO and WTP**

### **5.3.1 Circulation anomalies related to the MJO and WTP**

The MJO and WTP are major modes of subseasonal/intraseasonal variability in the tropics and the northern high latitudes, respectively. Many studies indicate that the MJO has its impact on the extratropical circulation as well. Results from the last section also show that North Pacific low-frequency anomalies are preceded by some coherent intraseasonal convection in the tropics. On the other hand, the retrograding character of perturbations in high latitudes is typical of the WTP. It is therefore instructive to consider circulation anomalies related to the MJO and WTP, and compare them with those presented in previous sections.

Lau and Nath (1999) showed that the WTP is the dominant mode of variability with subseasonal time scales in high latitudes. To characterize its related variability, the leading CEOF of  $Z_{300}$  over the region of  $55^{\circ}\text{-}90^{\circ}\text{N}$ ,  $90^{\circ}\text{E}\text{-}90^{\circ}\text{W}$  is found, following essentially the same procedure in Lau and Nath (1999). Data is first filtered to retain 10-45-day fluctuations, and only those from selected grid points are used, based on an equal-area consideration. The leading CEOF explains about 35% of variability of the filtered data. To study the MJO, leading CEOF of the 200-mb velocity potential and its temporal coefficients are used, as in Ch. 3.  $Z_{300}$  composite maps are constructed, for both the MJO and WTP, based on the same method<sup>4</sup> introduced in Ch. 3. For brevity, the eight phase bins  $\pi/4, \pi/2, \dots, 2\pi$ , which divide a complete cycle, will be relabeled as phase 1, 2, ..., 8, respectively.

---

<sup>4</sup>Key to this method is the selection of strong MJO or WTP events: a strong event is identified if the amplitude of leading principal component (PC) is greater than 0.75 standard deviation for no less than 20 consecutive days, with a total change of the phase of  $2\pi$  or more.

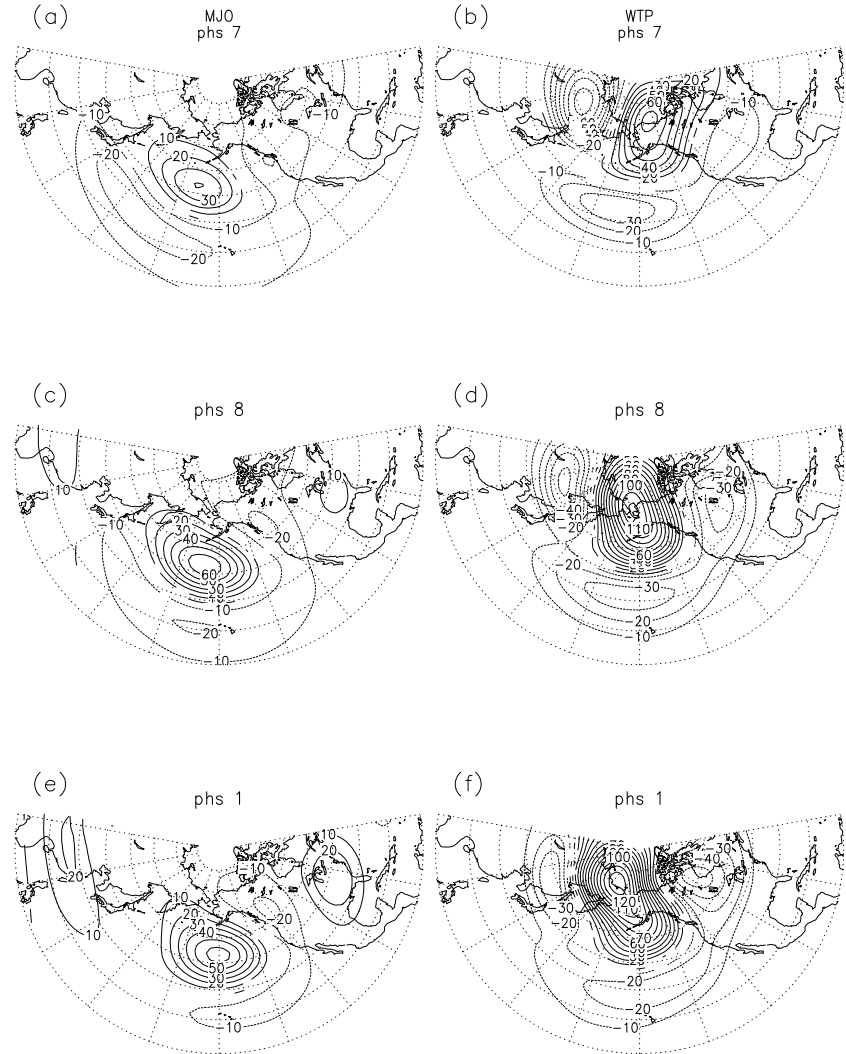


Figure 5.9: Composite maps of 300-mb height for the MJO [(a), (c) and (e)] and WTP [(b), (d) and (f)], at phase 7, 8 and 1 for the MJO and WTP, in the upper, middle and lower panels, respectively. Results based on GCM data, with values significant to the 99% level. Unit: m.

Composites of  $Z_{300}$  for the MJO and WTP are shown in Fig. 5.9, for phases 7, 8 and 1. For the MJO, a wavetrain originating from western subtropical Pacific into the extratropics is apparent. Anomalies are found to grow over the North Pacific, with development in northwestern U.S.. Further to the southeast,

perturbations reach the southeast U.S. bordering Gulf of Mexico. Throughout these phases the high over central Northern Pacific remains almost stationary, while the subtropical low has its center shifted eastward. Anomalies broadly resemble the PNA pattern during phase 8, when centers of action are close to the PNA ones.

For the WTP, a broad ridge over Alaska is found at phase 7, with negative height anomalies to its east and west, forming a wavy pattern. The anomalous ridge is seen to propagate westward and gains strength as it passes the Asia-America land bridge. Anomalies are strongest in high latitudes, but there is also a well-defined trough in mid latitudes, directly to the south of the ridge. The swift change of sign of anomalies at about  $40^{\circ}\text{N}$  is also present in results of Branstator (1987), Kushnir (1987) and Lau and Nath (1999). Over continental Asia, negative height anomalies in northeastern Russia are found to migrate southward.

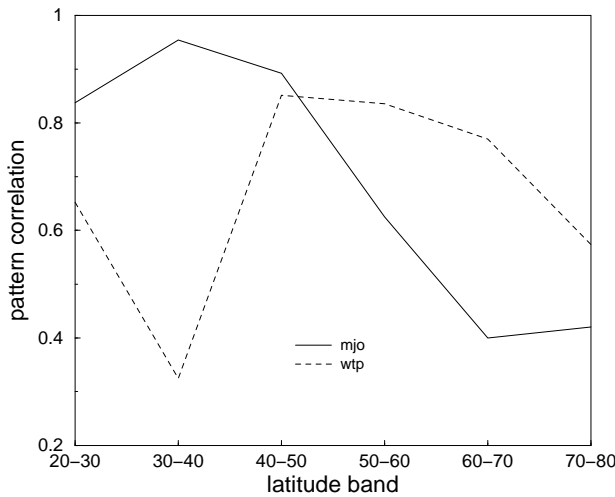


Figure 5.10: Pattern correlation between MJO (solid line) and WTP (dashed) anomalous  $Z_{300}$  at phase 8 of their cycle (see middle panels of Fig. 5.9), and the same field during the mature stage of the low-frequency anomalies (see Fig. 5.3). Values of correlation over strips  $10^{\circ}$  wide in latitude, and with longitudinal boundaries at  $120^{\circ}\text{E}$  and  $120^{\circ}\text{W}$ , are shown from  $20^{\circ}$  to  $80^{\circ}\text{N}$ .

It is noticed that the MJO and WTP-related anomalies have spatial features, as well as their temporal evolution, very similar to those of the low-frequency  $Z_{300}$  anomalies considered in section 5.2.2 (see Fig. 5.3). Resemblance with the MJO is found in subtropical to mid-latitude Pacific, and also over part of continental America. WTP perturbations, on the other hand, look like the patterns in the North Pacific in high latitudes, and over northeastern Asia as well. Some of these similarities can be quantified by computing the pattern correlation between various composite charts. Values of correlation are shown in Fig. 5.10, between  $Z_{300}$  anomalies at phase 8 of both MJO and WTP, and those during the mature stage of North Pacific low-frequency anomalies (see Fig. 5.3 (c)). They are calculated over band-shaped domains with latitudinal width of  $10^{\circ}$  and boundaries at longitudes of  $120^{\circ}\text{E}$  and  $120^{\circ}\text{W}$ . Results confirm the above visual impression: the MJO and anomalous  $Z_{300}$  map in Fig. 5.3 (c) are alike in the subtropics and mid latitudes, but this resemblance decreases sharply north of  $40^{\circ}\text{N}$ . The WTP in general behaves the opposite way: there is great similarity in the extratropics, and less so south of  $40^{\circ}\text{N}$ . The value of correlation rises again at  $20\text{-}30^{\circ}\text{N}$ , apparently due to a subtropical low in that region.

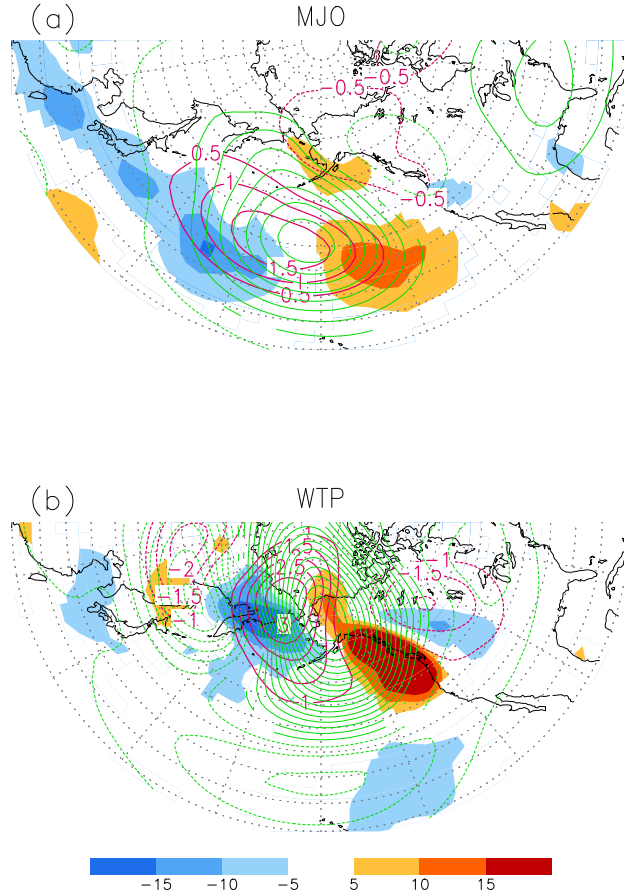


Figure 5.11: As in middle panels of Fig. 5.4, but for composite anomalies of (a) MJO and (b) WTP at phase 8. Contouring for the temperature field starts with  $\pm 0.5^{\circ}\text{C}$  for (a), and  $\pm 1^{\circ}\text{C}$  for (b). All fields exceed the 95% significance level.

The above results imply that both MJO- and WTP-related circulation anomalies resemble low-frequency recurrent perturbations over the North Pacific. This resemblance is present not just in upper levels but in low levels as well. Fig. 5.11 shows the 700-mb anomalous temperature, geopotential and vertical velocity related to the MJO and WTP. Composite maps of anomalies at phase 8 are shown. These maps should be compared with those in Fig. 5.4 (b), depicting the same set of variables during the mature stage of low-frequency perturbations. Again

there is a considerable degree of similarity between them. For the MJO, positive temperature perturbations are located slightly to the west of the 700-mb high, with rising motion to the west of the latter feature, indicating a westward tilt of geopotential anomalies in the vertical. This is very similar to the situation shown in Fig. 5.4 (b). However, these disturbances are mostly confined over the mid-latitude ocean. WTP perturbations, on the other hand, are strong in high latitudes. They also have clear baroclinic signatures. For instance, there are warm anomalies displaced to the west of the ridge. These perturbations and their configuration are similar to those in Fig. 5.4, especially over northwestern American continent/Gulf of Alaska as well as northeastern Asia.

Resemblance between MJO perturbations and the recurrent anomalies over the North Pacific suggests that indeed the latter are much affected by convection in the intraseasonal time scale. However, it seems that the MJO *alone* cannot account for the low-frequency variability in the extratropics- WTP or WTP-like perturbations are also present. It is also noteworthy that there is some distinctly baroclinic development during cycles of the MJO and the WTP, and this again resembles the recurrent low-frequency perturbations. It is probable that these perturbations, and also those related to MJO and WTP, are able to extract energy from the time mean flow through some common dynamical processes, which in turn have a mixed barotropic-baroclinic nature. In fact, results of Kushnir (1987) regarding the WTP, and those of Black and Dole (1993) about persistent circulation anomalies, indicate that baroclinic processes are at least as important as barotropic ones.

Finally, because the two patterns overlap in the vicinity of the key region, there is the interesting possibility that WTP and MJO perturbations can inter-

fere constructively and destructively with each other. In the next section, this possibility will be investigated by considering how a dual presence of both the MJO and WTP can affect circulation over the North Pacific.

### 5.3.2 Circulation related to MJO-WTP interaction

Geopotential height perturbations related to the MJO and WTP are studied using multiple regression. The following equation for the variation of  $Z_{300}$  is proposed, with a linear combination of two MJO and two WTP related time series serving as predictors:

$$\hat{Z}_{300} = \Phi_{a_r} a_r + \Phi_{a_i} a_i + \Phi_{b_r} b_r + \Phi_{b_i} b_i,$$

where  $a_r$  and  $a_i$  are the real and imaginary part of the leading PC of  $Z_{300}$ , respectively, that were used to characterize the WTP. Time series  $b_r$  and  $b_i$  are real and imaginary parts of the leading PC of 200-mb  $\chi$ , used to characterize the MJO. These time series  $a$ 's and  $b$ 's can be readily related to the phase and amplitude of their respective PC temporal coefficients. The  $\Phi$ 's are coefficients obtained from multiple regression. Regression analysis is carried out for each grid point, i.e.  $\Phi$ 's denote maps of regression coefficients.

Values of  $\Phi$ 's are shown in Fig. 5.12 (a) to (d). Each of the  $\Phi$ 's can be interpreted as the contribution to anomalous  $Z_{300}$  from various time series normalized to unit standard deviation. It is found that correlation between *any* two time series is small, i.e. each of them are practically independent of the others. For the WTP coefficients, amplitudes are large in high latitudes, with those associated with  $a_r$  (real part of PC) having a strong ridge over the Asia/North America land bridge and extending into the North Pacific. In fact, comparison with the

leading CEOF patterns (not shown) reveals that the regression coefficients are almost the same as the EOF's themselves. Given that time series  $a_i$  is leading  $a_r$  by one-fourth of a cycle, Fig 5.12 (a) and (b) could also be interpreted as snapshots of  $Z_{300}$  with the former leading the latter by one quarter of a period. Together they depict retrograding perturbations, as expected for the WTP, and can be compared with the WTP composite maps in Fig 5.9.

Regression maps related to the MJO can be interpreted in a similar fashion. They have moderate magnitudes and are weaker than those related to the WTP. Again, Fig 5.12 (c) can be interpreted as leading Fig 5.12 (d) by one quarter of a cycle. In the former figure (showing the imaginary part of CEOF), wavetrain-like perturbations are found, connecting centers of action in the subtropical western Pacific, the North Pacific and the northwestern U.S. seaboard. In the latter figure (real part of CEOF), positive perturbations reside over a large region in the North Pacific, with anomalies reaching southeast U.S.. Together, these patterns indicate a wavetrain originating from the subtropics, with growth in the North Pacific and development in the east to southeast direction. This is essentially the same as the evolution of anomalies depicted by the MJO composite maps in Fig 5.9.

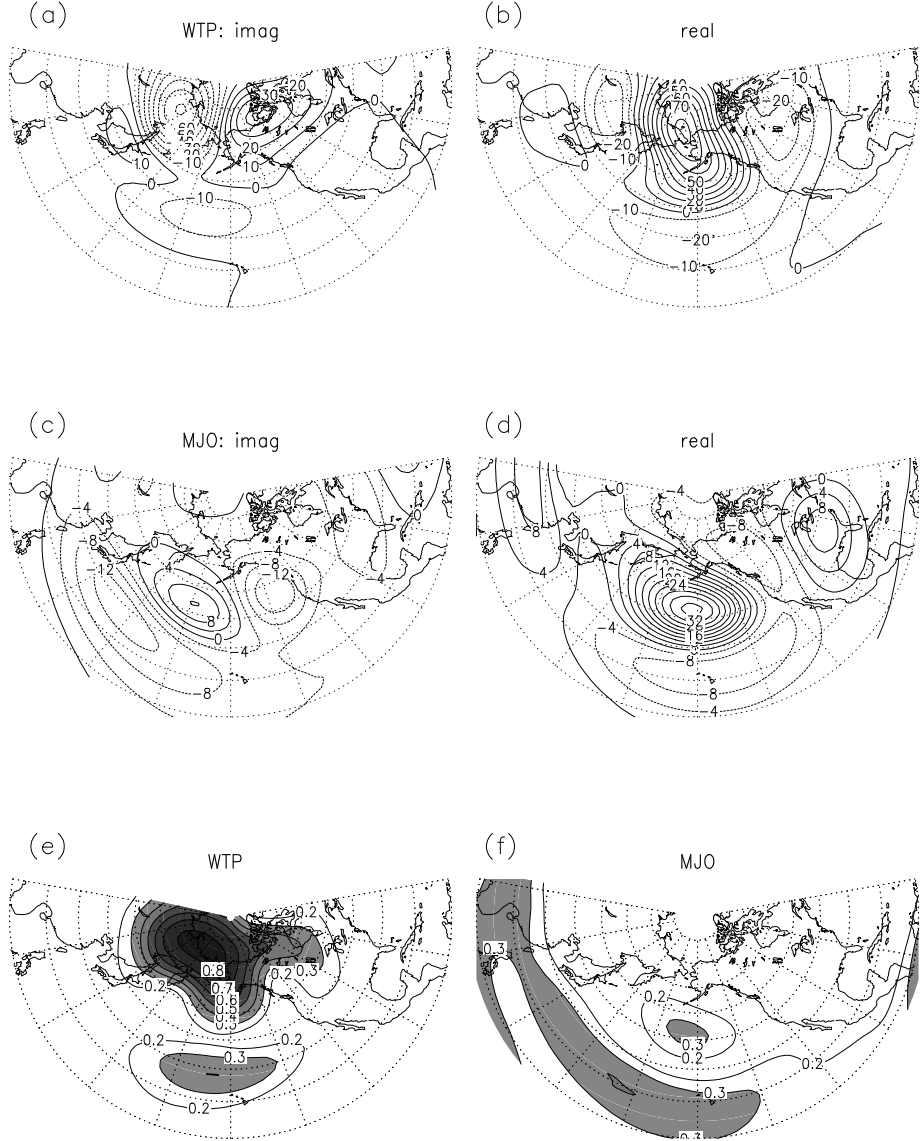


Figure 5.12: Multiple regression coefficients of 10-60-day filtered 300-mb height with (a) imaginary part, (b) real part of the PC of the leading CEOF of  $Z_{300}$ , and (c) imaginary part and (d) real part of the PC of  $\chi_{200}$  (Unit: m). PC time series can be related to phase and amplitude of the WTP and MJO (see text for detail). Lower panels show amplitudes of 300-mb height explained by (e) WTP and (f) MJO, divided by the rms of the height field. Results are based on GCM data.

Fig. 5.12 (e) and (f) give the normalized magnitudes of  $\hat{Z}_{300}$ , explained by the MJO and WTP separately. For instance, the quantity shown for WTP is the

rms value of  $\hat{Z}_{300}$  by setting  $\Phi_{b_r}$  and  $\Phi_{b_i}$  to zero, while for the case of MJO,  $\Phi_a$ 's are set to zero<sup>5</sup>. Final results are divided by the rms of 10-60-day filtered  $Z_{300}$ , giving a dimensionless quantity. Notice that since  $a$ 's and  $b$ 's are uncorrelated, the sum of squares of the two maps also gives the variance ratio of  $\hat{Z}_{300}$  to the filtered  $Z_{300}$ .

As expected, the WTP component of the rms of  $\hat{Z}_{300}$  is strongest in high latitudes. It decreases as one moves southward, but there is also a moderate increase at about 30°N. The MJO component behaves almost in the opposite way: it has moderate amplitudes over a large subtropical region, but otherwise small in the extratropics except over a localized domain in the North Pacific. Over the key region, however, both MJO and WTP contribution are comparable, implying that they are equally important in affecting low-frequency activity there.

Even though the MJO and the WTP are linearly independent, they can still interact in the sense that their related perturbations can produce a combined effect over extratropical Pacific, much like an interference process. Such interference would depend on the phase of both the MJO and the WTP- strong positive (or negative) height perturbations over the North Pacific can be formed from a constructive interference when both phenomena happen to give positive (negative) perturbations there, for some suitable combination of their phases. On the other hand, MJO and WTP can also interfere destructively when they have the opposite phases.

Perturbations associated with this type of MJO-WTP interaction can be shown explicitly in a composite sense. The method is to construct composite maps based on anomalies from periods in the data record when strong MJO and

---

<sup>5</sup>This procedure is justified because time series  $a$ 's and  $b$ 's are uncorrelated. Otherwise correlation due to 'cross terms' between MJO and WTP could lead to ambiguities in interpretation.

WTP events occur at the same time. This can be achieved by using the same MJO and WTP selection criteria; periods during which both criteria are satisfied are noted. A certain combination of the phase of the MJO and WTP will be chosen as a 'time reference'<sup>6</sup>. Days with strong MJO and WTP events occurring, on which a particular phase combination is first reached are labeled as a 'key day'. Anomalies on 'composite day 0' are computed as averaged values of the 10-60-day filtered data over all key days. Composite maps on day  $\pm 1, \pm 2, \dots$  are found analogously, by taking the average of anomalies on  $\pm 1, \pm 2, \dots$  days separated from the key days. Composite maps constructed this way would be able to depict day-to-day evolution of anomalies, and with a certain phase combination of the MJO and WTP as a reference in time.

MJO-WTP composite maps for anomalous  $Z_{300}$  are shown in Fig. 5.13, with the phase 8 of both of their cycle as time reference (see Fig. 5.9). Composite maps are averaged over ranges of composite days of -3 to 0, 1 to 3 and 4 to 7. Comparison with Fig. 5.3 reveals that such MJO-WTP perturbations are strikingly similar to the recurrent low-frequency  $Z_{300}$  anomalies. When the North Pacific ridge begins to amplify, there is wave activity coming from both the subtropics and to a lesser extent northeast Asia. Development eastward over northwestern American seaboard is found. When the ridge attains its maximum amplitude, wave dispersion becomes more zonal, with part of it diverted equatorward into the subtropical eastern Pacific. Strong (horizontal) divergence is found over the southeastern side of the ridge, with export of activity into North America. During its decay, there is still some export of activity from the anomalous ridge. These dispersion characteristics are similar to those shown in Fig. 5.3. The main

---

<sup>6</sup>Recalling that each cycle is divided into eight phases, there are totally 64 combinations of phases one can choose from.

difference is that anomalies in high latitudes are stronger for MJO-WTP composite anomalies. The 700-mb vertical activity flux, which is closely associated with baroclinic development, is also examined (not shown). It is found to be largest during composite days 1 to 3, but much smaller during earlier and later times. Variation of the vertical activity flux is again similar to that related to low-frequency perturbations.

Composite charts with other phase combinations are also examined. The one with phase 4 of both MJO and WTP as time reference (denoted as phase (4,4), not shown) gives perturbation patterns that are almost mirror images of those of phase (8,8) just shown. On the other hand, for phase (4,8), i.e. with the MJO and WTP having the opposite phase, amplitudes of anomalies over the mid-latitude ocean is much reduced, as if there is a destructive interference between perturbations associated with the MJO and WTP separately.

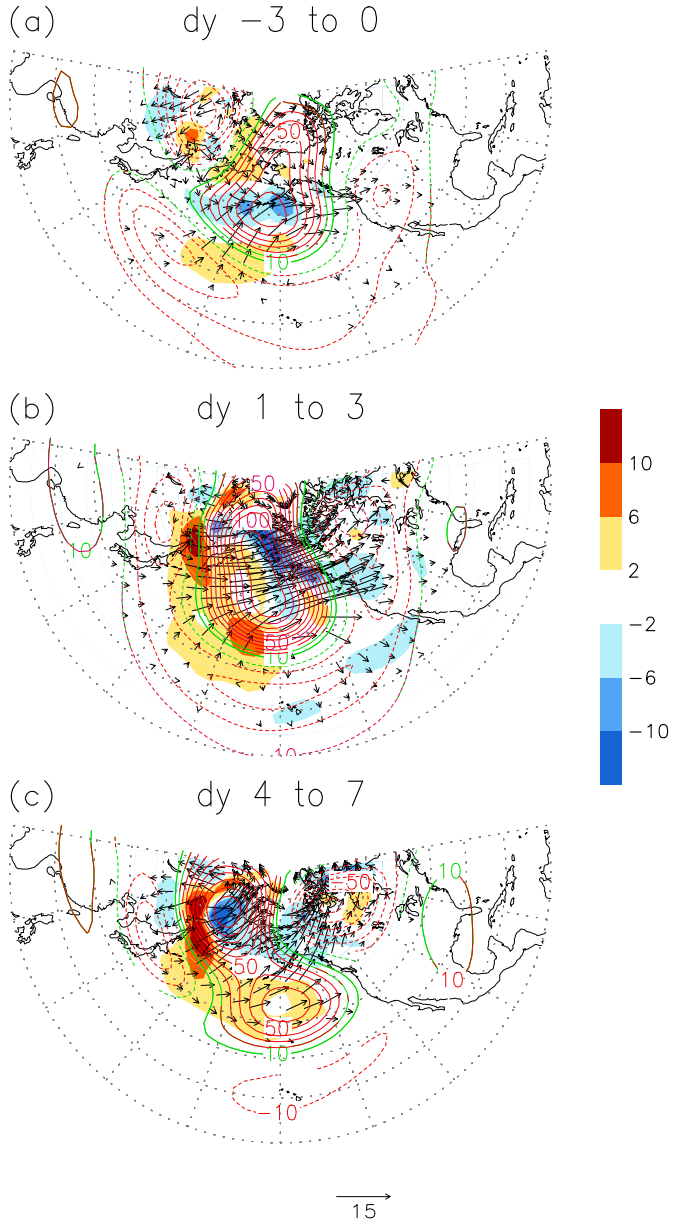


Figure 5.13: MJO-WTP composite maps of 300-mb height perturbations (in unit of m), averaged over composite days of (a) -3 to 0, (b) 1 to 3 and (c) 4 to 7. Anomalies are found with 'phase (8,8)' as time reference. Perturbations exceed 95% significance level are denoted by red contours, otherwise green, while zero contours are omitted. Also shown are wave activity vectors (magnitude in  $\text{m}^2 \text{s}^{-2}$ ) and their divergence (shading, in  $10^{-6} \text{ms}^{-2}$ ). Only vectors located where flux divergence exceeds  $10^{-6} \text{ms}^{-2}$  in magnitude are shown.

### 5.3.3 Linearity of MJO-WTP interaction

It appears that MJO-WTP anomalies resemble a superposition of those *independently* due to the MJO and WTP. This is consistent with the result that their related PC time series are linearly independent. There is also another way to test whether this superposition is linear. Suppose the MJO composite of 300-mb height field (for some chosen phase) is denoted by  $\Phi(s_\chi)$ , where  $s_\chi$  is the threshold for the selection of strong MJO events (see also Ch. 3). Composite maps shown in Fig. 5.9, for instance, are found with  $s_\chi = 0.75$  sd of the amplitude of the PC. The functional dependence on  $s_\chi$  is written out explicitly; in general, magnitudes of anomalies composite would depend on the value of threshold being used. Larger values of  $s_\chi$  imply stronger MJO events being selected in the compositing procedure, therefore resulting in stronger anomalous circulation. Similarly, one can denote MJO-WTP composite anomalies as  $\tilde{\Phi}(s_\chi, s_Z)$ . Again threshold values related to both MJO and WTP selection would affect amplitudes of the resulting anomalies. Defining a set of composite maps  $\delta_\chi \Phi$  and  $\delta_\chi \tilde{\Phi}$  as follows:

$$\begin{aligned}\delta_\chi \Phi &\equiv \Phi(s_\chi) - \Phi(s_\chi^*); \\ \delta_\chi \tilde{\Phi} &\equiv \tilde{\Phi}(s_\chi, s_Z) - \tilde{\Phi}(s_\chi^*, s_Z),\end{aligned}$$

where  $s_\chi^*$  is some reference threshold value (say 0.5 sd). The  $\delta \Phi$  or  $\delta \tilde{\Phi}$ 's can be treated as deviations of anomalous  $Z_{300}$  associated with a change of the MJO amplitude alone, while that of WTP remains unchanged for  $\tilde{\Phi}$ . If MJO-WTP anomalies are due to a linear superposition of independent MJO and WTP signals, then one would expect an increase of MJO amplitudes alone would lead to the same enhancement of amplitudes for both the  $\Phi$  or  $\tilde{\Phi}$  maps. In other words

$\delta_\chi \Phi = \delta_\chi \tilde{\Phi}$ . WTP composite maps  $\Phi(s_Z)$  and  $\tilde{\Phi}(s_\chi, s_Z)$  can also be compared in a similar way, by varying the threshold value  $s_Z$  for selecting WTP events. By the same token, if MJO-WTP perturbations are the result of a linear superposition, then  $\delta_Z \Phi = \delta_Z \tilde{\Phi}$  should hold.

To verify the linearity of superposition, deviation maps sequence for the  $\delta\Phi$  and  $\delta\tilde{\Phi}$ 's are compared. First, a 'reference' map  $\Phi(s_\chi^*)$  with  $s_\chi^* = 0.5$  sd is found for the MJO phase 8. Composite maps with  $s_\chi$  varying from 0.75 to 2.5 sd, in steps of 0.25 sd, are used to compute a set of deviation maps  $\delta_\chi \Phi$ . Fig. 5.14 (a) and (c) show the reference map and deviation from it for  $s_\chi = 2.5$  sd, respectively. Notice that amplitudes of anomalies from the deviation are comparable to those of the reference map.

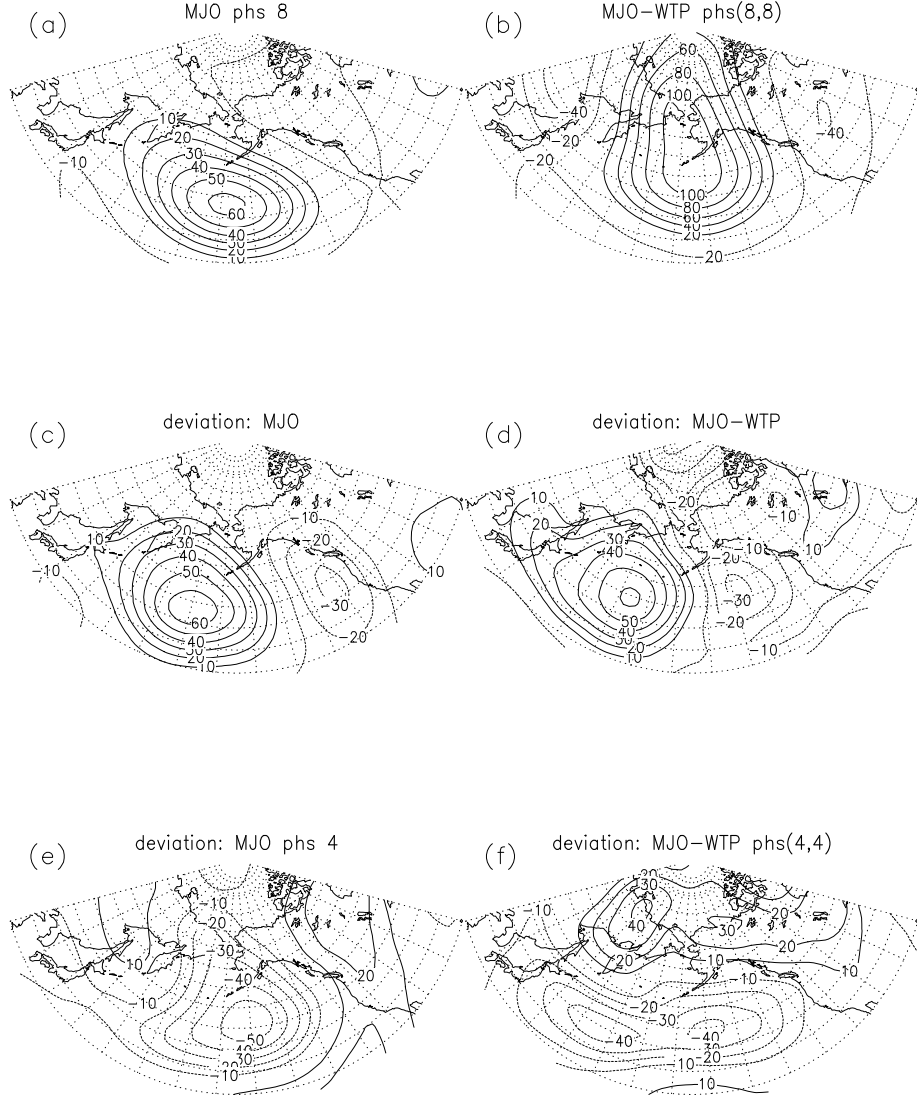


Figure 5.14: 300-mb height anomalies reference map for (a) MJO phase 8, and (b) MJO-WTP phase (8,8). These reference composite anomalies are found by setting the selection threshold for MJO events  $s_\chi^*$  to be 0.5 sd. See text for further details. Deviation from these reference maps, for those with  $s_\chi = 2.5$  sd, are shown in the middle panels for the (c) MJO (i.e.  $\delta_\chi \Phi$ ) and (d) MJO-WTP ( $\delta_\chi \tilde{\Phi}$ ) composites. (e) and (f) are the same as the middle panels excepts for composites of MJO phase 4, and MJO-WTP phase (4,4), respectively. Calculation based on GCM data. Unit: m

The reference map and a sequence of deviation maps  $\delta_\chi \tilde{\Phi}$  for MJO-WTP composites can be found in the same way. For all composite maps, the same

threshold value of  $s_Z = 0.75$  sd is used for WTP selection. Fig. 5.14 (b) and (d), respectively, show the reference and deviation map for the phase (8,8). It is seen that in fact  $\delta_\chi\Phi$  and  $\delta_\chi\tilde{\Phi}$  compare reasonably well. The method is applied on different phase combination as well. Lower panels of Fig. 5.14 show results for the MJO phase 4 and MJO-WTP phase (4,4) composites. Broad features of these two also agree, with negative perturbations having comparable magnitudes, although there are some differences in high latitudes.

The maps  $\delta_\chi\Phi$  and  $\delta_\chi\tilde{\Phi}$  are compared in a more quantitative fashion, by computing pattern correlation between corresponding members of the two sets and also by comparing their rms amplitudes over a certain region. The domain of  $120^\circ\text{E}-90^\circ\text{W}, 30^\circ\text{-}90^\circ\text{N}$  is chosen for this purpose. For instance, correlation between patterns in Fig. 5.14 (c) and (d) is 0.65, while that between the lower panels is 0.59. All four deviation maps have roughly the same rms amplitude of about 20m. Amplitudes of  $\delta_\chi\Phi$  and  $\delta_\chi\tilde{\Phi}$  are plotted in Fig. 5.15 (a), which includes data based on eight distinct combinations of the MJO and WTP phases. For each of these combinations, the sets of  $\delta\Phi$  and  $\delta\tilde{\Phi}$ 's are again derived by varying the value of  $s_\chi$ . If  $\delta_\chi\Phi = \delta_\chi\tilde{\Phi}$ , then all data points should lie on the slope-one line passing through the origin. The result shows that most data points are close to that line. Although there are some outliers, there is no systematic deviation from the straight line, even for some deviation maps with large amplitudes.

Pattern correlations between each pair of  $\delta_\chi\Phi$  and  $\delta_\chi\tilde{\Phi}$  maps are also computed. Although there are times when correlation is particularly low, there are many high values as well. Also, no apparent decreasing trend is found as one moves to higher thresholds. The average pattern correlation for all data shown is 0.55. Overall, these results indicate that  $\delta_\chi\Phi$  and  $\delta_\chi\tilde{\Phi}$  have very similar patterns

with almost the same magnitudes. Finally,  $\delta_Z\Phi$  and  $\delta_Z\tilde{\Phi}$  or WTP and MJO-WTP deviation maps are compared. Rms amplitudes of the two sets of deviation maps  $\delta_Z\Phi$  and  $\delta_Z\tilde{\Phi}$  match well, and pattern correlation values are quite high (with the average over all data being 0.77). These results strongly suggest that the MJO-WTP anomalies can be treated as a result of linear superposition of those related to the MJO and WTP independently.

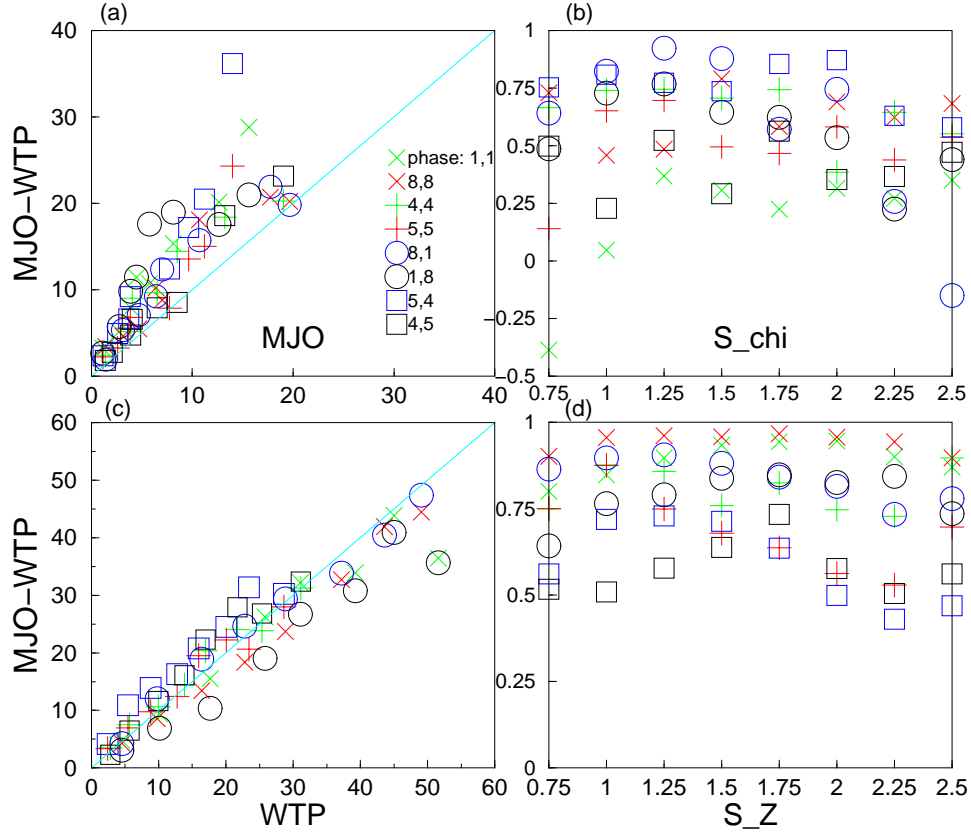


Figure 5.15: (a) Rms amplitudes, in unit of m, of MJO-WTP 300-mb height anomalies deviation maps ( $\delta_\chi \tilde{\Phi}$ ) vs. those of the MJO ( $\delta_\chi \Phi$ ). Rms amplitudes are found within the region of 120°E–90°W, 30°–90°N. MJO-WTP and the MJO deviation maps related to the same threshold value are paired up. Their amplitudes are plotted, for eight different phase combinations for MJO-WTP composites. A line with slope one through the origin is added. (b) Pattern correlation between each pair of MJO-WTP and the MJO deviation maps, as a function of the MJO selection threshold  $s_\chi$ . (c) and (d) are same as (a) and (b), respectively, except that deviation maps ( $\delta_Z \tilde{\Phi}$ ) and those of the WTP ( $\delta_Z \Phi$ ) are compared.

### 5.3.4 Discussion and Conclusion

Based on results from a GCM experiment, interannual variability of low-frequency activity in the extratropics is examined. It shows a region in the North Pacific

over which the external variance is particularly large. By the design of the GCM experiment, such variability is attributed to the changing SST imposed within the tropical Pacific. Circulation anomalies in the vicinity of this region are studied, using both GCM data and NCEP-NCAR reanalyses. Upper-level height anomalies take the form of an subtropical-extratropical wavetrain which resembles the PNA pattern, but there is also an east-west wavy pattern in high latitudes. Strong dispersion is found east to southeast of the prominent North Pacific ridge, leading to development over North America. Wave-activity flux is computed, and results are consistent with the above influences on downstream dispersion. Activity vectors also reveal incoming activity from east Asia and the subtropical Pacific, during the early stage of the life cycle of anomalies.

Strong vertical wave activity is also present, indicating baroclinic growth of perturbations. In fact, circulation anomalies show a clearly baroclinic configuration. Local baroclinic development is found to play an instrumental role in the amplification of low-frequency anomalies. This is consistent with the energy and enstrophy budget considerations of Dole and Black (1990) and Black and Dole (1993), who indicated that baroclinic conversion is comparable or even exceeds the barotropic one. Many of the empirical findings here match the idea that these disturbances are three-dimensional instabilities of the time mean flow (Frederiksen 1982; 1983). On the other hand, feedback from synoptic-scale eddies does not play a strong role in the intensification of low-frequency perturbations.

Coherent, eastward propagating convective as well as large-scale divergent signals in the tropics are found to be associated with North Pacific low-frequency circulation anomalies. The latter also show a retrograding behavior in high latitudes. Anomalies in the extratropics related to the MJO and WTP are studied,

and are found to resemble those characterizing the low-frequency flow, in their respective active regions. This resemblance holds in a three-dimensional sense, i.e. distinct baroclinic signatures are also present for MJO and WTP disturbances. This suggests that all these modes of low-frequency variability are probably governed by similar barotropic-baroclinic dynamics.

The interaction of the MJO and the WTP is considered. Characterized by the temporal coefficients of the leading CEOF of low-frequency height field and the velocity potential, these two phenomena are shown to be linearly independent of each other. Their associated perturbations in the extratropics can interfere, and this is demonstrated in a composite sense. Moreover, this interference is found to follow a simple linear superposition principle. When a constructive interference happens, resulting circulation patterns and those related to recurrent low-frequency anomalies are strikingly alike.

# **Chapter 6**

## **Low-Frequency Circulation Anomalies- the Impact of ENSO**

### **6.1 Introduction**

#### **6.1.1 Observational and modeling studies**

Although phenomena of low-frequency circulation interest many researchers in meteorology, there are relatively few studies on their variability associated with ENSO. Namias (1986) reported that anomalous flows tend to have stronger month-to-month persistence over North America during El Niño winters, providing hints that low-frequency variability is sensitive to ENSO. Motivated by the extended-range forecast problem, Palmer (1988) found that the growth of rms errors of 9-day forecasts over the Pacific sector is closely related to a PNA-like mode of variability (Wallace and Gutzler 1981). His results from barotropic model experiments suggest that the negative PNA state gives rise to a more unstable background flow.

Palmer's finding has a direct consequence on how ENSO affects low-frequency variability, since during warm events changes of the seasonal mean circulation do look like a positive PNA, while changes during cold events resemble a negative PNA mode (Horel and Wallace 1981). Based on observational data, Renwick and Wallace (1996) laid down some firm evidence that blocking frequencies are strongly influenced by the ENSO cycle. Blockings are found to be less likely to occur during warm ENSO years than otherwise, and this modulation of occurrence frequency is strongest over the Bering Strait. From the cold-to-warm variance ratio of the 10-30-day filtered 500-mb height field, it is seen that activity is stronger over the eastern Siberian coast, Alaska and northwestern Canada during cold events. That ENSO has an even stronger impact on blocking frequencies in the southeastern Pacific is shown in the follow-up study of Renwick (1998).

Results from various GCM experiments also show an impact of ENSO on low-frequency activity, broadly consistent with observations. Mullen (1989)'s modeling study indicates that during La Niña-like situations, the total number of block days is increased over the Aleutians and decreased over the northeastern Canadian coast. The more recent study of Chen and van den Dool (1997) shows that blocking frequencies are enhanced (reduced) from the Pacific to North America, during cold (warm) events. ENSO-related changes of variability over a range of time scales were studied by Compo et al. (2001), based on modeling experiments with large ensemble sizes. Both tropical and extratropical intraseasonal activity are found to be strongly affected by ENSO, and GCM results within the Pacific sector compare well with those based on NCEP-NCAR reanalyses. Renshaw et al. (1998) found that the negative (positive) PNA state is more preferred during cold (warm) ENSO years in their GCM simulations, in agreement with observations

(see Palmer 1988).

### 6.1.2 Possible mechanisms considered in previous studies

As mentioned before, Palmer (1988) suggested that the presence of negative PNA-like anomalies would result in a more unstable flow. In his study, numerical experiments are conducted, using the climatological flow with either a positive or negative PNA-like pattern added as the basic state. It is found that the negative PNA state consistently leads to stronger instabilities. Since typical seasonal mean circulation anomalies during ENSO resemble the PNA pattern, this result suggests that flow stability can account for the impact of ENSO on low-frequency activity.

As discussed in Compo et al. (2001), besides changes of the mean background flow, there might be other factors relevant to the problem, such as the variability of tropical convection and feedback from synoptic-scale eddies. The view that modulation of the Pacific storm tracks during ENSO can affect blocking frequencies in high-latitude regions was proposed by Chen and van den Dool (1997). They suggested that, because high-frequency eddies are more active in the northern-latitude Pacific during cold events, blockings there are more effectively forced and maintained. Their argument seems consistent with the fact that monthly-to-seasonal mean flow anomalies and storm tracks tend to covary, in such a way that there is a mutual feedback between them (Lau 1988). It must be mentioned, however, that Chen and van den Dool (1997) did not show explicitly how blocking flows interact with synoptic-scale eddies, and more importantly how the presumed feedback processes could lead to changes of blocking charac-

teristics during ENSO. Although the response of extratropical flow to ENSO is known to be strongly influenced by the feedback from transient eddies (Held et al. 1989), how changes of *intraseasonal* activity are related to those of the *seasonal mean* storm tracks during ENSO is unclear.

### 6.1.3 Questions to be asked

The previous chapter is concerned with the climatological behavior of low-frequency activity. In particular, some specific recurrent low-frequency circulation patterns in the North Pacific sector are considered. Wave activity is found to originate from east Asia and the subtropical western Pacific, with development of activity in the latter region apparently associated with some coherent signals of intraseasonal convection. The growth of perturbations in the extratropics has a mixed barotropic-baroclinic signature. These anomalies also project onto both WTP- and MJO-related circulation.

Concerning what mechanisms through which ENSO affects low-frequency activity, a number of questions can be raised, based on the aforementioned findings:

- Is there any change in the intraseasonal convective signals, themselves precursors of extratropical anomalies, during ENSO? Is there any associated change in the incoming wave activity and the life cycle of anomalies?
- What is the effect of having different background states on low-frequency activity?
- How do changes of the WTP- and MJO-related circulation during ENSO compare with those of the anomalies recurrent over North Pacific?

The goal of this chapter is to examine the impact of ENSO and study its potential mechanisms by focusing on the above questions. It will be shown that changes of intraseasonal convection during ENSO could have an impact on the development and evolution of extratropical perturbations. Changes of the three-dimensional basic state also play a role. There are hitherto no studies devoted to some of these possibilities; results presented might provide new ideas on the problem.

## 6.2 How ENSO Affects Low-Frequency Activity in the North Pacific Sector

### 6.2.1 Intraseasonal variability and occurrence of persistent events

As a starting point for considering the impact of ENSO on low-frequency activity, the variance of 10-60-day filtered  $Z_{300}$  during warm and cold events, for the period of November to March, is compared. Cold-to-warm ratio of variance is plotted in Fig. 6.1, for both GCM and NCEP-NCAR reanalyses data. Here, as in subsequent sections, reanalyses data within the period of 1950-99 is used. This figure shows that the activity during cold events is stronger, over a broad region from the subtropics to high-latitude Pacific, compared with that during warm events. For GCM data, strongest enhancement of variability is found over the Aleutian Islands, with a hint of disturbances being more active over the northwestern seaboard of America. Suppressed activity over the mid-latitude eastern North Pacific is also found.

Reanalyses results agree reasonably with those based on GCM data. Both

show approximately same regions where variability is enhanced within the Pacific, during cold ENSO events. Even the reduction of activity over the subtropical eastern Atlantic is roughly consistent; however, changes over east Asia do not agree between the two datasets. Another difference is that the strongest change of variance, for the reanalyses data, is found in higher latitudes, namely over a region centered at the Bering Strait. This discrepancy might be related to the different climatological behavior of activity between GCM and NCEP-NCAR datasets; disturbances in the latter have larger amplitudes in high latitudes and also over North America, while those of the GCM are more active to the south over oceanic regions (see Fig. 5.1). Overall, these results are in line with those from Renwick and Wallace (1996) and Compo et al. (2001).

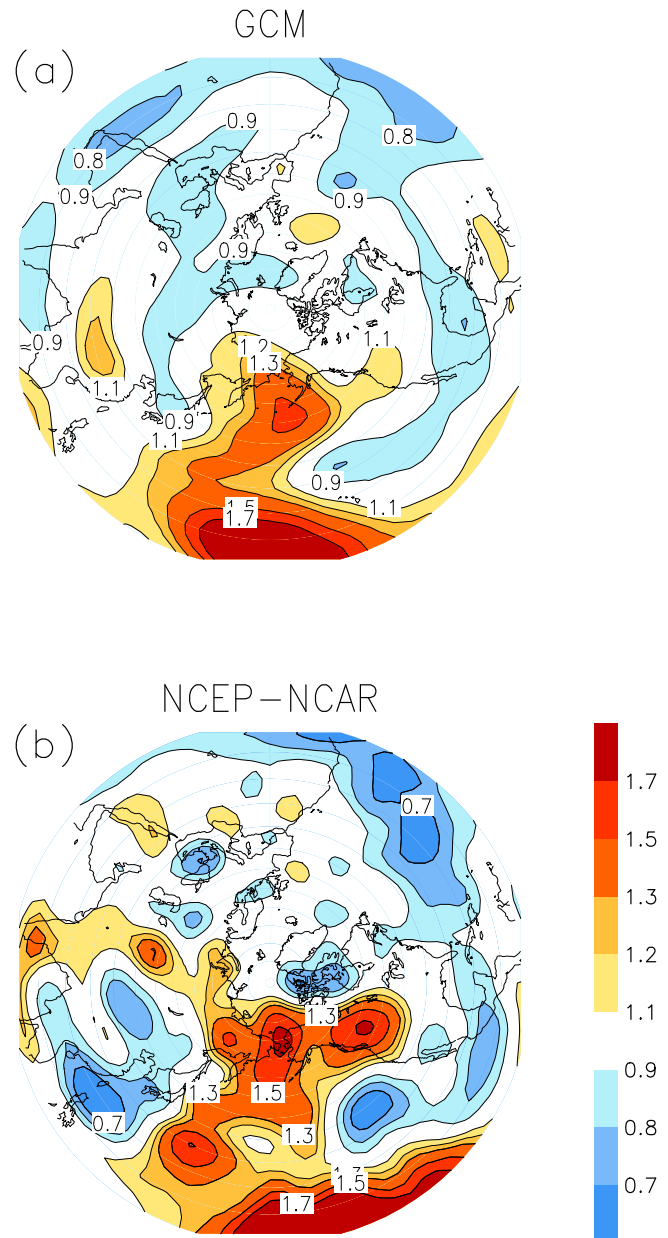


Figure 6.1: Cold-over-warm variance ratio of 10-60-day filtered 300-mb geopotential height, for the period of November to March. Calculations are based on datasets from (a) GCM and (b) NCEP-NCAR reanalyses. GCM results exceed 95% significance level for values greater (less) than 1.1 (0.9). Reanalyses results are 95% significant for values greater (less) than 1.3 (0.7).

The impact of ENSO on North Pacific low-frequency circulation can also be assessed based on a different approach. During the warm and cold ENSO phase, occurrence frequencies of persistent circulation episodes are found. To define a persistent episode, time series of the 10-60-day filtered  $Z_{300}$ , averaged over the region of  $170^{\circ}\text{E}-150^{\circ}\text{W}$ ,  $40^{\circ}\text{-}65^{\circ}\text{N}$ , is first obtained<sup>1</sup>. The domain for area-averaging is chosen based on inspection of Fig. 6.1. The rms value ( $\sigma$ ) of this time series, based on data from all years, is calculated. Time series of the filtered variable  $Z_{300}$  is then re-examined. An episode of persistent circulation occurs whenever the daily value of the area-averaged  $Z_{300}$  has its absolute magnitude greater than  $0.5\sigma$ , for at least 10 consecutive days. This method is essentially the one used by Dole and Gordon (1983) for selecting persistent anomalies cases; similar criteria were also employed by Lau and Nath (1996) for studying persistence characteristics of the extratropical circulation in their GCM experiments. Frequencies of occurrence of these ‘ $0.5\sigma$  episodes’ are found for warm and cold events, and they are shown in Fig. 6.2 for both GCM and reanalyses data. It is clear that persistent episodes happen more frequently during cold ENSO years, for both GCM and NCEP-NCAR datasets. Computation is repeated using GCM data, for  $0.75\sigma$  and  $1\sigma$  events (defined analogously as  $0.5\sigma$  events). Again, persistent events are more likely to occur in the cold than the warm ENSO phase, indicating that such a difference of occurrence frequency is not sensitive to the choice of the threshold magnitude. Statistics of blocking given by Renwick and Wallace (1996) shows very similar sensitivity to ENSO.

---

<sup>1</sup>This covers the key region in section 5.2.1

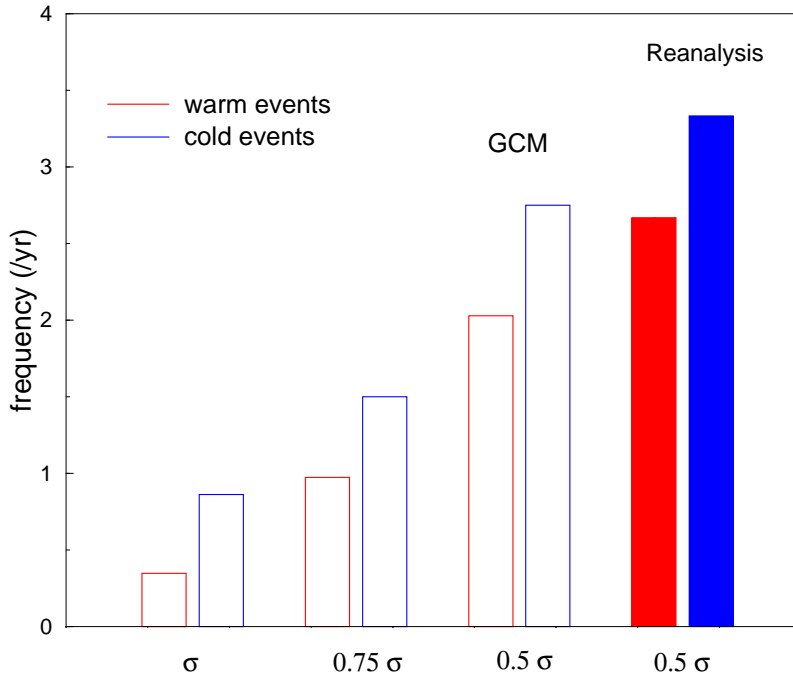


Figure 6.2: Frequency of occurrence (per year) of  $0.5\sigma$  persistent circulation episodes, for both GCM (first set of open rectangles from the right) and NCEP-NCAR datasets (filled rectangles), during warm and cold ENSO years. See text for definitions. Also shown are frequencies of  $0.75\sigma$  and  $1\sigma$  episodes, for GCM data.

Statistics of ‘positive’ and ‘negative’ persistent episodes (i.e. episodes further stratified according to the sign of anomalies), for warm and cold events, are also compared. For GCM results, occurrence of episodes of both signs (not shown) are affected in the same way, with higher frequencies found during cold events. Thus one might regard the impact of ENSO to be approximately linear, in the sense that persistent episodes with either sign are affected during ENSO in the same manner. This is also consistent with results of Chen and van den Dool (1997), who showed that frequencies of both blocking and deep trough flow are enhanced (reduced) during cold (warm) events over the North Pacific.

### 6.2.2 Anomalous circulation features

In the last section, it is shown that amplitudes of low-frequency activity over the North Pacific are greatly affected by ENSO. Changes of circulation features are also of great interest. To look for any such changes, life cycles of anomalies during warm and cold ENSO events are examined. As in Ch. 5, the anomalous  $Z_{300}$  field is found using a lag regression analysis<sup>2</sup>. Charts of anomalies during warm and cold events are shown in Fig. 6.3 in various stages of their life cycle, based on GCM data. Again as in the previous chapter, the developing, mature and decay stage refer to the period of -5 to -2, -1 to 1 and 2 to 5 lag day, respectively. Wave activity vectors, computed from regression maps in various stages, are also shown together with their horizontal divergence (see section 5.2.2 for the definition and interpretation of activity vectors).

As in the climatological situation, the upper most panels of Fig. 6.3 indicate activity coming from the subtropics and east Asia in the developing stage. However, during cold ENSO events, subtropical wave activity is much stronger. Associated with these is a stronger subtropical cyclone, and the North Pacific ridge also has larger magnitudes during its incipient stage. There is also stronger convergence of wave activity flux into the ridge center. Downstream dispersion east of the ridge is present during cold events, but less obvious during warm events at this stage. Fig. 6.4 shows the same set of charts based on NCEP-NCAR data, and results agree with those from GCM in many aspects. Again in the developing stage, there are stronger subtropical perturbations, more convergence of activity flux as well as a more prominent development downstream, in the cold compared

---

<sup>2</sup>Regression is computed based on a reference time series, which comprises daily values of the 10-60-day filtered  $Z_{300}$ , averaged over the key region of  $180^{\circ}$ - $150^{\circ}$ W,  $40^{\circ}$ - $60^{\circ}$ N.

with the warm ENSO phase.

For GCM results, it is noteworthy that there is still a substantial amount of activity from the subtropics during cold events, when the anomalous ridge becomes mature (see middle panels of Fig. 6.3). Also, strongest cyclonic flow tends to remain within the western to central Pacific, while during warm events it is located over the eastern part of the ocean. During cold ENSO events, stronger dispersion is found from the stronger ridge, with a pronounced wavetrain directed southeast over the United States. Activity fluxes for the warm case seem to have an obvious split; the majority of them are directed to northwestern part of North America while there are some to the subtropical eastern Pacific. Reanalyses results also show larger amplitude of the ridge and stronger southeastward dispersion are found in La Niña years.

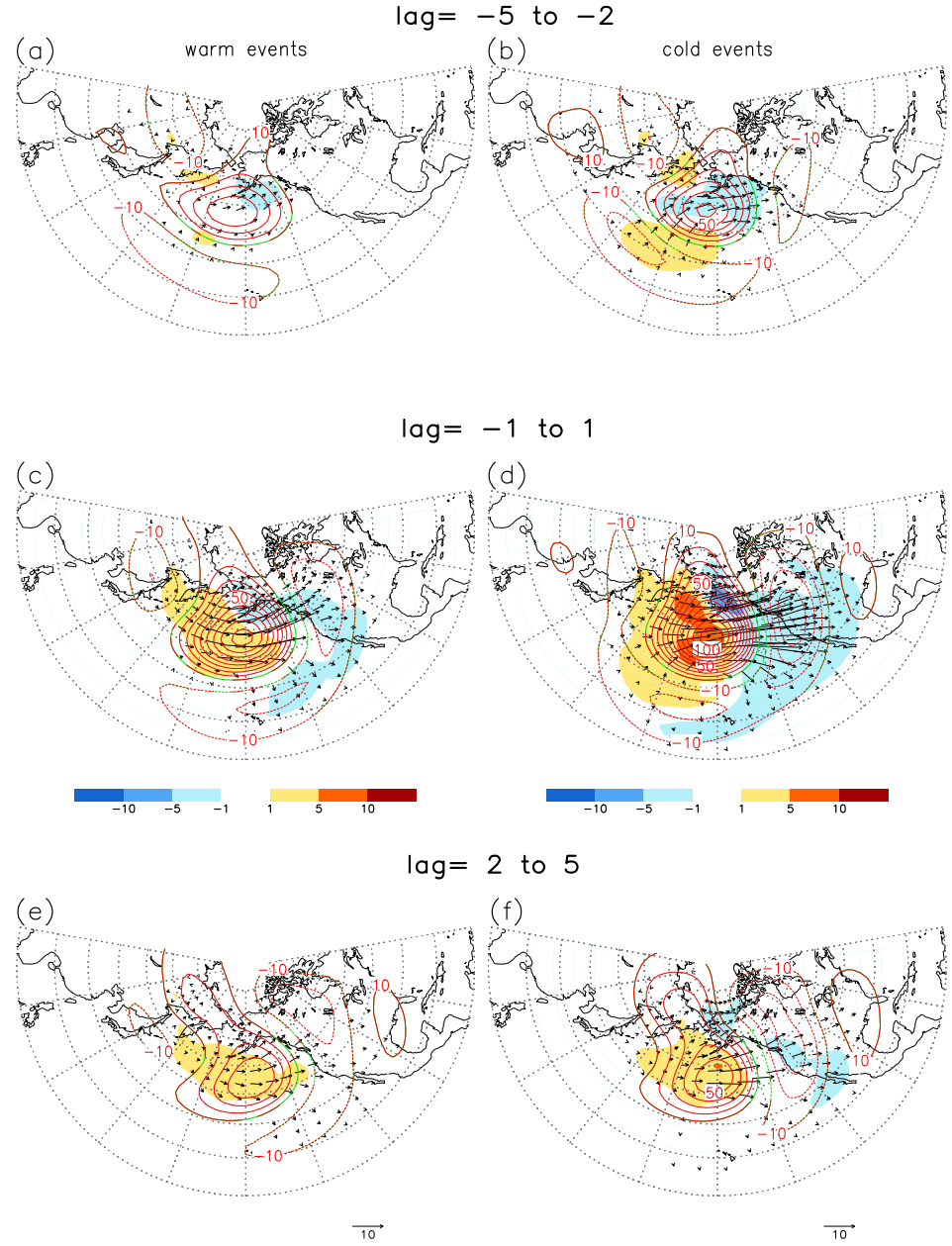


Figure 6.3: 300-mb height perturbations, in contours, based on lag regression using GCM data (see text). Regression maps are averaged over period of -5 to -2, -1 to 1, and 2 to 5 lag days, and results for warm and cold events are shown in the left [(a), (c) and (e)] and right panels [(b), (d) and (f)], respectively. Associated wave-activity vectors (magnitude in  $\text{m}^2\text{s}^{-2}$ ) and their divergence (shading, in  $10^{-6}\text{ms}^{-2}$ ) are also shown. Only vectors collocating divergence with absolute magnitudes no less than  $0.5 \times 10^{-6}\text{ms}^{-2}$  are displayed. Height anomalies exceeding 95% significance level are denoted by red contours, otherwise green. Zero contours are omitted.

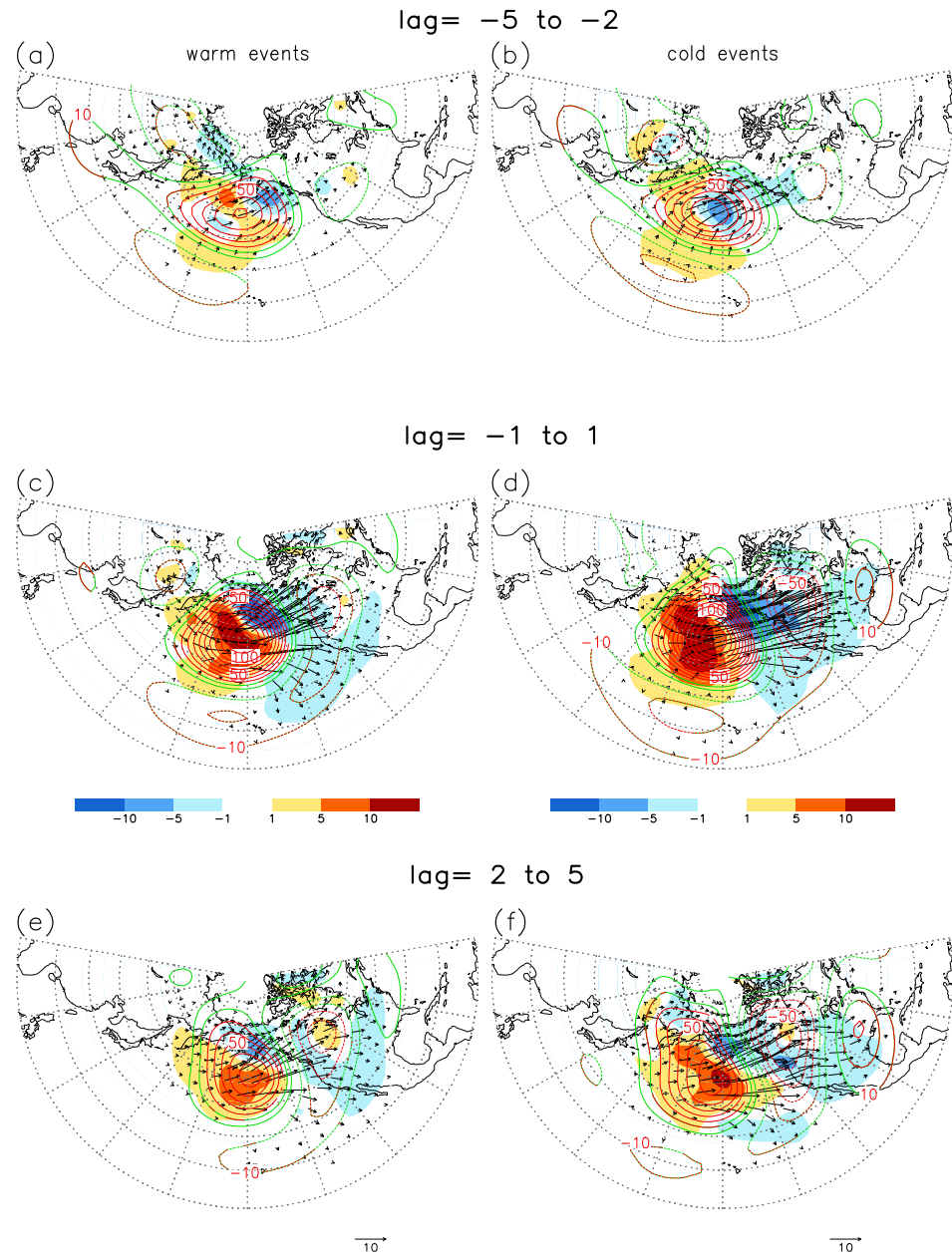


Figure 6.4: As in 6.3 but for NCEP-NCAR reanalyses.

Amplitudes of the ridge are much reduced at the decay stage, although there is still a clear wavetrain over continental America. The latter has larger amplitudes over the northwestern North American seaboard during cold events. A difference

of the downstream wavetrain is also present for the reanalyses results; anomalies are found to be strongest over southeast U.S. during cold ENSO episodes, while during warm events the wavetrain seems to be directed more eastward, with anomalies reaching the Atlantic.

The anomalous circulation in low levels is also considered. As shown in Ch. 5, low-frequency anomalies are distinctly baroclinic during part of their life cycle. Consideration of the wave-activity flux also reveals that its vertical convergence, indicating baroclinic growth, is instrumental in amplifying perturbations over the North Pacific. Variables indicating baroclinic signatures are therefore examined, in different ENSO phases. Fig. 6.5 shows anomalous temperature, geopotential height and pressure velocity at 700 mb, based on the GCM dataset. These fields are computed using the regression method as before. At the developing stage, the low-level ridge is stronger during cold events, accompanied with larger positive temperature perturbations to its southwest, suggesting stronger baroclinic growth. At the mature stage, the ridge extends slightly more to the north, and temperature anomalies over northwestern Canada/Alaska and northeastern Russia are also stronger. Moreover, these perturbations are located to the west of the anomalous height field, indicating a westward tilt in the vertical and hence the baroclinic nature of the flow. At the decay stage, perturbations become more equivalent barotropic, and also have their amplitudes reduced.

Thus, during the part of the life cycle when perturbations are growing, there are clear signs of baroclinic activity. Moreover, those in high-latitude regions and near the northwestern part of North America are significantly enhanced during cold events. Based on observations, Smith and Sardeshmukh (2000) found stronger surface temperature variance over Gulf of Alaska and its neighboring

regions during La Niña years; their results are consistent with those on low-level temperature perturbations presented above.

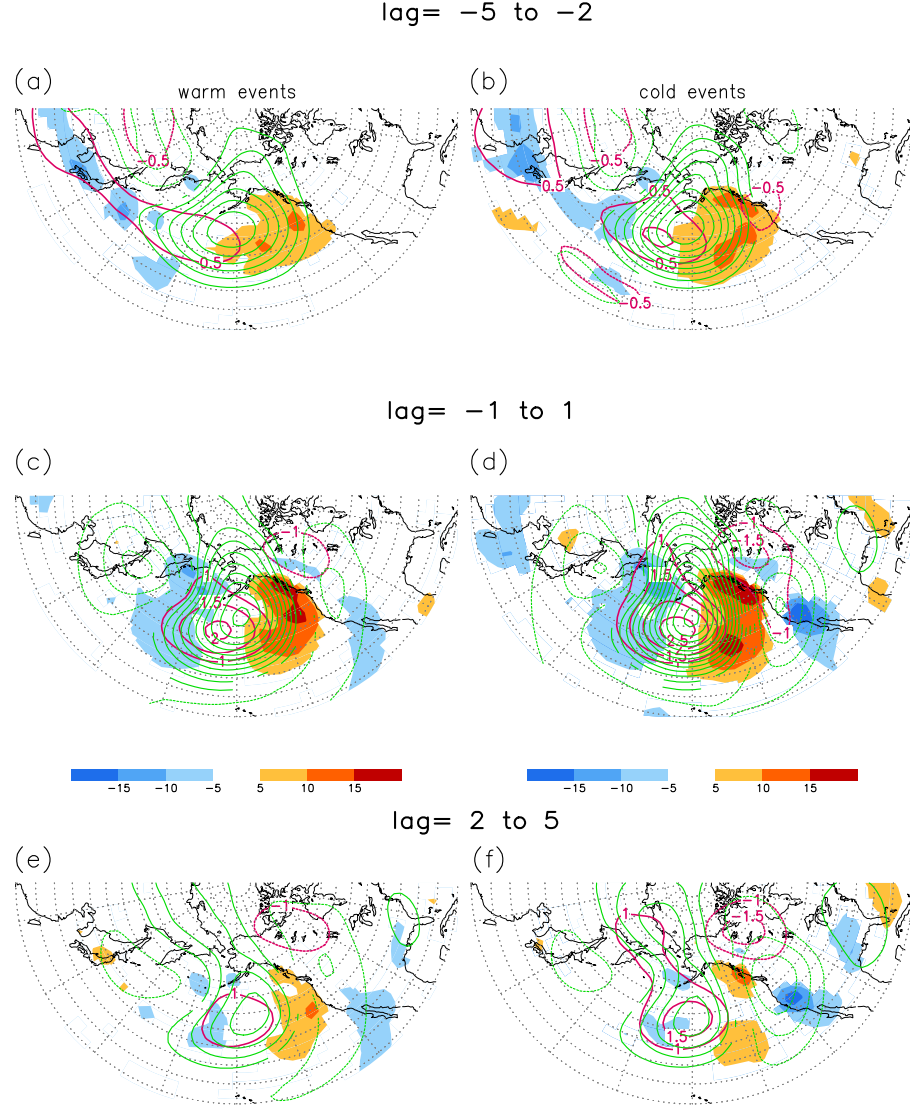


Figure 6.5: As in Fig. 6.3 but for 700-mb temperature (magenta contours, in unit of  $^{\circ}\text{C}$ ), pressure velocity (shading, in  $\text{mbday}^{-1}$ ) and height perturbations (green contours, in intervals of 5m), based on GCM data. All fields exceed 95% significance level. Notice that contours of temperature perturbations start from  $\pm 0.5^{\circ}\text{C}$  for (a) and (b), but from  $\pm 1^{\circ}\text{C}$  for all other panels.

As discussed, baroclinic processes would lead to upward wave activity, which

usually has the largest amplitude in low levels. Vertical activity flux at 700 mb is found during the mature stage, and its values for both warm and cold ENSO events are shown in Fig. 6.6 (a) and (b), respectively, based on GCM data. Also shown are the contemporaneous 300-mb height anomalies. In agreement with earlier analysis, vertical activity is stronger during cold events over the Aleutians, Gulf of Alaska and also to its north over the continent. Reanalyses results, shown in Fig. 6.7 (a) and (b), depict a very similar impact of ENSO; activity flux stronger over a broad region over the central-eastern North Pacific.

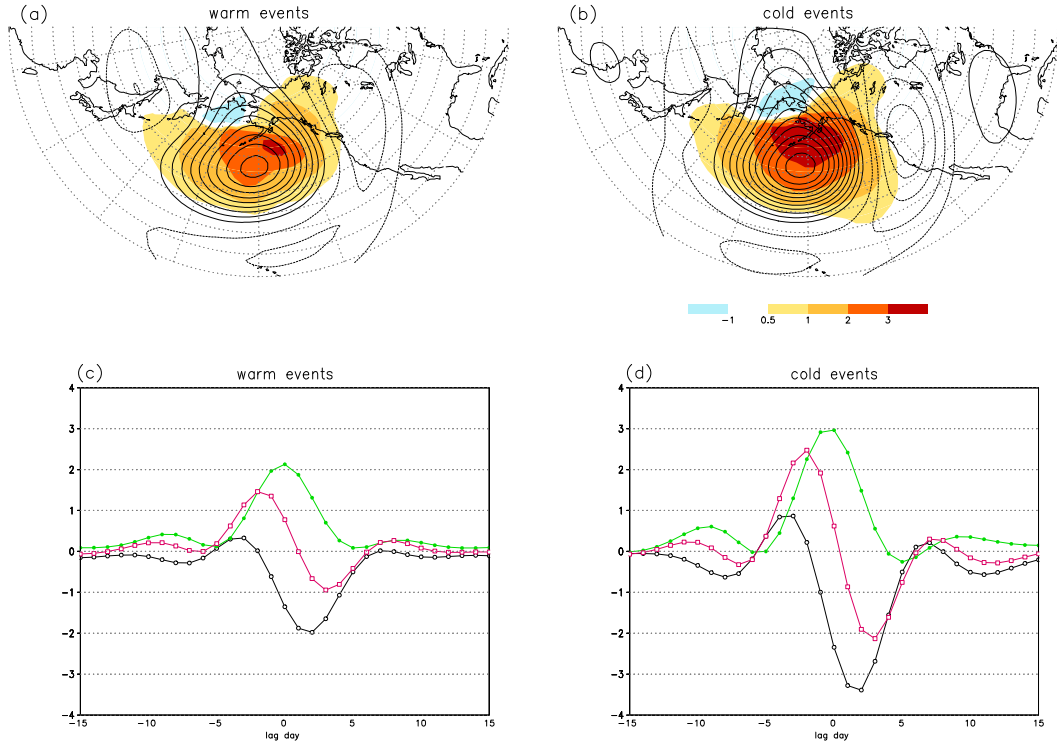


Figure 6.6: Upper panels show the vertical component of 700-mb wave-activity flux (shading, in unit of  $0.1\text{Pa ms}^{-2}$ ) and 300-mb height perturbations (contours with 10m intervals, zero contours omitted), during the lag days -1 to 1. Lower panels show the horizontal (black contour) and vertical (green) convergence of wave activity at the 300-mb surface, with results averaged over  $170^\circ\text{E}-150^\circ\text{W}$ ,  $40^\circ-65^\circ\text{N}$ . Also shown is the three-dimensional convergence (in magenta). Unit of flux convergence:  $10^{-6}\text{ms}^{-2}$ . Left and right panels give results for warm [(a) and (c)] and cold ENSO events [(b) and (d)], respectively. Results based on GCM dataset.

Stronger upper-level ridge during cold events is also found aloft of the enhanced vertical wave activity. In fact, this configuration implies convergence of vertical fluxes in the vicinity of the ridge, and it may be recalled that such convergence can lead to amplification of anomalies (see again section 5.2.2). The horizontal, vertical and three-dimensional convergence of wave activity at 300 mb are shown in Fig. 6.6 (c) and (d), for warm and cold events. Wave flux convergence is area-averaged over the region of  $170^\circ\text{E}-150^\circ\text{W}$ ,  $40^\circ-65^\circ\text{N}$ . There is

stronger convergence in the three dimensional sense during cold events, consistent with the stronger growth of the upper-level ridge. Vertical flux convergence is obviously greater, while the horizontal convergence is also enhanced in the developing stage in cold ENSO phase. More export (divergence) of activity in the decay stage is also found, apparently resulting in the pronounced downstream dispersion discussed before. Fig. 6.7 (c) and (d) show results from the reanalyses dataset: again, during cold events, upward activity is stronger, leading to stronger amplification of disturbances. Stronger horizontal flux convergence is also found in the developing stage.

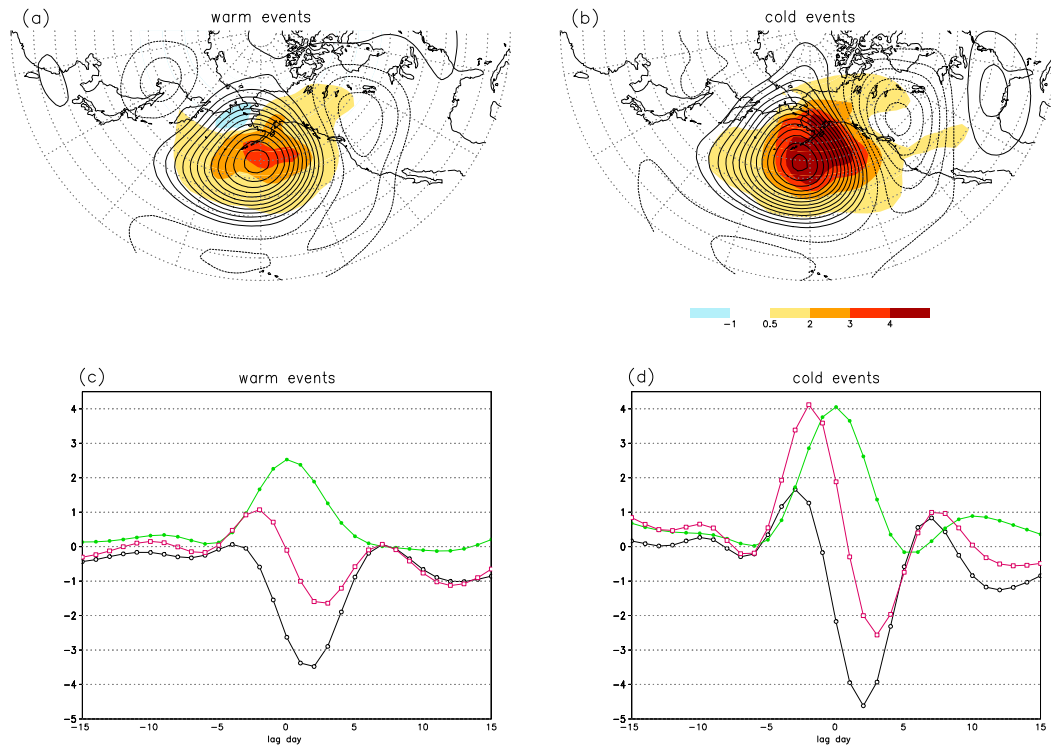


Figure 6.7: As in Fig. 6.6 but based on NCEP-NCAR reanalyses.

Thus it is seen that during ENSO, low-frequency anomalies experience changes in both their magnitudes and circulation features, and patterns of the downstream

dispersion from the anomalous ridge are also modified. Consideration of local energetics should give some ideas on how this is attained. Baroclinic processes are also affected, especially in high latitudes. Since regions with strong baroclinic activity are also known to be shifted during ENSO, a relationship between baroclinicity of the mean flow and low-frequency variability is therefore hinted at, which is certainly worth investigating. There is also stronger wave activity from the subtropics during cold events, related to the stronger subtropical cyclone which remains rather stationary over the western-central Pacific. Based on results found in the climatological situation, development of such subtropical flow anomalies is further associated with intraseasonal convection, making it imperative to consider tropical variability as well. These leads are pursued in the next section.

## 6.3 Relationship with Basic State Variations and Tropical Convection

### 6.3.1 The role of changes of mean circulation during ENSO

Barotropic energy conversion between anomalies and the ambient flow is now examined. Such a diagnostic is useful in considering low-frequency variability, as found by many studies. Following Wallace and Lau (1985), eddy-related  $\mathbf{E}$  vectors given by Hoskins et al. (1983), and their associated conversion from the mean to eddy kinetic energy are shown in Fig. 6.8 (a) and (b), during warm and cold ENSO events respectively. Also shown is the time mean zonal wind at 300 mb, and results are based on GCM data. The  $\mathbf{E}$  vector is given by  $(-\overline{u'^2} + \overline{v'^2}, -\overline{u'v'})$ ,

where primed values are lag regression of variables onto the reference time series (see footnote 1 in section 6.2.2). Overbars denote averaging over the range of -15 to 15 lag days. Energy conversion, from the mean flow to eddies, is computed as  $\mathbf{E} \cdot \nabla U$ , where  $U$  is the mean zonal flow.

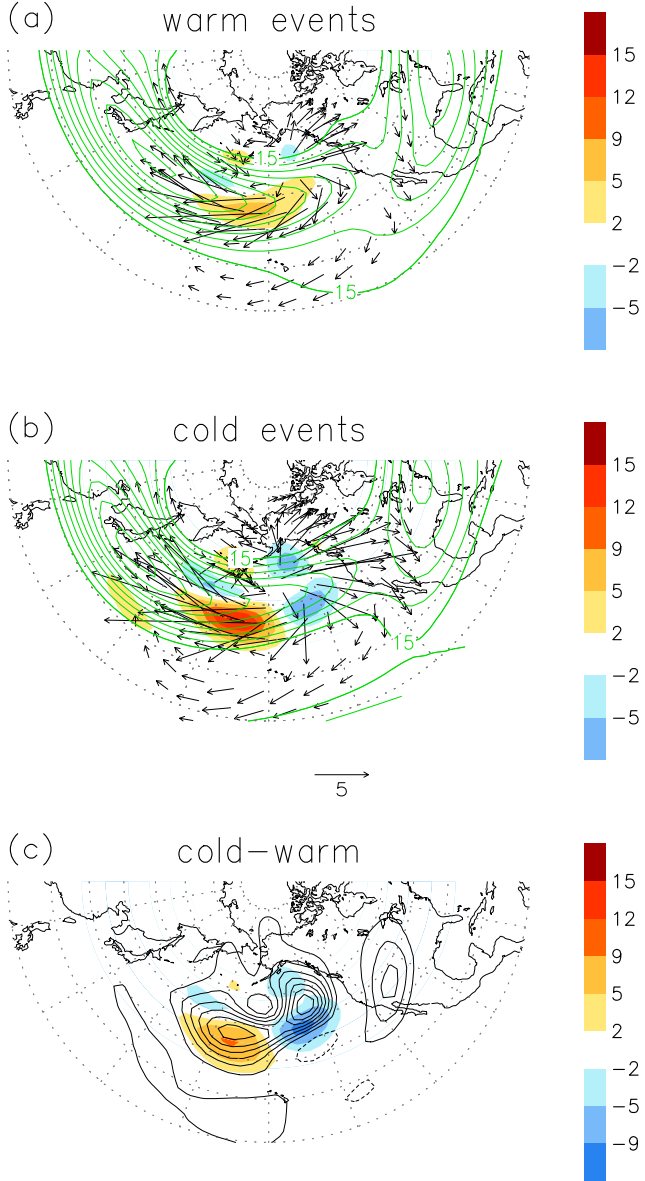


Figure 6.8: **E** vectors (magnitudes in  $\text{m}^2\text{s}^{-2}$ ), barotropic energy conversion from the mean to eddy circulation (shading) and time mean zonal wind at 300-mb (contours), during (a) warm and (b) cold events. **E** vectors are computed based on 300-mb wind anomalies throughout life cycle of low-frequency perturbations (see text for details). Cold-minus-warm 300-mb kinetic energy (contours, with intervals of  $1\text{m}^2\text{s}^{-2}$ ) and barotropic conversion terms (shading) are shown in (c). Note that shading information of (c) is different from (a) and (b), with negative side of scales reaching  $-9 \times 10^{-5}\text{m}^2\text{s}^{-3}$ . Contour levels of the mean zonal wind: 15, 20, 25, 30, 35, 40, 45, 50, 55 and  $60\text{ms}^{-1}$ . Unit of barotropic conversion:  $1 \times 10^{-5}\text{m}^2\text{s}^{-3}$ . Calculations are based on GCM data.

Strongest barotropic conversion occurs near the Pacific jet exit, where  $\mathbf{E}$  vectors are mainly zonally oriented and pointing up-gradient of  $U$ . This is due to the strong zonal wind perturbations in that location, and this agrees with the analyses of Wallace and Lau (1985) concerning low-frequency eddies in general. For cold ENSO episodes, stronger barotropic conversion is found. This can be partially attributed to the more negative  $\partial U / \partial x$ , although eddies (and hence components of  $\mathbf{E}$  vectors) are also stronger themselves. It is noteworthy that energy conversion is located more to the west for about  $10^\circ$  compared with warm events. It seems that strong zonal wind perturbations tend to be found where  $\partial U / \partial x$  is most negative. In fact during warm events, the jet extends more into the eastern part of the mid-latitude ocean, whereas it decelerates sharply around  $170^\circ\text{E}$  during cold events.

In the cold ENSO phase, it is noticed that there is also stronger negative barotropic conversion, in other words conversion of eddy kinetic energy *to* the mean flow, over Gulf of Alaska and eastern mid-latitude Pacific. This is due to the much stronger meridional component  $E_y$  or  $-\overline{u'v'}$  over these regions. The latter can be understood from the fact that, during cold events, both the North Pacific ridge and the downstream trough are stronger, and the latter extends more into the eastern Pacific (see Fig. 6.3). Northwestward tilted height anomalies over Alaska/northwestern Canada (positive  $-\overline{u'v'}$ ), and also those tilted southwest over in the subtropics (negative  $-\overline{u'v'}$ ), have larger magnitudes, leading to greater amplitudes of  $E_y$ . Since  $\partial U / \partial y$  is positive in the subtropics and negative in higher latitudes,  $\partial U / \partial y \cdot E_y$  is strongly negative in these regions.

Cold-minus-warm values of barotropic conversion, as well as the kinetic energy averaged over the life cycle of anomalies, are shown in Fig. 6.8 (c). The

kinetic energy is computed as  $\frac{1}{2}\overline{(u'^2 + v'^2)}$ , following the same convention used for defining **E** vectors. There is more conversion from the mean to eddy kinetic energy around the dateline in mid latitudes during cold events. Consistent with this is the stronger local kinetic energy in the same region. However, it is noticed that over the northeastern Pacific where eddy kinetic energy is also enhanced, changes of barotropic conversion actually have the opposite sign. A simple consideration of barotropic conversion terms seems inadequate to account for the local maintenance of kinetic energy; a more complete energy budget calculation might be required here.

As discussed earlier, baroclinicity of the time mean flow could also have a potential effect on the behavior of low-frequency anomalies. In fact, perturbations with distinctly baroclinic features, especially in high latitudes, are enhanced during cold ENSO events. Fig. 6.9 (a) and (b) show correlation coefficients between 700-mb vertical shear of the zonal wind and the Nino-3 index. The wind shear is calculated using the expression  $\partial U / \partial z \approx -\frac{g}{f_0} \bar{\theta}_y / \bar{\theta}$ , where  $\bar{\theta}$  is the mean potential temperature (see, e.g., Nakamura 1992). For both GCM and reanalyses data, strongly enhanced (reduced) baroclinicity is found in a region spanning from Alaska to northeastern Russia, during cold (warm) events. Straus and Shukla (1997) considered changes of almost the same variable during ENSO, based on data from GCM experiments and ECMWF reanalyses; their results are very similar to those shown above. Compared with the vertical wave activity shown in Fig. 6.6 and Fig. 6.7, high-latitude regions with stronger wave activity during cold events are also where baroclinicity is enhanced. Time series of the rms values of the 10-60-day filtered  $Z_{300}$ , averaged over  $170^\circ$ - $150^\circ$ W,  $45^\circ$ - $55^\circ$ N is plotted, together with the 700-mb wind shear over the same region, for GCM data in Fig.

6.9 (c). These time series are highly correlated, with correlation of 0.78. For reanalyses results shown in Fig. 6.9 (d), calculation is carried out based on the different domain of  $180^{\circ}$ - $160^{\circ}$ W,  $55^{\circ}$ - $65^{\circ}$ N, and the correlation is found to be 0.58. These results suggest a possible role played by baroclinicity of the mean flow in determining the *local* amount of intraseasonal activity.

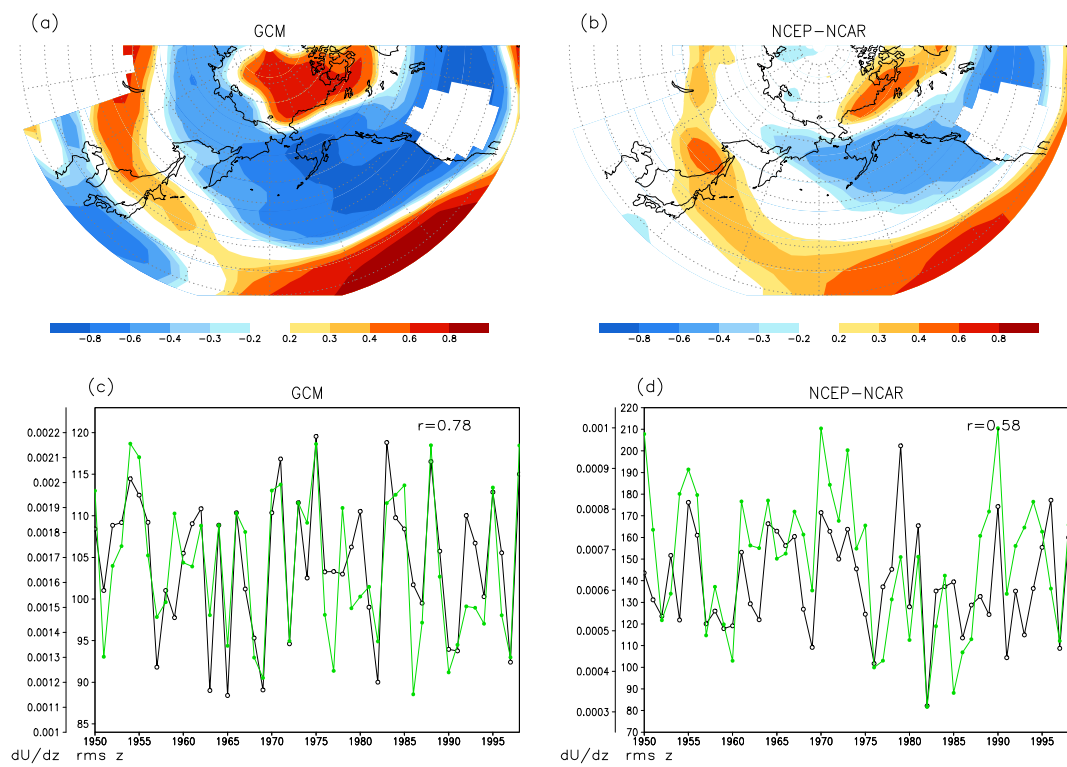


Figure 6.9: Correlation coefficients between 700-mb vertical shear of the zonal wind and the Niño-3 index, averaged over November to March, based on (a) GCM and (b) NCEP-NCAR data. Lower panels show the interannual variation of vertical wind shear (green, in  $s^{-1}$ ) and rms value of 10-60-day filtered  $Z_{300}$  (black, in m), area-averaged over the domain of  $170^{\circ}$ - $150^{\circ}$ W,  $45^{\circ}$ - $55^{\circ}$ N for (c) GCM, and over  $180^{\circ}$ - $160^{\circ}$ W,  $55^{\circ}$ - $65^{\circ}$ N for (d) NCEP-NCAR data.

### 6.3.2 Intraseasonal convection

In the last section, it is seen that during cold ENSO events, there is stronger wave activity from the subtropics, with wave sources more confined to the western Pacific, when extratropical perturbations are growing and become mature. Cold-minus-warm charts<sup>3</sup> of  $Z_{300}$  anomalies during their life cycle are plotted in Fig. 6.10 (together with anomalies during cold events), in order to accentuate differences from the cold to warm ENSO events. It is noteworthy that there are significant differences of cyclonic perturbations over the western Pacific. These anomalies based on the cold-to-warm difference are found to remain in the western to central subtropical ocean throughout the life cycle, reflecting the more stationary nature of the subtropical cyclone during cold events. In the extratropics, these difference maps attain maximum magnitudes over the Aleutians, northwestern North American seaboard and southeastern U.S.. Overall, they suggest the development of a wavetrain apparently forced from the western Pacific.

---

<sup>3</sup>Cold-minus-warm differences significant to the 95% level are shown. Levels of significance are estimated using a Monte Carlo method: two set of regression charts are computed, each as averages of those from nine distinct, randomly chosen years. The difference between these two sets constitutes a sample, and 100000 such samples are used for establishing significance levels.

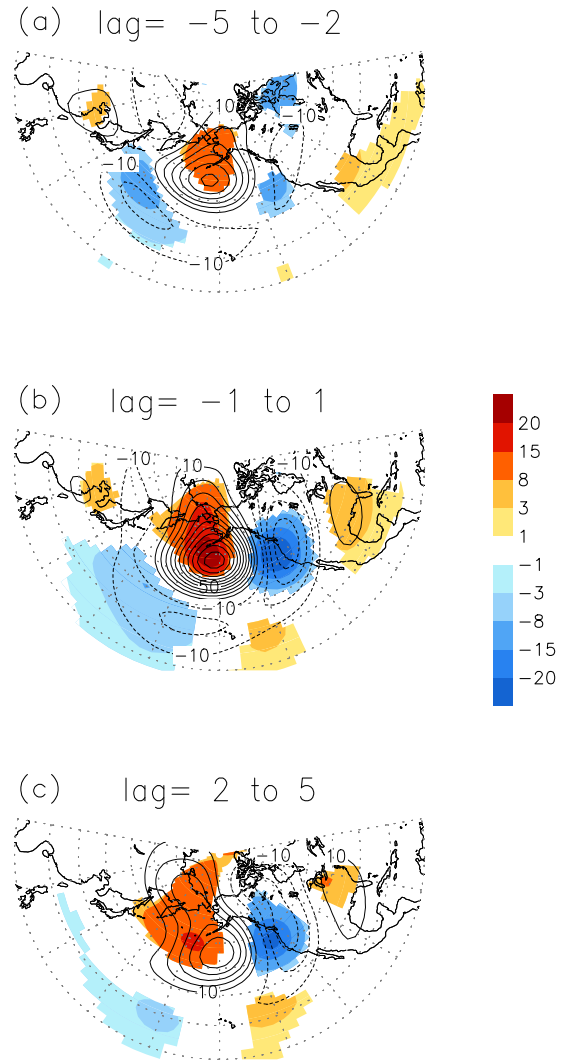


Figure 6.10: As in Fig. 6.3 but for cold-minus-warm anomalies (shading) and anomalies during cold events (contours). Cold-minus-warm values exceed 95% significance. Unit: m.

In the climatological situation, well defined signals of anomalous convection, very similar to those associated with the MJO, are found to precede and accompany development of low-frequency perturbations in the extratropics (see section 5.2.4). *It is hypothesized that the ENSO differences of anomalies shown in Fig. 6.10 are closely related to differences of these associated low-frequency tropical*

*convection.* To support such an idea, one seeks for evidence of different convection patterns and forcing, during different phases of ENSO. Consider first the Hovmoller diagrams of precipitation and 200-mb velocity potential anomalies, plotted in Fig. 6.11 (a) and (b) for warm and cold events, respectively. Anomalous fields are found based on the same lag regression method using the reference time series (footnote 1, section 6.2.2), and results are averaged over  $10^{\circ}\text{N}$ - $10^{\circ}\text{S}$ . The most obvious ENSO impact is that during warm events, convective anomalies are able to propagate more eastward than those during cold events. Such a difference of eastward extension is also reflected in velocity potential anomalies to a certain extent. It may be recalled that the MJO convection also exhibits different degree of extension during ENSO (see Ch. 3), similar to the results here. (The MJO extratropical response in different phases of ENSO is the subject of the next section.) The more stationary convection during cold events could provide a more stationary forcing in the western Pacific, thereby could be a factor leading to the difference of extratropical response as seen in Fig. 6.10.

Linearized Rossby wave source (RWS) is used to consider the vorticity balance of the quasi-stationary flow in the subtropics, as in section 5.2.4. One would expect, in general, that there is stronger RWS associated with stronger cyclonic flows. As a self-consistency check, anomalous RWS, streamfunction and divergent wind component at 300-mb level are shown in Fig. 6.12 (a) and (b), in the warm and cold ENSO phase respectively. Anomalies are averaged over the period of lag day -4 to day zero. Positive RWS perturbations south of Japan indeed have larger magnitudes during cold events, mainly due to the stronger convergence to its south. Stronger negative convection anomalies are also found there (about  $150^{\circ}\text{W}$ ,  $20^{\circ}\text{N}$ ; not shown), while during warm events convection is weaker and

extends eastward in the subtropical ocean. There are thus indications that the strength of the subtropical flow might be related to the variability of intraseasonal convection<sup>4</sup>.

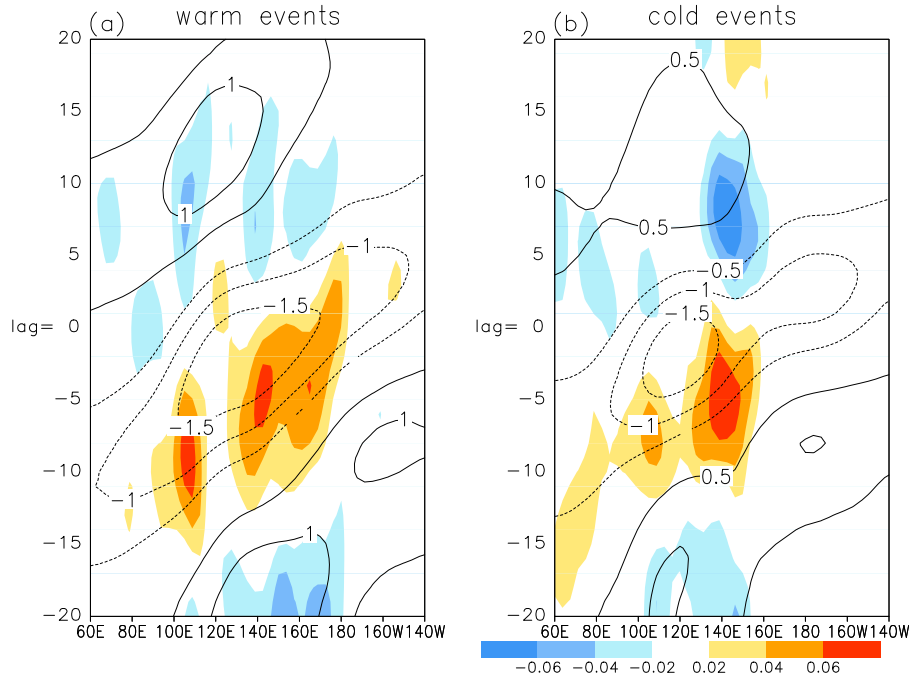


Figure 6.11: Hovmoller diagrams of anomalous precipitation (shading, in  $\text{cm day}^{-1}$ ) and 200-mb velocity potential (contour, in  $10^6 \text{ m}^2 \text{s}^{-1}$ ), averaged over  $10^\circ\text{N}$ - $10^\circ\text{S}$ , for (a) warm and (b) cold events. Values of the velocity potential field are significant to the 95% level. Calculations are based on GCM data.

Fig. 6.12 (c) and (d) show Hovmoller plots of the RWS and streamfunction anomalies, averaged over the latitudes of  $23^\circ$ - $33^\circ\text{N}$ . A stronger cyclone/anticyclone pair is found to sandwich the stronger RWS during cold events. Greater vorticity advection by rotational flow anomalies is therefore implied, and together with the RWS they are balanced by the negative vorticity tendency due to east-

<sup>4</sup>Strictly speaking, RWS in the subtropics (as opposed to the tropics), related to the divergence or divergent wind component, is not immediately associated with convection- see Held and Kang (1987) for their discussion. Comparison of the strength of RWS only serves as a hint of the association between intraseasonal convection and rotational circulation.

ward mean advection of the cyclone/anti-cyclone pair. During warm events the RWS is weaker, and associated with this, magnitudes of rotational anomalies are also found to be reduced.

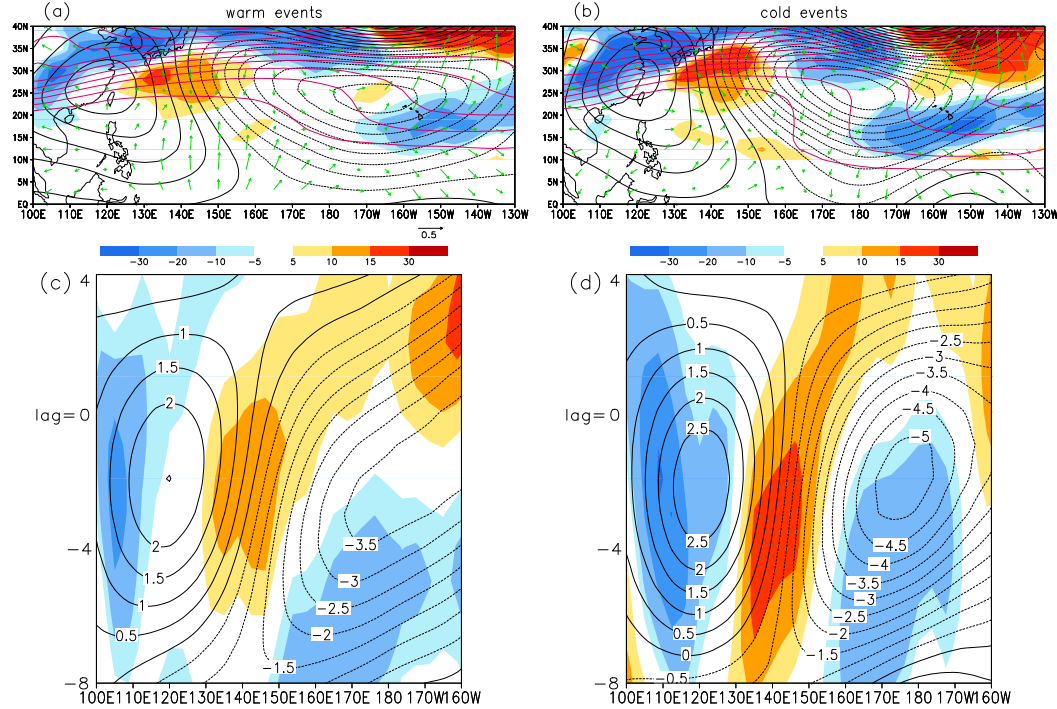


Figure 6.12: Linearized anomalous Rossby wave source (shading, in  $10^{-12}\text{s}^{-2}$ ), streamfunction (black contours, with intervals of  $0.5 \times 10^6\text{m}^2\text{s}^{-1}$ ) and divergent wind (magnitude in  $\text{ms}^{-1}$ ) at 300-mb level, during the lag days of -4 to 0, for (a) warm and (b) cold ENSO events. Rossby wave source south of  $10^\circ\text{N}$  is not shown. Mean absolute vorticity is also shown (magenta contours, starting from  $3 \times 10^{-5}\text{s}^{-1}$ , with  $10^{-5}\text{s}^{-1}$  intervals). Hovmöller diagrams showing Rossby wave source and streamfunction for (c) warm and (d) cold events, from lag day -8 to 4, with values averaged over  $23^\circ\text{-}33^\circ\text{N}$ . Shading information and contour intervals are the same as (a) and (b). Results are based on GCM data.

### 6.3.3 A brief summary

Consideration of energetics and E-vector analysis shed light on how low-frequency perturbations are influenced by ENSO. During cold events, eddies in the vicinity

of the Pacific jet exit are stronger, where greater deceleration of the zonal wind is also found. Together they lead to greater conversion of mean to eddy kinetic energy. On the other hand, there are indications that the baroclinicity of the mean state can also affect the growth of perturbations, especially in high-latitude regions. A possible connection between tropical and extratropical variability is also suggested. Intraseasonal convection behaves differently in different ENSO phases; the resulting different location and amplitudes of tropical forcing might lead to different extratropical responses. Changes of the recurrent low-frequency patterns during ENSO seem to support this idea.

In the next section, extratropical disturbances related to the MJO, WTP and their interaction during ENSO will be considered. As shown in the previous chapter, recurrent low-frequency patterns project well onto these two distinct modes of variability. Studying the impact of ENSO on their behavior is of interest in itself, and would also complement earlier results.

## **6.4 Effects of ENSO on Circulation Anomalies due to changes in the MJO and WTP**

### **6.4.1 MJO and WTP activity**

By examining the impact of ENSO on low-frequency perturbations in the extratropics, there appears to be a link to the variability of intraseasonal convection. One natural question to ask is: how is the MJO, and especially its extratropical response, affected by ENSO? This will be addressed presently. One might also ask the same question concerning the WTP. This section is concerned with the

impact of ENSO on these modes of variability and their related disturbances.

Composite charts of  $Z_{300}$  are shown in Fig. 6.13, in different phases of the MJO during warm and cold ENSO events. In phase 7, patterns of anomalies resemble a developing wavetrain, with a subtropical trough, a growing ridge and another downstream trough in higher latitudes. However, during cold ENSO years the ridge is much stronger, and the subtropical trough extends more to the western part of the ocean. The rather big difference of amplitudes of the ridge, comparing warm to cold events, might be related to its position relative to the jet exit in this phase. Based on numerical experiments using a barotropic model, Naoe et al. (1997) showed that Rossby waves tend to become stationary and grow near jet exit regions. In fact, stronger magnitudes are found in the next MJO phase, when anomalies are also closer to the exit of the Pacific jet. (Recall that the jet extends more eastward during El Niño events.)

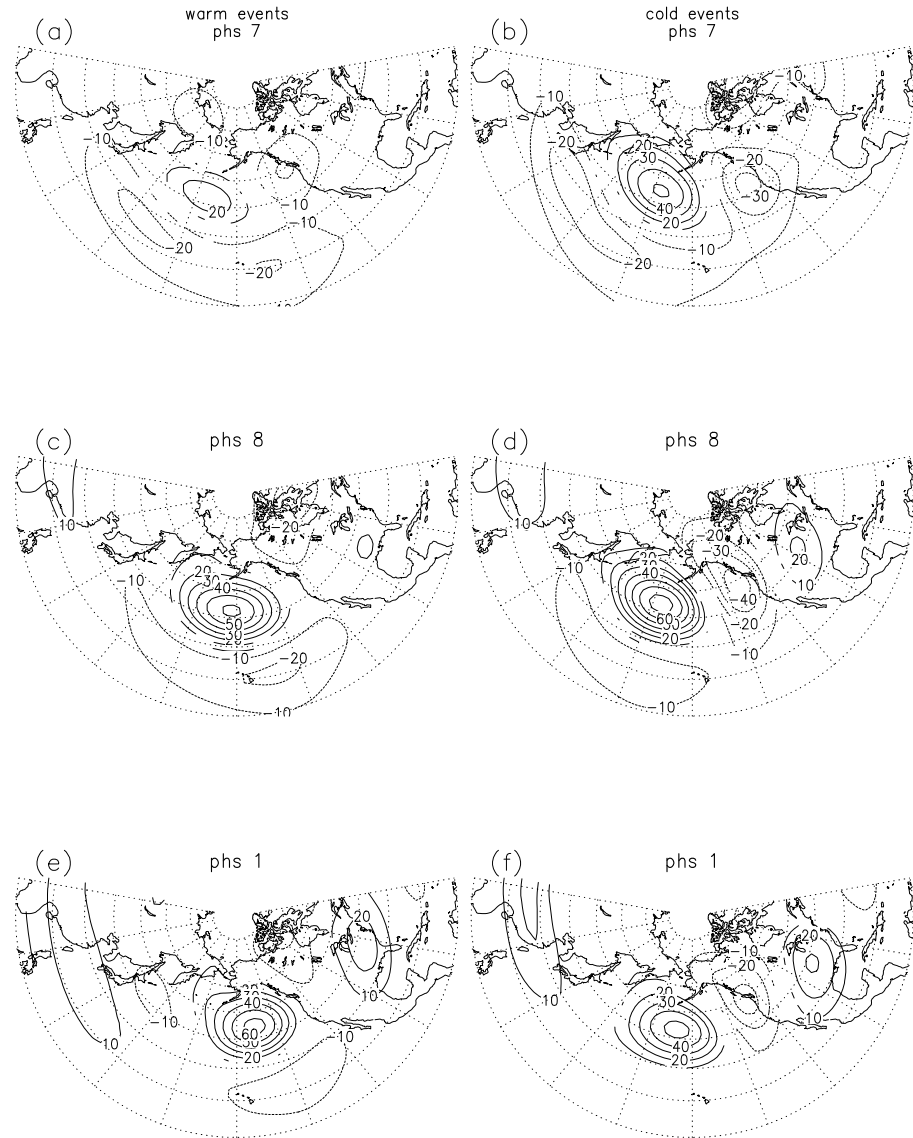


Figure 6.13: Composite 300-mb height anomalies for the MJO in phase 7, 8 and 1 for warm [(a), (c) and (e)] and cold events [(b), (d) and (f)], in the left and right panels, respectively. Values (in m) exceed the 95% significance level. Results are based on GCM data.

In the next phase, it can be seen that ENSO has some obvious impact on the pattern of perturbations. During cold events, part of the wavetrain pattern remains almost unchanged from the last MJO phase, while there is prominent

development over the northwestern North American seaboard. It is remarkable that this pattern looks very similar to the cold-minus-warm circulation anomalies shown in Fig. 6.10 (b), suggesting a projection of the latter onto the MJO perturbations. During warm events the situation is different, in which strong cyclonic anomalies are found in the subtropical eastern Pacific. This is reminiscent of the recurrent perturbations during warm events, with dispersion from the ridge southeastward into the eastern subtropical ocean (see Fig. 6.3). Downstream of the ridge in the extratropics, an adjacent trough is found over northern Canada; this is again different from the situation during cold events. It is also noticed that the North Pacific ridge has its maximum located about  $20^\circ$  east of its cold ENSO counterpart. Such a displacement might have an impact on the dispersion of Rossby waves related to ENSO.

To relate dispersion characteristics with the structure of the time mean flow, the total wavenumber  $K_s$  is found, based on the mean 300-mb zonal wind  $U$  during warm and cold events. Given by the expression  $\sqrt{(\beta - U_{yy})/U}$  (standard meteorological convention),  $K_s$  represents the local wavenumber of stationary Rossby waves. Hoskins and Ambrizzi (1993) showed that  $K_s$  can be also treated as a refractive index, in the sense that waves are refracted toward regions with higher values. Jet streams tend to produce local maxima of  $K_s$  in their vicinity, thus serving as wave guides for Rossby waves.

Both  $K_s$  and centers of action of geopotential anomalies in phase 8 of the MJO cycle are shown in Fig. 6.14. These centers indicates approximate locations of the North Pacific ridge and anomalies to its east (see Fig. 6.13). The approximate position of the jet stream, indicated by regions with strong zonal wind, is also shown. During both warm and cold ENSO episodes,  $K_s$  is largest at about the jet

core with decreasing values as one moves poleward or equatorward. Interestingly during cold events,  $K_s$  is found to decrease rapidly and even acquires imaginary values southward on the subtropical side of the jet. On the other hand during warm events, the rate of decrease of  $K_s$  is smaller for this subtropical region. Because of less refraction and hence less effective trapping, the wave guide could become more leaky on this side of the jet.

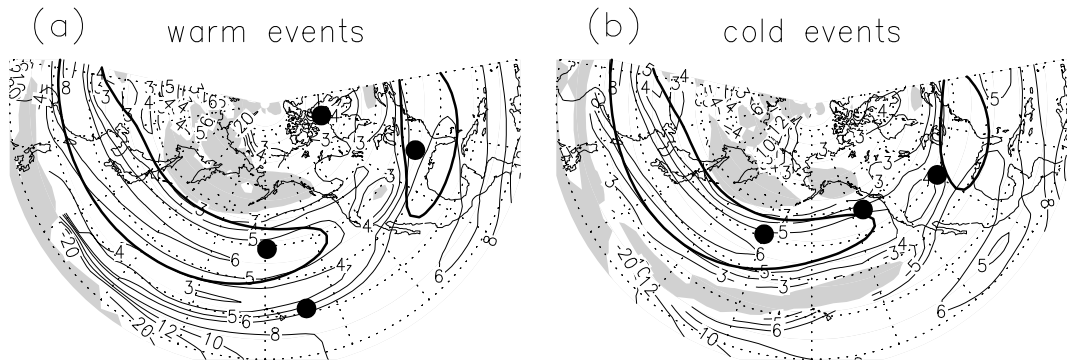


Figure 6.14: Total wavenumber  $K_s$  (contours for values of 3, 4, 5, 6, 8, 10, 12, 20; gray shading for imaginary values), based on 300-mb mean zonal flow during (a) warm and (b) cold events. Black dots denote approximate centers of action from  $Z_{300}$  composite anomalies of the MJO at phase 8, (see middle panels of Fig. 6.13). Thick contours represent regions with the mean zonal wind greater than  $30\text{ms}^{-1}$ . Results are based on GCM data.

This difference of  $K_s$  can be further related to changes of the mean wind during ENSO. During warm events, the Pacific jet is enhanced over the subtropical central-eastern Pacific (see again Fig. 6.8), while meridional gradient of relative vorticity (or  $-U_{yy}$ , not shown) is also larger at about  $25^\circ\text{N}$ , leading to larger  $K_s$  there. On the other hand  $K_s$  becomes smaller or even attains imaginary values during cold events, because of the weaker zonal wind in the same region.

Consistent with the idea that the wave guide becomes more leaky over the

subtropical eastern Pacific during warm events, dispersion from the ridge (its center denoted by the dot at about  $160^{\circ}\text{W}$ ) is directed more to the southeast. It should also be pointed out that the ridge center is rather close to end of the jet, which could be another factor leading to less trapping of waves. During cold events, on the other hand, the ridge is located at about the dateline. 'Deep' within the waveguide, trapping of Rossby waves seems more effective. In fact the adjacent trough lies immediately to its east within the jet stream, very different from the situation during warm events.

Many of these differences between MJO perturbations during warm and cold events are similar to those shown in Fig. 6.10, concerning North Pacific recurrent low-frequency patterns. These similarities include, during cold compared with warm events, the fact that (i) the subtropical cyclone is more confined within the western Pacific during the development of the extratropical wavetrain, and remains rather stationary thereafter; (ii) the ridge over the North Pacific is stronger, and that (iii) dispersion downstream of the ridge is directed more toward the west coast of U.S..

As shown in Ch. 4, there is more eastward extension of the MJO convection during warm events, while precipitation anomalies tend to be confined to the far western Pacific near New Guinea with stronger magnitudes during cold events. As expected, these differences of convection are also consistent with the MJO extratropical response just considered. To help relating MJO convection patterns with circulation anomalies, precipitation at phase 7 of the MJO are shown again in Fig. 6.15 (same as those in Fig. 4.8), together with the contemporaneous streamfunction anomalies at 300 mb. The aforementioned difference of eastward extension of anomalies is clearly seen. At the next phase (see Fig. 4.8), anomalous

precipitation remains within the western Pacific and is relatively more intense during cold events, while it continues to extend and develops further eastward to about the dateline during warm events. Streamfunction perturbations are also stronger, comparing the cold to warm ENSO phase, over the western Pacific and with less extension eastward, consistent with the difference of intraseasonal convection.

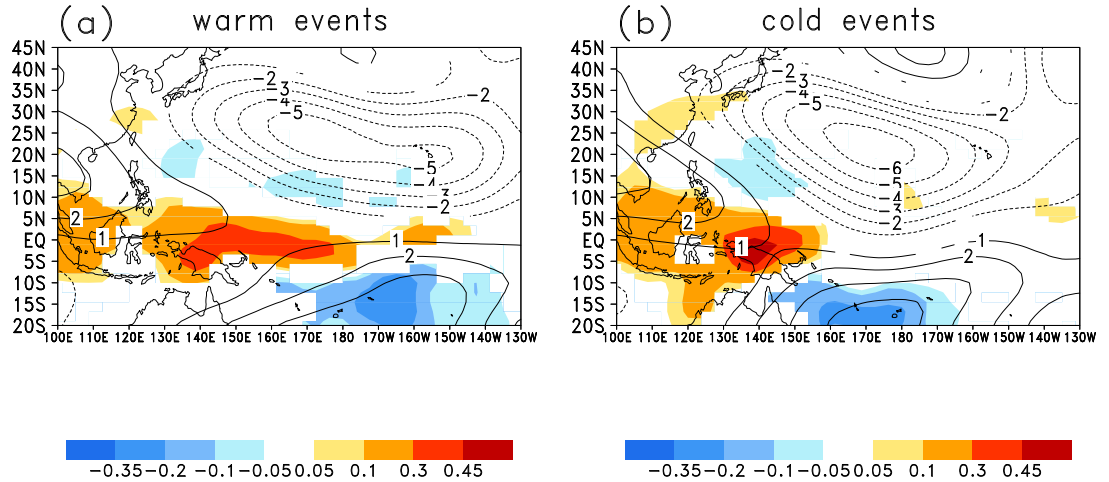


Figure 6.15: MJO composite maps of precipitation (shading, in unit of  $\text{cm day}^{-1}$ ) and 300-mb streamfunction anomalies (contours, in unit of  $10^6 \text{ m}^2 \text{s}^{-1}$ ) at phase 7, during (a) warm and (b) cold events. All fields exceed 95% significance level.

The ENSO influence on the WTP is also examined. Composite maps of the  $Z_{300}$  field at phase 8 of the WTP are shown in Fig. 6.16. Perturbation amplitudes are found to be greater comparing cold to warm events, in the high-latitude region from northeast Asia to northern Canada. In contrast to the MJO, however, patterns of perturbations in the warm and cold ENSO phase are rather alike. Comparison of patterns from CEOF analyses, carried out separately based on warm and cold ENSO data (not shown), confirms the impression that WTP

circulation features are very similar during the two different ENSO phases.

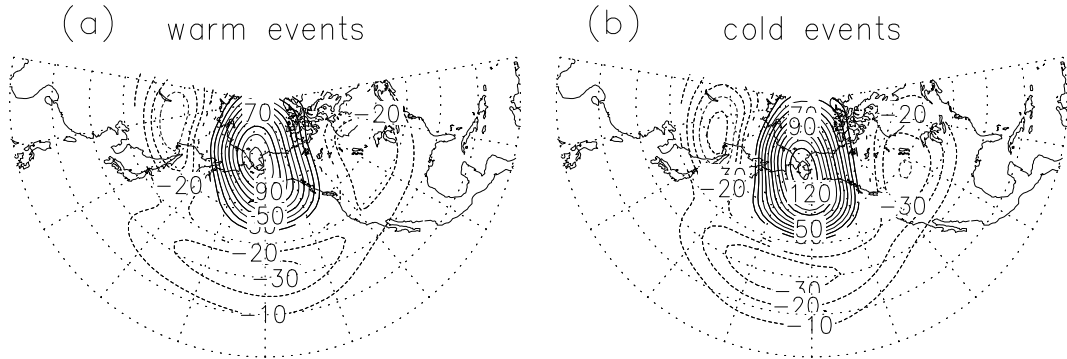


Figure 6.16: As in Fig. 6.13 but for WTP at phase 8 for (a) warm and (b) cold events.

Based on the similarity of low-frequency perturbations with circulation anomalies related to the MJO and WTP, one expects that their low-level features would also be affected by ENSO. Fig. 6.17 shows MJO and WTP composite maps of the anomalous temperature, geopotential height as well as pressure velocity at 700 mb, in their respective phase 8 during warm and cold events. For the MJO, warm anomalies west of the low-level ridge indicate a westward tilt in the vertical, and this tilt is slightly stronger in the cold than warm ENSO phase. Also, stronger temperature perturbations are found over a broad region around Alaska. Circulation anomalies there also have a rather baroclinic nature; for instance, geostrophic wind anomalies near Gulf of Alaska are advecting cold perturbations southeastward. Stronger temperature perturbations could be related with stronger meridional temperature gradient (or stronger vertical wind shear) in the region during cold events (see Fig. 6.9). Such a baroclinic configuration of variables is not obvious in high-latitude regions during warm events.

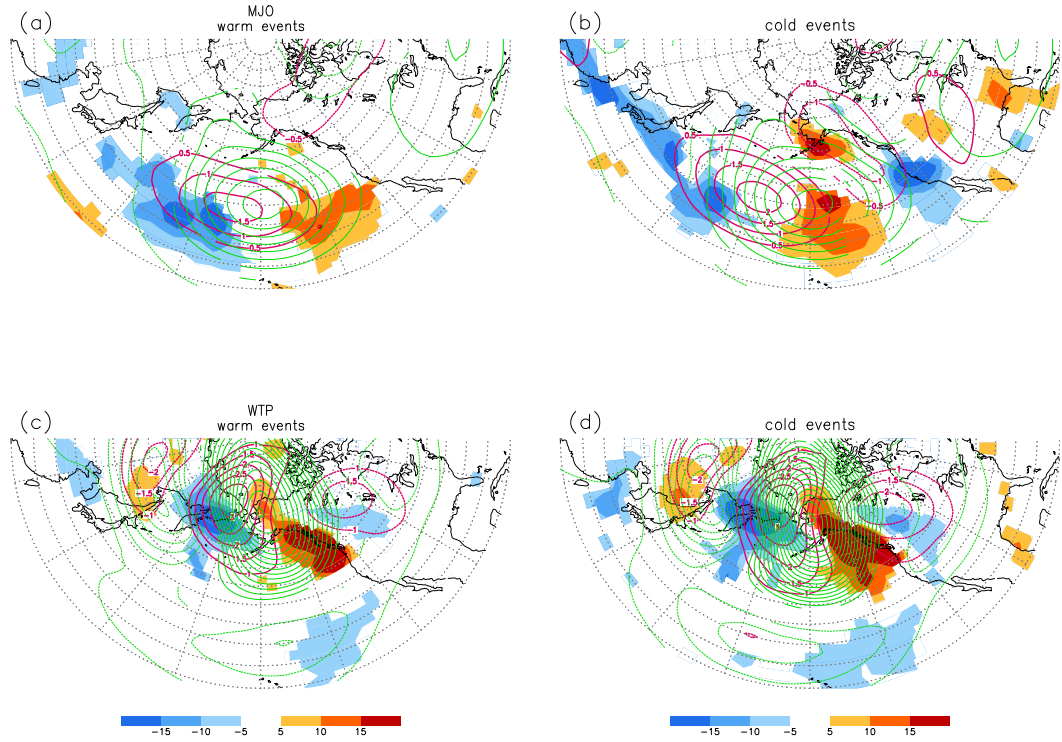


Figure 6.17: As in middle panels of Fig. 6.5, but for MJO [(a) and (b)] and WTP [(c) and (d)] at phase 8 of their cycle. Contouring for the temperature field starts with  $\pm 0.5^{\circ}\text{C}$  for (a) and (b), and  $\pm 1^{\circ}\text{C}$  for (c) and (d). All fields exceed 95% significance level.

For WTP anomalies during the cold ENSO phase, the low-level ridge provides stronger northeasterly flow in northwestern part of North America, leading to greater temperature anomalies. Again the stronger baroclinicity of the basic state could play a role in enhancing the amplitudes of disturbances. Similar to upper-level perturbations, these variables in low levels exhibit changes of their amplitudes but with little change of their structure during ENSO.

E-vector analyses and computation of barotropic conversion (not shown) for the MJO and WTP cycles are also carried out. Results are similar to those depicted in Fig. 6.8. During cold events, zonal wind perturbations of both the

MJO and WTP have large amplitudes near the Pacific jet exit, and together with the larger deceleration of the jet these factors lead to stronger barotropic conversion of mean to eddy kinetic energy.

Both MJO and WTP perturbations in the extratropics are found to be affected by ENSO in various ways. While those of the WTP exhibit a general increase of amplitudes but otherwise little modification of their patterns, the MJO wavetrain is modified in terms of both its magnitudes and its pattern. Compared with recurrent low-frequency circulation, both MJO and WTP perturbations share with the former some similar impact due to ENSO- most noticeably their enhanced amplitudes as well as more pronounced baroclinic signatures in high latitudes. There is also a remarkable resemblance between changes of the MJO wavetrain and the recurrent anomalies. Again, ENSO-induced variability of intraseasonal convection seems to have an impact on the MJO extratropical response as well. Such apparently strong projection of the ENSO modulation onto the MJO-related circulation pattern highlights a rather interesting role of the MJO on the low-frequency variability in the extratropics.

#### **6.4.2 MJO-WTP interaction**

In Ch. 5, it is shown that perturbations due to the MJO-WTP interaction resemble the low-frequency circulation anomalies recurrent over the North Pacific. These perturbations can be understood as the result of both the MJO and WTP events being present, with their respective anomalies interfering constructively in a linear sense. How such an MJO-WTP interaction is affected by ENSO will be considered briefly, mainly serving to demonstrate how ENSO influences on the

MJO and WTP separately can be added together in a combined manner.

$Z_{300}$  anomalies for MJO-WTP events in phase (8,8) are shown in Fig. 6.18. Composite anomalies are computed based on the criteria that both MJO and WTP events happen simultaneously, for a particular combination of their phases (see section 5.3.2 of the previous chapter for details). The most obvious impact of ENSO is that, during cold events, the ridge over the North Pacific is found to be much stronger, with a difference of about 60m in magnitude between the two ENSO phases. This is due to enhanced amplitudes of both WTP and the MJO wavetrain (see Fig. 6.13 and Fig. 6.16), which also interfere constructively for this particular combination of phase. The ridge maximum is also slightly displaced westward, consistent with different patterns of MJO extratropical response discussed earlier. During warm events, prominent troughs downstream of the North Pacific ridge are found over northern Canada and the subtropical eastern Pacific; again this is consistent with the difference of MJO wavetrains in different ENSO phases (Fig. 6.13).

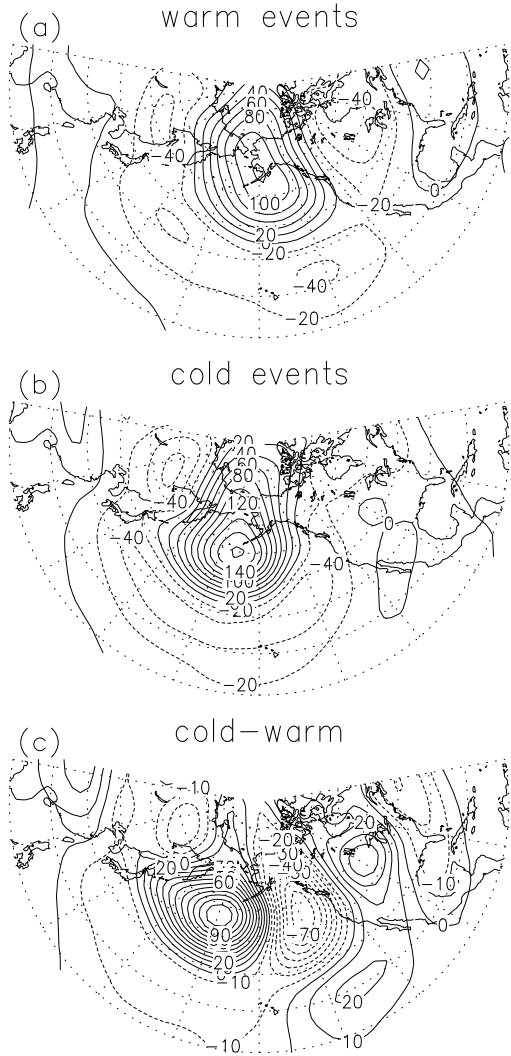


Figure 6.18: MJO-WTP phase (8,8) composite anomalies of 300-mb anomalous height for (a) warm and (b) cold ENSO events. Cold-minus-warm difference is shown in (c). Calculations based on GCM data. Unit: m

Fig. 6.18 (c) shows the cold-minus-warm difference of the two patterns; this should be compared Fig. 6.10 (b), and in fact there is much similarity between these two. For instance, a ridge is located over the North Pacific near the dateline, and a trough is found to its east bordering the northwestern American coast. It is noteworthy that, even though perturbations have considerable amplitudes in

high latitudes (say north of  $50^{\circ}\text{N}$ ) for each composite maps during warm and cold events, their difference has less magnitudes in these regions. This is consistent with the fact that WTP anomalies exhibit less change of their pattern; one would expect their cold-to-warm difference to have some cancellation. Overall it is seen that earlier results concerning the MJO and WTP are combined in a composite sense, and the effect of ENSO on the MJO-WTP interaction agrees reasonably with that on the recurrent circulation patterns.

## 6.5 Discussion

Results of Palmer (1988) suggest that during cold ENSO events, the basic state becomes more unstable in the barotropic sense, resulting in stronger low-frequency activity compared with the warm ENSO situation. The more recent study of Naoe et al. (1997), again using a barotropic model, suggests that stagnation and subsequent growth of waves in jet exit regions might be more relevant processes than simple modal growth of perturbations associated with barotropic instabilities. In any case both Palmer and Naoe et al. (though the latter researchers did not directly address the ENSO problem) highlighted the importance of the structure of mean barotropic flow on determining low-frequency variability. Consistent with this idea, consideration of local energetics indicates stronger barotropic conversion from the mean to eddy kinetic energy over the North Pacific during cold events. In fact,  $\partial U / \partial x$  is more negative at the jet exit during cold events, such that the conversion would be stronger even for the same eddy amplitudes. There are also indications that *local* baroclinicity of the basic state could influence the amount of activity. This seems to be in line with suggestions of Frederiksen

(1983) that the evolution of blocking flows is closely related to instabilities of the three-dimensional time mean flow. In view of the strong baroclinic signature of low-frequency eddies during their development, the effect of changes of the full three-dimensional basic state during ENSO certainly requires more attention.

It should be mentioned that the role of the variability of storm tracks during ENSO is not considered here. However, based on the climatological consideration in the previous chapter (see section 5.2.3), forcing by synoptic-scale eddies is in fact quite modest. In any case, the possibility that changes of blocking activity are related to modified storm tracks during ENSO, as proposed by Chen and van den Dool (1997), is not ruled out. Notice that intraseasonal activity considered here is not identical to blocking flows, which was shown to be greatly affected by high-frequency eddies by Nakamura et al. (1997), at least for strong blocking events. Some detailed analyses are required in order to discern their role in blocking variability related to ENSO.

Also interesting is that anomalous intraseasonal convection during ENSO could have an effect on low-frequency variability in the extratropics. GCM results indicate that there are different tropical forcing and associated extratropical anomalies in the intraseasonal time scales, during ENSO. However, since changes of the basic state and those of the tropical forcing happen at the same time, their relative importance on extratropical low-frequency variability cannot be easily answered by the diagnostic tools used in this study. To address this issue, some simple numerical experiments are suggested as possible future works: barotropic or baroclinic models (as in Ting and Sardeshmukh 1993) can be used, using the mean flow during different ENSO events as basic states and using different MJO forcing (vorticity source or diabatic heating) patterns, in order to investigate the

impact due to changes of either (or both) of these mean flow and forcing components on extratropical low-frequency activity. Given the sensitivity of this type of experiment to the choice of the background flow, results using the GCM mean state and those based on observations should also be compared.

## 6.6 Conclusion

The impact of ENSO on the amplitude and the life cycle of low-frequency circulation anomalies over the North Pacific sector has been examined. Based on GCM and NCEP-NCAR data, it is found that intraseasonal activity is enhanced over a large region in the North Pacific during cold compared to warm ENSO events. This is consistent with a number of previous studies concerning changes of blocking frequencies and intraseasonal activity during ENSO. Downstream from anomalies over the northern ocean, there are also different patterns of Rossby wave dispersion over North America in different phases of ENSO.

Local energetics reveals stronger barotropic conversion from the mean to eddy kinetic energy during cold ENSO episodes, and this can be at least partially attributed to the stronger deceleration of the Pacific jet. There are also indications that the baroclinicity of the basic state might play a role in determining intraseasonal variability locally, especially in high-latitude regions.

During different phases of ENSO, there are different patterns of tropical intraseasonal convection, the latter being a prominent precursor of recurrent extratropical low-frequency anomalies. While changes of the local basic state must have a substantial influence on extratropical variability, it is suggested that changes of low-frequency tropical forcing might also play a role. In fact, both GCM and, to

a lesser extent, NCEP-NCAR reanalyses data, show stronger wave activity coming from the subtropical western Pacific during the initial growth of extratropical perturbations in cold ENSO events. Based on GCM data, differences of wavetrain patterns are consistent with those of intraseasonal convection and Rossby wave sources during ENSO.

Based on the GCM dataset, both WTP and the MJO-related extratropical circulation are also found to be affected by ENSO. In general, their magnitudes are enhanced during cold events. Changes of the three-dimensional basic state seems to govern both MJO and WTP characteristics, similar to the case of recurrent low-frequency anomalies. However, the WTP experience little change of their spatial structure, while the MJO extratropical response is greatly attenuated during ENSO. Wavetrain patterns related to the latter are sensitive to the ENSO cycle, with those during cold events being more stationary with more prominent dispersion from the North Pacific ridge to the west coast of U.S.. On the other hand during warm events, there is an obvious split of waves downstream of the ridge, with dispersion directed southeast into the subtropics and northeast to northern Canada. Differences of both the waveguide nature of the Pacific jet and the position of the ridge relative to the jet seem to be responsible for the change of the dispersion characteristics of waves. Many of the ENSO differences of recurrent low-frequency anomalies are found to project strongly on these changes of the MJO wavetrain patterns.

# Chapter 7

## Variability of Synoptic-scale Activity in the Tropics

### 7.1 Introduction

#### 7.1.1 Synoptic-scale disturbances

Tropical synoptic-scale disturbances have interested meteorologists for decades. Riehl (1945) first referred to the disturbances over the Caribbean as ‘easterly waves’. Summertime synoptic-scale waves over various ocean basins have long been believed to be associated with the formation of tropical cyclones (see Wallace 1971). From the late 1960’s, objective analyses (such as spectral and composite methods) were used in a number of studies, concerned with activity over the western Pacific and in the western Africa/Atlantic region (Wallace and Chang 1969; Chang and Wallace 1970; Reed and Recker 1971; Burpee 1972, 1974.)

Based on the above studies, wave characteristics and the structure of disturbances are summarized as follows. Having a wavelength of about 2000 to 4000km,

these perturbations are westward propagating with a period of 4-5 days over the western Pacific (3-4 days in western Africa/Atlantic). Inferred from the variance of the meridional wind, largest amplitudes are found in the lower troposphere at about 850 mb (700 mb for African waves). Horizontal northeast-southwest tilt of the low-level  $v$ -wind is also found for waves over some active regions. Their vertical structure however varies from place to place. Within lower to middle troposphere, an eastward tilt with height is found over the Atlantic, while the structure evolves from being slightly tilted eastward east of the central Pacific, to having little tilt in the western Pacific. Variation of the vertical structure with longitudes can be ascribed to the different vertical wind shear of the mean zonal flow. This argument is supported by the numerical study of Holton (1971), who examined the effect of wind shear on the circulation response to imposed heating in the tropics.

Lau and Lau (90, 92; referred to as LL90 and LL92 respectively), based on 1980-87 ECMWF gridded data, carried out comprehensive studies of the behavior of synoptic-scale disturbances, as well as dynamical processes associated with the propagation and maintenance of activity. The main feature in LL90 and LL92 is the use of low-level vorticity as the key variable for various statistical and composite methods, from which wave characteristics and fluctuations of meteorological variables are obtained. Enhanced activity, associated with coherent wave-like propagating disturbances, is identified in western Africa/Atlantic, the eastern Pacific, the western Pacific and Bay of Bengal/India. Prominent spectral peaks within the period range of 3 to 8 days are found. There is westward to northwestward propagation in all these regions, accompanied by strong growth (decay) over the eastern (western) portion of the 'storm tracks'. Within the west-

ern Pacific, disturbances are found to have a wavelength of  $\sim 2500\text{-}2800\text{km}$ , and propagation speed of about  $5\text{ms}^{-1}$ .

Based on analyses of the vorticity balance of disturbances, LL92 found that wave propagation can be primarily attributed to the advection of vorticity by the mean flow and by transient motion. Over the western Pacific, there is barotropic conversion from the mean to eddy kinetic energy. This happens where mean eastlies are increasing poleward ( $\partial\bar{u}/\partial y < 0$ ) and where a northeast-southwest wave tilt is found such that  $\overline{u'v'} > 0$ . There is large conversion from eddy available potential energy, especially in the northwestern portion of paths of disturbances, indicating that diabatic heating, through the generation of eddy available potential energy, is an important energy source for synoptic-scale activity in the region.

### 7.1.2 Relationship with equatorial waves

Much research effort has been devoted to identify equatorial perturbations in the atmosphere with theoretical wave solutions given by Matsuno (1966) and Lindzen (1967). Unlike disturbances previously discussed, these equatorial waves are trapped along the equator. Takayabu (1994) and more recently Wheeler and Kiladis (1999) demonstrated the existence of equatorial waves which are also coupled with convection.

Of particular interest are low-level mixed Rossby gravity (MRG) waves identified by Liebmann and Hendon (1990), which are most active during late boreal summer to fall. Synoptic-scale circulation anomalies over the equatorial central Pacific are found to resemble the theoretical solutions for the MRG wave mode.

These disturbances are westward propagating, and have periods of 3-5 days and wavelength in the range of 3500 to 8000km. Longest waves are found in the vicinity of the central Pacific. Based on the dispersion relation  $\omega = kc[\frac{1}{2} - \frac{1}{2}(1 + \frac{4\beta}{k^2 c})^{1/2}]$ , where  $c = \sqrt{gh_e}$  and  $h_e$  is the equivalent depth (see Holton 1992), it is found that over the central Pacific values of  $h_e$  lie within the range of  $\sim 5$  to 50m. Over the western Pacific, values are larger and for some locations there is no solution for  $h_e$ , suggesting that disturbances there do not always look like MRG waves.

MRG waves during northern summer are studied by Takayabu and Nitta (1993), and they are compared with ‘TD-type’ disturbances over the western Pacific- a designation used to distinguish synoptic-scale perturbations off the equator from equatorial MRG waves. It is found that while the MRG waves are longest at about the dateline, perturbation scales become shorter further west in the western Pacific. Inspection of circulation patterns over the western Pacific reveals that the waves in the region are less equatorially trapped and become more like TD-type perturbations. Their vertical structure also becomes deeper in western longitudes, resembling more the TD-type. Dunkerton and Baldwin (1995) reported very similar findings, and noticed a transition between the two wave types at about 160°E. The case study of Dickinson and Molinari (2002) also provides evidence that 6-10-day MRG waves over the western Pacific could transform into TD-type disturbances. These perturbations seem to affect cyclogenesis in the region.

### 7.1.3 Wave accumulation theory

Adopting the ideas of Webster and Chang (1988) and Chang and Webster (1990), Holland (1995) proposed that the low-level confluent flow over the western Pacific could be effective in the trapping of wave energy. It is argued that *westward* dispersion of equatorial waves could be slowed down or even stalled while entering the western Pacific, resulting in amplification of waves. At the heart of this argument is the existence of waves with group propagation directed toward the region of confluence. Short waves, because of their small intrinsic or flow-relative group speed, would have their group velocity mainly following the ambient flow, therefore pointing toward the confluent zone. Moreover, based on simple ray tracing argument, these waves will be shortened as they enter the region, making outward energy transfer more difficult.

These ideas were followed up by Sobel and Bretherton (1999, hereinafter referred to as SB99). Arguing that barotropic dynamics is applicable at least over a portion of the storm tracks, formulation of Plumb (1986) is used to estimate wave activity and also the local values of group velocity over the western Pacific. The group velocity can be written as  $\mathbf{c}_g = \bar{\mathbf{u}} + (\mathbf{c}_g)_{\text{int}}$ , where  $\bar{\mathbf{u}}$  is the mean flow and  $(\mathbf{c}_g)_{\text{int}}$  is the intrinsic group velocity, the latter being determined by eddy statistics. They found that  $(\mathbf{c}_g)_{\text{int}}$  is small compared with  $\bar{\mathbf{u}}$ . SB99 attributed this to the short length scales of synoptic-scale disturbances. If convergence of  $\mathbf{c}_g$  can be regarded as the growth rate based on this wave-activity accumulation theory, then convergence of the background flow itself would provide a mechanism for the amplification of activity within the western Pacific.

#### **7.1.4 Previous studies on the impact of ENSO**

It is well known that during El Niño events, cyclogenesis over the western Pacific takes place more eastward compared with that during La Niña events (see, e.g., Lander 1994; Wang and Chen 2002). There are also indications of a similar eastward shift of synoptic-scale activity in the warm ENSO phase. Gu and Zhang (2001) provided evidence of increased (decreased) amount of westward propagating synoptic-scale convective activity over the western-central Pacific, during northern summer of warm (cold) events. Sobel and Maloney (2000) attributed such variability of disturbances to the difference of accumulation of wave activity, primarily due to changes of the low-level circulation during ENSO.

Takayabu and Nitta (1993) reported that during a warm ENSO event, near-equatorial disturbances over the western Pacific resemble more the TD-type perturbations, while during cold events they become more like MRG waves *in the same longitudes*. The earlier study of Chang and Miller (1977) also showed that vertical structure of waves is sensitive to the phase of the ENSO cycle. In other words, ENSO also affects the selection of the dominate wave type. Factors such as changes of the vertical wind shear during ENSO could be responsible for the different wave structures at the same geographical locations.

The main objective of this chapter is to study the variability of synoptic-scale disturbances, with special attention to that over the western Pacific, and its modulation due to ENSO. To this end, reanalyses data and GCM outputs will be used. While assessing the realism of activity from simulations, various diagnostic tools will be introduced. They are also used for examining the impact of ENSO on the magnitudes, propagation, wavelengths and dispersion of eddies. Their relationship with the change of the mean flow during ENSO will be studied.

## **7.2 Climatological Behavior**

### **7.2.1 Amplitudes, propagation and growth rates of wave-like disturbances**

LL90 shows that rms of vorticity at 850 mb can provide information on the amplitudes of synoptic-scale activity in the tropics. Rms charts of vorticity based on both NCEP-NCAR and GCM data are plotted in Fig. 7.1, for the extended summer season of May to September. In this section, NCEP-NCAR reanalyses from 1979 to 1999 are used for studying the climatological behavior of disturbances. The vorticity variable is bandpass-filtered to retain fluctuations with periods from 2 to 15 days. Spectral peaks of vorticity in various active regions are known to fall within this frequency range (see LL90). In the same figure, climatological mean 850-mb flow in the same season is depicted by streamlines.

Both reanalyses and GCM results indicate strong activity located in the region of western Africa/Atlantic, eastern Pacific, western Pacific and Bay of Bengal/India. These are well-known regions with enhanced variability, much of which associated with wave-like disturbances. Reanalyses results here give a geographical distribution very similar to the rms map shown in LL90.

As inferred from the reanalyses data, activity over the western Pacific has large amplitudes east of the Philippines extending southeastward. In particular, strong activity is approximately located where westerlies and easterlies meet. It is interesting that there is a broad region in the subtropical central Pacific where disturbances are rather weak, even though large amplitudes tend to lie in the latitude band of 10°-25°N in all active regions.

The behavior of synoptic-scale variability from the GCM is similar to ob-

servations, except for the following noticeable differences. First, eddies from simulations are too strong. The rms values from GCM are almost twice of their reanalyses counterpart. Over the eastern Pacific, large amplitudes are located more to the east near Mexico. It can be seen that GCM results also show the dual maxima of activity in Asia. However, the maximum to the west is located in Indochina instead of over the Bay of Bengal as found in observations. Over the western Pacific, large perturbation amplitudes are distributed rather zonally, covering much of the western part of the ocean and reaching the central Pacific. Strongest disturbances are also displaced  $\sim 10^\circ$  eastward compared with observations. This might be related to the fact that the simulated monsoon westerlies are too strong and protruding more eastward, compared with observations.

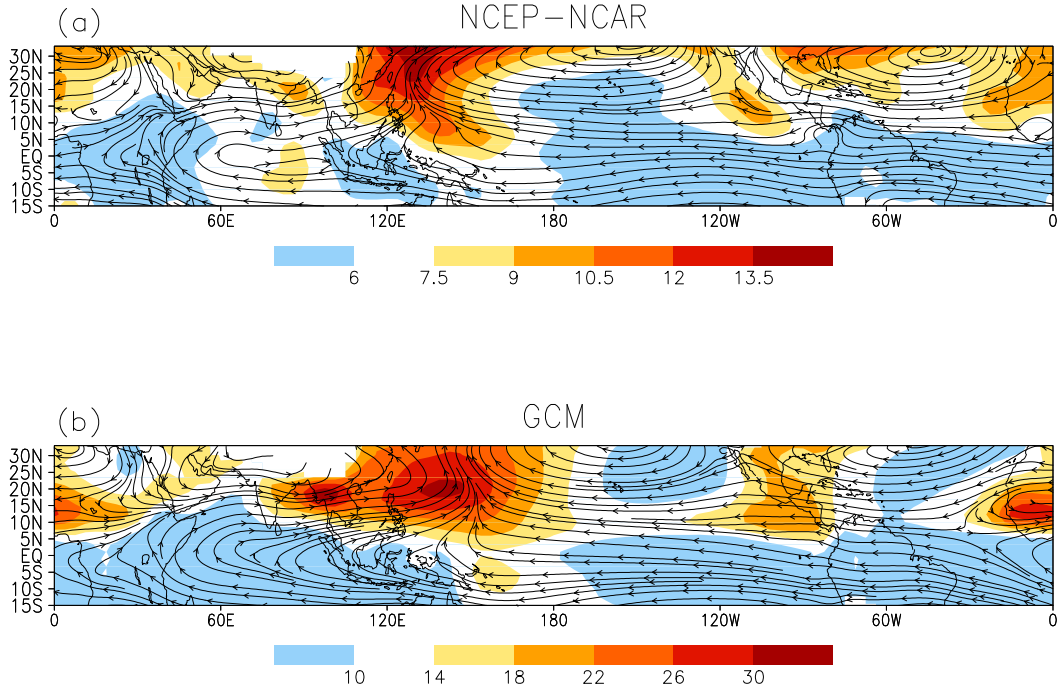


Figure 7.1: Root-mean-squares of 2-15-day filtered vorticity at the 850-mb level (shading, in  $10^{-6}\text{s}^{-1}$ ) from (a) NCEP-NCAR reanalyses and (b) GCM data, for the period of May to September. Mean 850-mb circulation is also shown as streamlines. Note that (a) and (b) have different shading information.

While the rms of vorticity provide a measure of synoptic-scale variability, they are not necessarily associated with wave-like disturbances. Large vorticity variance could be related to fluctuations with little coherence or monopolar vorticities. To highlight the regions with ‘wavy’ disturbances, teleconnectivity based on the same filtered 850-mb vorticity is computed exactly as in LL90, and results for both reanalyses and GCM data are shown in Fig. 7.2. Based on one-point correlation maps computed for every grid point, the teleconnectivity at each point is defined as the magnitude of the most negative correlation that appeared in such maps. One expects a high value from coherent wave-like disturbances, in which substantial amplitudes of both polarities are present.

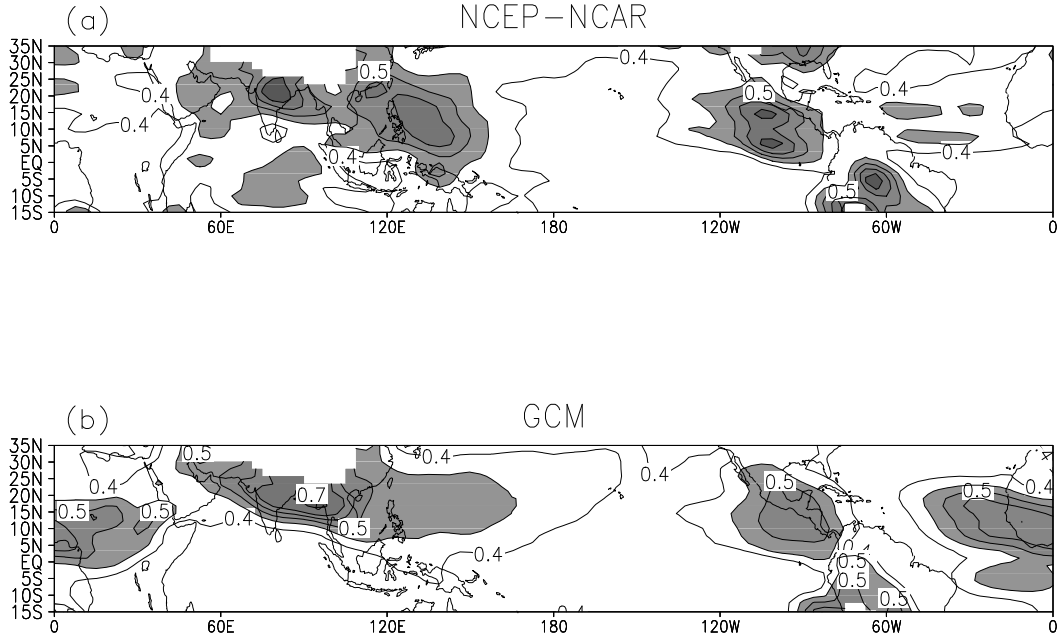


Figure 7.2: Teleconnectivity of 2-15-day filtered vorticity at 850 mb for (a) NCEP-NCAR reanalyses and (b) GCM data. Values greater than 0.45 are shaded. Contour levels: 0.4, 0.45, 0.5, 0.55, 0.6 and 0.7.

In the northern hemisphere, NCEP-NCAR data give large teleconnectivity over the eastern Pacific, the western Pacific and India/Bay of Bengal, and moderate values are found within the Atlantic. Teleconnectivity of 0.5 or more is often found, and results here are consistent with those presented in LL90. As discussed in LL90, these maps also show aspects of disturbances not immediately obvious from the rms vorticity charts. For instance, from reanalyses results, there are wave-like characters at the equator in part of the western Pacific, and disturbances are found to be wavy over much of the Atlantic with a dual north-south maxima of teleconnectivity. GCM results are in broad agreement with those based on reanalyses data. Overall, it can be seen that for both the observations and the simulations, much of the synoptic-scale variability is also associated

with wave-like fluctuations. There are also some obvious differences between the GCM and reanalyses results. Teleconnectivity from the simulations is stronger in Africa, but weaker over the western Pacific, and in the latter region it has a more zonal distribution, which seems to be related with the zonally elongated region of strongest activity as shown in Fig. 7.1.

The phase velocity and growth/decay rate of disturbances, based on the same vorticity variable, are shown in Fig. 7.3. The temporal coherence, a measure of how well perturbations retain their identities as they propagate, is also computed. Computation of these quantities follows closely procedures used in LL90<sup>1</sup>. For both GCM and reanalyses data, arrows shown in the figure cover regions with teleconnectivity exceeding 0.45 (i.e. shaded regions in Fig. 7.2) and the temporal coherence larger than 0.65 for reanalyses (0.6 for GCM). Arrows shown here therefore represent propagation of disturbances which are very coherent and have a wave-like nature.

---

<sup>1</sup>Based on  $\pm 1$ -day lag correlation maps, locations with maximum backward and forward lag correlation are found. The mean of these maximum correlation values gives the temporal coherence. Phase velocity is estimated from the displacement vector drawn from the backward to forward location, while growth of perturbations is defined as the difference of regression values as evaluated at these two locations. Results are divided by the time interval of 2 days to arrive at phase velocity and growth rates. Quantities are computed for each year, and averages are taken over the whole data record in order to obtain the climatological mean.

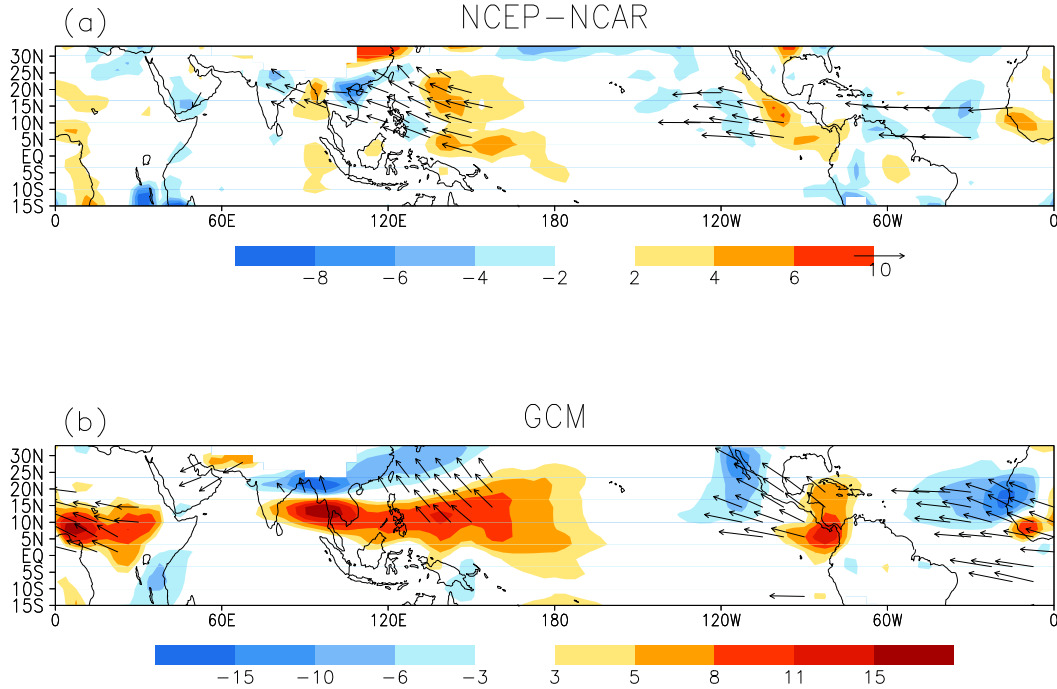


Figure 7.3: Phase propagation vectors (magnitude in  $\text{ms}^{-1}$ ) and growth/decay rates (shading, in  $10^{-7}\text{s}^{-1}\text{day}^{-1}$ ) based on 2-15-day filtered 850-mb vorticity for (a) NCEP-NCAR and (b) GCM data. Arrows shown cover regions with teleconnectivity greater than 0.45 and temporal coherence greater than 0.65 (0.6) for NCEP-NCAR (GCM) data.

In general, there is westward propagation in all active regions. Perturbations exhibit obvious growth-and-decay behavior from the eastern to western part of their ‘storm tracks’. For NCEP-NCAR results, disturbances in the western hemisphere have a rather zonal propagation, while those over the western Pacific, the South China Sea to Bay of Bengal propagate northwestward. Both GCM and reanalyses give roughly the same phase speed, which is largest in the Atlantic and smallest near the Indian subcontinent. Over the western Pacific it is about 4 to 5  $\text{ms}^{-1}$ , in agreement with LL90.

The storm tracks and disturbances characters from the GCM are similar to

those based on observations, e.g. the westward to northwestward propagation of waves, their typical growth-decay patterns and also their approximate geographical locations. It is noticed that the growth rates from simulations are twice as big as those from observations, apparently related to the larger rms values from the GCM. Values of temporal coherence (not shown) tend to be smaller than those found in observations, i.e. simulated transients are slightly less coherent. Another noteworthy difference is that, over the western Pacific, the propagation is directed more to the north for disturbances from simulations. Meridional phase velocity is greater, while the magnitude of the zonal component is reduced (i.e. slower westward propagation). Inspection of the mean 850-mb flow in the region (see Fig. 7.1) suggests that this is due to the difference of the ambient flow from the two datasets. In fact for the GCM, a large fraction of disturbances in this region are embedded within the monsoon westerlies, the latter reaching about 150°E. On the other hand, the zonal flow becomes weak and changes sign east of the Philippines for the reanalyses. Thus the westward propagation of disturbances is reduced in the GCM, due to advection effect. Similarly, the faster meridional propagation might be associated with the stronger southerlies in roughly the same region. Finally, the different growth/decay pattern over the western Pacific, compared with observations, is consistent with the more zonally extended distribution of the rms vorticity, and that wave propagation is directed more northward. The result is a more north-south oriented dipole, instead of an southeast-northwest pattern as appeared in reanalyses results.

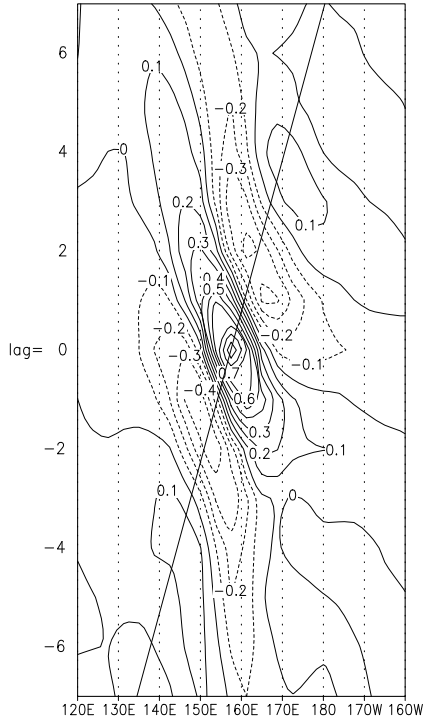
Using diagnostic tools developed in LL90, synoptic-scale activity from reanalyses and GCM data are examined. Reanalyses results are in agreement with those presented by LL90, in which a different data set was used. The GCM is

able to reproduce some essential characteristics of disturbances. However, amplitudes and growth/decay rates are too strong compared with those based on the NCEP-NCAR dataset. Next, dispersion characteristics of wave-like disturbances will be considered.

### 7.2.2 Wave dispersion of synoptic-scale activity

As mentioned in the introduction, the dispersion of wave energy could be important in understanding the variability of synoptic-scale disturbances. SB99, assuming barotropic dynamics to be valid and using wave-activity flux based on Plumb (1986), provided estimates of group velocity over the western Pacific monsoon region. However, their assumption might break down over regions where perturbations are known to be baroclinic or where vertical motion is important, e.g. in locations where equatorial waves are prevalent or the more northwestern portion of storm tracks.

It would be of interest to obtain the group velocity directly, and in fact this was done by Liebmann and Hendon (1990) for MRG waves along the equator. The method of estimating group velocity is illustrated by Fig. 7.4, which shows the lag correlation of 2-15-day filtered 850-mb meridional wind ( $v_{850}$ ) at the reference point of about 160°E at the equator. Notice that  $v_{850}$  is chosen to study the dispersion of eddies, instead of vorticity which might not be a good choice for near equatorial perturbations. It is obvious that as the waves propagate to the west, there is also eastward dispersion at the same time. The group velocity can be estimated by joining correlation centers, as in Fig. 7.4. The zonal group velocity found this way is about  $4\text{ms}^{-1}$ .



Results of group velocity  $\mathbf{c}_g$  are shown in Fig. 7.5, from both reanalyses and GCM data. To highlight areas with coherent propagating disturbances, vectors shown are located at the grid points where the value of the temporal coherence is greater than 0.6 for the NCEP-NCAR dataset (0.55 for GCM). To be consistent, the temporal coherence is computed using the same  $v_{850}$  variable.

Both datasets show positive zonal group velocity in many locations, except over western Atlantic where  $c_{gx}$  is negative. The direction of dispersion is confirmed by inspection of one-point lag regression maps over many locations. This computation method tends to give smaller magnitudes of  $\mathbf{c}_g$  than, say, those based on inspection of hovmoller diagrams (see Fig. 7.4). For instance,  $c_{gx}$  shown here at 160°E is about 2.5ms<sup>-1</sup>. This is probably a statistical effect due to non-uniform wave dispersion. Positive zonal group velocity is also found in the central to eastern Pacific, but values are not shown due to the relatively small temporal coherence there. Positive  $c_{gx}$  of MRG waves along the equatorial Pacific was found by Liebmann and Hendon (1990), Dunkerton and Baldwin (1995) and Wheeler et al. (2000). Values of the group speed from the GCM are larger over the Indian-Asian monsoon region, where simulated low-level westerlies are very strong.

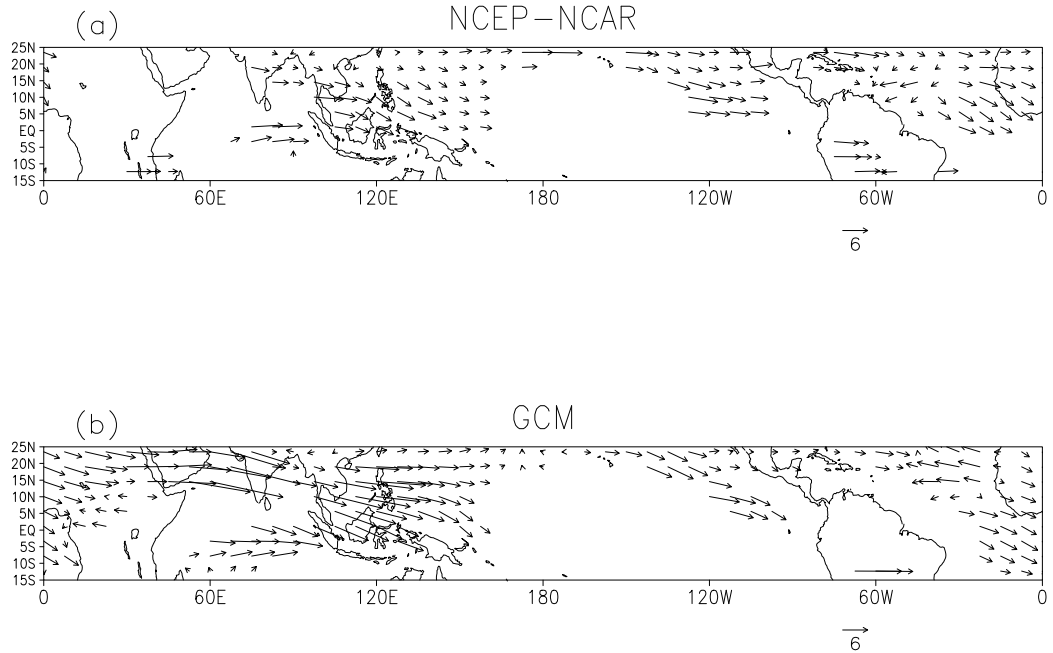


Figure 7.5: Group velocity vectors (magnitudes in  $\text{ms}^{-1}$ ) based on 2-15-day filtered  $v_{850}$ , based on (a) NCEP-NCAR and (b) GCM data. Arrows shown are located at grid points with temporal coherence greater than 0.6 for reanalyses, 0.55 for GCM results.

The most striking feature, however, is that there is a southward component of  $\mathbf{c}_g$  in many regions with coherent synoptic-scale perturbations, especially over the western Pacific. Southward dispersion is obvious from both the GCM and reanalyses results. Based on reanalyses data, the most negative value of  $c_{gy}$  within the western Pacific is about  $-2\text{ms}^{-1}$  near the Philippines, and the average value over the region is about  $-1\text{ms}^{-1}$ . For GCM results,  $c_{gy}$  is most negative near the maritime continent.

If disturbances can be regarded as barotropic Rossby waves, then southward dispersion would follow from a northeast-southwest tilt of eddies. Starting from the Rossby waves dispersion relation, it can be easily shown that the meridional

group velocity is give by

$$c_{gy} = \frac{2\beta kl}{(k^2 + l^2)^2} = \frac{\beta}{k^2 + l^2} \sin 2\theta ,$$

where  $k$  and  $l$  are components of the wavenumber vector  $(k, l)$ ,  $\sin 2\theta = 2kl(k^2 + l^2)^{-1}$ , and  $\theta = \tan^{-1}(l/k)$  is the angle subtended by the wavenumber vector with the  $x$ -axis. For disturbances with a northeast-southwest tilt, wavenumber is northwest (or southeast) pointing, meaning that  $k$  and  $l$  would have opposite signs. Negative  $c_{gy}$  then follows since  $kl < 0$ . The quantity  $\sin 2\theta$  thus indicates the horizontal tilt and is also proportional to  $c_{gy}$  for barotropic Rossby waves.

Local wavenumber is first estimated based on the simultaneous correlation maps of the filtered  $v_{850}$ . Values of  $\sin 2\theta$ , together with southward directed  $\mathbf{c}_g$  over the western Pacific, are plotted in Fig. 7.6. Results indicate that the empirically determined values of  $c_{gy}$  and  $\sin 2\theta$  tend to have the same sign, and they are negative over a region roughly covering the western Pacific storm tracks. In other words,  $c_{gy} < 0$  is consistent with the Rossby wave dispersion suggested by the horizontal tilt of waves. For GCM data, in which the southward dispersion extends more to the east compared with reanalyses, most negative values of  $\sin 2\theta$  are also located more eastward. Notice that mean southerly flow is found over the region (see Fig. 7.1). Therefore the negative  $c_{gy}$  cannot be due to the mean flow advection. SB99 also found southward flow-relative group velocity. Their expression for intrinsic  $c_{gy}$ , based on Plumb's wave-activity flux, is proportional to  $\overline{u'v'}$ .

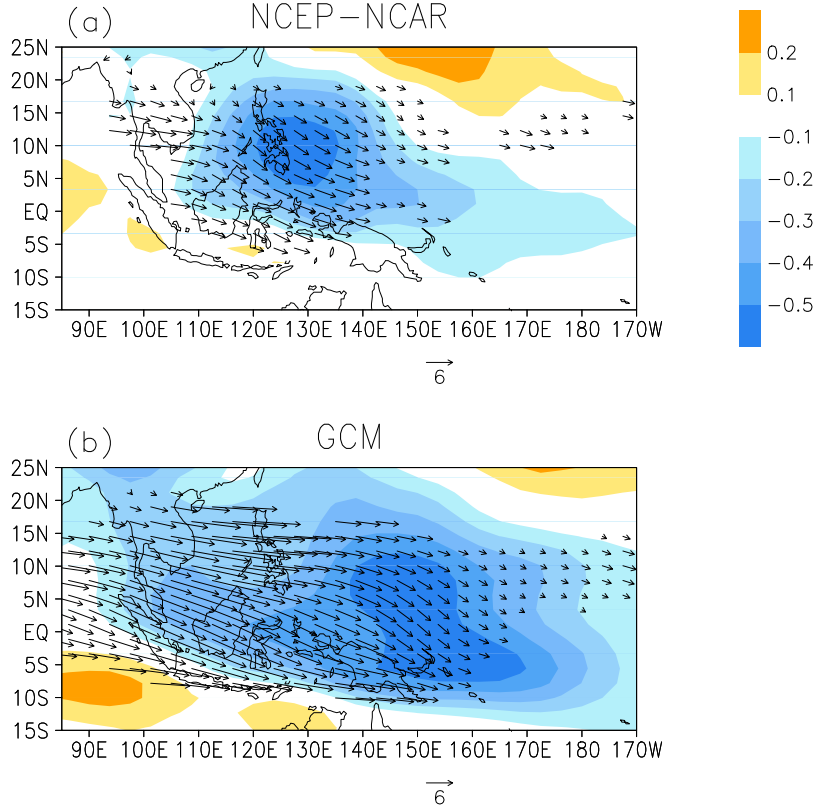


Figure 7.6: Southward directed group velocity vectors and the quantity  $\sin 2\theta = 2kl(k^2 + l^2)^{-1}$  (shading) based on components of local wavenumber (see text for detail), from (a) NCEP-NCAR and (b) GCM data.

There are also indications that variation of zonal group velocity  $c_{gx}$  reflects that of the mean zonal flow. At  $5^\circ$ - $10^\circ\text{N}$  slightly east of Indochina,  $c_{gx}$  is about  $6\text{ms}^{-1}$  and it decreases almost monotonically over the western Pacific, apparently following the decreasing zonal flow in the region. The zonal variation of  $c_{gx}$  is even more dramatic for GCM results.

Convergence of  $\mathbf{c}_g$  is also compared with that given by SB99. Their results show the strongest convergence in the domain of  $10^\circ\text{N}$  to the equator and about  $90^\circ$  to  $150^\circ\text{E}$  (see their Fig. 14). Some similarity is found between  $\nabla \cdot \mathbf{c}_g$  here and results of SB99. Strongest convergence, based on  $\mathbf{c}_g$  from reanalyses data,

is located close to the equator from about  $120^{\circ}\text{E}$  extending eastward, with the maximum magnitude of  $3 \times 10^{-6}\text{s}^{-1}$  (not shown). Convergence near the equator is mainly due to the meridional variation of southward dispersion. Decrease of  $c_{gx}$  in the zonal direction over Indochina also gives large convergence there. Similar results are found for GCM data.

Before focusing on the western Pacific activity, the behavior of synoptic-scale disturbances over other regions is briefly considered. Fig. 7.7 shows one-point lag regression maps of the filtered  $v_{850}$ , with reference grid point at these locations:  $105^{\circ}\text{E}, 10^{\circ}\text{N}$  (east of India/Bay of Bengal),  $115^{\circ}\text{W}, 10^{\circ}\text{N}$  (the eastern Pacific) and  $48^{\circ}\text{W}, 12^{\circ}\text{N}$  (the Atlantic). For perturbations extending from north India to Indochina, southeastward dispersion can be inferred. This can be judged from the shift of approximate locations with the strongest amplitudes, comparing anomalies on lag day -1 to +1. Similar eastward dispersion can also be found in the eastern Pacific. The dispersion as inferred from these plots is consistent with the group velocity shown in Fig. 7.5. Over the Atlantic, dispersion patterns look more complicated. There is development to the east of the wavetrain over west Africa, but as a whole there seems to be a *westward* shift of the center of mass of amplitudes. This is also consistent with Fig. 7.5. Westward dispersion could be a result of the strong easterlies over west Atlantic extending into the Caribbean at about  $10^{\circ}\text{-}15^{\circ}\text{N}$  (see Fig. 7.11).

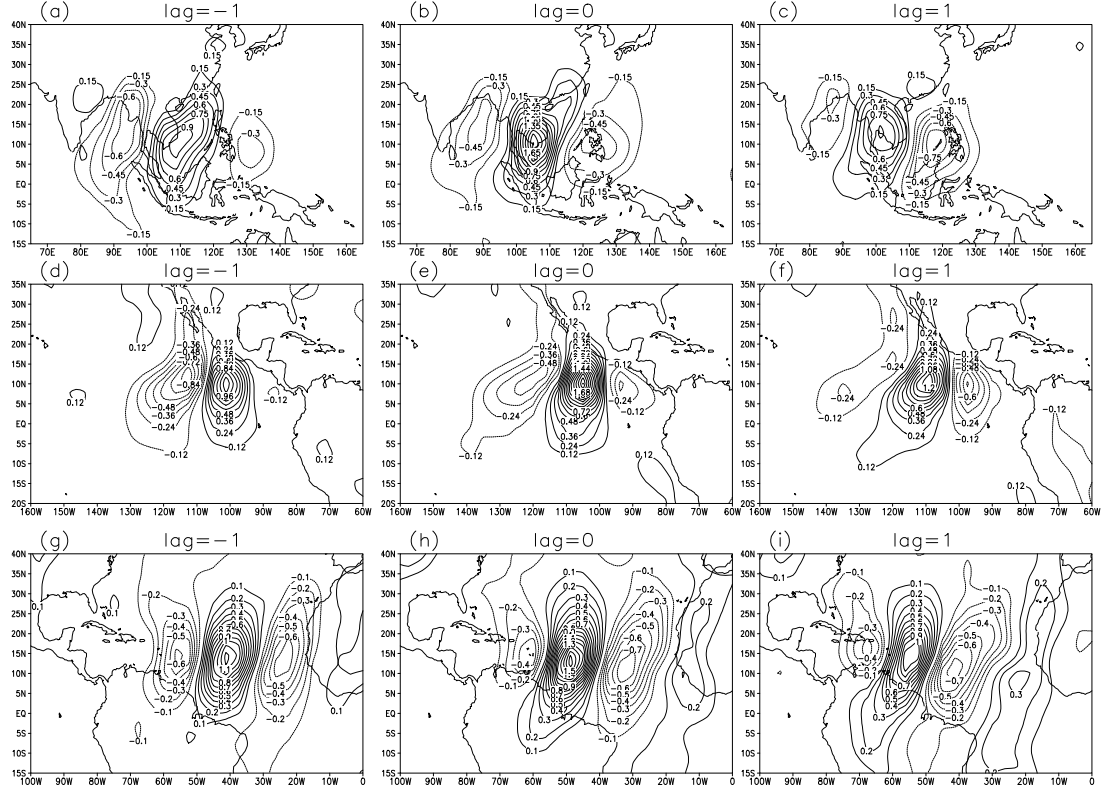


Figure 7.7: Lag regression of 2-15-day filtered  $v_{850}$ , with reference grid point at  $105^{\circ}\text{E}, 10^{\circ}\text{N}$  [(a), (b) and (c)],  $115^{\circ}\text{W}, 10^{\circ}\text{N}$  [(d), (e), and (f)] and  $48^{\circ}\text{W}, 12^{\circ}\text{N}$  [(g), (h) and (i)]. Regression values are shown for the lag of -1 (left panels), 0 (middle panel) and 1 day (right panels). Unit:  $\text{ms}^{-1}$ .

### 7.2.3 Western Pacific activity

To take a closer look at the propagation and dispersion of disturbances within the western Pacific near the equator, correlation plots of 2-15-day filtered  $v_{850}$  at the lag of -1, 0 and +1 day are shown in Fig. 7.8. The reference point is located at about  $160^{\circ}\text{E}$  at the equator. Westward propagating perturbations with a wavelength less than 4000km are found. Near the reference point and to

its east, associated low-level circulation anomalies (not shown) resemble those presented by Liebmann and Hendon (1990) concerning MRG waves. There is also development of anomalies in the eastward direction. Comparing day -1 to day +1, the group of strongest anomalies is seen to shift from the range of 150°-160°E to about 155°-165°E. Again the implied direction of dispersion is consistent with Fig. 7.5. Inspection of lag regression maps (instead of correlation) reveals essentially the same evolution.

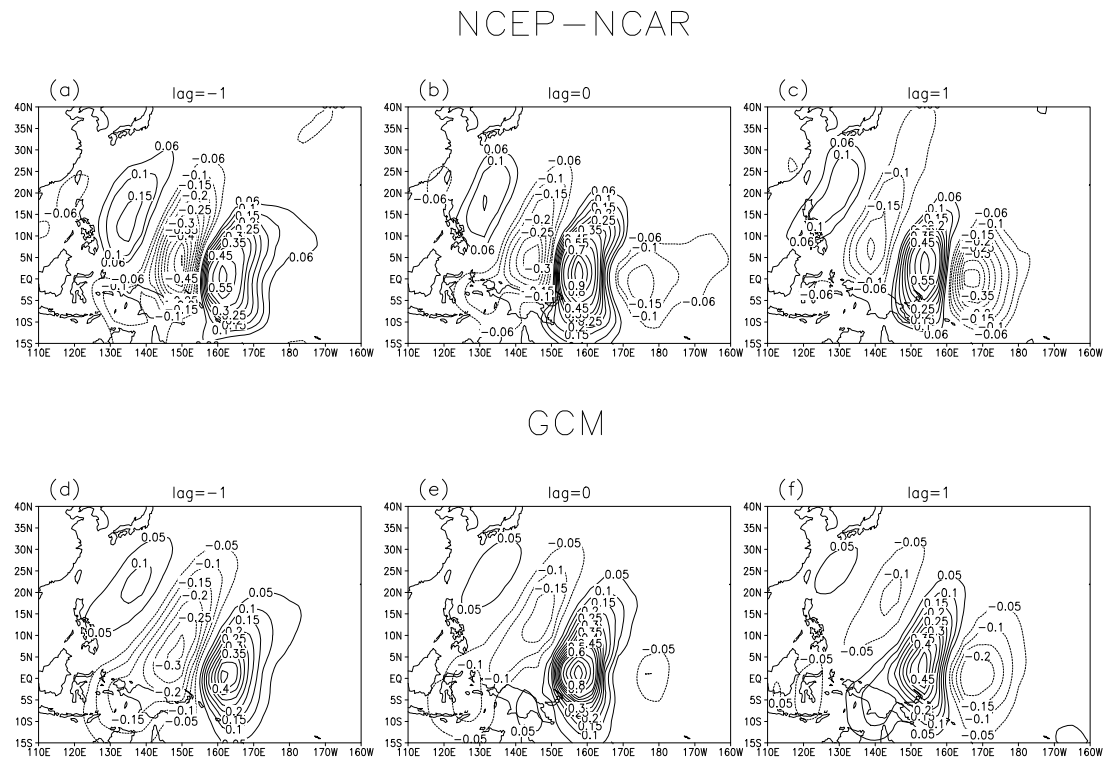


Figure 7.8: Lag correlation of 2-15-day filtered  $v_{850}$ , with reference grid point at about 160°E, equator. Results at lag = -1, 0 and 1 day are shown for NCEP-NCAR reanalyses [(a), (b) and (c)] and GCM data [(d), (e) and (f)]. Reanalyses (GCM) results exceed the 95% (99%) significance level.

It is also noticed that disturbances further west are not trapped along the

equator; in fact they have a tilt reminiscent of that associated with the TD-type disturbances (see Fig. 4 of LL90). Analyses here indicate a transformation from the MRG to the TD-type waves; on the other hand, the dispersion characteristics suggest the transfer of energy from the TD to MRG wave type. GCM results also show very similar dispersion; equatorial waves are seen to be excited by disturbances to the northwest. Compared with reanalyses results, TD-type disturbances in the GCM are more northward directed, consistent with the results concerning their local wavenumber and tilt near 160°E (see Fig. 7.6). It is noticed that GCM perturbation signals are slightly less coherent.

Fig. 7.9 shows the 850-mb wind, vorticity and precipitation anomalies computed as in Fig. 7.8 based on regression, using GCM data. Close to the equator, convection tends to be collocated with  $v_{850}$  of the same sign with the maximum amplitude at the latitude of about ±5° to 10°. This is consistent with the circulation structure of theoretical MRG waves, with the strongest convergence located off the equator (see Takayabu 1994). On day -1 and day +2, there are also indications of a quadrapole pattern of convection, similar to the pattern of OLR anomalies shown by Liebmann and Hendon (1990). On the other hand, off-equatorial vorticity anomalies have the northeast-southwest tilt typical of TD-type disturbances. Associated with these off-equatorial disturbances, however, the convection seems slightly lagging vorticity anomalies of the same sign, instead of being in phase or even leading the vorticity centers as shown in LL90 (see their Fig 14).

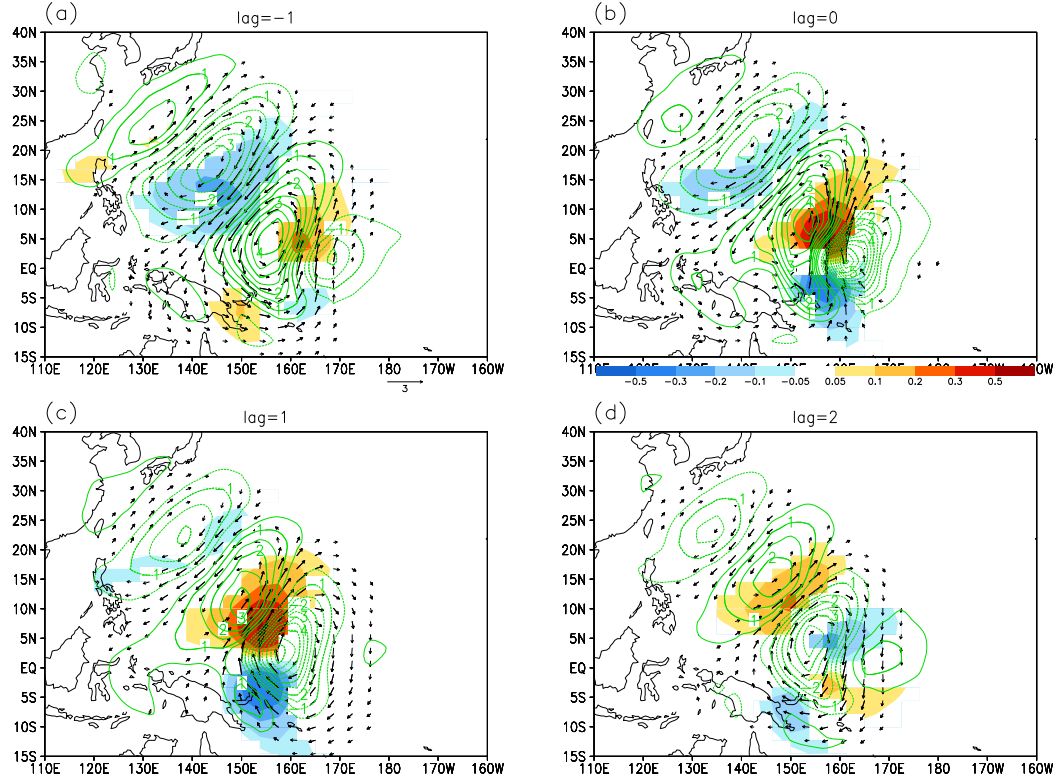


Figure 7.9: Regression of 850-mb wind (magnitudes in  $\text{ms}^{-1}$ ), vorticity (contours, with interval of  $10^{-6}\text{s}^{-1}$ ) and precipitation (shading, in  $\text{cmday}^{-1}$ ), computed as in Fig. 7.8. Only wind vectors with magnitudes greater than  $0.3\text{ms}^{-1}$  are shown; zero contours are removed for vorticity perturbations. Wind (precipitation) regressions are significant to 99% (95%) level. Regression values are shown for the lag of (a) -1, (b) 0, (c) 1 and (d) 2 day.

The study of Dickinson and Molinari (2002) suggests the existence of 6-10-day MRG wave packets. The MRG waves shown here could be aggregates of those wave packets. It has also been suggested in many works that MRG waves might 'seed' TD-type disturbances. Here it is shown that, in a statistical sense, energy transfer is directed southeastward from TD-type disturbances to MRG waves. It is possible that once TD-type disturbances are initiated, they would serve as sources for activity located to their southeast. In fact, Dickinson and

Molinari (2002) also showed equatorial waves being excited once the TD-type disturbances become active in the region. Their results are thus consistent with those presented here.

As mentioned before, the variation of the zonal group velocity suggests the influence of the ambient flow field. To further investigate the advection effect of the mean wind, correlation coefficients between the interannually varying  $c_{gx}$  and the mean zonal flow at various vertical levels are computed. Values of zonal wind and  $c_{gx}$  are first averaged over the domain of 5°N-5°S, 130°E-170°W before computation, and results are shown in Fig. 7.10. Group velocity in the region is found to be best correlated with low-level winds, with maximum correlation reaching 0.6 for NCEP-NCAR data, and about 0.8 for GCM data. Similar results are obtained from correlating the zonal phase speed with the mean flow at various levels (not shown), consistent with Liebmann and Hendon (1990). These results indicate strong advecting effect by the low-level ambient flow on the dispersion and propagation of synoptic-scale disturbances along the equator.

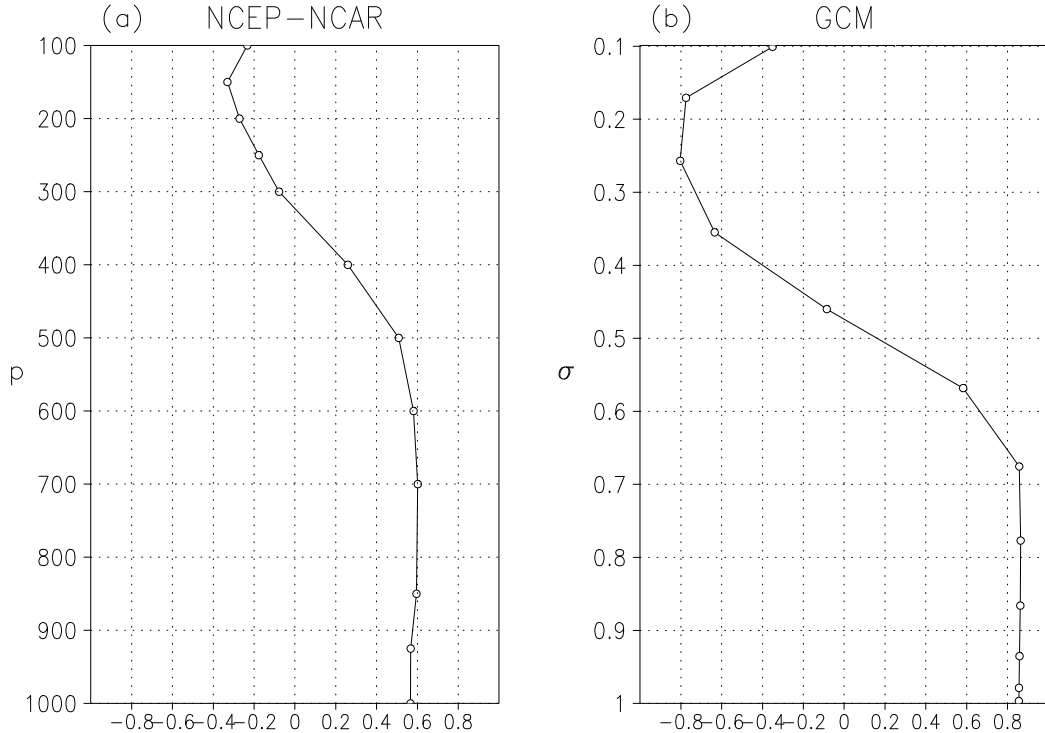


Figure 7.10: Correlation coefficient between zonal group velocity and zonal wind at various pressure levels for (a) NCEP-NCAR, and at different  $\sigma$  levels for (b) GCM data. Values of velocity and wind are first averaged over the region of  $130^{\circ}\text{E}-170^{\circ}\text{W}$ ,  $5^{\circ}\text{N}-5^{\circ}\text{S}$ , before computation.

A test is carried out to see whether perturbation characteristics satisfy the dispersion relation of MRG waves. Assuming 850 mb as the effective advecting level, one can estimate the quantities  $(\omega)_{\text{int}}$  and  $k$ , where  $(\omega)_{\text{int}} = \omega - kU$  is the intrinsic frequency,  $\omega$  being the ground-based frequency, and  $k$  and  $U$  are the zonal wavenumber and 850-mb mean zonal flow respectively. The local value of  $\omega$  is inferred from auto correlation function of the filtered  $v_{850}$ . Taking area average for the domain of  $100^{\circ}\text{-}170^{\circ}\text{E}$ ,  $10^{\circ}\text{N}\text{-}5^{\circ}\text{S}$  for NCEP-NCAR data, wavenumber and intrinsic frequency are found to be  $2\pi \cdot (4900\text{km})^{-1}$  and  $2\pi \cdot (5.2\text{day})^{-1}$ , respectively. For GCM data, the corresponding values are  $2\pi \cdot (5500\text{km})^{-1}$  and

$2\pi \cdot (4.9\text{day})^{-1}$  (averaged over  $120^\circ\text{E}-170^\circ\text{W}, 10^\circ\text{N}-5^\circ\text{S}$ ). Values of wavelength are shorter than those of MRG waves over the central Pacific, but longer than those typical of the TD-type disturbances. Substituting into the theoretical dispersion relation of MRG waves, reduced gravity wave speed  $c$  of about  $35\text{ms}^{-1}$  is found for both reanalyses and GCM data. A similar exercise, but using intrinsic  $c_{gx}$  to fit in the corresponding theoretical expression<sup>3</sup>, gives a value of  $c$  of about  $25\text{ms}^{-1}$  (see also Fig. 23). Characteristics of disturbances along the equator are therefore consistent with those related to the theoretical MRG waves. These estimates imply an equivalent depth  $h_e$  of approximately 60 to 120m.

#### 7.2.4 Wavelength of disturbances

Holland (1995) argued that packets of equatorial waves, while propagating westward from the central to western Pacific, would experience contraction of disturbances wavelength due to the presence of a confluent background flow. Ray tracing calculations of SB99, using dispersion relation of barotropic Rossby waves, suggest a similar change of wave scales but for off-equatorial synoptic-scale perturbations. This could have important implications for the synoptic-scale variability over the western Pacific, because short waves tend to have slower group speed, making the escape of wave energy less effective.

Estimates of the wavelength of synoptic-scale activity at different locations are presented in Fig. 7.11. From correlation maps of the filtered  $v_{850}$ , local wavelength is found based on positions of most negative signals neighboring the reference grid point. Values are seen to range from less than 4000 to about

---

<sup>3</sup>Group velocity of MRG waves is give by  $\frac{c}{2}(1 - kc/\sqrt{k^2c^2 + 4\beta c})$

8000km or more for reanalyses data, while there are even longer waves for the GCM. The former dataset gives a distinct band of large-scale disturbances along the equator from the central to eastern Pacific, extending eastward into south America; long waves are also seen in Africa. Further west from the dateline, the wavelength of disturbances decreases rapidly as one moves toward the western Pacific. In general, shortest waves are found in regions with enhanced synoptic-scale variability. Liebmann and Hendon (1990) also noticed that wave scales decrease by almost a factor of two from the central to the western Pacific. GCM results are in broad agreement with those based on reanalyses data concerning the variation of wavelength. Estimation using the same method but based on 850-mb vorticity results in values from 2000km to 9000km (not shown). The vorticity variable tends to emphasize smaller scales, but the variation of wave scales is very similar to that shown in Fig. 7.11.

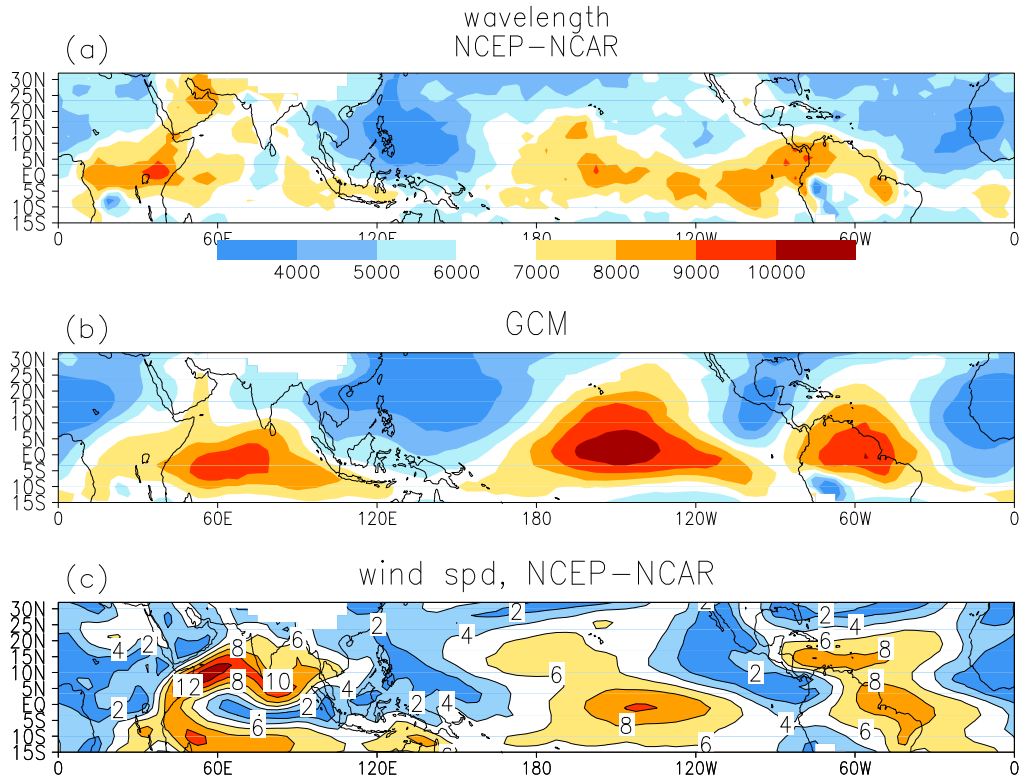


Figure 7.11: Wavelength (in km) of synoptic-scale disturbances as inferred from 2-15-day filtered  $v_{850}$ , based on (a) NCEP-NCAR and (b) GCM data. Speed (in  $\text{ms}^{-1}$ ) of the 850-mb mean flow for NCEP-NCAR reanalyses is shown in (c).

It is interesting that the wavelength of perturbations increases swiftly along the equator in the zonal direction, east of about  $150^\circ\text{E}$ . Based on ray tracing theory, the rate of change of wavenumber  $k$  following a wave packet with speed  $c_g$  is given by

$$\frac{dk}{dt} = -k \frac{\partial U}{\partial x} - \frac{\partial \omega}{\partial x},$$

where  $d/dt = \partial/\partial t + c_g \cdot \partial/\partial x$ ,  $U$  is the ambient flow, and the last term arises from any explicit dependence of the dispersion relation on position (see SB99, or Lighthill 1978 for details). If this last term can be ignored, then the above expression means that within regions of convergence (divergence), there should

be an increase (decrease) of  $k$  in the direction of group propagation.

However, the previous result of  $c_{gx} > 0$  and the fact that  $\partial U / \partial x < 0$  would imply  $\partial k / \partial x > 0$  eastward of about  $150^\circ\text{E}$ , which is certainly not the case. If ray tracing or WKB assumption is still valid, then one possibility is that wave dispersion relation in this transition zone between MRG and TD-type waves has a strong dependence on geographical locations. For instance,  $h_e$  might vary in different zonal positions. It is noted that the vertical structure of disturbances also changes according to longitudinal positions in this region.

Fig. 7.11 (c) shows the speed of the mean 850-mb flow from reanalyses data. Compared with Fig. 7.11 (a), there is a good match in terms of geographical distribution between the wavelength and the wind speed. Short-scale disturbances in the western and the eastern Pacific are located in regions with low wind speeds, while long waves are found in the equatorial central Pacific with strongest low-level easterlies. Low wind speed region over Africa also partially overlaps where short waves are found in the vicinity. A similar relationship between wave scales and the wind speed also exists for the GCM (not shown). This empirical finding, at least in off-equatorial regions where short waves dominate, seems consistent with ray tracing calculations of SB99 as discussed before: packets of short waves would largely follow the background flow, and hence experience contraction as they move westward toward low-wind-speed regions where easterlies decrease. Over the equatorial central-eastern Pacific where long waves dominate, this argument might not apply, as noted before.

It is instructive to compare the intrinsic group speed with the wavelength of disturbances. For MRG waves and Rossby wave-like perturbations, one would expect lower intrinsic group speeds for shorter waves. Scatter plots with values of

intrinsic group speed and wavelength are shown in Fig. 7.12, for both reanalyses and GCM data. Data points here are selected within most of the tropical Pacific sector:  $20^{\circ}\text{N}-10^{\circ}\text{S}$ ,  $110^{\circ}\text{E}-90^{\circ}\text{W}$  for reanalyses data ( $130^{\circ}\text{E}-90^{\circ}\text{W}$  for GCM). There is a strong correlation between the wavelength and group speed based on GCM data, while indications of such a relationship can also be found for reanalyses results. The largest group speed is found over the central-eastern Pacific, where longest wave scales are also located; shortest waves over the western Pacific, on the other hand, have the smallest group speed. There is thus a positive correlation between length scales and group speeds of disturbances, in accordance with theoretical consideration.

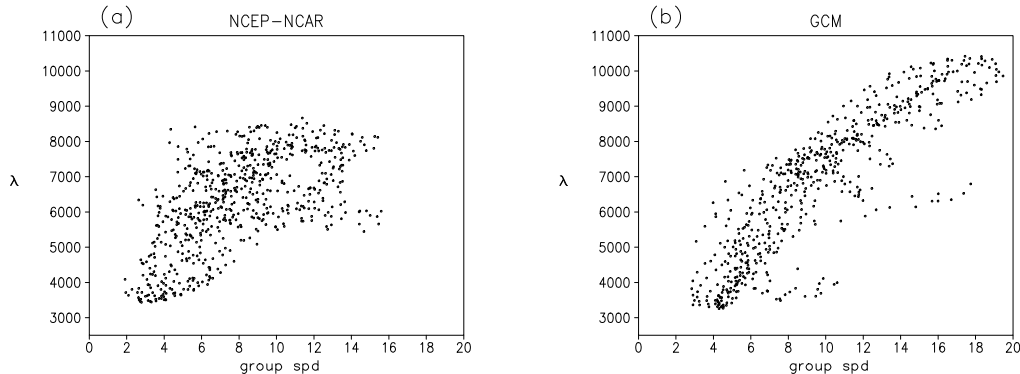


Figure 7.12: Wavelength of disturbances (in km) as seen in Fig. 7.11 verses intrinsic group speed (in  $\text{ms}^{-1}$ ), for (a) NCEP-NCAR and (b) GCM results. For reanalyses dataset, results within  $110^{\circ}\text{E}-90^{\circ}\text{W}, 20^{\circ}\text{N}-10^{\circ}\text{S}$  are shown; for GCM, results within  $130^{\circ}\text{E}-90^{\circ}\text{W}, 20^{\circ}\text{N}-10^{\circ}\text{S}$  are shown.

### 7.2.5 A brief summary

Diagnostic tools developed in LL90 are used to study synoptic-scale variability in the tropics. For both reanalyses and the GCM, disturbances in regions with

enhanced variability are found to be wave-like, westward propagating and they exhibit typical growth-and-decay behavior. Eddies from the GCM are, however, slightly less coherent but with much larger amplitudes. Reasonable simulations of their trajectories seem to be dependent on the realism of the background flow in the GCM.

Estimates of the group velocity are also provided. Dispersion is found to be eastward or southeastward directed from regions with strong eddy amplitudes. The southward dispersion is found to be accompanied by northeast-southwest tilted perturbations. Over the western Pacific, the implied energy transfer could be important for the growth of disturbances near the equator. These near-equatorial eddies resemble MRG waves, but they are also seen to transform into TD-type disturbances as they propagate. At the equator over the western-central Pacific, dispersion characteristics are consistent with those expected of the theoretical MRG waves.

The wavelength of synoptic-scale disturbances in various geographical locations is also examined. Short waves are found in regions with enhanced variability, where there is also convergence of the mean flow and low wind speeds in low levels. Over the Pacific sector, disturbances with short wavelengths also tend to have smaller intrinsic group speeds.

In the next section, the impact of ENSO on synoptic-scale variability will be considered. The same diagnostic tools will be used to study changes of wave characteristics.

## 7.3 Behavior during ENSO

### 7.3.1 Impact of ENSO on western Pacific activity

First, the effect of ENSO on the propagation of synoptic-scale disturbances is considered. Fig. 7.13 shows phase velocity vectors based on the 850-mb vorticity variable (computed as in Fig. 7.3) during warm and cold events, for reanalyses and GCM data. Based on reanalyses results, more coherent disturbances are found in the southeast portion of storm tracks during warm ENSO events. (It may be recalled that the arrows displayed indicate locations with the temporal coherence larger than a certain threshold value.) In fact disturbances have larger amplitudes in a broad region east of the Philippines (see also Fig. 7.14). GCM simulations show an analogous change during ENSO. There is an eastward extension of storm tracks during warm events, although overall the effect of ENSO is seen to be an east-west shift of where most coherent perturbations are located. During warm events, disturbances are also stronger at about 160°E.

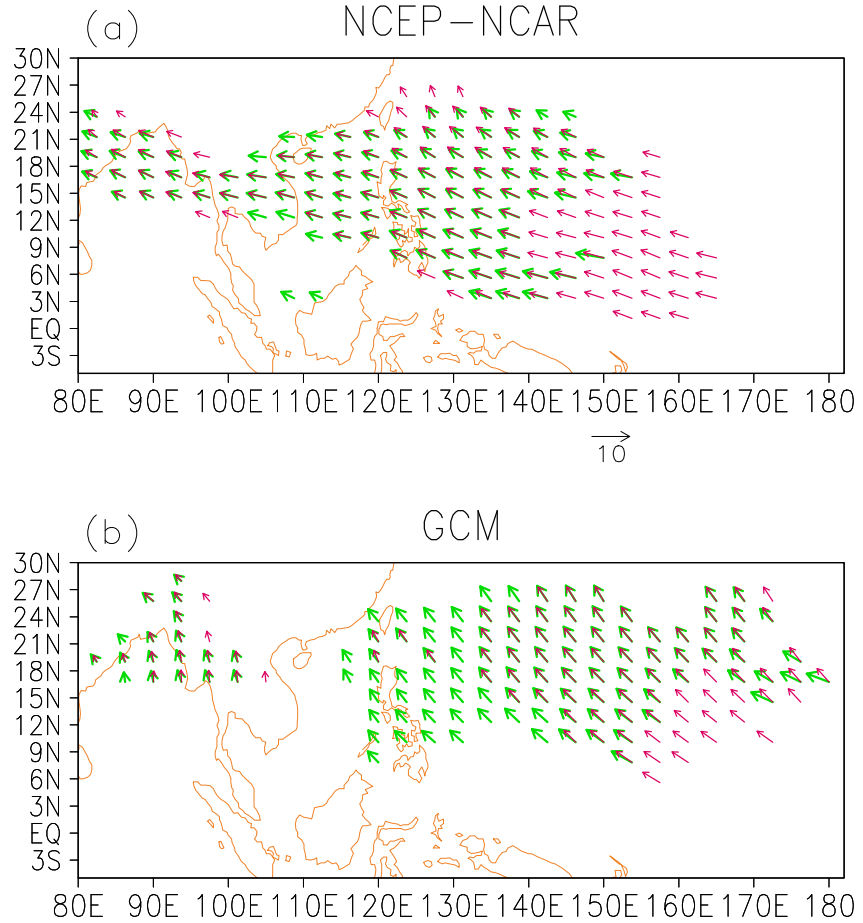


Figure 7.13: Propagation vectors (magnitudes in  $\text{ms}^{-1}$ ) based on the 2-15-day filtered 850-mb vorticity, during warm (red arrows) and cold (green arrows) events. Results from (a) NCEP-NCAR and (b) GCM dataset. For vectors displayed, the local value of teleconnectivity is greater than 0.45 and temporal coherence is greater than 0.65 (0.6 for reanalyses (GCM) data.

To gain some insight into the physical processes involved in affecting the perturbation amplitudes, barotropic conversion from the mean to eddy kinetic energy is considered. Maloney and Hartmann (2001) studied the effect of the MJO on high-frequency disturbances. Their work suggests that barotropic conversion can be useful in understanding the variability of these disturbances. Hartmann and Maloney (2001), using a stochastic barotropic model, further demonstrated

that barotropic dynamics might account for the concentration of energy for high-frequency perturbations due to the background flow.

Analyses carried out here essentially follow those of Maloney and Hartmann (2001). Barotropic conversion is given by  $-\overline{u'^2}\partial_x U - \overline{v'^2}\partial_y V - \overline{u'v'}(\partial_y U + \partial_x V)$ , with  $U$  and  $V$  being the mean zonal and meridional wind at 850 mb. Primed quantities are lag regression of wind components with the reference time series being the 2-15-day filtered vorticity at the location of 150°E, 10°N for NCEP-NCAR data (160°E, 10°N for GCM). Regression values of the wind found this way should represent circulation anomalies associated with typical synoptic-scale activity within a localized region. The idea is similar to that of LL92, who used composites of variables based on the EOF's of vorticity for various budget calculations. An overbar denotes averaging over the period of lag of -15 to +15 days. Local eddy kinetic energy, computed as  $\frac{1}{2}(\overline{u'^2} + \overline{v'^2})$ , is also shown.

Fig. 7.14 shows barotropic conversion from the mean to eddy kinetic energy during warm and cold events. It can be inferred that, during warm events, eddy amplitudes are larger in the vicinity of the reference grid point, as evidenced by the strong kinetic energy there. There is also much stronger conversion in about the same region, compared with the cold ENSO situation. For reanalyses results, positive conversion takes place where the easterlies are increasing northward or  $-\partial_y U > 0$ , but during warm events the mean cyclonic circulation east of the Philippines is obviously much stronger. It seems that, in El Niño years, the anomalous eastward protrusion of the monsoon trough could be an important factor leading to stronger barotropic conversion. The pattern of the mean circulation also suggests stronger low-level convergence in about the same region during warm events, supported by inspection of the mean divergence (not shown). The

implied change of conversion terms proportional to  $-\partial_x U$  or  $-\partial_y V$  means that the convergence of the ambient flow might also be a reason for larger barotropic conversion. Sobel and Maloney (2000) argued that the stronger convergence would lead to more accumulation of wave activity, resulting in an eastward extension of strong variability during El Niño events.

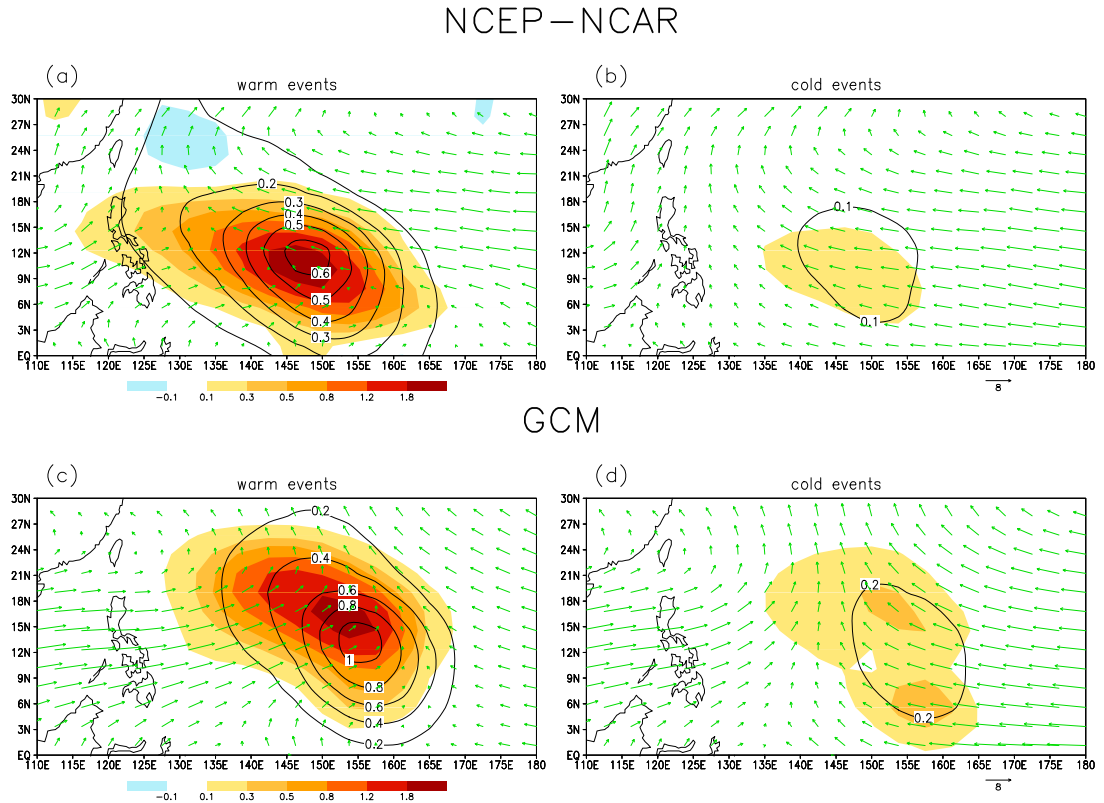


Figure 7.14: 850-mb barotropic conversion (shading, in  $10^{-6}\text{m}^2\text{s}^{-3}$ ) from the mean to eddy kinetic energy. Left and right panels show respectively results during warm and cold events. Computations are based on NCEP-NCAR [(a) and (b)] and GCM [(c) and (d)] dataset. Corresponding mean flow at 850-mb level (vectors, with magnitude in  $\text{ms}^{-1}$ ) and values of local eddy kinetic energy (contour, in  $\text{m}^2\text{s}^{-2}$ ) are also shown. See text for computation method.

GCM results are in many aspects similar to those based on reanalyses data.

During warm events, there is an eastward extension of the monsoon trough. Enhanced conversion largely collocates where stronger shear is found. Much weaker conversion is found during cold events, as the monsoon trough is located more to the west.

To investigate the relative importance of different processes, the warm-minus-cold value of barotropic conversion is broken down into several terms. Ignoring the part proportional to  $\partial_x V$  due to its small magnitude, the warm-minus-cold conversion can be written as six different terms, proportional to each of the following quantities:  $\delta(-\partial_y U)$ ,  $\delta(-\partial_x U)$ ,  $\delta(-\partial_y V)$ ,  $\delta(\bar{u}'v')$ ,  $\delta(\bar{u}'^2)$  and  $\delta(\bar{v}'^2)$ . Here  $\delta(\cdot)$  represents the operation of subtracting the cold from the warm ENSO values of different variables<sup>4</sup>. The first three terms can be interpreted as contributions due to changes of the mean circulation only. On the other hand, the last three terms can be regarded as those related to changes of eddy statistics. Results are shown in Fig. 7.15. Values are averaged over the region of 130°-160°E, 5°-20°N for reanalyses data, and 140°-165°E, 5°-25°N for the GCM.

---

<sup>4</sup>It can be readily shown that, for the quadratic term  $ab$ , its warm-minus-cold difference  $\delta(ab) \equiv a_w b_w - a_c b_c = \frac{b_w + b_c}{2} \delta a + \frac{a_w + a_c}{2} \delta b$ ; these two expressions are interpreted as the contributions proportional to  $\delta a$  and  $\delta b$ .

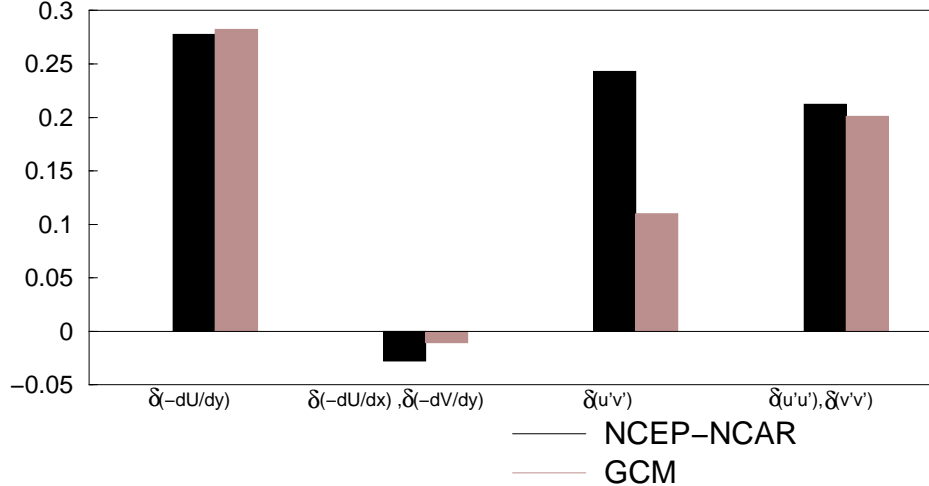


Figure 7.15: Contribution to warm-minus-cold barotropic conversion from the following terms:  $\delta(-\partial_y U)$ ,  $\delta(-\partial_x U)$ ,  $\delta(-\partial_y V)$ ,  $\delta(\bar{u}'\bar{v}')$ ,  $\delta(\bar{u}'^2)$  and  $\delta(\bar{v}'^2)$ . Results of  $\delta(-\partial_x U)$  and  $\delta(-\partial_y V)$  are combined, and likewise for  $\delta(\bar{u}'^2)$  and  $\delta(\bar{v}'^2)$ . Values are averaged over the area of  $130^\circ$ - $160^\circ$ E,  $5^\circ$ - $20^\circ$ N for NCEP-NCAR (in black),  $140^\circ$ - $165^\circ$ E,  $5^\circ$ - $25^\circ$ N for GCM data (brown). Unit:  $10^{-6} \text{m}^2 \text{s}^{-3}$

It can be seen that among the terms  $\delta(-\partial_y U)$ ,  $\delta(-\partial_x U)$  and  $\delta(-\partial_y V)$ , the first one related to cyclonic shear dominates. Magnitudes of conversion related to  $\delta(-\partial_x U)$  and  $\delta(-\partial_y V)$  are a few times smaller than all other terms; they are added together for the ease of presentation. Conversion terms proportional to  $\delta(\bar{u}'\bar{v}')$ ,  $\delta(\bar{u}'^2)$  and  $\delta(\bar{v}'^2)$  (the latter two are combined in the figure) have comparable magnitudes for the GCM; for reanalyses results, the  $\delta(\bar{u}'\bar{v}')$  term is the strongest. Overall, it can be said that the process related to  $-\bar{u}'\bar{v}'\partial_y U$  is most important in accounting for the difference of barotropic conversion during ENSO, and the change of cyclonic shear have the larger contribution to such a difference. Maloney and Hartmann (2001) also noticed the importance of  $-\bar{u}'\bar{v}'\partial_y U$  to the barotropic conversion for western Pacific activity. It is noteworthy that  $\delta(\bar{u}'\bar{v}')$  is larger during warm events probably due to eddies being stronger in the first place, but it can also be related to other factors such as the change of tilt of

disturbances. In the next section, it will be shown that are in fact changes of the horizontal tilt for perturbations in the region of interest here. This also have consequences on the dispersion characteristics of eddies in the region.

### 7.3.2 Modulation of dispersion characteristics

To examine the effect of ENSO on dispersion of synoptic-scale activity, the group velocity during warm and cold events is plotted in Fig. 7.16. For reanalyses results, there is a zone extending eastward from the Philippines where dispersion is directed more to the southeast during warm events. During cold events, on the other hand, southward dispersion is most prominent in more western longitudes. GCM results show a similar shift of the region with southward-directed dispersion, which seems to follow the shift of the storm tracks (see Fig. 7.13). Increased zonal group velocity  $c_{gx}$ , during warm events, is found broadly where the 850-mb zonal flow is enhanced (not shown). This is most likely a result due to the mean flow advection, as suggested by the correlation between the low-level flow and zonal group velocity in Fig. 7.10. For NCEP-NCAR results, warm-minus-cold value of  $c_{gx}$  is about  $2 \text{ ms}^{-1}$ , while change of the mean flow  $U$  is about  $4\text{ms}^{-1}$  within the western-central Pacific near the equator. Interestingly in the same region, the wavelength of disturbances is also shorter comparing the warm to cold ENSO phase (see Fig. 7.17). More short waves are found over western-central Pacific, which could be related to an extension of the confluence zone during warm events (not shown). This shortening of length scales might act to reduce the advecting effect of  $U$  on changes of  $c_{gx}$ .

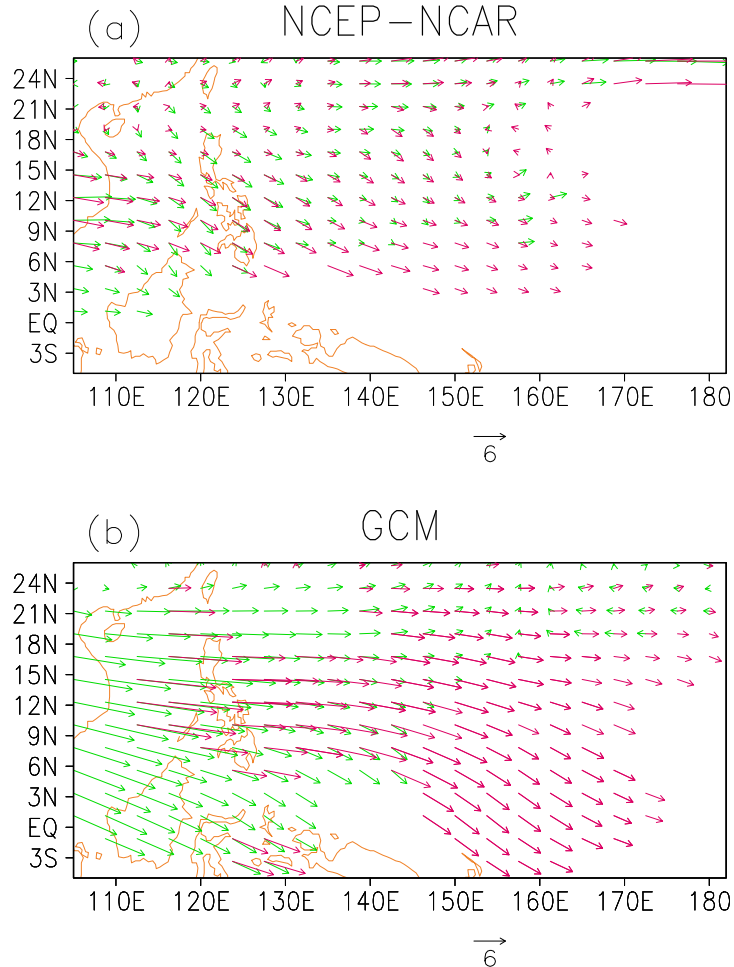


Figure 7.16: Group velocity (magnitudes in  $\text{ms}^{-1}$ ) computed as in Fig. 7.5 during warm (red arrows) and cold (green arrows) events, based on (a) NCEP-NCAR and (b) GCM dataset. Arrows are shown wherever temporal coherence is greater than 0.6 for reanalyses, 0.55 for GCM data. Furthermore, for GCM data during warm events, arrows are displayed only when group velocities are significantly different (to 95% level, for either of their components) from those during cold events.

For near-equatorial disturbances which resemble MRG waves, it would be of interest to examine the relationship between their group velocity and wavelength and to compare it with the theoretical dispersion relations. To this end, the value of the intrinsic zonal group velocity versus the zonal wavenumber is plotted in

Fig. 7.17. All data points displayed are results averaged over the domain of  $130^{\circ}\text{E}-170^{\circ}\text{W}$ ,  $5^{\circ}\text{N}-5^{\circ}\text{S}$ . Climatological mean, values during nine warm and nine cold events as well as their mean values are shown. A set of theoretical curves of group velocity for MRG waves are also plotted, for different values of the reduced gravity wave speed  $c$ .

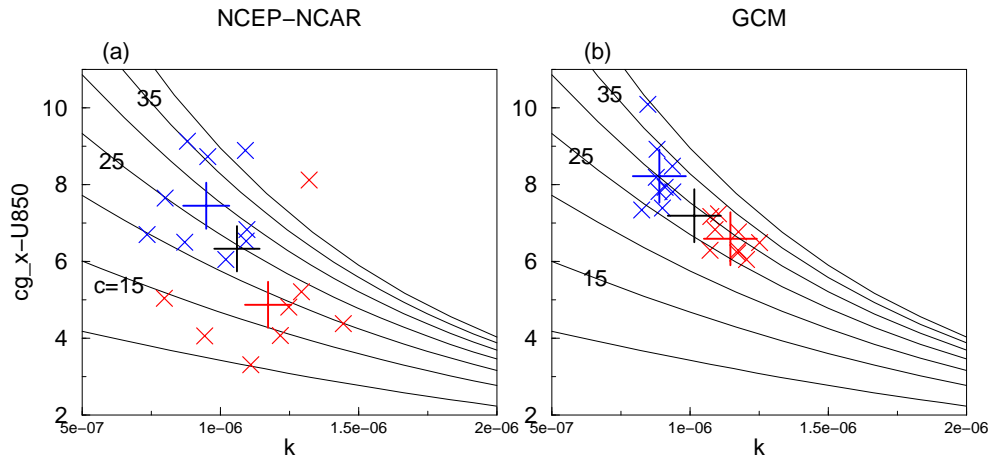


Figure 7.17: Intrinsic zonal group velocity (in  $\text{ms}^{-1}$ ) verses zonal wavenumber (in  $\text{m}^{-1}$ ) during the nine warm (red crosses) and nine cold (blue crosses) events, based on (a) NCEP-NCAR and (b) GCM dataset. Values are averaged over the region  $130^{\circ}\text{E}-170^{\circ}\text{W}, 5^{\circ}\text{N}-5^{\circ}\text{S}$ . The mean value during warm events, cold events and the climatological mean are also shown (as red, blue and black plus signs, respectively). Group velocity as a function of wavenumber, derived from theoretical dispersion relation of MRG waves, are shown as a family of curves with reduced gravity wave speed  $c$  equal to 10, 15, 20, 25, 30, 35 and  $40 \text{ ms}^{-1}$ .

First, the climatological values of the zonal wavenumber and group velocity indicate that  $c$  is about  $25 \text{ ms}^{-1}$  for NCEP-NCAR data, and  $28 \text{ ms}^{-1}$  for the GCM. Inspection of the mean values during both ENSO phases suggests a slight reduction of  $c$  or equivalent depth during warm events, based on reanalyses results. On the other hand, there is only a small change of  $c$  for the GCM. Nevertheless, it is clear that there is a decrease of intrinsic  $c_{gx}$ , associated with an increase

of wavenumber  $k$ , from cold to warm events. In fact smaller (larger) intrinsic  $c_{gx}$  tend to be found for individual El Niño (La Niña) events. This relationship between the group velocity and the wavelength is consistent with disturbances being MRG or Rossby-wave like. Similar results are also found for the GCM.

Results from section 7.2.2 suggest that barotropic dynamics might help to understand the dispersion characteristics of TD-type disturbances. Fig. 7.18 shows the warm-minus-cold 'E-vector' of Trenberth (1986), i.e. the vector  $(\frac{\overline{-u'^2} + \overline{v'^2}}{2}, -\overline{u'v'})$ . Primed quantities are components of the 2-15-day filtered 850-mb wind, while an overbar represents taking the time mean. If barotropic dynamics applies, then E-vector can be shown to be parallel to the local group velocity relative to the time mean flow.

Based on the reanalyses data, E-vectors displayed here suggest that more southward dispersion is present within a region east of the Philippines. This is due to the larger values of  $\overline{u'v'}$  there during warm ENSO events. From GCM results, the region with more southward directed E-vector is found east of about 140°-150°E. It is noteworthy that the difference of dispersion implied here is qualitatively similar to that suggested by Fig. 7.16 in different phases of ENSO, even though these results are obtained from completely different methods and with different dynamical assumptions.

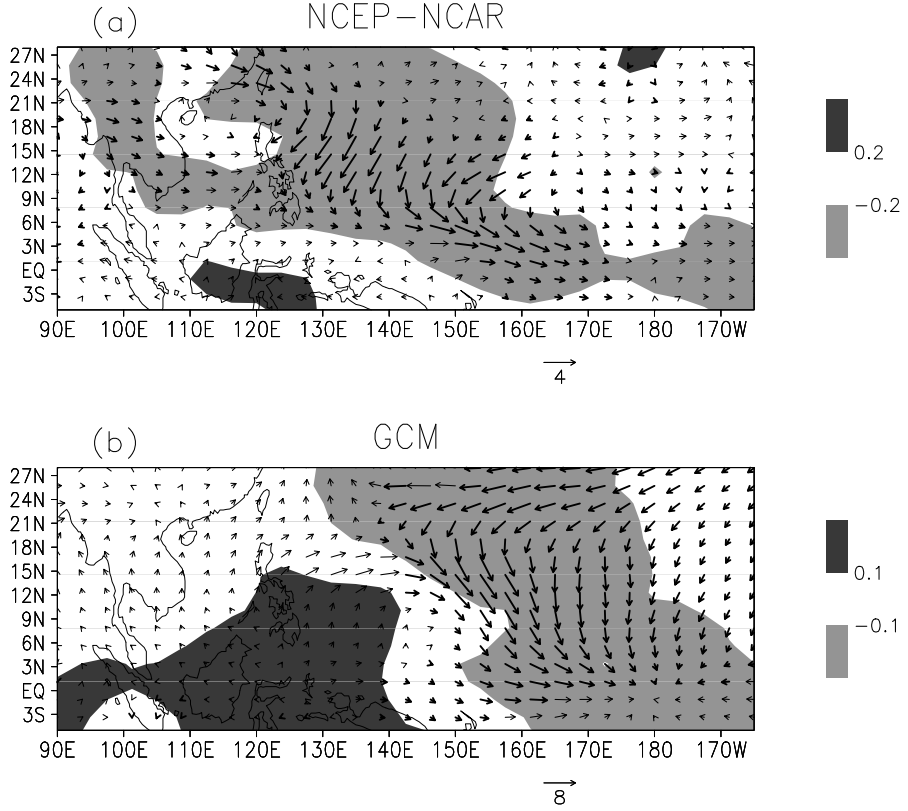


Figure 7.18: Warm-minus-cold values of both the **E**-vector ( $\frac{\overline{-u'^2}+\overline{v'^2}}{2}, -\overline{u'v'}$ ) (arrows, magnitudes in  $\text{m}^2\text{s}^{-2}$ ) and  $2kl(k^2 + l^2)^{-1}$  (shading), based on (a) NCEP-NCAR and (b) GCM data. Vectors with a negative component are indicated by bold arrows.

Warm-minus-cold values of the quantity  $\sin 2\theta = 2kl(k^2 + l^2)^{-1}$  are also shown in Fig. 7.18. As discussed before,  $\sin 2\theta$  is related with the horizontal tilt of disturbances, and is also proportional to  $c_{gy}$  for barotropic Rossby waves (see section 7.2.2). It can be seen that the value of  $\sin 2\theta$  is more negative over a broad region in the western Pacific during warm events, based on reanalyses results. It is noticed that this region also largely overlaps where the **E**-vector points more southward. The same association between the **E**-vectors and the wave tilt can also be found for GCM results. In other words, stronger equatorward dispersion

during warm events is accompanied by a change of wave tilt, which is consistent with dispersion of barotropic Rossby waves.

It is likely that the different southward dispersion would have an impact on the variability of disturbances near the equator. To examine this idea, the time series of the 850-mb eddy kinetic energy averaged over an equatorial region in the western Pacific, as well as the time series of the negative of  $c_{gy}$  over a more northern region covering part of the storm tracks, are plotted in Fig. 7.19. For the eddy kinetic energy, the area of  $140^{\circ}\text{E}-180^{\circ}$ ,  $5^{\circ}\text{N}-5^{\circ}\text{S}$  is selected, while for the group velocity, the region of  $135^{\circ}-155^{\circ}\text{E}$ ,  $5^{\circ}-25^{\circ}\text{N}$  is chosen for area averaging for reanalyses data ( $135^{\circ}-165^{\circ}\text{E}$ ,  $20^{\circ}\text{N}-5^{\circ}\text{S}$  for GCM)<sup>5</sup>. These quantities are found to be well correlated on the interannual basis, with correlation coefficients of 0.61 and 0.58 for reanalyses and GCM results, respectively. In other words, more southward dispersion is correlated with stronger equatorial disturbances. Without ruling out other mechanisms, it seems that the energy dispersion from active disturbances further north could be important for the growth or maintenance of synoptic-scale activity in the western Pacific close to the equator.

---

<sup>5</sup>SB99 showed an analogous plot comparing the amount of activity over the western Pacific and zonal wind entering the region (their Fig. 10); their idea is borrowed here.

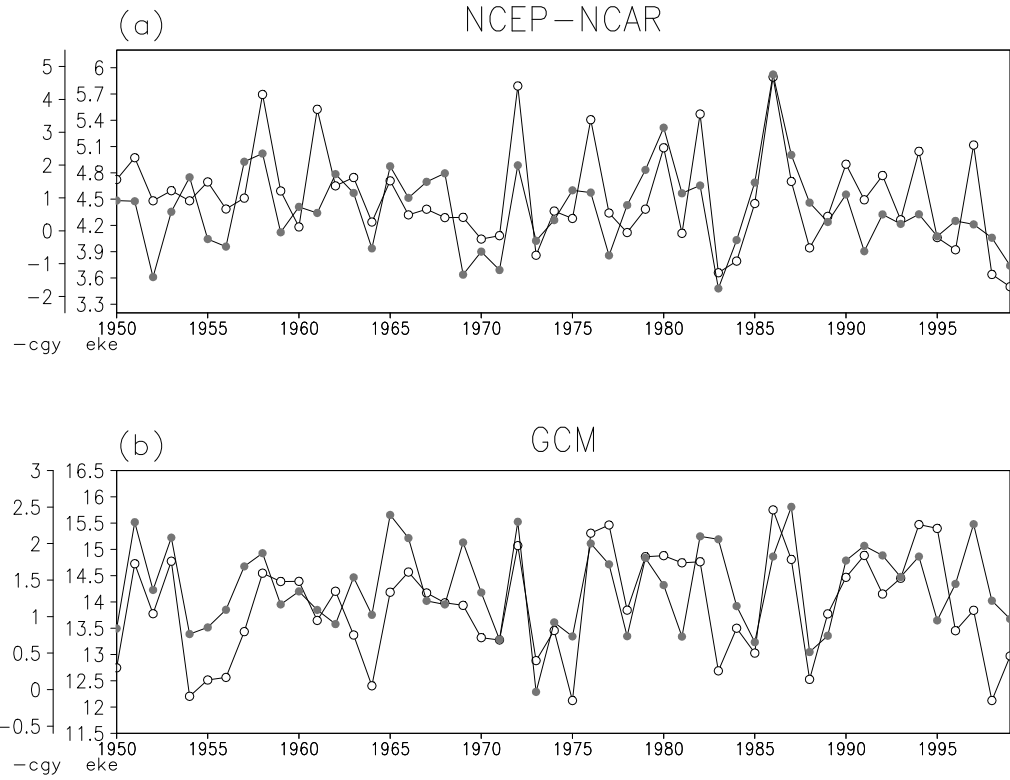


Figure 7.19: (a) Time series of eddy kinetic energy (open circle, in  $\text{m}^2\text{s}^{-2}$ ) averaged over the domain of  $140^\circ\text{E}-180^\circ, 5^\circ\text{N}-5^\circ\text{S}$ , and negative meridional group velocity (filled circle, in  $\text{ms}^{-1}$ ), based on (a) NCEP-NCAR and (b) GCM data. For reanalyses data, group velocity values are averaged over  $135^\circ-155^\circ\text{E}, 5^\circ\text{N}-25^\circ\text{N}$ ; for GCM data, averaging is carried out over  $135^\circ-165^\circ\text{E}, 5^\circ\text{S}-20^\circ\text{N}$ .

### 7.3.3 Effects on equatorial disturbances

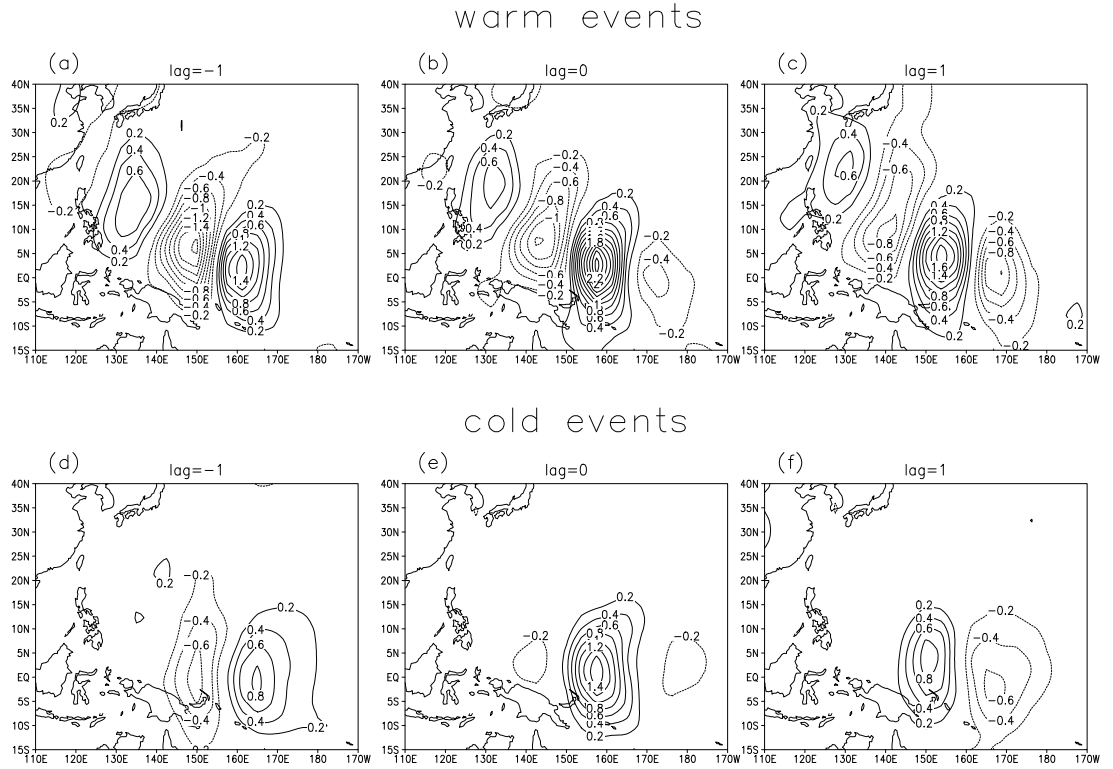


Figure 7.20: Lag regression of 2-15-day filtered  $v_{850}$ , with reference grid point at about  $160^{\circ}\text{E}$ , equator, during warm [(a), (b) and (c)] and cold [(d), (e) and (f)] events. Results for the lag of -1, 0 and 1 day are shown. Computation is based on NCEP-NCAR reanalyses. Unit:  $\text{ms}^{-1}$ .

In section 7.2.3 it is shown that MRG waves tend to transform into TD-type disturbances as they propagate westward. It is found that such transformation of wave types is also affected by ENSO. Fig. 7.20 shows the one-point lag regression of the filtered  $v_{850}$  with the reference point at about  $160^{\circ}\text{E}$  at the equator. Comparing the regression maps in different ENSO phases, the most striking feature is the different tendency of equatorial waves to transform into TD-type perturba-

tions. Strong perturbations with a northeast-southwest tilt are found east of the Philippines during warm events, and together with equatorial disturbances they take the form of a wavetrain. As in the climatological situation, southeastward dispersion can also be inferred (see Fig. 7.5). During cold events, activity along the equator is weaker. Unlike the warm ENSO case, however, MRG waves do not transform into any TD-type perturbations. The interpretation of these findings is that, while the existence of MRG waves do not depend on TD-type disturbances, the latter can be important source of energy (or wave activity) for MRG waves.

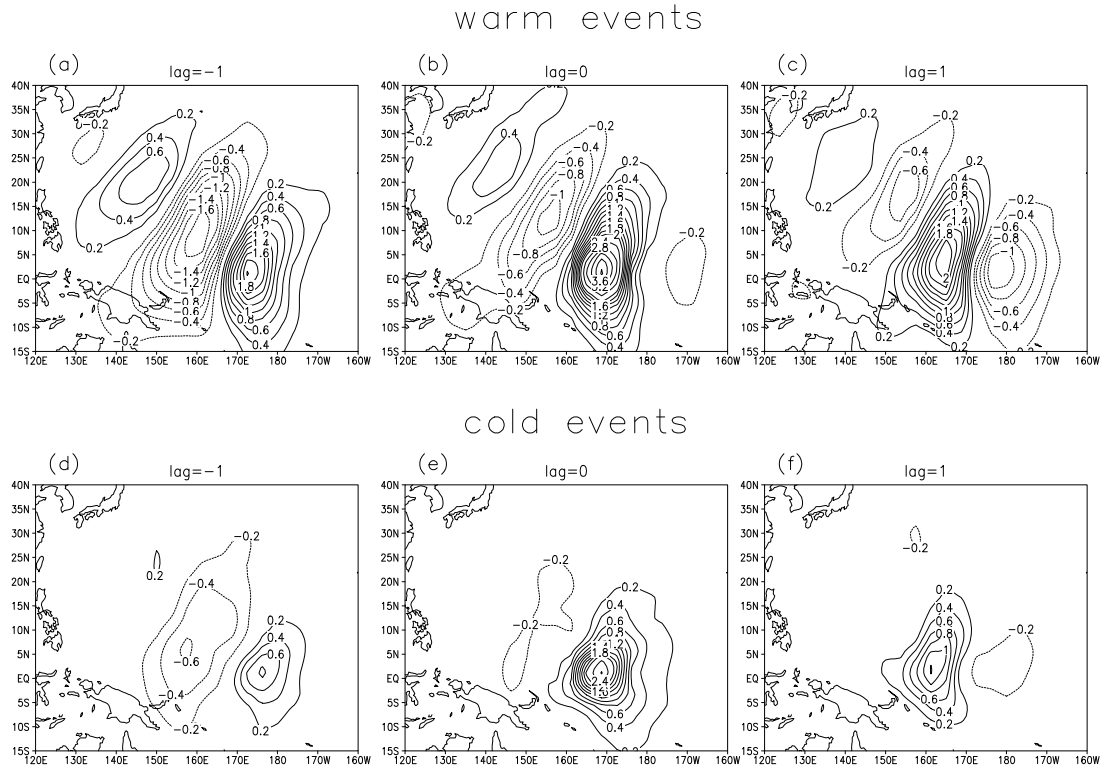


Figure 7.21: As in Fig. 7.20 but using GCM data, for the reference point of  $170^{\circ}\text{E}$ , equator.

Analogous regression results based on GCM data are shown in Fig. 7.21, with

the reference point at about  $170^{\circ}\text{E}$ . Again there is a dramatic difference between the evolution of disturbances during warm and cold events. Perturbations along the equator are seen to transform into those of the TD-type during warm events. During cold ENSO events on lag day -1, there is a hint of some tilted perturbations west of the reference grid point, but overall they do not evolve into anything with large amplitudes off the equator.

Regression of the 850-mb wind, vorticity and precipitation, with the same  $v_{850}$  variable at about  $170^{\circ}\text{E}$ ., are also shown in Fig. 7.22. Results are based on GCM data from warm and cold events. A wavetrain of vorticity disturbances with a northeast-southwest tilt is found in the northwestern part of the domain during warm events. Again, southeastward dispersion can also be inferred from the evolution of anomalies. During cold events, there is a hint of perturbations in off-equatorial regions but they are rather weak and not very coherent. It is noteworthy that, close to the equator, the anomalous convection during warm and cold events are actually quite comparable in magnitude at zero lag. Yet there is no prominent TD-type disturbances found during cold events at the lag of +1 day. Numerical experiments of Sobel and Horinouchi (2000), using on a basic state at rest, showed that imposed heating located at about  $10^{\circ}$  should effectively excite TD-like perturbations. The selection or transformation into TD-like anomalies seen here is likely to be related to environmental factors, such as the horizontal and vertical wind shear.

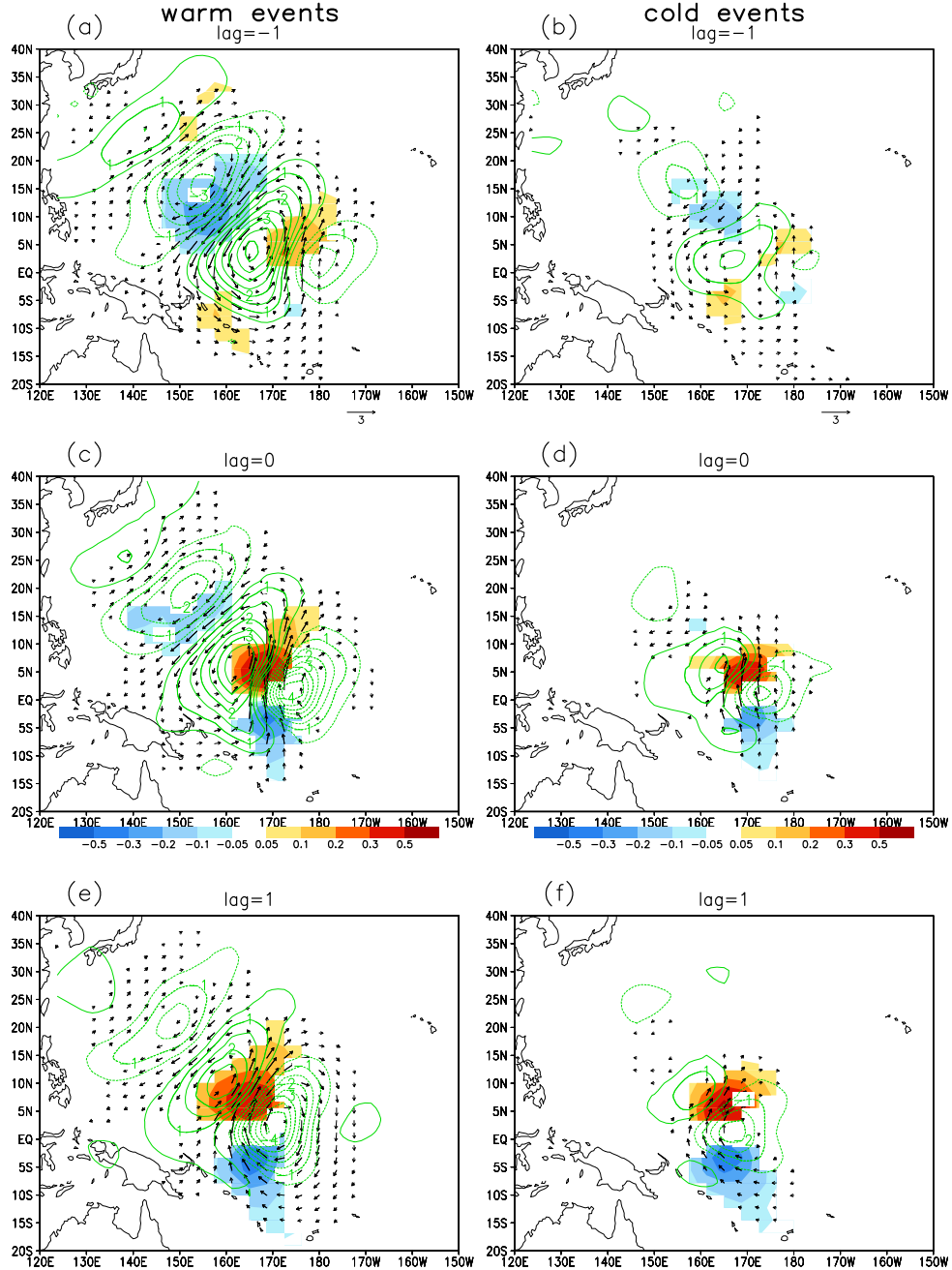


Figure 7.22: Lag regression of 850-mb wind (vectors, with magnitude in  $\text{ms}^{-1}$ ), vorticity (contours, in  $10^{-6}\text{s}^{-1}$ ) and precipitation (shading, in  $\text{cmday}^{-1}$ ), computed as in Fig. 7.21 using GCM data. Left and right panels show results during warm and cold events, respectively. Plotting conventions for wind vectors and vorticity are the same as Fig. 7.9. Wind and precipitation anomalies exceed the 95% significance level.

The vertical structure of equatorial disturbances is also affected by ENSO. Fig. 7.23 shows the cross section of simultaneous regression map of  $v$ -wind at various levels with  $v_{850}$ , during warm and cold events. Computation is based on GCM data, with the same reference point as in Fig. 7.21. During El Niño years perturbations near the selected grid point is seen to extend vertically with the same sign to about the level of  $\sigma = 0.4$ , above which there is a swift change of sign. On the other hand, during La Niña years perturbations are shallower, with a hint of anomalies being tilted eastward with height. Reanalyses data show very similar results, despite the fact that the barotropic component during warm events extends further up to about 300 mb. Essentially the same effect of ENSO on the vertical structure of perturbations were reported in observational studies of Chang and Miller (1977) and Takayabu and Nitta (1993). As mentioned in these studies, such a difference is probably the result of different vertical shear of the zonal flow over the western-central Pacific, as suggested by the findings of Holton (1971). Here it is seen that a similar change of the vertical structure of synoptic-scale disturbances during ENSO is also present in GCM simulations.

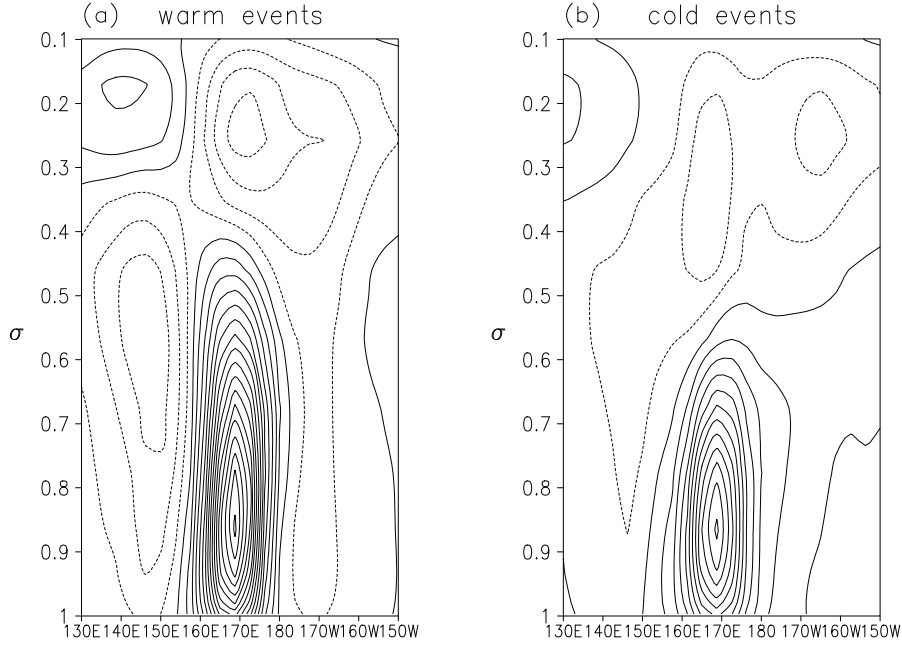


Figure 7.23: Regression of 2-15-day filtered  $v$ -wind at different vertical levels, onto 2-15-day filtered  $v_{850}$  at about  $170^\circ\text{E}$ , equator, during (a) warm and (b) cold events. Cross-section along the equator is shown; results based on GCM data. Contours in  $0.2\text{ms}^{-1}$ .

### 7.3.4 Discussion

Holland (1995) argued that, should equatorial waves acquire westward group propagation, they could be important source of wave activity for disturbances over the western Pacific. It is therefore worth noting that MRG waves are found to have eastward group velocity over much of the equatorial Pacific, in accordance with a number of studies (Liebmann and Hendon 1990; Dunkerton and Baldwin 1993). In other words, MRG waves over the western-central Pacific cannot serve as sources of wave activity. While it is claimed that these long MRG waves have positive zonal group velocity, results here do not necessarily contradict SB99, in

which westward group propagation from the central to western Pacific north of about  $5^{\circ}\text{N}$  is found for short Rossby wave-like perturbations.

The sign of the zonal group velocity for MRG waves within the western-central Pacific can be small and ambiguous, however, as noted by SB99. For mean easterlies of about  $5\text{ms}^{-1}$  at the dateline, westward dispersion would follow if  $h_e$  is less than 25m (based on wavelength of approximately 7500km); this value lies in the middle of the range of 5 to 50m provided by Liebmann and Hendon (1990). On the other hand, results here suggest that  $h_e$  can be as large as 120m, as estimated by fitting  $(\omega)_{\text{int}}$  and  $k$  to the theoretical dispersion relation. Values of  $h_e$  given here are also larger than those provided by Dickinson and Molinari (2002). Nevertheless, they also showed eastward propagation of MRG wave packets.

The dispersion of the TD-type disturbances indicate an equatorward transfer of energy, which might serve to excite MRG waves near the equator. This could be an important mechanism for the continuous development of disturbances in the southeastern portion of the storm tracks (provided that environmental factors such as those favorable to convection remain unchanged). SB99 made a similar remark based on the convergence of their wave-activity flux over the western Pacific. However, statistical analyses presented here cannot not answer the question of how TD-type disturbances are initiated in the first place. Concerning how these disturbances are 'seeded', Dickinson and Molinari (2002) suggested that MRG waves themselves might be responsible. Hartmann and Maloney (2001) showed that small-scale eddies can appear in regions with energy concentration, based on integrations of a stochastic barotropic model without any convective coupling.

While only the barotropic conversion is considered in section 7.3.1, processes

such as conversion from eddy available potential energy is also important for the maintenance of eddy kinetic energy. In fact it is probably stronger than the barotropic conversion, especially in the northwestern part of the storm tracks (see Fig. 10 of LL92). It is expected that there is also stronger conversion from eddy available potential energy, which is related to diabatic heating, in more eastward locations during warm events, contributing to the increased variability there.

One interesting question is what controls the transformation of MRG waves into the TD-type as they propagate in the western Pacific. Takayabu and Nitta (1993) suggested that the vertical shear of the mean zonal wind governs the selection of wave type. Wang and Xie (1996) found that easterly shear would result in stronger low-level perturbations as well as a stronger barotropic component which is not trapped along the equator, for equatorial Rossby waves and MRG waves. It is also noteworthy that for the GCM experiment, SST over most part of the western Pacific is fixed at climatological values. In other words, the difference of wave type transformation during ENSO cannot be due to variability of the underlying local SST.

### 7.3.5 Conclusion

Summertime synoptic-scale disturbances are studied based on the NCEP-NCAR reanalyses and GCM simulations. Diagnostic tools developed in LL90 are employed for examination of the propagation and growth/decay rate of activity. Reanalyses results are consistent with those presented in LL90. Disturbances from GCM data are westward propagating and their storm tracks depict typical growth-and-decay patterns, as found in observations. Amplitudes of the pertur-

bations from the GCM are too strong, however, while their propagation could be sensitive to the simulated low-level mean flow.

Dispersion of synoptic-scale waves is examined for both reanalyses and GCM datasets. Eastward dispersion is found in many locations, while there is also a prominent southward component over the western Pacific where enhanced variability is found. The negative meridional group velocity in the region is accompanied by a northeast-southwest tilt of perturbations, consistent with the dispersion characteristics expected for barotropic Rossby waves.

The implied equatorward energy transfer of TD-type disturbances seems important for the variability of MRG waves within the western-central Pacific. On the other hand, MRG waves are found to transform into TD-type perturbations as they propagate eastward. Characteristics of these equatorial waves are consistent with the theoretical dispersion relation expected for MRG waves, with a value of equivalent depth  $h_e$  of about 60 to 120m. The GCM is able to simulate the evolution of this complex sequence of disturbances and transformation of wave types, with approximately same values of  $h_e$ . MRG waves are also found to have positive zonal group velocity, suggesting that these relatively long waves cannot serve as the source of activity for western Pacific synoptic-scale disturbances. Overall, short waves are found within regions with enhanced variability where confluence of the mean flow is also present in the vicinity. Short-scale perturbations over the Pacific sector tend to have small intrinsic group speeds.

The impact of ENSO on synoptic-scale variability over the western Pacific is examined, with emphasis on the propagation and dispersion characteristics, as well as the selection and transformation of wave types. Eastward extension of storm tracks is found during warm events. Disturbances are more coherent

with larger amplitudes, east of where they are most active in the climatological sense. Over this eastern sector of the ocean basin, stronger barotropic conversion from the mean to eddy kinetic energy is also found. Important for such stronger conversion is the enhanced cyclonic wind shear, related to the eastward penetration of low-level monsoon trough during warm ENSO events. NCEP-NCAR and GCM results agree in terms of the enhanced variability found more to the east during warm events, as well as the importance of the cyclonic shear on changes of barotropic conversion during ENSO.

Associated with the modulation of the storm tracks is the change of dispersion characteristics of synoptic-scale activity. During warm events, the prominent southeastward dispersion is found to extend more eastward, in longitudes approximately where the eddy amplitudes are also enhanced. Stronger eastward dispersion is likely to be due to the advection by the increased zonal flow. Enhanced southward directed group velocity is accompanied by perturbations having with a more prominent northeast-southwest tilt in the region, and is consistent with the dispersion of barotropic Rossby waves. **E**-vector analysis also shows a similar change of the meridional group velocity during ENSO.

Different dispersion patterns during ENSO are seen to affect the variability of the MRG waves, from both reanalyses and GCM results. A positive correlation exists between southward dispersion and eddy kinetic energy in the western-central Pacific near the equator. During warm compared to cold events, MRG waves have a stronger tendency to transform into the TD type at the same longitude. GCM simulations are able to capture this wave type selection during different phases of ENSO.

# **Chapter 8**

## **Discussion and Summary**

In this study, the influence of ENSO on the MJO, North Pacific low-frequency activity and summertime synoptic-scale disturbances are examined. Data from both a GCM experiment and NCEP-NCAR reanalyses are used to study these transient phenomena and how ENSO affects the behavior of eddies. In particular, the propagation, growth rates and wave dispersion of transient activity, as well as its related circulation features, are considered. To achieve these goals, different analysis methods and diagnostic tools are applied for considerations of different phenomena, yielding much information about the impact of ENSO and its related mechanisms. Extensive comparisons between results from the GCM and reanalyses are carried out. Overall, results based on the simulations and the observations are in broad agreement. Results based on ensemble GCM integrations are less noisy and have greater statistical significance. Also, by the design of the numerical experiment, climate variability from the ensemble can be attributed to the variation of the changing SST. ENSO-related signals from the experiment are more robust than those based on observations. Overall, it is demonstrated

that the GCM is a useful tool for studying the interannual variability of eddies in both tropical and extratropical regions.

In order to obtain information on the phase and amplitude of the MJO, CEOF analysis is carried out based on the velocity potential. Circulation associated with the MJO can be found by either a composite procedure or as lag regression onto the PC time series. More eastward penetration of MJO convective anomalies over the central Pacific is found, during warm ENSO episodes. Regions of strong large-scale divergent flow, as well as growth-and-decay patterns of the velocity potential, are also shifted eastward in the warm ENSO phase. For summertime synoptic-scale disturbances, information on their coherence, wave-like character, growth rates and propagation are extracted by analysis tools developed in LL90. During warm events in the western Pacific, there is also an eastward displacement of their storm tracks and regions with large amplitudes. In general, regions of enhanced variability in both the synoptic and intraseasonal time scale are shifted eastward from the western Pacific, comparing warm to cold events.

These changes of eddy behavior associated with ENSO can be attributed to different mechanisms. Based on GCM data, accumulation of the low-level moist static energy is found to precede strong convection of the MJO at the equator, due to frictional convergence of moisture. An instability index, defined as the negative vertical gradient of the moist static energy, is found to precede convective signals, consistent with the idea that pre-conditioning is required for MJO convection to occur. During warm events, stronger signals of this index are found near the dateline, sustaining a more continuous eastward propagation of MJO

convective anomalies. This is mainly due to the difference of moisture accumulation, which can be partially attributed to the different low-level mean moisture in the region during the ENSO cycle.

For synoptic-scale variability, there is stronger barotropic conversion from the mean to eddy kinetic energy over the eastern sector of the western Pacific during warm ENSO events. Increased low-level cyclonic wind shear is found to play an important role; the latter feature is related to the anomalous eastward protrusion of the monsoon trough during warm events. The shift of the storm tracks also affects the dispersion pattern related to synoptic-scale activity. Comparing warm to cold events, the region with prominent southward dispersion is found more to the east, largely following where disturbances with a horizontal northeast-southwest tilt are located.

However, there are exceptions to this general pattern of change of activity. Intraseasonal upper-level wind anomalies are found to be stronger near the central Pacific and over the extreme eastern Pacific during cold events. Stronger mean westerlies in upper levels, which modify wave propagation characteristics in these equatorial regions, could be responsible for the increased eddy amplitudes in the cold ENSO phase.

To study the life cycle of low-frequency anomalies recurrent over the North Pacific, a lag regression method is used in which the lowpass 300-mb geopotential height field, averaged over some key region, serves as the reference time series. Wave-activity flux based on Takaya and Nakamura (2001) is found to be useful in

depicting the three-dimensional wave activity throughout the life cycle. There are incoming wave activity from the subtropical western Pacific and east Asia, while local baroclinic development contributes significantly to the growth of perturbations. Furthermore, it is found that coherent intraseasonal convective signals in the tropics are precursors of extratropical anomalies, based on GCM simulations. In fact for the GCM, low-frequency anomalies bear much resemblance with the constructive interference of the MJO- and WTP-related perturbations, the latter being a dominant mode of variability in high latitudes. The MJO and WTP phenomena are found to be independent of each other, and their interference follows a simple linear superposition principle.

Over the North Pacific sector, low-frequency variability is generally enhanced during cold ENSO episodes. Consideration of local energetics suggests that stronger deceleration of the Pacific jet could be important for the increased amplitudes of eddies during cold events. During the development of anomalies recurrent over the North Pacific, there is stronger incoming wave-activity flux from the western Pacific. More prominent dispersion downstream from the northern ocean to the west coast of U.S. is also found in the cold ENSO phase.

One of the most interesting results of this study is that, based on GCM simulations, the difference of low-frequency patterns seems to be related to the fact that strong intraseasonal convection is located differently during the ENSO cycle. In this regard, it is noteworthy that the MJO extratropical wavetrain is also influenced by ENSO. Extratropical anomalies tend to be more stationary over the North Pacific, with more prominent downstream dispersion to the west

coast of U.S.. The different dispersion patterns could be related to the change of the structure of the Pacific jet during ENSO, which affects its waveguide nature. Many of these features reflect those associated the low-frequency anomalies discussed above. This suggests that tropical intraseasonal variability could play a role on how ENSO affects extratropical low-frequency activity.

More work can be done in order to substantiate some of the results in this study. For instance, from the observations of the OLR, signals related to the intraseasonal oscillation can be extracted using the composite methods in Ch. 3, or those associated with synoptic-scale variability by the methods in Ch. 7, and valuable information can be obtained concerning the convective activity associated with these phenomena. In view of its potential importance on the extratropical circulation, the nature of the MJO-WTP interaction should be further studied, based on observations and also by using different GCMs. The results of Ch. 6 suggest a role of the intraseasonal oscillation on how ENSO affects low-frequency circulation in the extratropics. However, its relative importance compared with that due to the change of the basic state during ENSO is not assessed. The use of mechanistic models with a prescribed background state and with imposed heating or wave sources could answer this important question.

It is shown that the GCM can be a useful tool for studying the ENSO-related variability of atmospheric transient phenomena. Ensemble GCM experiments, with integrations carried out based on the same SST forcing, can provide some robust results which are often hard to obtain from observations. However, one has to be cautious when interpreting results from the GCM, since some of their

features can be model dependent. This can be a problem especially for studying the variability of the tropical climate. It is thus desirable to apply the same diagnostic tools to other observational datasets and data from integrations of different GCMs, in order to test the robustness of results presented in this study. Some of these diagnostics might also be useful for studying the interannual variability of transient activity not necessarily related to ENSO.

# Appendix A

## Analysis of Variance (ANOVA)

The method of ANOVA used by Rowell et al. (1995) is outlined here. Further details can be found in von Storch and Zwiers (1999).

Suppose a set of values  $\sigma_{ij}$  results from some ensemble GCM experiment with imposed SST that varies interannually. Here  $i = 1, 2, \dots, N$  and  $j = 1, 2, \dots, M$ , with  $N$  being the total number of years and  $M$  the number of ensemble members, an unbiased estimate of internal variance of the variable  $\sigma$  is defined as

$$\hat{var}_{\text{internal}} \equiv \frac{1}{(M-1)N} \sum_{j=1}^M \sum_{i=1}^N (\sigma_{ij} - \{\sigma\}_i)^2;$$

where  $\{\sigma\}_i = \frac{1}{M} \sum_{j=1}^M \sigma_{ij},$

is the ensemble mean of  $\sigma$  for each year. Notice that  $\hat{var}_{\text{internal}}$  would be small for small intra-ensemble variation. An estimate of external variance is given by:

$$\hat{var}_{\text{external}} \equiv \frac{1}{N-1} \sum_{i=1}^N (\{\sigma\}_i - \{\bar{\sigma}\})^2;$$

where  $\{\bar{\sigma}\} = \frac{1}{NM} \sum_{i=1}^N \sum_{j=1}^M \sigma_{ij},$

is the time mean of  $\{\sigma\}_i$ , i.e. the value of  $\sigma$  averaged over all years and ensemble members. An unbiased estimate of variance due to varying SST common to all ensemble members is

$$\hat{var}_{SST} = \hat{var}_{external} - \frac{1}{M} \hat{var}_{internal}.$$

As discussed in Rowell et al. (1995), this step can be interpreted as removing a 'residual' amount of variance in  $\hat{var}_{external}$  due to the presence of internal variability. (In practice,  $\hat{var}_{SST}$  could be negative over some region, and its value is set to zero wherever this occurs.) A 'total variance' is then given by the estimate:

$$\hat{var}_{total} = \hat{var}_{SST} + \hat{var}_{internal}.$$

The ratio  $\hat{var}_{SST}/\hat{var}_{total}$  can be interpreted as the fraction of variability attributed to SST, compared to the total amount of variability. Fig. 5.2 shows the square root of this ratio, based on the rms statistics of the 300-mb height field.

# References

- Alexander, A.M., and J.D. Scott, 1995: *Atlas of Climatology and Variability in the GFDL R30S14 GCM*. CIRES, University of Colorado, 121 pp.
- \_\_\_\_\_, I. Bladé, M. Newman, J.R. Lanzante, N.-C. Lau, and J.D. Scott, 2002: The atmospheric bridge: The influence of ENSO teleconnections on air-sea interaction over the global oceans. *J. Climate*, **15**, 2205-2231.
- Anyamba, E.K., and B.C. Weare, 1995: Temporal variability of the 40-50-day oscillation in tropical convection. *Int. J. Climatol.*, **15**, 379-402.
- Black, R.X. 1997: Deducing anomalous wave source regions during the life cycles of persistent flow anomalies. *J. Atmos. Sci.*, **54**, 895-907.
- \_\_\_\_\_, and R.M. Dole, 1993: The dynamics of large-scale cyclogenesis over the North Pacific Ocean. *J. Atmos. Sci.*, **50**, 421-442.
- Blackmon, M.L., Y.-H. Lee, J.M. Wallace and H.-H. Hsu, 1984: Time variation of 500 mb height fluctuations with long, intermediate and short time scales as deduced from lag-correlation statistics. *J. Atmos. Sci.*, **41**, 981-991.
- Bladé, I., and D.L. Hartmann, 1993: Tropical intraseasonal oscillations in a simple nonlinear model. *J. Atmos. Sci.*, **50**, 2922-2939.
- Branstator, G., 1987: A striking example of the atmosphere's leading traveling pattern. *J. Atmos. Sci.*, **44**, 2310-2323.

- \_\_\_\_\_, and I. Held, 1995: Westward propagating normal modes in the presence of stationary background waves. *J. Atmos. Sci.*, **52**, 247-262.
- Broccoli, A.J., and S. Manabe, 1992: The effects of orography on midlatitude northern hemisphere dry climates. *J. Climate*, **5**, 1181-1201.
- Burpee, R. W., 1972: The origin and structure of easterly waves in the lower troposphere of North Africa. *J. Atmos. Sci.*, **29**, 77-90.
- \_\_\_\_\_, 1974: Characteristics of North African easterly waves during the summers of 1968 and 1969. *J. Atmos. Sci.*, **31**, 1556-1570.
- Chang, C.-P., 1977: Viscous internal gravity waves and low-frequency oscillations in the tropics. *J. Atmos. Sci.*, **34**, 901-910.
- Chang, C.-P., and C.R. Miller 1977: Comparison of easterly waves in the tropical Pacific during two contrasting periods of sea surface temperature anomalies. *J. Atmos. Sci.*, **34**, 615-628.
- \_\_\_\_\_, V.F. Morris, and J.M. Wallace, 1970, A statistical study of easterly waves in the western Pacific: July-December 1964. *J. Atmos. Sci.*, **27**, 195-201.
- Chang, H.-R., and P.J. Webster, 1990: Energy accumulation and emanation at low latitudes. Part II: Nonlinear response to strong episodic equatorial forcing. *J. Atmos. Sci.*, **47**, 2624-2644.
- Charney, J.G., and J.G. DeVore, 1979: Multiple flow equilibria in the atmosphere and blocking. *J. Atmos. Sci.*, **38**, 1205-1216.
- Chatfield, C. 1989: *The analysis of time series : an introduction*. Chapman and Hall, 241 pp.
- Chen, W.Y., and H.M. van den Dool, 1997: Asymmetric impact of tropical SST anomalies on atmospheric internal variability over the North Pacific. *J. Atmos. Sci.*, **54**, 725-740.

- Compo, G.P., P.D. Sardeshmukh, and C. Penland, 2001: Changes of subseasonal variability associated with El Niño. *J. Climate*, **14**, 3356-3374.
- Dickinson, M. and J. Molinari, 2002: Mixed Rossby-gravity waves and western Pacific tropical cyclogenesis. Part I: Synoptic evolution. *J. Atmos. Sci.*, **59**, 2183-2196.
- Dickson, R.R., and J. Namias, 1976: North American influences on the circulation and climate of the North Atlantic sector. *Mon. Wea. Rev.*, **104**, 1255-1265.
- Dole, R.M., 1986a: Persistent anomalies of the extratropical northern hemisphere wintertime circulation: structure. *Mon. Wea. Rev.*, **114**, 178-207.
- , 1986b: The life cycles of persistent anomalies over the North Pacific. *Advances in Geophysics*, Vol. 29, Academic Press, 31-69.
- , and R.X. Black, 1983: Life cycles of persistent anomalies. Part II: The development of persistent negative height anomalies over the North Pacific Ocean. *Mon. Wea. Rev.*, **118**, 824-846.
- , and N.D. Gordon, 1983: Persistent anomalies of the extratropical northern hemisphere wintertime circulation: Geographical distribution and regional persistence characteristics. *Mon. Wea. Rev.*, **111**, 1567-1586.
- Dunkerton, T.J., and M.P. Baldwin, 1995: Observation of 3-6-day meridional wind oscillation over the tropical Pacific, 1973-1992: Horizontal structure and propagation. *J. Atmos. Sci.*, **52**, 1585-1601.
- Emanuel, K.A., 1987: An air-sea interaction model of intraseasonal oscillations in the tropics. *J. Atmos. Sci.*, **44**, 2324-2340.
- Feldstein, S., 1998: The growth and decay of low-frequency anomalies in a GCM. *J. Atmos. Sci.*, **55**, 415-428.
- Fink, A., and P. Speth, 1997: Some potential forcing mechanisms of the year-to-year

- variability of the tropical convection and its intraseasonal (25-70-day) variability.  
*Int. J. Climatol.*, **17**, 1513-1534.
- Frederiksen, J.S., 1982: A unified three-dimensional instability theory of the onset of blocking and cyclogenesis. *J. Atmos. Sci.*, **39**, 969-982.
- , 1983: A unified three-dimensional instability theory of the onset of blocking and cyclogenesis. II. Teleconnection patterns. *J. Atmos. Sci.*, **40**, 2593-2609.
- , 1998: Precursors to blocking anomalies: The tangent linear and inverse problems. *J. Atmos. Sci.*, **55**, 2419-2436.
- Gill, A.E., 1980: Some simple solutions for heat-induced tropical circulation. *Quart. J. Roy. Meteor. Soc.*, **106**, 447-462.
- Gordon, C.T., and W.F. Stern, 1982: A description of the GFDL global spectral Model. *Mon. Wea. Rev.*, **110**, 625-644.
- Gu, G., and C. Zhang, 2001: A spectrum analysis of synoptic-scale disturbances in the ITCZ. *J. Climate*, **14**, 2725-2739.
- Gutzler, D.S., 1991: Interannual fluctuations of intraseasonal variance of near-equatorial zonal winds. *J. Geophys. Res.*, **96**, 3173-3185.
- Hartmann, D.L., and E.D. Maloney 2001: The Madden-Julian oscillation, barotropic dynamics, and North Pacific tropical cyclone formation. Part II: Stochastic barotropic modeling. *J. Atmos. Sci.*, **58**, 2559-2570.
- Hayashi, Y., 1971: A generalized method of resoling disturbances into progressive and retrogressive waves by space Fourier and time cross-spectral analyses. *J. Meteor. Soc. Japan*, **49**, 125-128.
- , and D.G. Golder, 1993: Tropical 40-50 and 25-30-day oscillation appearing in realistic and idealized GFDL climate models and the ECMWF dataset. *J.*

- Atmos. Sci.*, **50**, 464-493.
- Hayashi, Y.-Y., and A. Sumi, 1986: The 30-40 day oscillations simulated in an "aqua planet" model. *J. Meteor. Soc. Japan*, **64**, 451-467.
- Held, I. M., and I.-S. Kang, 1987: Barotropic models of the extratropical response to El Niño. *J. Atmos. Sci.*, **44**, 3576-3586.
- \_\_\_\_\_, S.W. Lyons, and S. Nigam, 1989: Transients and the extratropical response to El Niño. *J. Atmos. Sci.*, **46**, 163-176.
- Hendon, H.H., 2000: Impact of air-sea coupling on the Madden-Julian oscillation in a general circulation model. *J. Atmos. Sci.*, **57**, 3939-3952.
- \_\_\_\_\_, and B. Liebmann, 1990: A composite study of onset of the Australian summer monsoon. *J. Atmos. Sci.*, **47**, 2227-2240.
- \_\_\_\_\_, and M.L. Salby, 1994: The life cycle of the Madden-Julian oscillation. *J. Atmos. Sci.*, **51**, 2225-2337.
- \_\_\_\_\_, C. Zhang, and J.D. Glick, 1999: Interannual variation of the Madden-Julian oscillation during austral summer. *J. Climate*, **12**, 2538-2550.
- Higgins, R. W., and K.C. Mo, 1997: Persistent North Pacific circulation anomalies and the tropical intraseasonal oscillation. *J. Climate*, **10**, 223-244.
- Holland, G.J., 1995: Scale interaction in the western Pacific monsoon. *Meteor. Atmos. Phys.*, **56**, 57-79.
- Holton, J.R. 1971: A diagnostic model for equatorial wave disturbances: The role vertical wind shear of the mean zonal wind. *J. Atmos. Sci.*, **28**, 55-64.
- Honda, M., H. Nakamura, J. Ukita, I. Kousaka, and K. Takeuchi, 2001: Interannual seesaw between the Aleutian and Icelandic lows. Part I: Seasonal dependence and life cycle. *J. Climate*, **14**, 1029-1042.
- Horel, J.D., 1984: Complex principal component analysis: Theory and examples.

- J. Appl. Meteor.*, **23**, 1660-1673.
- \_\_\_\_\_, and J.M. Wallace, 1981: Planetary-Scale atmospheric phenomena associated with the southern oscillation. *Mon. Wea. Rev.*, **109**, 813-829.
- Hoskins, B.J., and T. Ambrizzi, 1993: Rossby wave propagation on a realistic longitudinally varying flow. *J. Atmos. Sci.*, **50**, 1661-1671.
- \_\_\_\_\_, I.N. James, and G.H. White 1983: The shape, propagation and mean-flow interaction of large-scale weather systems. *J. Atmos. Sci.*, **40**, 1595-1612.
- \_\_\_\_\_, and D.J. Karoly, 1981: The steady linear response of a spherical atmosphere to thermal and orographic forcing. *J. Atmos. Sci.*, **38**, 1179.1196.
- Hubert, L.F., 1949: On the formation of typhoons. *J. Meteorol.*, **5**, 247-264.
- Jones, C., and B.C. Weare, 1996: The role of low-level moisture convergence and ocean latent heat fluxes in the Madden and Julian oscillation: an observational analysis using ISCCP data and ECMWF analyses *J. Climate*, **9**, 3086-3104.
- Kalnay, E., and Coauthors, 1996: The NCEP/NCAR 40-year Reanalysis Project. *Bull. Amer. Meteor. Soc.*, **77**, 437-471.
- Kemball-Cook, S.R., and B.C. Weare 2001: The onset of convection in the Madden-Julian oscillation. *J. Climate*, **14**, 780-792.
- Kiladis, G.N., and K.M. Weickmann, 1992: Circulation anomalies associated with tropical convection during northern winter. *Mon. Wea. Rev.*, **120**, 1900-1923.
- Kistler, R., and Coauthors, 2001: The NCEP-NCAR 50-year reanalysis: Monthly means CD-ROM and documentation. *Bull. Amer. Meteor. Soc.*, **82**, 247-268.
- Knutson, T.R., and K.M. Weickmann 1987: 30-60 day atmospheric oscillations: composite life cycles of convection and circulation anomalies. *Mon. Wea. Rev.*, **115**, 1407-1436.
- Krishnan, R., C. Zhang and M. Sugi 2000: Dynamics of breaks in the Indian summer

- monsoon. *J. Atmos. Sci.*, **57**, 1354-1372.
- Kushnir, Y., 1987: Retrograding wintertime low-frequency disturbances over the North Pacific Ocean. *J. Atmos. Sci.*, **44**, 2727-2742.
- Kutzbach, J.E., 1970: Large-scale features of monthly mean northern hemisphere anomaly of sea-level pressure. *Mon. Wea. Rev.*, **98**, 708-716.
- Lander, M.A., 1994: An explanatory analysis of the relationship between tropical storm formation in the western North Pacific and ENSO. *Mon. Wea. Rev.*, **122**, 636-651.
- Lau, K.-H., 1991: An observational study of tropical summertime synoptic scale disturbances. Ph.D. dissertation, Princeton Univ., New Jersey, 243 pp.
- \_\_\_\_\_, and N.-C. Lau, 1990: Observed structure and propagation characteristics of tropical summertime synoptic scale disturbances. *Mon. Wea. Rev.*, **118**, 1888-1913.
- \_\_\_\_\_, and \_\_\_\_\_, 1992: The energetics and propagation dynamics of tropical summertime synoptic-scale disturbances. *Mon. Wea. Rev.*, **120**, 2523-2539.
- Lau, K.-M., and P.H. Chan 1985: Aspects of the 40-50 day oscillation during the northern winter as inferred from outgoing longwave radiation. *Mon. Wea. Rev.*, **113**, 1889-1909.
- \_\_\_\_\_, and L. Peng, 1987: Origin of low-frequency (intraseasonal) oscillations in the tropical atmosphere. Part I: Basic theory. *J. Atmos. Sci.*, **44**, 950-972.
- Lau, N.-C., 1988: Variability of the observed midlatitude storm tracks in relation to low-frequency changes in the circulation pattern. *J. Atmos. Sci.*, **45**, 2718-2743.
- \_\_\_\_\_, I.M. Held, and J.D. Neelin 1988: The Madden-Julian oscillation in an idealized general circulation model. *J. Atmos. Sci.*, **45**, 3810-3832.
- \_\_\_\_\_, and K.-M. Lau, 1986: The structure and propagation of intraseasonal

- oscillations appearing in a GFDL general circulation model. *J. Atmos. Sci.*, **43**, 2023-2047.
- , and M.J. Nath, 1996: The role of the "atmospheric bridge" in linking tropical Pacific ENSO events to extratropical SST anomalies. *J. Climate*, **9**, 2036-2057.
- , and ———, 1999: Observed and GCM-simulated westward-propagating, planetary-scale fluctuations with approximately three-week periods. *Mon. Wea. Rev.*, **127**, 2324-2345.
- , and ———, 2003: Atmosphere-ocean variations in the Indo-Pacific sector during ENSO episodes. *J. Climate*, **16**, 3-20.
- Lejenäs, H., and R.A. Madden, 1992: Traveling planetary-scale waves and blocking. *Mon. Wea. Rev.*, **120**, 2821-2830.
- Liebmann, B., and H.H. Hendon, 1990: Synoptic-scale disturbances near the equator. *J. Atmos. Sci.*, **47**, 1463-1479.
- Lighthill, J., 1978: *Waves in fluids*. Cambridge University Press, 504 pp.
- Lindzen, R.D., 1967: Planetary waves on Beta-planes. *Mon. Wea. Rev.*, **95**, 441-451.
- Lorenc, A.C., 1984: The evolution of planetary scale 200 mb divergent flow during the FGGE year. *Quart. J. Roy. Meteor. Soc.*, **110**, 427-441.
- Madden, R.A., and P.R. Julian 1971: Detection of a 40-50 day oscillation in the zonal wind in the tropical Pacific. *J. Atmos. Sci.*, **28**, 702-708.
- , and ——— 1972: Description of global-scale circulation cells in the tropics with a 40-50 day period. *J. Atmos. Sci.*, **29**, 1109-1123.
- , and ——— 1994: Observation of the 40-50-day tropical oscillation- a review. *Mon. Wea. Rev.*, **122**, 814-837.

- Maloney, E.D., and D.L. Hartmann 1998: Frictional moisture convergence in a composite life cycle of the Madden-Julian oscillation. *J. Climate*, **11**, 2387-2403.
- , and ————— 2001: The Madden-Julian oscillation, barotropic dynamics, and North Pacific tropical cyclone formation. Part I: Observations. *J. Atmos. Sci.*, **58**, 2545-2558.
- Manabe, S., J. Smagorinsky, and R.F. Strickler, 1965: Simulated climatology of a general circulation model with a hydrological cycle. *Mon. Wea. Rev.*, **93**, 769-798.
- Matsuno, T., 1966: Quasi-geostrophic motions in the equatorial area. *J. Meteor. Soc. Japan*, **44**, 25-42.
- Meehl, G.A., G.N. Kiladis, K.M. Weickmann, M. Wheeler, D.S. Gutzler, and G.P. Compo, 1996; Modulation of equatorial subseasonal convective episodes by tropical-extratropical interaction in the Indian and Pacific Ocean regions. *J. Geophys. Res.*, **101**, 15033-15049.
- Mullen, S.L., 1989: Model experiments on the impact of Pacific sea surface temperature anomalies on blocking frequency. *J. Climate*, **9**, 997-1013.
- Nakamura, H., 1992 Midwinter suppression of baroclinic wave activity in the Pacific. *J. Atmos. Sci.*, **49**, 1629-1642.
- , M. Nakamura, and J.L. Anderson, 1997: The role of high- and low-frequency dynamics in blocking formation. *Mon. Wea. Rev.*, **125**, 2074-2093.
- , and J.M. Wallace, 1990: Observed changes in baroclinic wave activity during the life cycles of low-frequency circulation anomalies. *J. Atmos. Sci.*, **47**, 1100-1116.
- Namias, J. 1978: Multiple causes of the North American abnormal winter 1976-77. *Mon. Wea. Rev.*, **106**, 279-295.

- \_\_\_\_\_, 1986: Persistence of flow patterns over North America and adjacent ocean sectors. *Mon. Wea. Rev.*, **114**, 1368-1383.
- Naoe, H., Y. Matsuda, and H. Nakamura, 1997: Rossby wave propagation in idealized and realistic zonally varying flow. *J. Meteor. Soc. Japan*, **75**, 687-700.
- Neelin, J.D., I.M. Held, and K.H. Cook, 1987: Evaporation-wind feedback and low-frequency variability in the tropical atmosphere. *J. Atmos. Sci.*, **44**, 2341-2348.
- Palmer, T.N., 1988: Medium and extended range predictability and stability of the Pacific/North America mode. *Quart. J. Roy. Meteor. Soc.*, **114**, 691-713.
- Parrish, D.F., and J.C. Derber, 1992: The National Meteorological Center's spectral statistical-interpolation analysis system. *Mon. Wea. Rev.*, **120**, 1747-1763.
- Plumb, R.A. 1986: Three-dimensional propagation of transient quasi-geostrophic eddies and its relationship with the eddy forcing of the time-mean flow. *J. Atmos. Sci.*, **43**, 1657-1678.
- Raymond, D.J., 2001: A new model of the Madden-Julian oscillation. *J. Atmos. Sci.*, **58**, 2807-2819.
- Reed, R.J. and E.E. Recker, 1971: Structure and properties of synoptic-scale wave disturbances in the equatorial western Pacific. *J. Atmos. Sci.*, **28**, 1117-1133.
- Reihl, H., 1945: Waves in the easterlies and the polar front in the tropics, *Misc. Rep. No. 17*, University of Chicago Press, Ill.
- \_\_\_\_\_, 1948: On the formation of typhoons. *J. Meteorol.*, **16**, 247-264.
- Renshaw, A.C., D.P. Rowell, and C.K. Folland, 1998: Wintertime low-frequency weather variability in the North Pacific-American sector 1949-93. *J. Climate*, **11**, 1073-1093.
- Renwick, J.A., 1998: ENSO-Related variability in the frequency of South Pacific blocking. *Mon. Wea. Rev.*, **125**, 3117-3123.

- \_\_\_\_\_, and J.M. Wallace, 1986: Relationships between North Pacific wintertime blocking, El Niño, and the PNA pattern. *Mon. Wea. Rev.*, **124**, 2071-2076.
- Rowell, D.P., C.K. Folland, K. Maskell and M.N. Ward, 1995: Variability of summer rainfall over tropical north Africa (1906-92): Observations and modelling. *Quart. J. Roy. Meteor. Soc.*, **121**, 669-704.
- Salby, M.L., and H.H. Hendon 1994: Intraseasonal behavior of clouds, temperature, and motion in the tropics. *J. Atmos. Sci.*, **51**, 2207-2224.
- Sardeshmukh, P.D., and B.J. Hoskins, 1988: The generation of global rotational flow by steady idealized tropical divergence. *J. Atmos. Sci.*, **45**, 1228-1251.
- Shinoda, T., H.H. Hendon, and J. Glick, 1999: Intraseasonal surface fluxes in the tropical western Pacific and Indian oceans from NCEP reanalyses. *Mon. Wea. Rev.*, **127**, 678-692.
- Simmons, A.J., J.M. Wallace, and G.W. Branstator, 1983: Barotropic wave propagation and instability, and atmospheric teleconnection patterns. *J. Atmos. Sci.*, **40**, 1363-1392.
- Slingo, J.M., D.P. Rowell, K.R. Sperber, and F. Nortley, 1999: On the predictability of the interannual behaviour of the Madden-Julian oscillation and its relationship with El Niño. *Quart. J. Roy. Meteor. Soc.*, **125**, 583-609.
- Smith, C.A., and P.D. Sardeshmukh, 2000: The effect of ENSO on the intraseasonal variance of surface temperatures in winter. *Int. J. Climatol.*, **20**, 1543-1557.
- Sobel, A.H., and C.S. Bretherton, 1999: Development of synoptic-scale disturbances over the summertime tropical northwest Pacific. *J. Atmos. Sci.*, **56**, 3160-3127.
- \_\_\_\_\_, and T. Horinouchi, 2000: On the dynamics of easterly waves, monsoon depressions, and tropical depression type disturbances. *J. Meteor. Soc. Japan*, **78**, 167-173.

- \_\_\_\_\_, and E.D. Maloney, 2000: Effect of ENSO and the MJO on western North Pacific tropical cyclones. *Geophys. Res. Lett.*, **27**, 1739-1742.
- Straus, D.M., and J. Shukla, 1997: Variations of midlatitude transient dynamics associated with ENSO. *J. Atmos. Sci.*, **54**, 777-790.
- Takaya, K., and H. Nakamura, 2001: A formulation of a phase-independent wave-activity flux for stationary and migratory quasigeostrophic eddies on a zonally varying basic flow. *J. Atmos. Sci.*, **58**, 608-627.
- Takayabu, Y.N., 1994: Large-scale cloud disturbances associated with equatorial waves. Part I: Spectral features of the cloud disturbances. *J. Meteor. Soc. Japan*, **72**, 433-448.
- \_\_\_\_\_, and T. Nitta, 1993: 3-5 day-period disturbances coupled with convection over the tropical Pacific Ocean. *J. Meteor. Soc. Japan*, **71**, 221-246.
- Thorncroft, C.D., and D.P. Rowell, 1998: Interannual variability of African wave activity in a general circulation model. *Int. J. Climatol.*, **18**, 1305-1323.
- Ting, M., and P.D. Sardeshmukh, 1993: Factors determining the extratropical response to equatorial diabatic heating anomalies. *J. Atmos. Sci.*, **50**, 907-918.
- Trenberth, K.E., 1986: An assessment of the impact of transient eddies on the zonal flow during a blocking episode using localized Eliassen-Palm flux diagnostic. *J. Atmos. Sci.*, **43**, 2070-2087.
- \_\_\_\_\_, 1997: The definition of El Niño. *Bull. Amer. Meteor. Soc.*, **78**, 2771-2777.
- \_\_\_\_\_, G.W. Branstator, D. Karoly, A. Kumar, N.-C. Lau, and C. Ropelewski, 1998: Progress during TOGA in understanding and modeling global teleconnections associated with tropical sea-surface temperatures. *J. Geophys. Res.*, **103**, 14291-14324.

- Vincent, D.G., A. Fink, J.M. Schrage, and P. Speth, 1998: High- and low-frequency intraseasonal variance of OLR on annual and ENSO timescales. *J. Climate*, **11**, 968-986.
- von Loon, H.R., and J.C. Rogers, 1978: The seesaw in winter temperatures between Greenland and northern Europe. Part I: General description. *Mon. Wea. Rev.*, **106**, 296-310.
- von Storch, H., and Zwiers, F.W., 1998: *Statistical analysis in climate research*. Cambridge University Press, 484 pp.
- Waliser, D. E., K.M. Lau, and J.-H. Kim, 1999: The influence of coupled sea surface temperatures on the Madden-Julian oscillation: A model perturbation experiment. *J. Atmos. Sci.*, **56**, 333-358.
- Wallace, J.M., 1971: Spectral studies of tropospheric wave disturbances in the tropical western Pacific. *Rev. Geophys. Space Phys.*, **9**, 577-612.
- \_\_\_\_\_, and C.-P. Chang, 1969: Spectrum analysis of large-scale wave disturbances in the tropical lower troposphere. *J. Atmos. Sci.*, **26**, 1010-1025.
- \_\_\_\_\_, and D.S. Gutzler, 1981: Teleconnections in the geopotential height field during the Northern hemisphere winter. *Mon. Wea. Rev.*, **109**, 784-812.
- \_\_\_\_\_, and N.-C. Lau, 1985: On the role of barotropic energy conversions in the general circulation. *Advances in Geophysics*, Vol. 28, Academic Press, 33-74.
- \_\_\_\_\_, G.-H. Lim, and M.L. Blackmon, 1988: Relationship between cyclone tracks, anticyclone tracks and baroclinic waveguides. *J. Atmos. Sci.*, **45**, 439-462.
- \_\_\_\_\_, E.M. Rasmusson, T.P. Mitchell, V.E. Kousky, E.S. Sarachik, and H. von Storch, 1998: On the structure and evolution of ENSO-related climate variability in the tropical Pacific: Lessons from TOGA. *J. Geophys. Res.*, **103**, 14241-14260.

- Wang, B., 1988: Comments on "An air-sea interaction model of intraseasonal oscillation in the tropics". *J. Atmos. Sci.*, **22**, 3521-3525.
- , and J.C.L. Chan, 2002: How strong ENSO events affect tropical storm activity over the western North Pacific. *J. Climate*, **15**, 1643-1658.
- , and T. Li, 1994: Convective interaction with boundary-layer dynamics in the development of a tropical intraseasonal system. *J. Atmos. Sci.*, **51**, 1386-1400.
- , and X. Xie, 1998: Coupled modes of the warm pool climate system. Part I: The role of air-sea interaction in maintaining Madden-Julian oscillation. *J. Climate*, **11**, 2116-2135.
- Wang, X.-L., and T. Murakami, 1988: Intraseasonal disturbance activity before, during and after the 1982-83 ENSO. *J. Atmos. Sci.*, **45**, 3754-3770.
- Webster, P.J., and H.-R. Chang, 1988: Equatorial energy accumulation and emanation regions: Impacts of a zonally varying basic state. *J. Atmos. Sci.*, **45**, 803-829.
- , and J.R. Holton, 1982: Cross-equatorial response to middle-latitude forcing in a zonally varying basic state. *J. Atmos. Sci.*, **39**, 722-733.
- Weickmann, K.M., and S.J.S. Khalsa, 1990: The shift of convection from the Indian ocean to the western Pacific Ocean during a 30-60 day oscillation. *Mon. Wea. Rev.*, **118**, 964-978.
- , G.R. Lussky, and J.E. Kutzbach, 1985: Intraseasonal (30-60 Day) fluctuations of outgoing longwave radiation and 250 mb streamfunction during northern winter. *Mon. Wea. Rev.*, **113**, 941-961.
- Wheeler, M., and G.N. Kiladis, 1999: Convectively coupled equatorial waves: Analysis of clouds and temperature in the wavenumber-frequency domain. *J. Atmos. Sci.*, **55**, 374-399.

- \_\_\_\_\_, \_\_\_\_\_, and P.J. Webster, 2000: Large-scale dynamical fields associated with convectively coupled equatorial waves. *J. Atmos. Sci.*, **57**, 613-640.
- Yamagata, T., and Y. Hayashi, 1984: A simple diagnostic model for the 30-50 day oscillation in the tropics. *J. Meteor. Soc. Japan*, **62**, 709-717.
- Yano, J.-I., and K. Emanuel, 1991: An improved model of the equatorial troposphere and its coupling with the stratosphere. *J. Atmos. Sci.*, **48**, 377-389.
- Yu, J.-Y., C. Chou, and J.D. Neelin, 1998: Estimating the gross moist stability of the tropical atmosphere. *J. Atmos. Sci.*, **55**, 1354-1372.